Università degli Studi dell'Insubria

Dipartimento di Scienza e Alta Tecnologia

Tesi di Dottorato in
Scienze Chimiche ed Ambientali

Employing Theoretical Methods for Chemical Prediction: a Ticket into Copolymerization, Metal-Organic Catalysis and Antioxidants

Supervisor

Prof. Massimo Mella

Candidate

Mario Vincenzo La Rocca

XXX Cycle - 2014/2017

Abstract

This thesis presents computational investigations aimed to the prediction of several chemical properties and reactivities. Density functional theory combined with kinetic Monte Carlo methods has been used to simulate experiments by means of theoretical models. At the beginning, the thesis shows an example of how computational chemistry can provide useful information about the chemistry in solution of anion receptor, otherwise not available by experimental measurements. The second discussed topic, developed during my visiting period in Paris in the group of Prof. Carlo Adamo, regards the prediction of antioxidant activity, *via* determining an energetic parameter that correlate well with experimental data. Then, the attention moves on the description of a Copper catalyzed alkoxyhalogenation of ureas and carbamates, in which we rationalized the mechanism providing indications about the crucial step of the reactions. Finally, we focus on the copolymerization mechanism: we proposed a synergistic DFT/kMC approach aimed to reproduce in depth the chain's microstructure of copolymers carried out by an atomic-transfer radical polymerization and a homogeneous catalyzed copolymerization; the results help to describe the copolymers' features, looking *via* a "virtual microscope" the way the comonomers distribute themselves along the chains.

Acknowledgments

First of all, I want to thank my supervisor, professor Massimo Mella, for the patience and the determination in instilling his knowledge and his way to make research. Without him nothing would have been possible. My thanks also go to dott. Lorella Izzo and Andrea Tagliabue for the precious scientific collaboration and personal support. I would like to thank professor Carlo Adamo, Ilaria Ciofini and all the group of ENSCP, past and present, where I spent my visiting PhD period, for the help in my growth that led to the work on antioxidants. My acknowledgement goes to prof. Gianluigi Broggini of Università dell'Insubria and prof. Valeria Amendola of Università di Pavia, for the collaborations on the studies about organic catalysis and anion receptor, respectively.

From the bottom of my hear I thank all the people not directly involved in my thesis, all my lifelong friends for the support during the PhD, despite the hundreds of kilometers that separated us.

Last but not least, I thank my family, for the devoted presence and the unconditional love they give me every moment in my life.

Author's Declaration

The work presented in this thesis is the original work of the author, except where references have been made to other sources.

Chapter 2 "*Halogen-Halogen bond: DFT contribution into rationalization and interpretation of experimental results*" is adapted from the paper of Amendola *et al.*[1] in accord with the copyright policy of the ©Royal Society of Chemistry.

The first half of Chapter 3 "*Benchmarking the DFT methodology for antioxidant properties prediction*" is adapted from the paper of La Rocca *et al.*[2] following the indication of ©Springer-Verlag Berlin Heidelberg.

The first half of Chapter 5 "*Prediction of Copolymer Composition*" is adapted from the paper of Mella *et al.*[3] in accord with the copyright policy of ©Wiley Periodicals.

No parts of this work have previously been submitted for any other degree.

[1] V. Amendola, G. Bergamaschi, M. Boiocchi, N. Fusco, M. V. La Rocca, L. Linati, E. Lo Presti, M. Mella, P. Metrangolo, A. Miljkovic, *RSC Advances*, **2016**, 6, 67540.

[2] M. V. La Rocca, M. Rutkowski, S. Ringeissen, J. Gomar, M.-C. Frantz, S. Ngom, C. Adamo, *Journal of Molecular Modeling*, **2016**, 22, 250.

[3] M. Mella, M. V. La Rocca, Y. Miele, L. Izz, *Journal of Polymer Science Part A:Polymer Chemistry*, **2018**, 16, 1366.

Contents

List of Figures

List of Tables

Chapter 1

Introduction

In this thesis, *ab initio* and DFT quantum chemical methods are employed for several in depth studies of molecular properties and reaction mechanisms. Well know post-Hartree-Fock quantum chemical methods and stochastic simulation approaches are intermixed, the synergy between them providing all the tools needed to evaluate the impact and validity of reaction mechanisms, for instance helping to rationalize radical and homogeneously catalyzed copolymerizations. The global aim of the thesis is thus to create the ability of recognizing which are the suitable theoretical methods to answer a chemical problem and how to combine them, in order to foster the potentially positive impact that theoretical chemistry can have in those contexts.

The theory of all *ab initio* methods starts from the goal of solving the Schrödinger equation [1] given the nuclear position, with the wavefunction needing to be antisymmetric to satisfy Pauli's exclusion principle, [2] it can be represented as a determinant of molecular orbitals called *Slater determinant.* [3–5] In this respect, the Hartree-Fock theory (HF) was one of the first approach hinging on the variational theorem proposed for the determination of an approximate wavefunction: indeed the HF algorithm makes a few simplifications, the most relevant is the neglect of electron correlation that leads to several deviations from experimental results. The methods that try to improve on such shortcoming are collectively called post-Hartree-Fock (pHF-M) methods and, depending on the need, there is at least one that can be employ to analyze specific chemical properties. One of pHF-M that incorporate electron correlation is the *configuration interaction (CI)*

method: it employs a linear combination of Slater determinants as wavefunction or, in other words, mixes different electronic configurations. [6] As the main problems of this method are the long CPU time and large memory required, it is *de facto* limited to relatively small systems. Besides, it not size consistent, a shortcoming corrected in 1966, when Čížek developed the *coupled cluster method* that efficiently treat electron correlation expanding exponentially the wavefunction (singles, doubles and triples excitations give the CCSD and CCSD(T) methods). As the new mathematic treatment allowed the calculation of the electronic structures of larger chemical systems reducing the computational time with respect the CI methods and it afforded a well-balanced description of electron correlation in practical computational times, CCSD(T) method received the epithet of *golden theory*.

Despite the evident advances, the main problem of the CI and related methods is the scaling with the number of electrons and basis functions, *de facto* the golden theory (CCSD(T)) has a scaling factor of N^7, while CCSD has a scaling factor of N^6; this reduces also the application of the coupled cluster methods to small systems and may induce a computationally oriented chemist toward alternative approaches. For instance, the Møller-Plesset perturbation theory applies the perturbation theory at different orders to evaluate correlation energy. [7] Unfortunately, MP theory at high orders is not always a convergent theory; besides, various molecular properties calculated at MP3 and MP4 level may not be better than their MP2 counterparts, even for small molecules. [6, 8] All these circumstances lead us to choose the MP2 as suitable method for the investigation of intramolecular interaction energies in the case shown in the **Chapter 2** of the thesis.

Chapter 2 is focused on the study of novel iodiopyridinium-based receptors, which are able to bind halogen anion in solution. The population analysis *via* Møller-Plesset perturbation theory of several receptor-halogen conformers helped clarifying the intensity of hydrogen-anion and halogen-anion interactions and helped the interpretation of ^{1}H-NMR titrations. [9] This is an example of a computational support on the experimental measurements in solution by means of the MP2 method; unfortunately, the study required also calculations on oligomeric

receptors (i.e. going from 26 to 61 atoms), systems for which the MP2 required too much hardware resources, a fact forcing upon us a change of strategy.

The Møller-Plesset perturbation theory at second order has a scaling factor of N^5, lower than CI and CC methods but still too high for big molecules or calculations requiring a large amount of energy/force calculation. In the 1990s the *density functional theory* (DFT) was proposed as an alternative way to incorporate electron correlation more efficiently, grounded on the Hartree-Fock method: the basic concept of DFT is to make possible performing high-speed calculations on many-electron systems by representing the energy as a functional no longer of the orbitals, but rather of the electron density, decreasing the scaling factor of at least of one integer power. Many exchange-correlation functionals were developed on the basis of different physical models and they can be classified based on their characteristics: *local density approximations (LDA)* are functionals of only the electron density; *generalized gradient approximation (GGA) functionals* correct LDA functionals introducing the density gradient; *meta-GGA functionals* correct GGA functionals exploiting the kinetic energy density, finally, *hybrid functionals* mix the Hartree-Fock exchange integrals at a constant ratio semiempirically defined to reproduce accurate properties. In this respect, the huge number of DFT methods proposed in literature can make the choice difficult when a new chemical problem is confronted. The study reported in the **Chapter 3** is an example of how theoretical chemistry can establish the suitable DFT method for the investigation of a molecular characteristic.

In the **Chapter 3**, the desire of developing a theoretical recipe to gauge the antioxidant properties of small organic molecules gave us the opportunity to investigate the behavior of several functionals in the evaluation of the key properties related to the activities of two prototypic anti-oxidants, namely quercetin and edaravone. To help choosing a functional, we obviously needed a benchmarking step, during which the performances of each functional were compared with a high-level theoretical method. Thus, we selected 21 hybrid exchange-correlation functionals and calculated the cumulative mean absolute error based on the bond dissociation enthalpy (BDE), ionization potential (IP) and proton dissociation enthalpy (PDE). Other computational parameters were also consid-

ered; for instance, we evaluated basis set and solvent effects. With the benchmark results suggesting the most appropriate method, we computed the BDE, IP, PDE, proton affinity (PA) and electron transfer enthalpy (ETE) of 15 flavonols and we correlated the DFT results to experimental data with the final aim to recognize which computed enthalpy could be employed for the theoretical prediction of antioxidant activity. [10]

Another important feature of DFT methods is the possibility to compute accurate transition state geometries and energies in a reasonable time. This fostered the diffusion of DFT as a tool to investigate reaction pathways in organic reactions, an exercise we carried out in **Chapter 4**. In particular, we investigated the mechanism of the alkoxyhalogenation of alkynyl ureas catalyzed by Copper(II) salt. The reaction mechanism proposed on chemical grounds and studied *via* DFT starts with a intramolecular cyclization assisted by $CuCl_2$ and leads to formation of a five-membered-ring intermediate. The intermediate undergoes halogenation by N-chlorine-succinimide, during which a chlorine substitutes the coordinated salt conserving the configuration of the double C=C bond. The final product is obtained *via* a loss proton. The DFT study carefully investigated also the monomers and dimers preequilibria involving copper salt to rationalize the reaction selectivity towards which heteroatom closed the cycle and the C=C double bond configuration. Having proved ourself able to justify the experimental products, an identical approach was exploited to study the mechanism of a similar reaction involving carbamates, an effort providing a first indication on the validity of our model and the prospect of revealing the key intermediate that may be useful to predict the final product.

Still focusing on reactivity, **Chapter 5** regards the use of DFT to study, first, a radical copolymerization, and subsequently a Ziegler-Natta homogeneous copolymerization of olefins. The goal of the Chapter is to provide a theoretical framework capable of simulating the chains' growth and the details of the microstructure of the copolymers. In this respect, it is worth remembering that the in-depth characterization of how the monomers are distributed along the chains can help the investigation of the process/phenomena that control the behavior of copolymerizations and thus the final properties of the copolymers. To

do this, we exploited DFT calculations to obtain the probabilities of all possible monomer-growing chain reactions *via* the Eyring's transition state theory. [11–13] In the initial case of the methylmethacrylate/2-(dimethylamino)ethyl methacrylate (MMA/DMAEMA) radical copolymerization in toluene, we also had to consider the fact that it can be influenced by different microphase compositions which influence the probabilities *via* monomers-chain segregation equilibria. In principle, the needed partition Ks could be computed via equilibrium Monte Carlo (MC) or Molecular Dynamics (MD) simulations employing explicit solvent models and appropriately tuned force fields; alternatively, one may simply optimize structural isomers with the DFT approach, select the minima with the lowest Gibbs' energy G and estimate the G for such a subset of species. The chain are obtained by directly simulating subsequent monomer additions exploiting the intrinsic stochastic nature of the "ultimate model" kinetic scheme *via* a *kinetic Monte Carlo* (kMC) code; this receives as input the $\Delta G^{\ddagger}$ and ΔG^{o} from DFT calculations. Such procedure allowed us to obtain all the distributions and correlation functions that we thought could help understanding all the structure-properties relations of the copolymers. [14] As for the I part of **Chapter 5**, a similar synergistic DFT/kMC approach was also employed but, this time, was applied to the much more complicate mechanism of the homogeneous catalyzed copolymerization. Thanks to DFT results, we were indeed able to reveal the complexity of the mechanism, while a kMC algorithm was exploited to simulate alternative kinetic models in order to evaluate the relative influence of mechanistic parameters. The results shed some light on a few aspects of thus reaction generally not placed in the foreground in previous literature and lay the foundations of a method for the prediction of copolymer microstructures.

Chapter 2

Halogen-Halogen Bond: DFT Contribution into Rationalization and Interpretation of Experimental Results

2.1   Introduction

Anion recognition has been an important issue in supramolecular chemistry for four decades, which is still attracting attention as shown, for instance, by the number of reviews published on the topic in 2015. [15–21] In particular, most purely organic receptors have been setting up their interactions with anions based on electrostatic forces and/or hydrogen bonding (HB). [22,23] The latter, in particular, has attracted the specialists in the field. [24,25] This is not surprising for several reasons: first of all, chemists feel inspired by Nature, and Nature mostly bases self-assembling and recognition processes on HB. Moreover, HB can be effective in polar solvents, allowing to achieve highly selective recognition of anionic species even in water. In the field of anion recognition, the importance of the so-called "non-conventional" HB interactions based on "weak" H-bond donors, e.g. nucleophilic aromatic C atoms, has also been recognized. [26]

Thanks to the work by Metrangolo and Resnati, another type of non-covalent interaction, i.e., halogen bonding, has become popular among supra- molecular chemists, and in the last few years it has been having a significant impact on the

supramolecular world. [27–30]

Halogen bonding (XB) was proved to have significant similarities with HB, allowing to build sophisticated supramolecular architectures and functional materials, and leading to selective anion recognition in competing media, as shown by Beer [31] and others. [32–38] HB and XB can be considered as the most relevant among non-covalent interactions. [39–41] They both are characterized by high directionality and strong attraction, leading to contact distances shorter than the sum of the van der Waals radii of the involved atoms. For both HB and XB, interaction involves an electrophilic species (i.e., H and X atoms for HB and XB, respectively) and a nucleophilic atom therefore binding has a dominant electrostatic contribution. However, recent theoretical and experimental studies have shown that polarization, charge transfer, and dispersion forces also play an important role. [42–45]

The similar features of HB and XB have stimulated chemists to compare and contrast (supra)molecular systems based on either one or the other type of interactions, with a special regard to the field of anion recognition in solution. [46, 47] An other experimental evidence regards the HB-donor group's influence: for example a stronger anion binding is obtained when several HB-donor groups converge towards the anionic guest, better if within a well-defined cavity. [48, 49] Moreover, positive charges close to HB-donor groups in a receptor have a synergistic effect, thus increasing the interaction.

The goal now is to move the field forward by studying the synergistic effect of positioning a number of positive charges, XB donors and non-classical HB donor groups (i.e. C–H) around the bowl-shaped cavity of a tripodal host. To do this, we studied new receptors containing three 3-iodopyridinium arms appended to trialkylbenzene platforms, using as a model compound the N-benzyl-3-iodopyridinium was choose. Such species were synthesized by the group of Amendola in Pavia [9] and their anion binding were investigated capabilities through NMR and UV-vis spectroscopies.

X-ray data in solid state showed peculiar structure where XB are present;

however, nuclear magnetic resonance and UV-Vis spectra are performed as titration methodology studying the complexes in solution. The compounds are able to interact *via* XB and HB but the only information about how they coordinate the anions came from the solid state; the equilibrium between XB and HB interaction in solution, however can be inspected only by means of DFT. For this purpose, we calculated the isomeric "ion pair dissociation energies" (IPDE) as a way to gauge the relative contribution provided by HB and XB to the stability of the complexes. The IPDE is defined as

$$IPDE = E(S^+/X^-) - E(S^+) - E(X^-) \tag{2.1}$$

where S^+ is the pyridinium cation and X^- is the anion. Furthermore, ^{1}H-NMR chemical shifts of all detected geometries of the complexes are computed in order to rationalize the experimental titration results.

2.2 Computational Details

All calculations were carried out with the Gaussian 09 package. [50] Conformation analysis and geometry optimizations were carried out at the MP2 level for complex $\mathbf{1a}^+/X^-$, $\mathbf{1b}^+/X^-$ and $\mathbf{1c}^+/X^-$. For the complex $\mathbf{2}^{3+}/X^-$, structural optimizations were carried out using the B3LYP functional due to the larger species size. [51–54] MP2 single point energies were subsequently obtained employing the B3LYP geometries. A polarized/augmented double zeta basis set (6-31+G(d,p) for light atoms and he LANL2DZ basis set augmented with the diffuse function from the aug-cc-pVDZ set for the halogen atoms) was used in all the calculations; effective-core potentials (LANL) were also used for Cl, Br, and I to reduce computational costs. Solvent effects were evaluated using the PCM model and different solvents were selected in order to reproduce the experimental conditions. [55] Basis set superposition errors were estimated via the Counterpoise approach at the MP2 level in all cases. The calculation of chemical shifts for the hydrogen atoms was carried out employing the GIAO procedure as implemented in Gaussian 09. [56, 57]
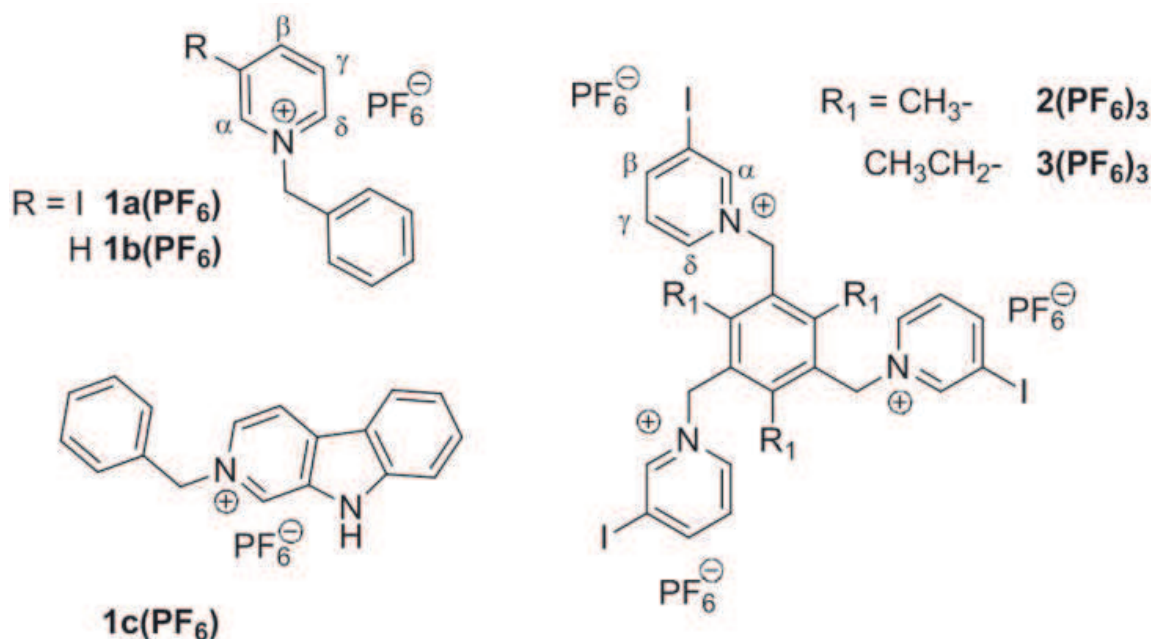
Figure 2.1: Pyridinium-based anion receptors studied.

Anion	$\log K_{11}/\mathbf{1a}^+$	$\log K_{11}/\mathbf{1b}^+$	$\log K_{11}/\mathbf{1c}^+$
Cl$^-$	2.30 [2.27]	2.06	[3.20]
Br$^-$	1.98 [2.08]	n.d.	[2.48]
I$^-$	1.70	n.d.	n.d.

Table 2.1: Affinity constants determined by ^{1}H-NMR titrations with halides as TBA salts; constants obtained through UV-Vis titrations are reported between square brackets.

2.3   Single-Branched Pyridinium-Based Systems

In Figure 2.1 we show the schematic structure of the proposed molecules. In the case of the model system $\mathbf{1a}^+$, the formation constants of the 1 : 1 complexes with chloride, bromide, and iodide were calculated from the fitting of the ^{1}H-NMR titration data (see Table 2.1). ^{1}H-NMR titrations with halides evidenced the preference of $\mathbf{1a}^+$ for the chloride anion, followed by bromide and iodine. This is not surprising, as it is the common trend observed in pyridinium systems.

Upon anion addition, protons in the ortho positions to the nitrogen, i.e. Hα and Hδ, are the most affected. Therefore, the corresponding signals undergo a significant downfield shift, e.g., $\Delta\delta=+0.53$ ppm and $+0.43$ ppm for Hα and Hδ, respectively (a titration example is reported in Figure 2.2). Notably, also protons Hβ in $\mathbf{1b}^+$ are deshielded even if to a lower extent ($+0.40$ ppm up to 20 eq. of chloride). In principle, the iodopyridinium-based model compound $\mathbf{1a}$ is capable
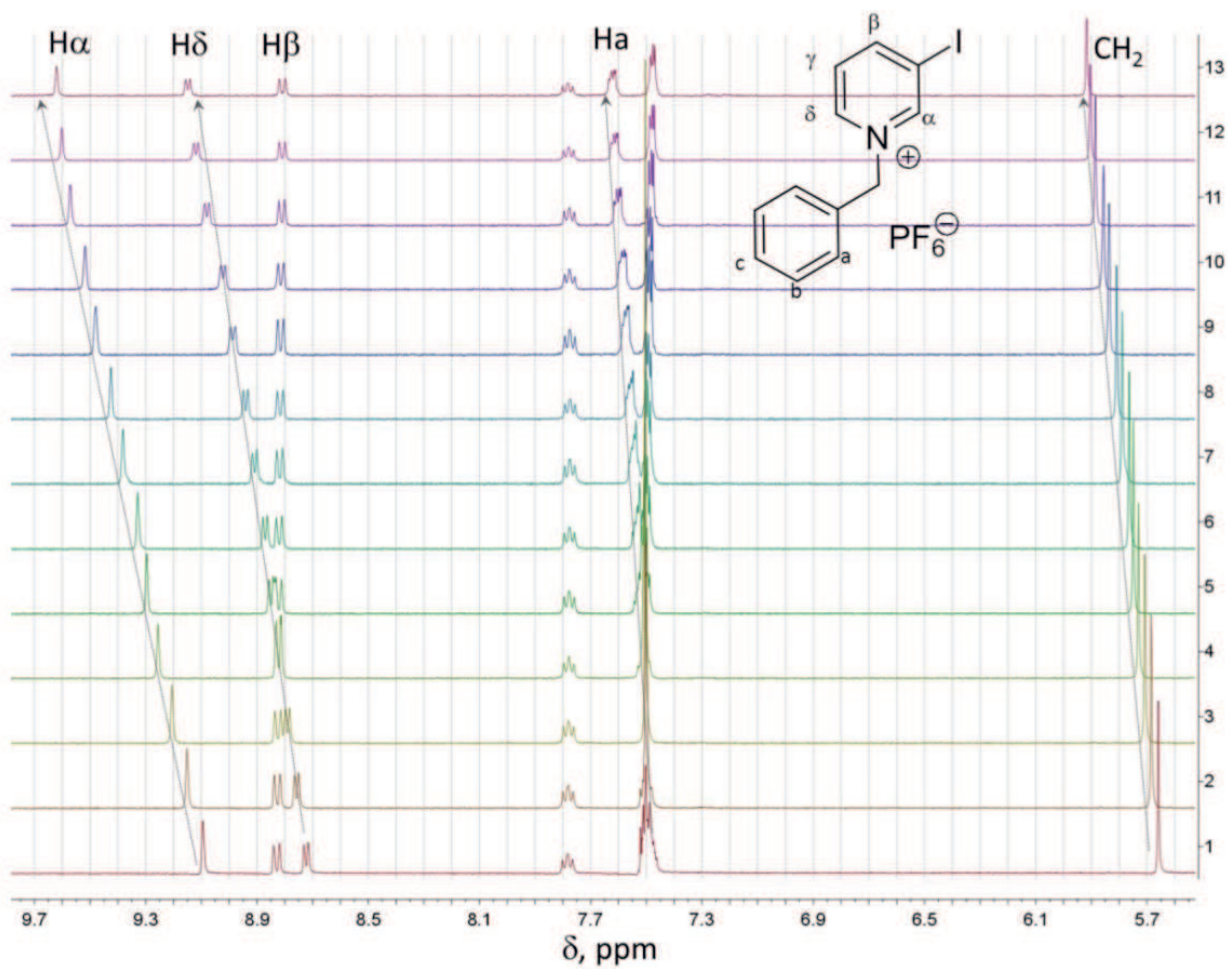
Figure 2.2: Family of ^{1}-NMR spectra for the titration of $\mathbf{1a}^+$ with TBACl.

of binding halide anions via different modes. XB is one, but also HB may be present, either in a mono- or bi-dentate fashion. Anion$\cdots\pi$ interactions may also play a role. [58] The observed downfield shifts are more indicative of HB rather than XB, for which upfield shifts would be expected. [59] However, disentangling the different contributions in solution is difficult as different binding modes may occur simultaneously. The binding constants of $\mathbf{1a}^+$ and $\mathbf{1b}^+$, shown in Table 2.1, point out that anion affinity is higher for $\mathbf{1a}^+$ than for the simple N-benzyl pyridinium analogue. It is possible thus to conclude that the iodine-substituent has a positive effect on the anion binding capabilities of pyridinium receptors, as a likely consequence of its electron withdrawing effect on the pyridine hydrogen atoms.

The interaction of $\mathbf{1a}^+$ with chloride and bromide was also studied by UV-vis titrations in acetonitrile. The molecular cation displays a band at 290 nm ($2.1\cdot10^3$ $M^{-1}cm^{-1}$), attributable to a charge transfer that involves the iodine substituent;

from the fitting of the profiles, the affinity constants for both chloride and bromide could be determined (2.27 and 2.08 log units, respectively), confirming the NMR titration results. Interestingly, the obtained affinity constants are lower than those determined in the same conditions by Amendola *et al.* [60] for the 9H-β-carbolin-2-ium system (see $\mathbf{1c}^+$ in Table 2.1). This suggests that the NH group in 9H-β-carbolin-2-ium may have a stronger impact on the affinity towards anions than the iodine-substitution in the studied pyridinium-based receptors.

2.3.1   Theoretical Contributions

To understand the origin of the higher anion affinity for $\mathbf{1a}^+$ compared to $\mathbf{1b}^+$, we computationally studied the two model systems in presence of Cl^- and Br^-. Several low-lying solution conformers were optimized. The corresponding IPDE values are within 1.8 kcal/mol (see Table 2.2), although the conformers show different "modes of interaction" with the anion (see Figure 2.3 and 2.4, for $\mathbf{1a}^+$ and $\mathbf{1b}^+$ with Cl^-, respectively). Regardless, the computational results strongly support the experimental data as far as the relative stability of the complexes is concerned (see also Figure 2.5 for $\mathbf{1c}^+/Cl^-$), even if this may be due to entropic effects due to the lower population of low lying isomers as in the iodide case. Our theoretical results suggest, in fact, that the halogen-bonded species (d) shown in Figure 2.3 lies at least 0.9 kcal/mol above the other stable conformers found for $\mathbf{1a}^+/Cl^-$ and $\mathbf{1a}^+/Br^-$ (i.e., Figure 2.3 (a) and (c), respectively), and has a lower IPDE, which indicate that it is not the most relevant species occurring in solution. Interestingly, the structures shown in Figure 2.3 and 2.4 also fully support the NMR assignments (presented as example in Figure 2.2) justifying the incremental shifts of the hydrogen atoms involved in the interaction with the anions.

Chemical shifts computed at the B3LYP/6-31+G(d,p)/GIAO level, in fact, suggest that Hα, Hδ and the methylene protons should all be substantially shifted downfield ($\Delta\delta$ = 1.0–3.3 ppm) for the species shown in Figure 2.3 (a) and (b). On the other hand, Hβ and Hγ should remain mostly unchanged. Only minor shifts are instead predicted for the X-bonding species (i.e., Fig. 2.3 (d)).

Compound	IPDE (kcal/mol) X=Cl$^-$	IPDE (kcal/mol) X=Br$^-$	IPDE (kcal/mol) X=I$^-$
1a$^+$	7.06$^{(a)}$; 6.67$^{(b)}$; 6.64$^{(c)}$; 5.86$^{(d)}$	6.48$^{(a)}$; 6.13$^{(b)}$; 6.84$^{(c)}$; 5.58$^{(d)}$	6.04$^{(a)}$; 5.68$^{(b)}$; 7.17$^{(c)}$; 5.34$^{(d)}$
	[5.65]$^{(a)}$; [5.39]$^{(b)}$; [4.93]$^{(c)}$; [4.12]$^{(d)}$	[4.84]$^{(a)}$; [4.95]$^{(b)}$; [5.07]$^{(c)}$; [3.91]$^{(d)}$	[4.58]$^{(a)}$; [4.34]$^{(b)}$; [5.12]$^{(c)}$; [4.24]$^{(d)}$
1b$^+$	6.50$^{(a)}$; 5.62$^{(b)}$	6.00$^{(a)}$; 5.78$^{(b)}$	n.d.
	[5.22]$^{(a)}$; [4.14]$^{(b)}$	[4.15]$^{(a)}$; [4.72]$^{(b)}$	n.d.
1c$^+$	9.83	8.75	n.d.
	[8.40]	[7.28]	n.d

Table 2.2: Ion pair dissociation energies. Solvent effects are introduced *via* PCM model. The order of the isomers is coherent with figures. Between square bracket, counterpoise corrected IPDE are reported.
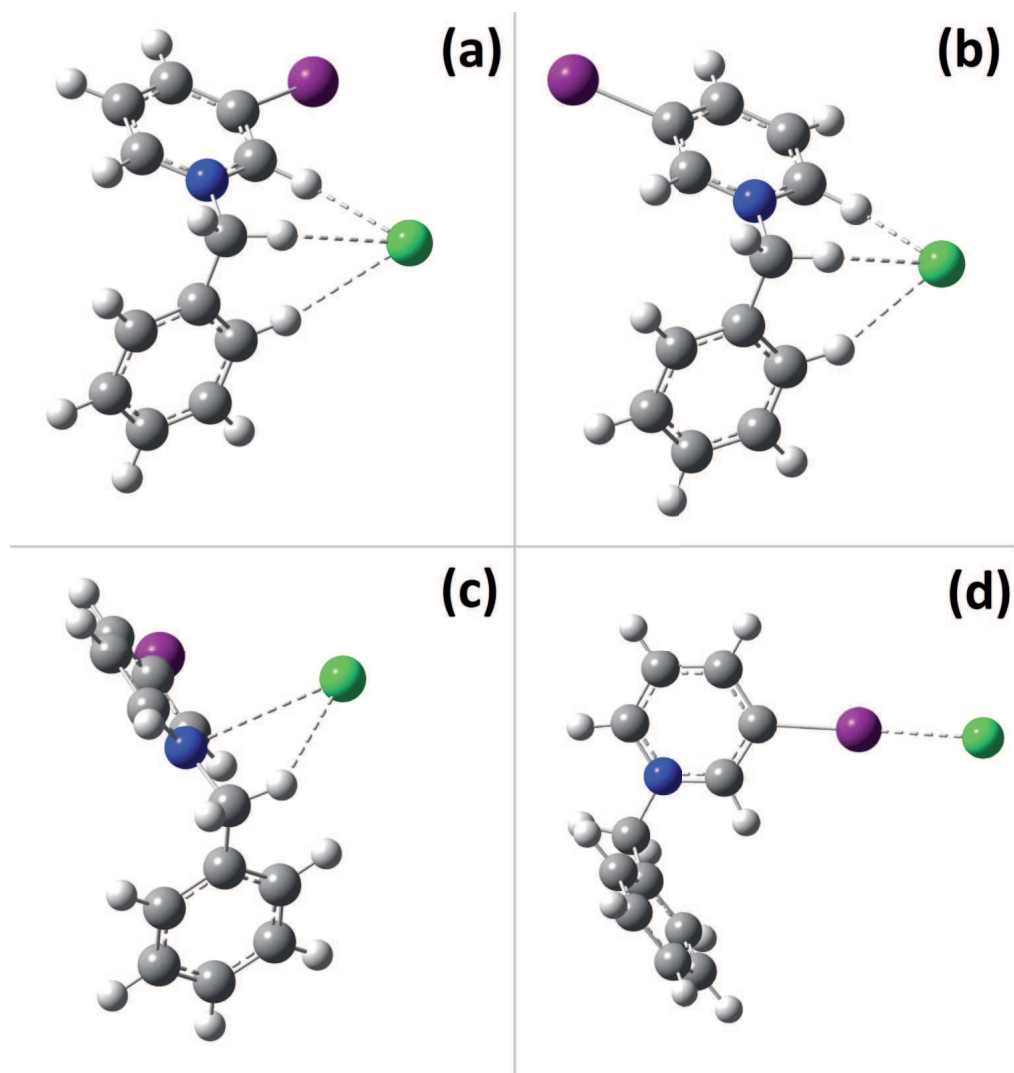
Figure 2.3: Geometries of four possible conformers for the binding of Cl^- by $\mathbf{1a}^+$.
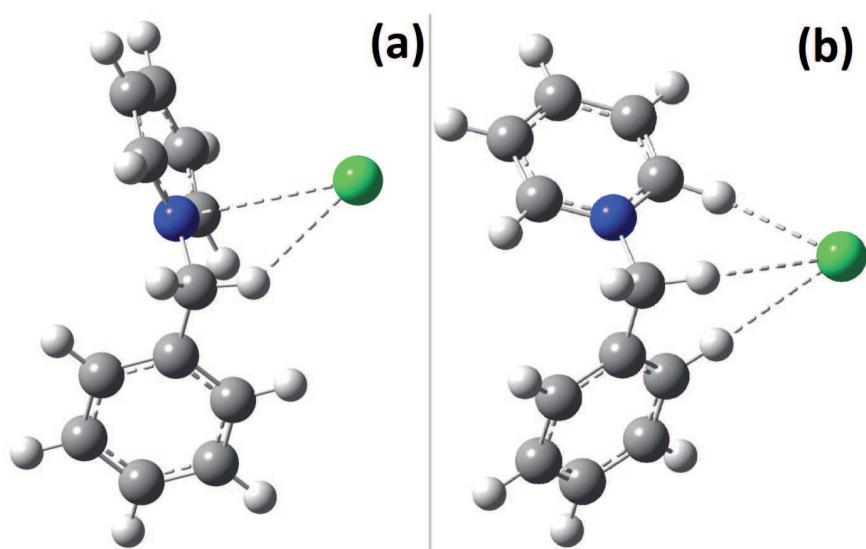
Figure 2.4: Geometries of two possible conformers for the binding of Cl^- by $\mathbf{1b}^+$.
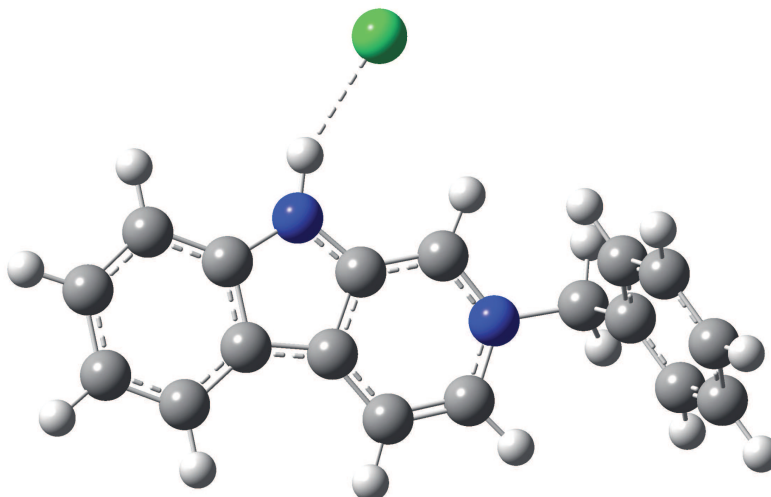
Figure 2.5: Optimized structure of the **1c**$^+$/Cl$^-$ complex, from which it is evidenced the strong HB with Cl$^-$.

As for the size of the computed chemical shifts, these appear larger than the experimental data. Such apparent discrepancy can be readily rationalized, considering that the measured shifts represent the average of all possible structures accessible within the time scale of the NMR measurement. In this respect, the small energy differences reported in Table 2.2 suggest that the ion pairs are highly fluxional, so that the structures in Figure 2.3 and 2.4 represent only limiting cases. This is corroborated by the energy profiles shown in Figure 2.6. The fluxionality also explains the presence in the NMR spectrum of a singlet for CH$_2$, instead of the double doublet expected on symmetry considerations (i.e., the symmetry-breaking induced by the interaction with the anion). Albeit lower in magnitude, Counterpoise corrected IPDE (Tab.2.2) support our conclusions.

2.4   Tripodal 3-iodopyridinium-Based Receptors

Bowl-shaped positively charged systems, such as those obtained by appending three pyridinium groups to a tris(alkyl) benzene scaffold, are known to form stable complexes with anions in acetonitrile solution. Studies performed by Steed, [61] and independently by Fabbrizzi, [60, 62] demonstrated that anion affinity is strongly influenced by (i) the receptor preorganization imparted by the alkyl chains on the platform, and depends on (ii) the presence of HB donor
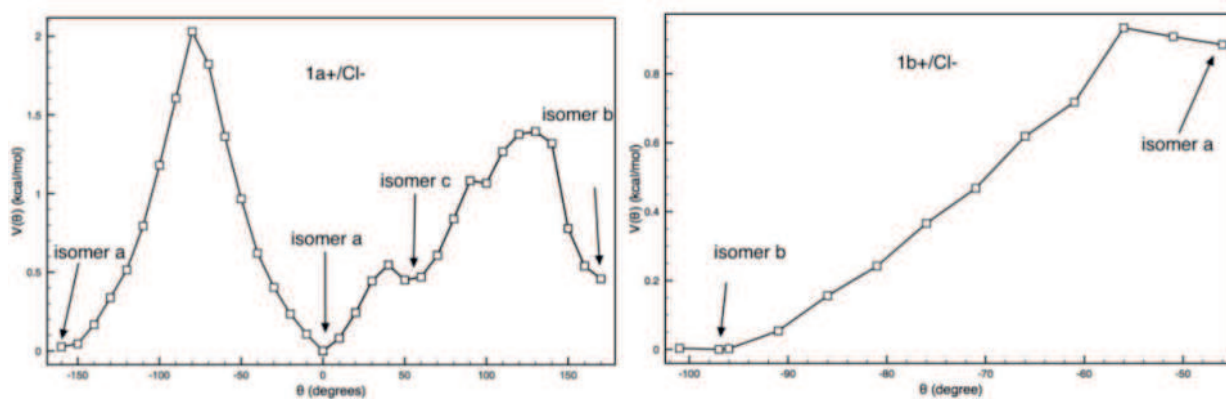
Figure 2.6: Relaxed torsional scan around the CH_2-N bond in the $\mathbf{1a}^+$/ Cl^- and $\mathbf{1b}^+$/Cl^- complexes.

groups on the pyridinium arms.

In order to shed light on how appending XB-donor groups on pyridinium-based tripodal receptors affects their anion binding capabilities, $\mathbf{2}(PF_6)_3$ and $\mathbf{3}(PF_6)_3$ were previously synthesised and experimental studied. Anion binding studies were performed by UV-vis and NMR titrations both in pure acetonitrile and in the presence of 10% DMSO. Both $\mathbf{2}^{3+}$ and $\mathbf{3}^{3+}$ display an absorption band at about 295 nm; upon anion addition (as the TBA salt), an hyperchromic effect was observed.

The fitting of the titration profiles suggested the presence of a single equilibrium, leading to the formation of a 1 : 1 complex with all anions. The binding constants are shown in Table 2.3. The affinity trend is similar in the two receptors (i.e., $Cl^- \gg Br^- > CH_3COO^- > HSO_4^-$, $NO_3^- > I^-$). However, stronger binding was observed for $\mathbf{3}^{3+}$ with spherical anions, Cl^- and Br^- in particular. This might be due to the higher preorganization imparted by triethyl arms to the bowl-shaped receptor, compared to the methyl groups of $\mathbf{2}^{3+}$.

Further information on the interaction of $\mathbf{3}^{3+}$ with anions in solution was obtained through the ^{1}H-NMR titration with TBACl (the family of spectra is shown in Figure 2.7). Protons Hδ, in the para position to Iodine, seem to be directly involved in the binding, undergoing a downfield shift of $\Delta\delta = +0.70$ ppm upon chloride addition (vs. +0.43 ppm for $\mathbf{1a}^+$). Protons Hα are also affected, even if to a significantly lower extent ($\Delta\delta$ +0.14 ppm for $\mathbf{3}^{3+}$ vs. +0.54 ppm for

Anion	$\log K_{11}/\mathbf{2}^{3+}$	$\log K_{11}/\mathbf{3}^{3+}$
Cl−	4.65 [3.70]	5.16 [4.07]
Br^-	4.46	4.91
I^-	3.59	3.71
CH_3COO^-	4.45	4.40
HSO_4^-	4.13	4.08

Table 2.3: Affinity constants determined by UV-Vis titrations with halides as TBA salts; constants obtained through ^{1}H-NMR titrations are reported between square brackets.

$\mathbf{1a}^+$). The slight shielding of protons Hβ can be attributed to the increase of the electron density on the receptor framework upon anion binding. These results indicate that the interaction with the chloride anion mainly involves the ortho-protons of pyridinium groups. Notably, in most examples in the literature and in the mono-branched compound $\mathbf{1a}^+$, the ortho-protons are the most affected by anion binding, due to the direct participation of C–H bonds in the interaction (as HB-donor groups). [60, 62]

2.4.1 Computational Contributions

The interpretation of the experimental data is fully supported by the theoretical analysis of the $\mathbf{2}^{3+}/Cl^-$ or $\mathbf{3}^{3+}/Br^-$ complexes (Table 2.4). As in the case of $\mathbf{1a}^+$, various conformers can be formed. Their structures differ in the relative position of the pyridinium groups with respect to the plane of the phenyl ring ("3-up" or "2-up, 1-down"). Differences are also observed in the position of the Hα and Hδ atoms pointing towards the anion. The four lowest lying species with Cl$^-$ are shown in Figure 2.8; these low energy conformers are all within 3.7 kcal/mol, a slightly wider interval than the one seen in the case of $\mathbf{1a}^+$. Notably, the substitution of Hδ with Hα (belonging to the same pyridinium ring) in the interaction with Cl$^-$ raises the energy by 0.8 kcal/mol for the "3-up" isomer, its two conformers (in Figure 2.8 (a) and (b)) being the most stable species in solution.

As the population of the remaining two species (Fig.2.8 (c) and (d)) is expected to be low, the energy data rationalize the smaller change in the chemical shift of Hα observed upon NMR titration with chloride. The Counterpoise cor-
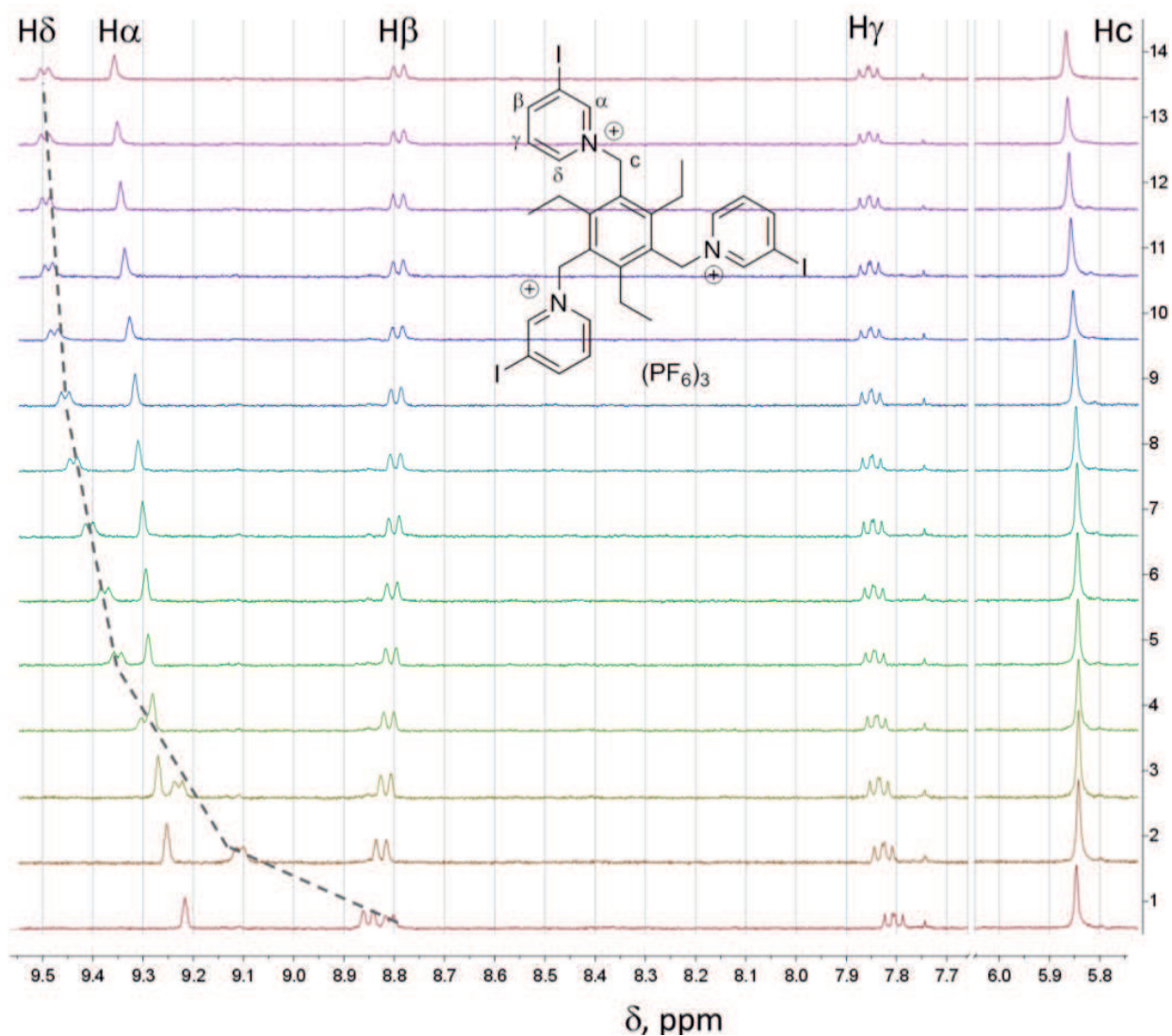
Figure 2.7: Family of ^{1}H-NMR spectra for the titration of $\mathbf{3}^{3+}$ with TBACl.

Compound	IPDE (kcal/mol) X=Cl$^-$	IPDE (kcal/mol) X=Br$^-$
$\mathbf{2}^{3+}$	$8.34^{(a)}$; $7.55^{(b)}$; $6.05^{(c)}$; $5.67^{(d)}$	$9.05^{(a)}$; $8.97^{(d)}$
	$[6.43]^{(a)}$; $[4.88]^{(b)}$; $[6.04]^{(c)}$; $[5.21]^{(d)}$	$[7.26]^{(a)}$; $[7.46]^{(d)}$

Table 2.4: Ion pair dissociation energies. Solvent effects are introduced *via* PCM model. The order of the isomers is coherent with figures. Between square bracket, counterpoise corrected IPDE are reported.
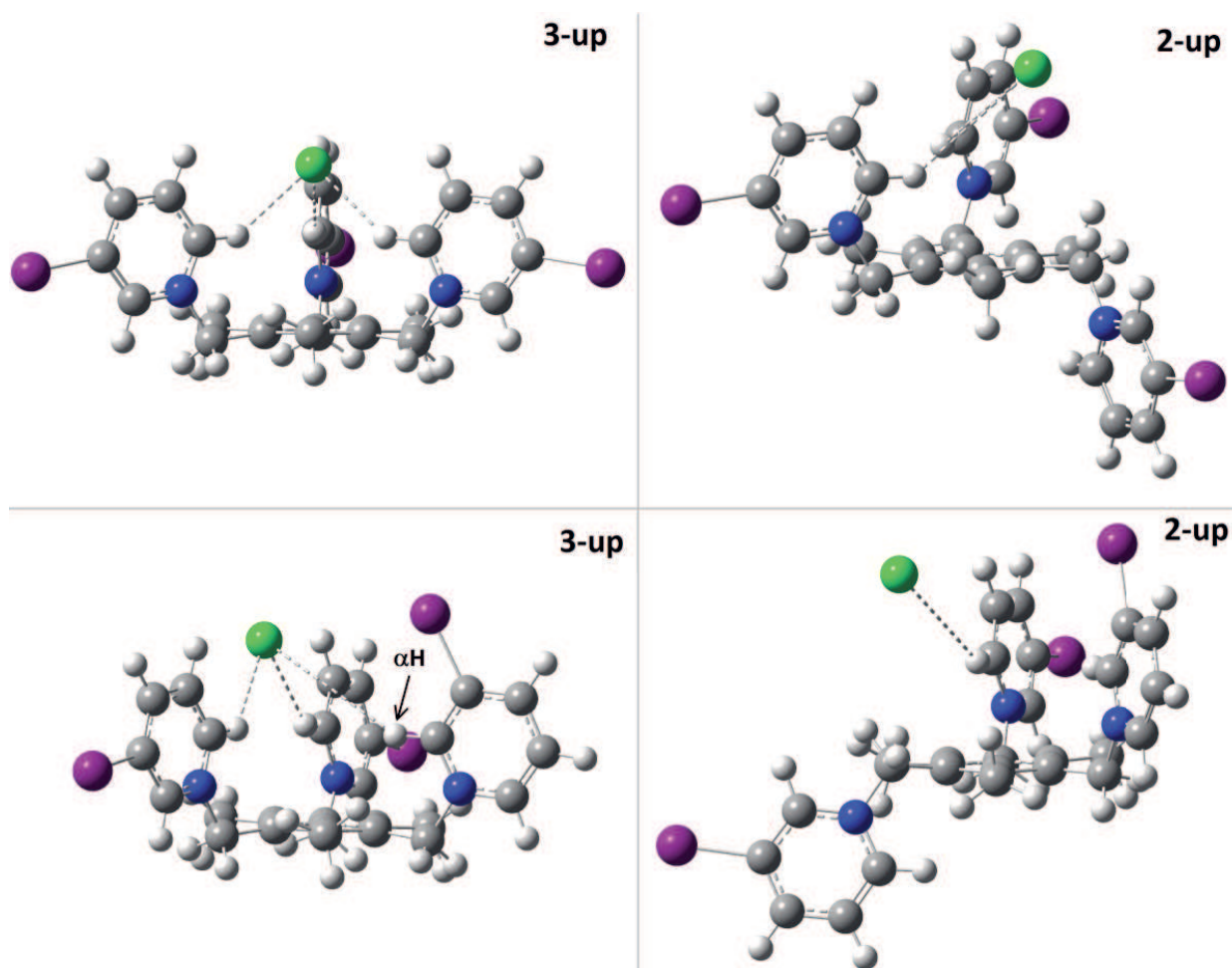
Figure 2.8: Lowest conformers for $\mathbf{2}^{3+}/\text{Cl}^-$. Note that top and bottom conformers differ due to the rotation of an iodo-pyridinium group in the up position around the CH$_2$-N bond. Such rotation substitutes Hα to Hδ in the contact with the anion.

rection supports this conclusion (Table 2.4).

2.5   Conclusion

In this work, we studied novel receptors based on 3-iodo-pyridinium units in which different types of interactions cooperate in the anion binding: (i) electrostatic forces; (ii) halogen-bonding and (iii) non-conventional hydrogen bonding interactions (i.e. with the receptor's C–H donor groups). Experimental studies in solution through UV-vis and NMR titrations pointed out that iodine atoms effectively enhance the anion binding tendencies of our pyridinium-based systems.

Computational investigation on the model compounds $\mathbf{1a}^+$ suggests that this finding may depend more on the electron withdrawing effect of iodine (on the coordinating pyridyl hydrogens) rather than on the occurrence of relevant halogen bonding in solution, despite this latter interaction dominates the binding of anions in the solid state. Notably, in the endo-coordination of the included anion, HB interactions are preferred over XBs. This may depend on the fact that all of the iodine atoms are oriented out of the cavity, due to steric congestion. In conclusion, the combination of multiple interactions within a single receptor brought about strong anion binding in solution, even in a competing medium. The results exposed herein represent a significant advance in the field of anion recognition based on HB and XB, provide valuable tips for those working in the field and encourage researchers to continue along this path, i.e. using multiple and diverse interactions within receptor cavities in order to obtain a higher selectivity.

Chapter 3

Benchmarking the DFT methodology for Antioxidant Properties Prediction

3.1   Introduction

Reactive oxygen species are constantly formed in human body by several means, including γ-rays, X-rays and UV radiations. [63–65] They play important roles in the oxidative damage of nucleic acids, lipids, proteins and carbohydrates that may result in cellular damage, aging, and human diseases. [66–71] Different studies [72, 73] have contributed to build the consensus that diets rich in fruits and vegetables have beneficial effects on human health, [74] due to their content of phenolic derivatives, well known for their antioxidant activity. [75] During the past decade, many molecules were discovered and synthesized and it is widely accepted that the radical scavenging abilities is mainly related to the presence of phenolic hydroxyl groups. [76] Their antioxidant activity as free radical scavengers can be then classified according to three possible mechanisms [76]:

- 1) hydrogen atom transfer (HAT)

$$R^{\bullet} + ArOH \rightarrow RH + ArO^{\bullet} \qquad (3.1)$$

  which corresponds to the breaking of the an hydroxyl (OH) bond

- 2) single electron transfer followed by proton transfer (SET-PT)

$$R^{\bullet} + ArOH \rightarrow R^{-} + ArOH^{+\bullet} \rightarrow RH + ArO^{\bullet} \qquad (3.2)$$

- 3) sequential proton loss electron transfer (SPLET)

$$ArOH \rightarrow ArO^- + H^+ \tag{3.3}$$

$$ArO^- + R^\bullet \rightarrow ArO^\bullet + R^- \tag{3.4}$$

$$R^- + H^+ \rightarrow RH \tag{3.5}$$
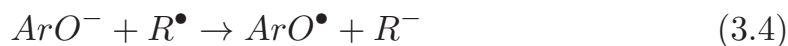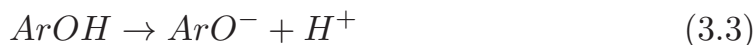
were ArOH is a general aromatic antioxidant with hydroxyl group and R$^\bullet$ a general radical.

The first mechanism is governed by the O-H bond dissociation enthalpy (BDE), which also gives an estimation of the stability of the produced radicals. The second is ruled by the ionization potential (IP) and proton dissociation enthalpy (PDE) and the third can be described by the proton affinity (PA) and the electron transfer enthalpy (ETE). [77] Others molecules, not presenting an hydroxyl group, could also have a relevant anti-oxidant activity and, in this chase, SP-LET mechanism could be dismissed. [78] The previous enthalpies can be calculated following the definitions:

$$BDE = H(\mathrm{R}^\bullet) + H(\mathrm{H}^\bullet) - H(\mathrm{R\text{–}H}) \tag{3.6}$$

$$PA = H(\mathrm{R}^-) + H(\mathrm{H}^+) - H(\mathrm{R\text{–}H}) \tag{3.7}$$

$$ETE = H(\mathrm{R}^\bullet) + H(\mathrm{e}^-) - H(\mathrm{R}^-) \tag{3.8}$$

$$IP = H(\mathrm{R}^{+\bullet}) + H(\mathrm{e}^-) - H(\mathrm{R\text{–}H}) \tag{3.9}$$

$$PDE = H(\mathrm{R}^\bullet) + H(\mathrm{H}^+) - H(\mathrm{R}^{+\bullet}) \tag{3.10}$$

An indication about antioxidant activity in solvent can be expressed by the ORAC-FL values, that is oxygen radical absorbance capacity. The assay measures the degradation of a fluorescent molecule (generally fluorescein) in presence of free radical source, the target molecule can protect the fluorescent molecule affecting the emission spectrum. Such value does not give indications about which mechanism the antioxidant go through and it is strongly dependent on the methodology. The enthalpies in the Equations 3.6, 3.7, 3.8, 3.9 and 3.10 can be evaluated using current quantum-chemical methods, i.e. several approaches were

already proposed in literature [77–94].

Focusing on the theoretical aspect, it has been clearly shown in the past that an accurate determination of the thermodynamics need the inclusion of the electronic correlation. Post Hartree-Fock methods (like couple cluster) are powerful tool but limited on systems with a limited number of atoms while the competitive accuracy/cost ratio of density functional theory (DFT) methods represent a viable alternative. However, this approach needs a calibration step where the performances of each exchange-correlation functional are assessed by a comparison with higher-level theoretical approaches (e.g., CC) or, if available, accurate experimental results. Such work, preliminary to any routine application of any DFT approach, have been carried out for reactions concerning hydrogen abstraction (see for instance References [95, 96]) suggested that functionals belonging to the so-called Minnesota family [97] are among the most reliable for energetic (see for instance Reference [94]).

In the present work, all methods belong to the so-called *Global Hybrid, Range Separated Hybrid and Double-Hybrid* functionals: hybrid functionals mix the Hartree-Fock exchange integral with generalize gradient approximation (GGA) exchange functionals at a constant ratio. As hybrid functionals, various types of functional have been developed, depending on the mixing ratios and number of parameters, among all the B3LYP [51], the first hybrid functional and most frequently used method. The range separated hybrid functionals were developed in order to fix the asymptotic decay of the potential from the global hybrid functionals: those methods include the exact HF exchange for the long-range interaction and employ the local DFT exchange for the short-range interaction by partitioning of the electron-electron interaction by some smooth range-separation function. These functionals are called long-range corrected (LC) functionals or Coulomb-attenuating method (CAM), in which the parameters are essentially determined in an empirical way. As in the case of global hybrids, usual procedure in obtaining the parameters for such functionals is the fit of a standard benchmark set of molecules to experimental thermochemical data. Finally, double-hybrid density functionals are based on a mixing of standard GGAs for exchange and correlation with Hartree-Fock exchange and a perturbative second-order correlation

part (PT2) that is obtained from the Kohn-Sham (GGA) orbitals and eigenvalues. The experiments expresses the antioxidant activity in terms of ORAC-FL but the way how they are estimated is not directly related to one of the enthalpies defined above. Therefore, the reference values used to evaluate the performance of the chosen methods are obtained *via* a theoretical Complete Basis Set method (CBS): the CBS-QB3 [98, 99], developed by George Petersson *et al.*, extrapolate several single-point energies to obtain a final "exact" energy using an infinitely large (complete) basis set. In principle this procedure removes any error due to the linear combination of atomic orbitals approximation, and any remaining disagreement with experiment is due to some other approximation such as the treatment of correlation, and represent one of the most numerically accurate theoretical method for all practical purposes.

Belonging to antioxidants are different classes of organic molecules, among which the most common are flavonols, phenolic acids, hydrozyindoles and hydroxytryptophan derivates, pyrazolones and pyrazolidones, chalcones and dihydrochalcones, phenols and triterphenes. For some of this classes, combined DFT/-experimental approach is carried out and sometimes there is good agreement between theoretical energies and experimental activities. Few examples are: resveratrol, [79] calcones, [80] edaravone and its related derivates, [87, 88, 94] hydroxybenzaldheydes and corresponding acids, [89] quercetin and taxifolin, [74] synthesized chalcones, [100] natural polyphenolic antioxidants [83] and phenols. [90, 91]

A systematic analysis on DFT performances for anti-oxidant related properties is, at the best of our knowledge, still lacking. In this context, the aim of this work is partially fulfill this gap by a deep investigation on two well-characterized antioxidants, namely edaravone and quercetin (see Figure 3.1).

Edaravone (3-methyl-1-phenyl-2-pyrazolin-5-one, EDA) also known as MCI-186 is a neuroprotective drug developed in Japan [101] while quercetin (2-(3,4-dihydroxyphenyl)-3,5,7-tri hydroxy chromen-4-one) is a member of a group of naturally occurring compounds, the flavonoids, widely distributed in plants. [102] Albeit showing very different structures, these two molecules have a similar antioxidant activity, also in vivo tests. [103] They have been therefore selected as
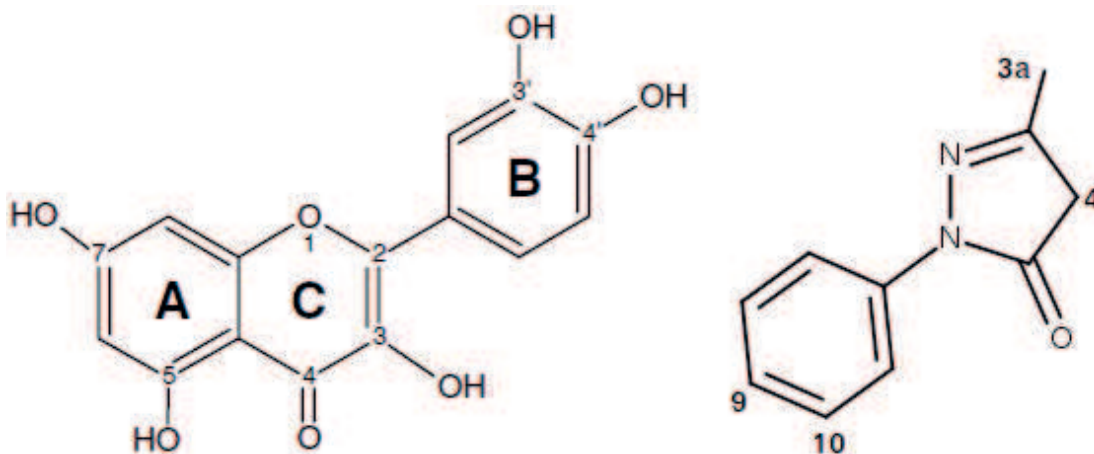
Figure 3.1: Sketches and atom labeling for quercetin (left) and edaravone (right).

test cases to study the performances of 21 functionals, selected among those most commonly used, with respect the main energetic quantities, namely IP, PDE and BDE, required to characterize the above mentioned reactions related to antioxidant activity. The other quantity, ETE, has not been considered, since the SPLET mechanism is not dominant in the edaravone, due to the absence of hydroxyl groups. [104] Others computational parameters, such as 4 basis sets and solvent model, were also considered and all the results compared to reference values obtained by a post-Hartree-Fock (HF) method developed for accurate thermochemistry (CBS-Q3) and to the few experimental data available.

After the benchmark, we define the way for a future protocol in order to predict the radial scavenger activity of OH-based antioxidants by a synergistic experimental/theoretical approach. The focused class of antioxidant is flavonols, because of the lack of previous studies and the large diffusion of these compounds. Fifteen flavonols are selected among all in order to collect much experimental data as possible and experimental data are compared with theoretical energies to carry out informations about the correlation.

3.2 Computational Details

All calculations were carried out with the Gaussian 09 package. [50] As mentioned, 21 exchange correlation functionals have been selected among those most commonly used. [51, 97, 105–123] They are reported in Table 3.1, together with the corresponding original references.

functional	% HF exchange[a]	Reference
Global hybrids		
B972	21	[105]
B1LYP	25	[106]
BMK	42	[107]
X3LYP	21	[108]
B3LYP	20	[51]
B3LYP-D	20	[51, 109]
BHandHLYP	50	[110]
mPW1PW91	25	[111]
mPW1K	42.8	[112]
PBE0	25	[113, 114]
M06-HF	100	[115]
M06	27	[97]
M06-2X	54	[116]
M05-2X	52	[116]
Range-separated hybrids		
CAM-B3LYP	19/65	[117]
LC-PBEPBE	0/100	[118]
LC-ωPBE	0/100	[119, 120]
ωB97XD	22/100	[121]
ωB97X	16/100	[122]
ωB97	0/100	[122]
Double hybrid		
B2PLYP	53	[123]

Table 3.1: Exchange-correlation functionals considered in the present study. [a]: min/max of HF exchange for range separated hybrids

For the benchmark of basis sets, conformation analysis and geometry optimizations were carried out using the B3LYP [51, 54, 124] method with 6-31G, 6-31G(d,p), 6-31+G(d,p) and 6-311++G(2d,2p) basis sets. The optimized structures were confirmed as true minima by vibrational analysis at the same level of theory. Solvent effects were evaluated using the C-PCM model [55] and different solvents were selected in order to roughly represent the physiological medium of human living cells (water) and lipid membranes (benzene), possible site of action for antioxidants. Methanol has been also considered for a direct comparison with the available experimental results. [80, 83, 86, 89, 90] Thermodynamic energetic quantities were evaluated using the procedure reported in Reference [125].

Spin contamination of all the considered radicals was found to be negligible, the expectation value of S^2 not exceeding 0.78 in all cases. Finally, in order to obtain accurate reference values, all the energies of interest where evaluated at CBS-QB3 level of theory. [98, 99]

In the second half of the work, conformation analysis and geometry optimizations were carried out using the M06-2X [116] method with 6-31+g(d,p) basis set. The optimized structures were confirmed as true minima by vibrational analysis at the same level of theory. Water effect was evaluated using the C-PCM model [55] in order to roughly represent the physiological medium of human living cells. The *sacc anion* and *radical* is referred to the products came from an hydroxyl on saccharoid.

3.3 Benchmark Results

The two considered antioxidants, quercetin and edaravone are sketched in Figure 3.1. Following the atom labeling reported in the same Figure, radicals will be labeled with the number of the carbon bearing the hydroxyl group losing a hydrogen. For instance, label **3'** corresponds to the radical formed by extracting of the hydrogen on the oxygen bonded to C3'.

Several theoretical studies were devoted to the study of the main physico-chemical parameters related to the antioxidant activity of quercetin. [74, 83, 93, 126] However, these studies have been mainly carried out using the robust B3LYP functional and the 6-311++G(3df,2p) basis set. The IP has been estimated to be 7.2 eV, while the BDE ranges between 3.14 (radical OH4') and 4.14 eV (radical OH5'). [83] Few data are instead available for edaravone: a BDE of 3.56 eV was computed at the B3LYP/6-31G(d) level of theory, [81] while values of 3.38 and 3.74 eV for the BDE of the radicals **4'** and **3**, respectively. The IP of edaravone has been experimentally evaluated at 8.0 eV. [127] At the best of our knowledge, no theoretical data have been reporting concerning the PDEs of the two considered molecules.

3.3.1   Basis Sets and Solvent Effects

As first step, we have effected a study on the basis set convergence, using the B3LYP functional, so to have a direct comparison with previous work and a first (rough) indication on the chosen properties. The results, collected in Table 3.2, clearly show that increasing the basis set from 6-31G to 6-311++G(2d,2p) leads to a systematic augmentation of the BDEs of quercetin. The largest effect is observed for the breaking of the OH7 bond leading to the **7** radical (+0.23 eV), while smaller variations, ranging from 0.16 to 0.10 eV, are observed for all the others radicals. The BDEs of edaravone radicals are less affected by basis, the increase being between 0.01 and 0.08 eV.

In all the cases, the order of the BDE is not affected by the basis set, as also previously reported. [83, 93] For quercetin, in particular, the lowest value is obtained for the breaking of the OH4' bond, giving radical **4'** (3.11 eV with the 6-31+G(d,p) basis), followed by the OH3' bond (**3'** radical, 3.22 eV, same basis). The other BDEs are at least 0.27 eV higher (see Table 3.2). Two are the effects ruling this behavior. Firstly, the strong intramolecular hydrogen bond between the two hydroxyl groups **3'** and **4'** is preserved in both **4'** and **3'** radicals, as well as the one involving hydroxyl 3 and carbonyl 4. [128] This latter is lost in radical **3**, which indeed has a higher BDE (about + 0.4 eV with respect to **4'**). The difference between **4'** and **3'** can be then rationalized in terms of electron delocalization and consequent stabilization of the resulting radical. Indeed, a simple analysis of the mesomeric structures, reported in Figure 3.2, clearly shows that a larger delocalization of the unpaired electron can be found in the **4'** radical with respect to **3'**. This effect is confirmed by the plot of the spin densities (fig.3.2). The same effects are, of course, at the basis of the values found for PDEs, where the lowest value is associated with **4'**, followed by the energy related to **3'**.

The most stable radical of edaravone is **4**, originated by the breaking of the C_4H bond which requires 3.19 eV, an energy slight higher than that required for the production of the most stable radical of quercetin (**4'** 3.11 eV), thus clearly indicating that the two molecules have a similar antioxidant activity, in case of the HAT mechanisms. The second radical is **3a**, generated by the elimination

	Radical	6-31G	6-31G(d,p)	6-31+G(d,p)	6-311++G(2d,2p)
			BDE		
quercetin					
	3	3.37	3.42	3.49	3.53
	3'	3.11	3.14	3.22	3.27
	4'	3.02	3.03	3.11	3.15
	5	4.04	4.08	4.10	4.14
	7	3.55	3.68	3.70	3.78
edaravone					
	3a	3.50	3.59	3.57	3.58
	4	3.19	3.26	3.26	3.28
	9	4.82	4.82	4.81	4.83
	10	4.78	4.78	4.77	4.80
			PDE		
quercetin					
	3	9.95	10.25	9.99	10.03
	3'	9.69	9.97	9.73	9.77
	4'	9.61	9.86	9.62	9.66
	5	10.62	10.91	10.61	10.64
	7	10.14	10.51	10.21	10.28
edaravone					
	3a	9.72	9.94	9.68	9.67
	4	9.41	9.61	9.37	9.37
	9	11.03	11.17	10.91	10.92
	10	11.00	11.14	10.88	10.89
			IP		
quercetin		7.12	6.87	7.19	7.20
edaravone		7.44	7.31	7.56	5.75

Table 3.2: Basis set effects on Bond Dissociation Energies (BDE, eV), proton dissociation enthalpy (PDE, eV) and Ionization Potential (IP, eV) of quercetin and edaravone. All computations have been carried out using the B3LYP functional.
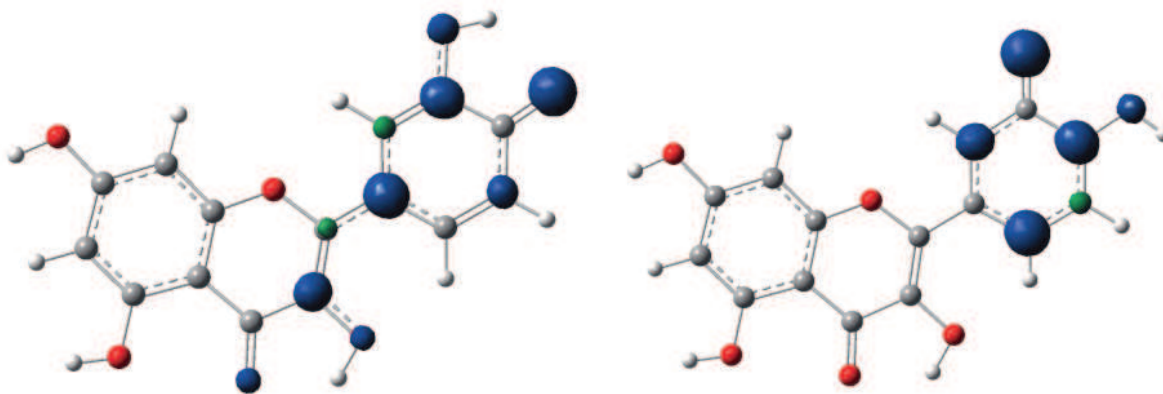
Figure 3.2: Spin density map (iso-contour = 0.05 a.u.) and mesomeric structure for the radical **3'** (left) and **4'** (right) of edaravone.
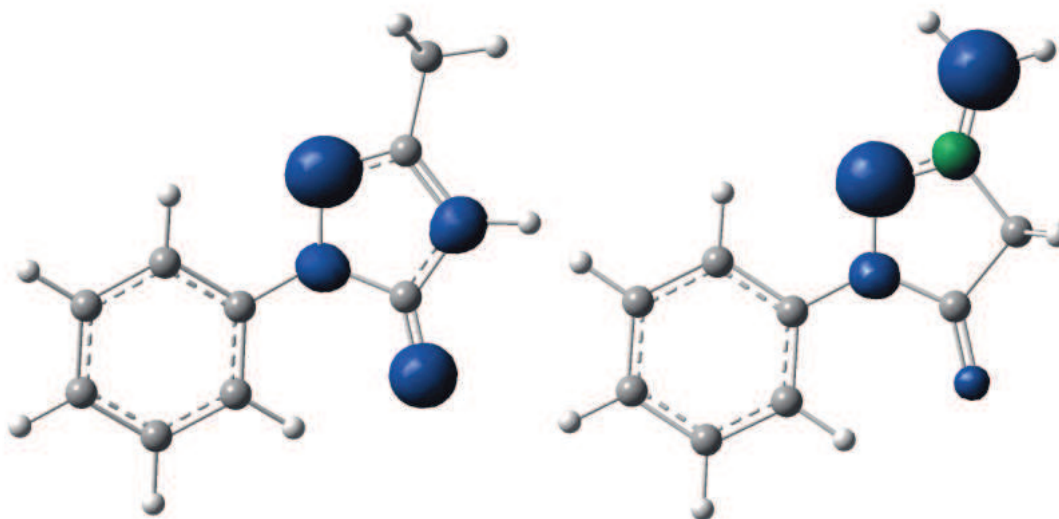
Figure 3.3: Spin density map (iso-contour = 0.05 a.u.) and mesomeric structure for the radical **3a** (left) and **4** (right) of edaravone.

of the H bound to the methyl C3a atom. As for quercetin, a quick look to the mesomeric structure and the associated spin density plot (Fig.3.3) evidences the largest electron delocalization in radical **4** with respect to **3a**, thus well correlating with the order of the computed BDEs.

Smaller variations with the basis set are, instead, observed for all the others properties (see Table 3.2). For instance, the largest deviation for PDE in quercetin is 0.14 eV (radical **7**), in going from 6-31G to 6-311++G(2d,2p), while in all the others cases it does not exceed 0.08 eV. Even smaller variations (max 0.11 eV) are found for edaravone's PDEs. A similar behavior is found also for IPs, where the largest variation is for the IP of edaravone (0.13 eV).

From these results, it appears as general trend that the 6-31+G(d,p) basis set provides results at convergence for all the energetic properties, with average deviations not larger than 0.04 eV with respect to the largest basis set. Therefore, only this latter basis will be considered in the following.

In a sake of completeness, the next step was to consider solvent effects on this properties. Albeit continuum models can be seen as an extreme approximation of complex liquid environments, they represent a fast and reliable approach for pure liquids, especially in absence of specific solute-solvent interactions. [129] The computed BDEs, IPs and PDEs of quercetin and edaravone in the gas phase and in three different solvents, benzene, methanol and water, are reported in Table 3.3.

Solvent has a relatively small effect on BDE, all the computed values decreasing of 0.25-0.05 eV in quercetin, while they are practically constant for edaravone. Since in a simple continuum model, the solvent effect is proportional to the dipole moment of solute, [130] the largest variations are for observed for quercetin, whose radicals have the largest variation of the dipole moment with respect to the neutral molecule (+ 3.0 D in **3'**). In contrast, a small variation (-1.8 D) is found for edaravone and its radical **4**. Interestingly, **3** and **3'** radicals of quercetin, having similar dipoles (4.8 and 4.5 D, respectively), become isoenergetic in water, even if radical **4** is always the most stable.

A significantly larger effect of the solvent can be instead found for PDEs and IPs, since the evaluation of these quantities involves charged species (proton and molecular cation), whose stabilization upon interaction with a (polar) solvent affects the involved chemical equilibrium. Indeed, in going from the gas phase to solvent, all the PDE values are divided by a factor ranging from 5 to 7. Then, smaller yet still important, variations can be found as function of the solvent: increasing the dielectric constant induces a stabilization of the charged products and then a decrease of the computed PDE.

Albeit large variations have been found for some of the investigated properties,

	Radical	6-31G	6-31G(d,p)	6-31+G(d,p)	6-311++G(2d,2p)
			BDE		
quercetin					
	3	3.49	3.41	3.30	3.29
	3'	3.22	3.24	3.28	3.28
	4'	3.11	3.13	3.16	3.16
	5	3.71	3.67	3.65	3.65
	7	4.10	4.02	3.87	3.86
edaravone					
	3a	3.57	3.59	3.62	3.638
	4	3.26	3.30	3.35	3.35
	9	4.81	4.81	4.81	4.81
	10	4.77	4.77	4.77	4.77
			PDE		
quercetin					
	3	9.99	1.44	0.89	0.47
	3'	9.73	1.26	0.48	0.45
	4'	9.62	1.157	0.77	0.33
	5	10.61	2.07	1.47	1.05
	7	10.21	1.69	1.25	0.82
edaravone					
	3a	9.68	1.32	0.97	0.53
	4	9.37	1.03	0.69	0.26
	9	10.88	2.05	2.11	1.68
	10	10.91	2.54	2.15	1.72
			IP		
quercetin		7.19	6.24	4.78	4.56
edaravone		7.59	6.54	5.05	4.82

Table 3.3: Solvent effects on Bond Dissociation Energies (BDE,eV), Proton Dissociation Enthalpy (PDE,eV) and Ionization Potential (IP,eV) for quercetin and edaravone. All calculations have been carried out at B3LYP/6-31+G(d,p)-PCM level of theory.

the relative stability order of the radicals is not affected by the solvent interaction. This fact, together with the limits of the chosen solvent models in representing the working environment of anti-oxidants, induced us in continuing the investigation using only gas-phase data.

3.3.2 Role of the Exchange-Correlation Functional

As for many other DFT-based studies, the key computational parameter is represented by the exchange-correlation functional, whose role overwhelms basis and solvent effects. The chosen functionals (see Table 3.1) belongs to three different categories, namely global hybrids (GHs), range-separated hybrids (RHs) and double hybrids (DH). Other functionals, such as those based on Generalized Gradient Approximation (GGA) and Local Density Approximation (LDA) are expected to provide larger deviations for the selected properties [131] and were not considered.

In Figure 3.4 are reported the computed BDE's values corresponding to the formation of radicals **4'**, **3'**, **3**, **7** and **5** of quercetin. The values of the first BDE and PDE (radical **4'**) as well as the IPs are also collected in Table 3.4, together with the CBS-Q3 reference values. As it clearly appears from the plots of Figure 3.4, all the considered functionals gives the same order of stabilities, that is **4'** < **3'** < **3** < **7** < **5**. This trend is in agreement with previous studies [74, 92] and shows that all of the considered functionals are able to catch the main features of the chemical effects discussed in the previous paragraphs.

The relative energies vary, however, with the functionals as it clearly appears, for instance, from the data obtained with the M06-HF, M05-2X and B2PLYP functionals. In order to better emphasize this behavior, the differences in energy between the two most stable radicals of quercetin, **4'** and **3'**, are reported in Figure 3.5, as function of the HF contribution. Results obtained with the RHs are, of course, not included in the plot. The 15 data are distinctly grouped in three sets: a first one for functionals containing about 20 % of HF exchange, a second one corresponding to a HF contribution between 40 and 60 % and a third one (1 case) for 100 % of HF exchange. Although these results somehow lack of statistical rigor, a clear reduction of the energy difference can be observed upon increasing
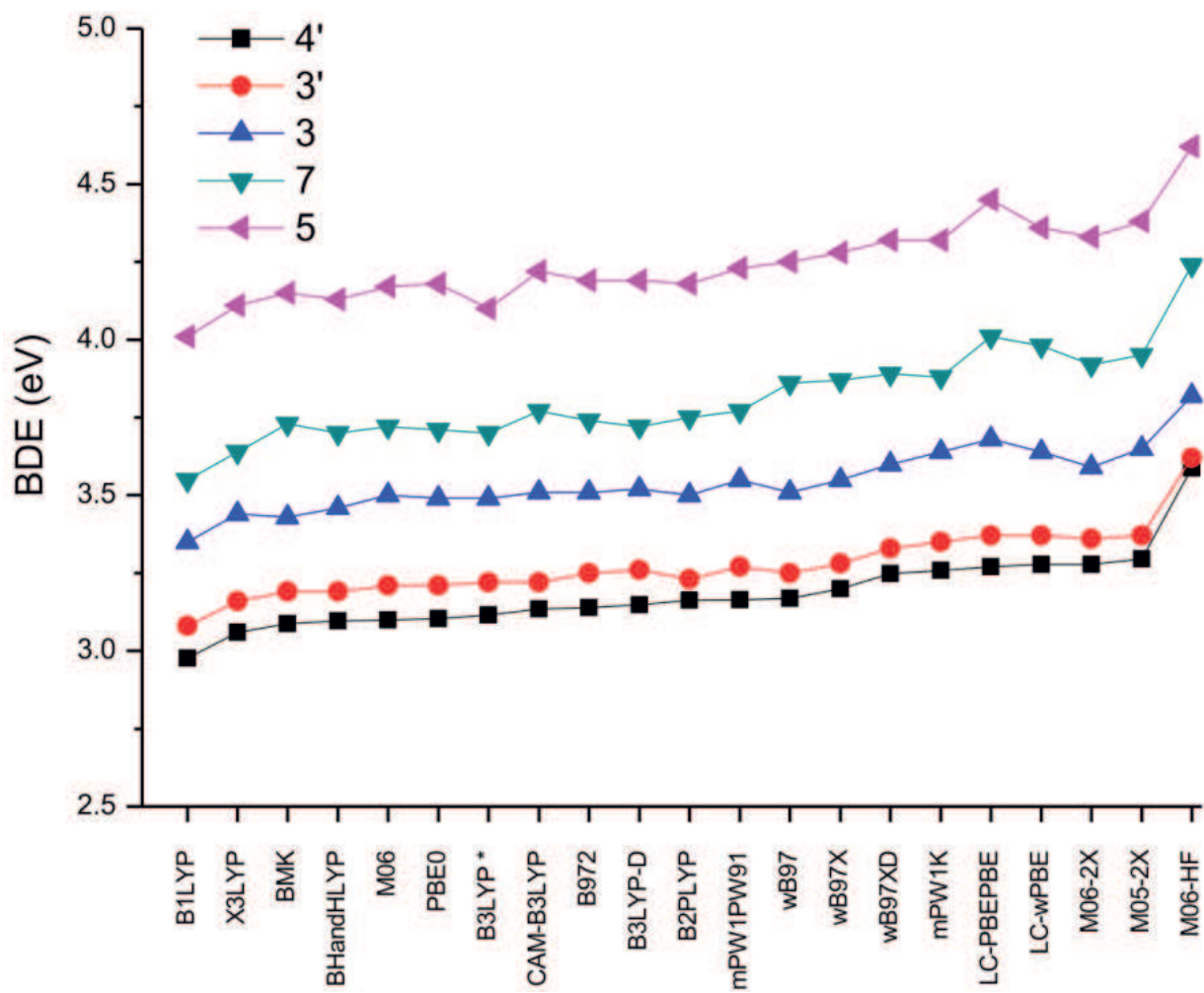
Figure 3.4: Bond dissociation energies (BDE, eV) for quercetin, computed using the 6-31+G(d,p) basis set. Energies of B3LYP are optimized energies.

functional	quercetin			edaravone		
	BDE	IP	PDE	BDE	IP	PDE
B972	3.14	7.15	9.69	3.26	7.53	9.44
B1LYP	2.98	7.11	9.56	3.22	7.44	9.31
BMK	3.09	7.31	9.48	3.29	7.66	9.32
X3LYP	3.06	7.20	9.56	3.15	7.56	9.28
B3LYP	3.11	7.19	9.62	3.26	7.59	9.37
B3LYP-D	3.15	7.22	9.62	3.25	7.59	9.35
BHandHLYP	3.10	7.31	9.48	3.16	7.53	9.32
mPW1PW91	3.16	7.27	9.60	3.23	7.63	9.29
mPW1K	3.26	7.42	9.54	3.30	7.69	9.30
PBE0	3.10	7.24	9.57	3.17	7.61	9.25
M06-HF	3.59	8.05	9.24	3.29	8.11	8.87
M06	3.10	7.28	9.52	3.24	7.65	9.28
M06-2X	3.28	7.55	9.4	3.23	7.83	9.09
M05-2X	3.30	7.58	9.42	3.24	7.80	9.13
CAM-B3LYP	3.13	7.44	9.39	3.22	7.72	9.19
LC-PBEPBE	3.27	7.75	9.22	3.37	8.02	9.04
LC-ωPBE	3.28	7.60	9.37	3.43	7.86	9.26
ωB97XD	3.25	7.41	9.54	3.34	7.70	9.33
ωB97X	3.20	7.49	9.41	3.33	7.75	9.27
ωB97	3.17	7.52	9.34	3.36	7.77	9.28
B2PLYP	3.16	7.30	9.56	3.18	7.61	9.26
CBS-Q3	3.26	7.57	9.43	3.36	7.85	9.21

Table 3.4:   Effect of the exchange-correlation functional on Bond Dissociation Energies (BDE,eV), Proton Dissociation Enthalpy (PDE,eV) and Ionization Potential (IP,eV) of quercetin and edaravone. All computations have been carried out with the 6-31+G(d,p) basis set.
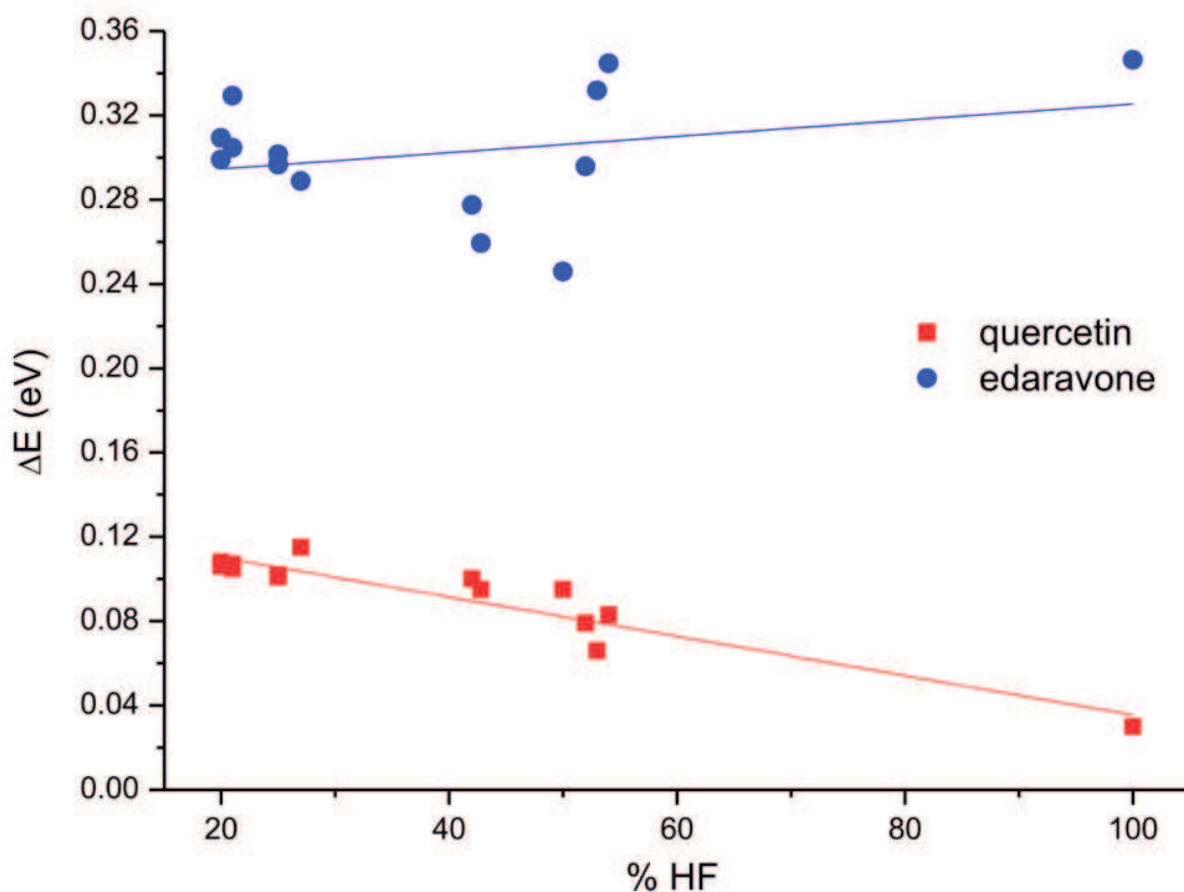
Figure 3.5: Energy differences (ΔE, eV) between the two most stable radicals of quercetin and edaravone as function of the HF exchange percentage in the exchange-correlation functionals. Results obtained with range-separated hybrids are not reported in the plot.

the HF exchange contributions, with variation ranging from 0.12 (M06) to 0.03 (M06-HF) eV. As for other chemico-physical properties, the HF exchange seems to have a role predominant with respect to the pure DFT contribution. It is also interesting to note that the functionals giving the lowest energy differences, as M06-HF and B2PLYP, are among those giving a mediocre description of H-bond features, [132] in line with the above arguments concerning the relative stabilities of **3'** and **4'** radicals.

A similar behavior is also observed for edaravone, as it clearly appears from Figure 3.6. In such, case, however, the energy differences for the two lowest radicals (**4** and **3a**) are larger than those found for quercetin, ranging between 0.25 (BH&H) and 0.35 (M06-HF) eV. The small difference observed for the two others radicals, **10** and **9**, is around 0.03-0.04 eV, independently of the functionals chosen. As for quercetin, three distinct clusters appear grouping the energy data as
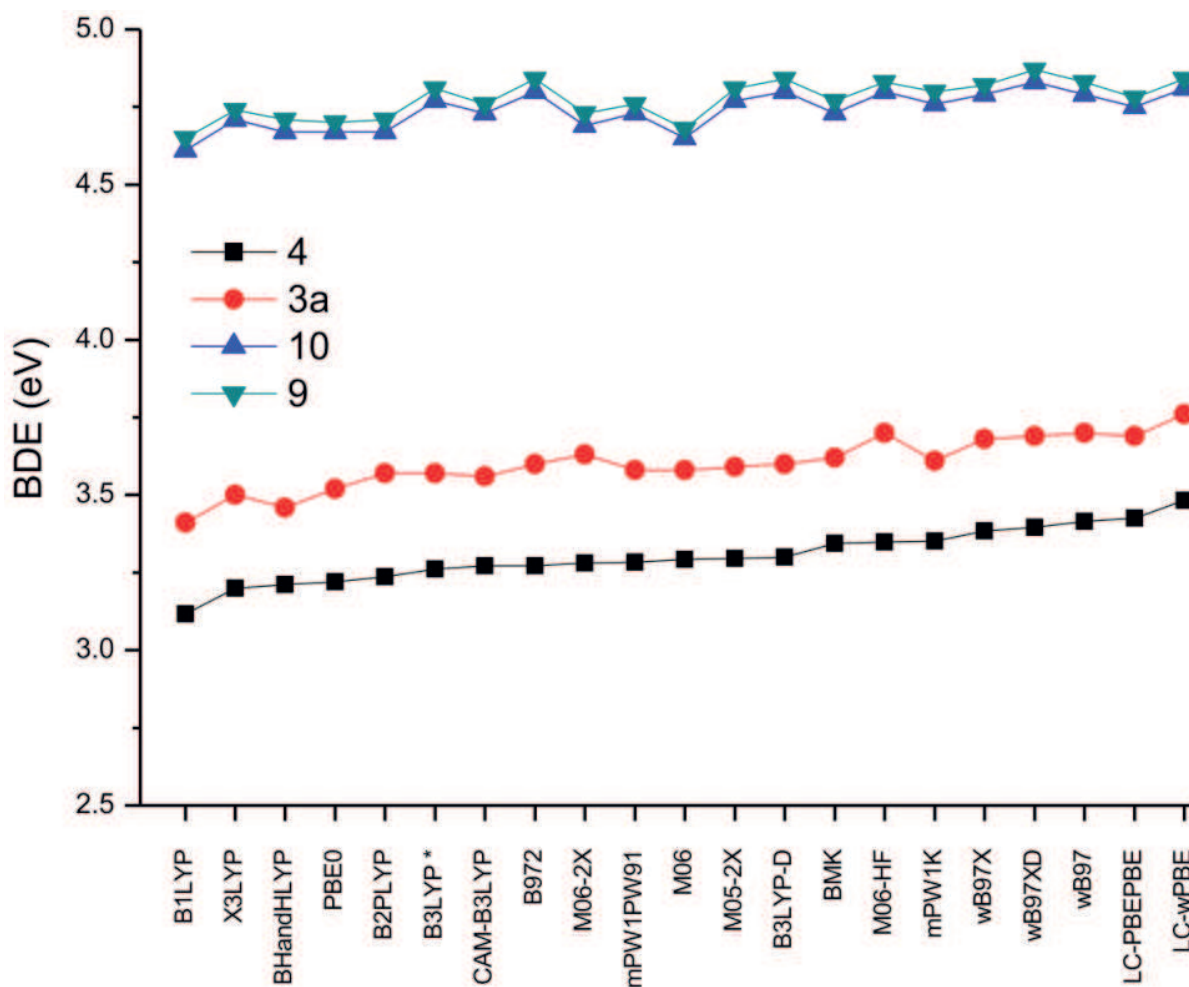
Figure 3.6: Bond dissociation energies (BDE, eV) for edaravone, computed using the 6-31+G(d,p) basis set.

function of the HF exchange, but the behavior is significantly more disordered. However, taken together, these results show that all the considered functionals are able to describe the electronic effects ruling the stabilities of the different radicals.

In this positive context about BDEs, all the computed values for BDE and PDE related to the most stable radicals of quercetin and edaravone, as well as the corresponding IPs, where compared to the reference values obtained at the CBS-Q3 level of theory. The data are collected in Table 3.4, while the corresponding errors are plotted in Figure 3.7. A quick look at these data suggests that no general trend easily emerges for the studied properties. For instance, the errors do not depend on the percent of HF exchange and have a large variation within a family (GH, RH or DH) for a given property. Furthermore, no functional provides the same performances for different properties: e.g. a high accuracy on BDE does not necessarily imply a similar behavior for IP.
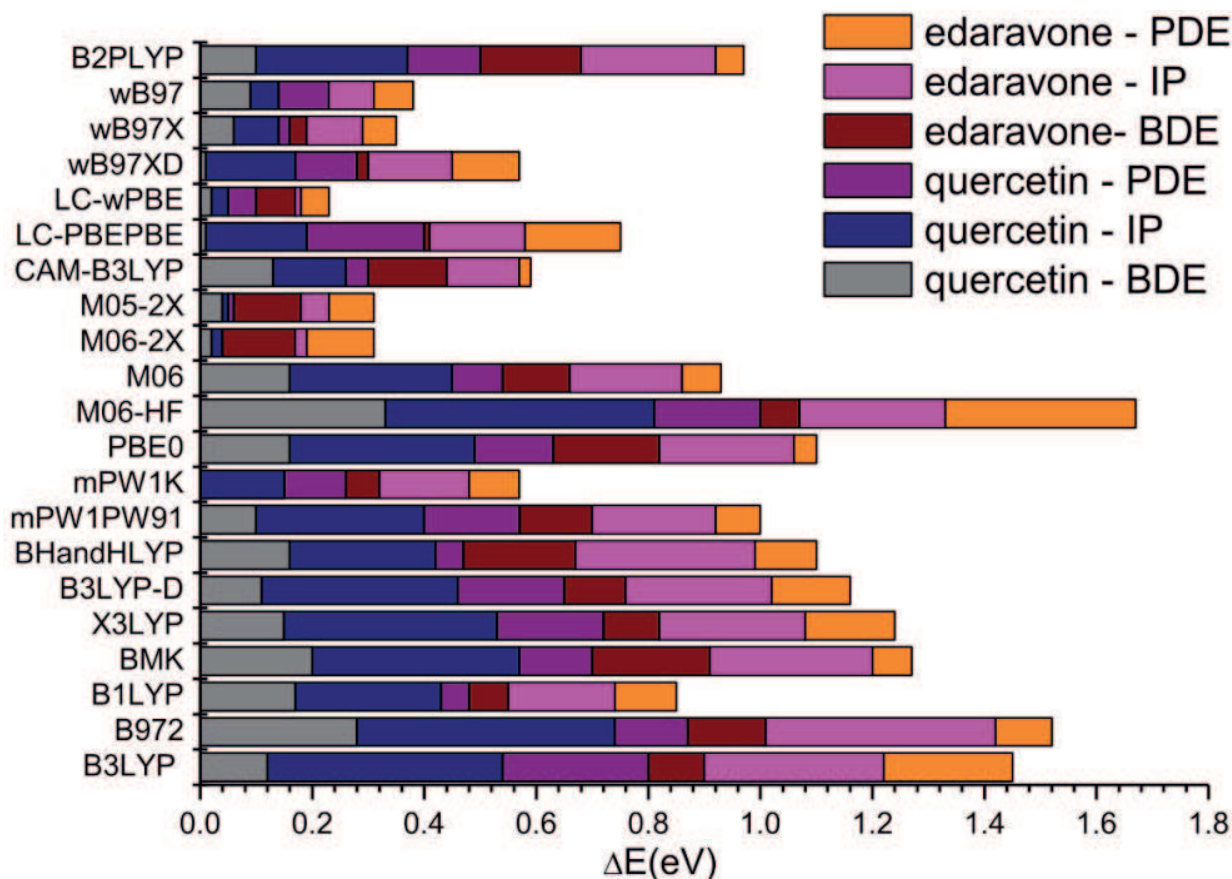
Figure 3.7: Errors (eV) for Bond dissociation energies (BDE), Ionization Potentials (IP) and Proton Dissociation Enthalpies (PDE) obtained for selected functionals with respect to CBS-Q3 references values.

Nevertheless, the best and worst performing functional clearly appears from the plot of Figure 3.8, where the sum of the mean average errors (labeled cumulative average errors, CMAE) is reported. Among the best, M05-2X, M06-2X and LC-ωPBE are the functionals giving a good average accuracy for the selected properties. They are more precise on quercetin than edaravone with deviations ranging between 0.01 eV (PDE of quercetin, M06-2X) to 0.13 eV (BDE of edaravone, M06-2X). These results well support the use of M05-2X for the evaluation of anti-oxidant activity. [87,88] B3LYP, B972 and M06-HF are, instead, the functionals giving the largest deviations, particularly on the IP of quercetin (0.28 and 0.33 eV for B972 and M06-HF, respectively).

More generally, the lowest deviations are found for the BDE, PDE (0.11 and 0.10 eV for quercetin as average on all the functionals) while larger errors can be observed for IP (0.24 eV for quercetin as average on all the functionals).
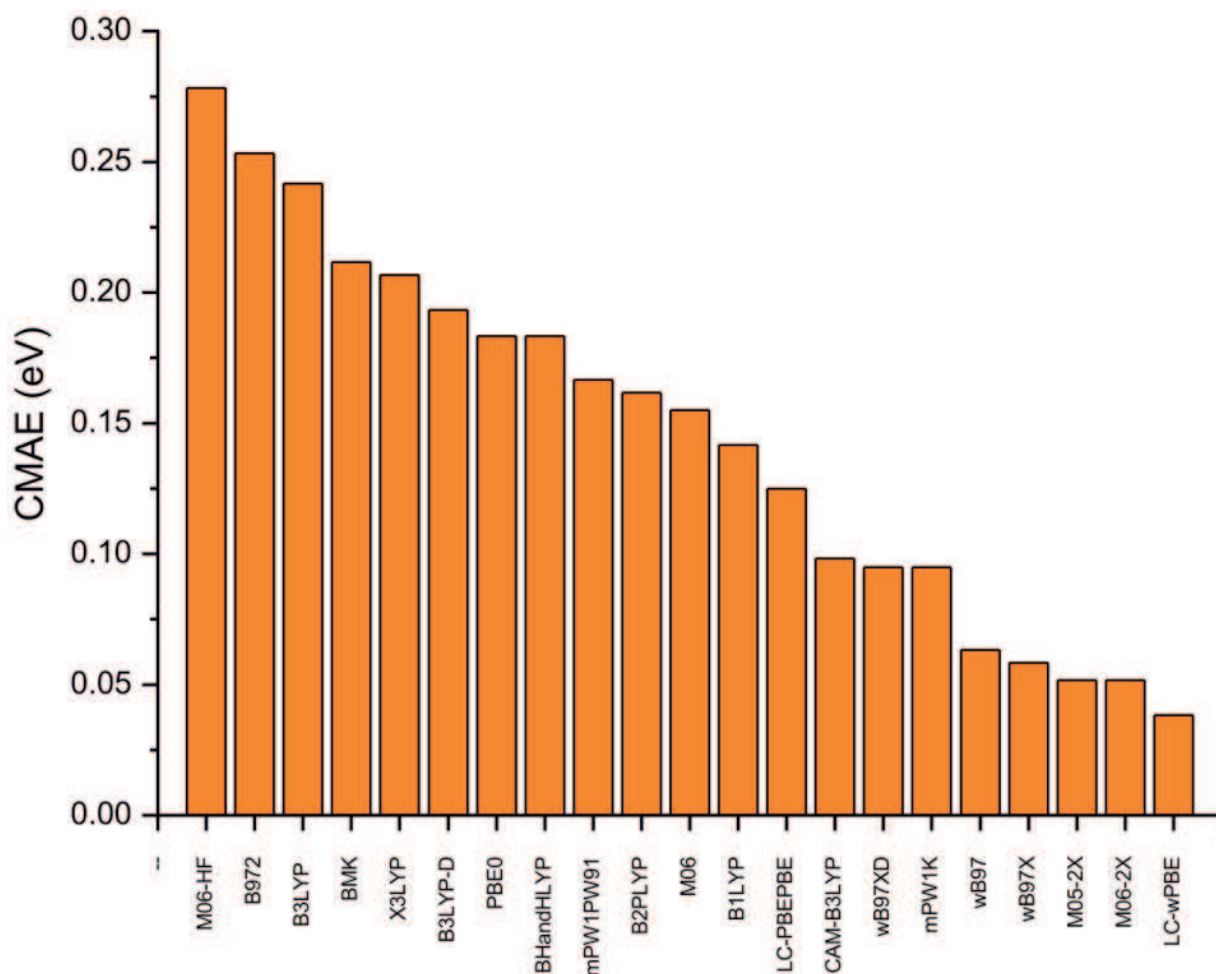
Figure 3.8: Cumulative Mean Absolute Error (CMAE, eV) for Bond dissociation energies (BDE), Ionization Potentials (IP) and Proton Dissociation Enthalpies (PDE) obtained for selected functionals with respect to CBS-Q3 references values.

Looking more in details to the different properties, the lowest errors on BDE are obtained with a GH, mPW1K, and a RSH, ωB97XD, functionals, while 2 GHs can be identified for the largest errors, X3LYP and B1LYP, both casting the BLYP function with similar amount of HF exchange (21 and 25 %). Indeed, the highest for quercetin is obtained at B1LYP level (-0.28 eV), while for edaravone it is -0.21 eV with X3LYP. It is also interesting to notice that, except for the two worst and the best cases, different accuracies are obtained on quercetin and edaravone. The BMK and LC-ωPBE functionals are an example of this behavior. It is also difficult to find a clear behavior for functionals sharing a similar framework, as for instance, in the case of the Minnesota family. Here the order of deviations is M06-2X < M05-2X < M06 < M06-HF, without any relation with the included HF contributions. Another order is for the ωB97-based function-

als, where the performances increase with the ration of HF exchange: ωB97XD (22/100%) < ωB97X (16/100%) < ωB97 (0/100%). It is interesting to notice that B3LYP and its homologous containing an empirical dispersion, B3LYP-D, do not give the same result (0.11 vs. 0.12 eV) suggesting a spurious effect, as already recently encountered in other system, where van der Waals interactions are supposed to be negligible. [133] Indeed, it has been evidenced that empirical corrections could lead to unphysical artifacts, in line with the present results. [134]

A slightly different picture appears from the analysis of the PDE data. In this case, B972 and M06-HF are the functionals giving the largest errors, while CAM-B3LYP is the best performing. Reassuring, some of the best functionals for BDE are also well placed in the PDE ranking, as ωB97XD, M06-2X and M05-2X. The less-performing functionals are two global hybrids (B972 and M06-HF), while B3LYP and B3LYP-D provide exactly the same error. As for BDE, different accuracies are obtained for quercetin and edaravone, with the exception of the best and worst cases.

Finally, a few similarities can be found between the trends of IP and BDE: M05-2X and M06-2X are among the best-performing functionals, together with ωB97X, while B1LYP, X3LYP and M06-HF deliver higher errors. The trends for the Minnesota family, already observed for BDE, is preserved, as well as that for the ωB97 group. Also for BDE, a small, but intriguing, difference (about 0.1 eV) is observed between B3LYP and B3LYP-D.

In summary, our results indicate that M05-2X and M06-2X are the two functionals, among the 21 selected, giving the lowest average errors on the molecules and being the most suitable for an accurate evaluation of energetic quantities related to antioxidant activities.

3.4   Experimental/Theoretical Correlation

Benchmark's results give the means to continue the investigation about antioxidant activity using the best computational method. The chosen one is M06-2X/6-31+G(d,p); the 15 computed antioxidants all belong to flavonol's class, the

	R3	R3'	R4'	R5'	R6'
quercetin	H	H	OH	H	H
rutine	rudinoside	H	OH	H	H
kaempferol	OH	H	OH	H	H
isoquercitrin	O-glucpyranoside	H	OH	OH	H
myricetin	H	H	H	OH	H
hyperine	O-β-galactoside	H	OH	OH	H
quercitrin	rhamnoside	H	OH	OH	H
astragalin	glucoside	H	OH	H	H
isorhamnetin	OH	H	OH	OMe	H
morin	OH	H	OH	H	OH
galangin	OH	H	H	H	H
quercetin 3,4'-diglucoside	glucoside	H	glucoside	OH	H
quercetin 4'-glucoside	OH	H	glucoside	OH	H
guajavarin	arabinoside	H	OH	OH	H
reynoutrin	D-xyloside	H	OH	OH	H

Table 3.5: Substituent of fifteen studied flavonols.

scheme of a generic flavonol and the list of substituents are reported in Figure 3.9 and Table 3.5 while the schematic structures of the flavonols are showed in Figure 3.10, 3.11 and 3.12. Bond dissociation enthalpies (BDEs) plus ionization potentials (IPs), proton dissociation enthalpies (PDEs), proton affinities (PAs) and electron transfer enthalpies (ETEs) calculated in vacuum are reported respectively in Table 3.6, Table 3.7 Table 3.8 and Table 3.9 (the *xxx* notations refer to the value lacks due to the unoptimized structure).

BDEs are the principal indicators of antioxidant activity and thanks to the data in Table 3.6 it is possible to recognize typical features of flavonols. In most cases the lowest BDE refers to **4'** or **5'** hydroxyl, situated on B ring that seems to be most important of A ring, according to a previous analysis. [126] The radical formed on **4'** hydroxyl group is stabilized by new H-bond from another vicinal hydroxyl; a clear evidence is the BDE of myricetin, that is the lowest among all examined flavonols thanks to the double stabilizing effect of **3'** and **5'** OH on the **4'** radical in the product. On the other hand, in absence of proximal OH groups on B ring, flavonols show the lowest BDE on hydroxyl in position 3, as the cases of kaempferol, isorhamnetin and morin: the reason is to be found in the radical electron delocalization on double aromatic ring. [79, 83] Planar

	BDE (eV)								IP (eV)
	rad 3	rad 3'	rad 4'	rad 5	rad 5'	rad 6'	rad 7	sacc	
quercetin	3.57	3.37	**3.28**	4.26	-	-	3.94	-	7.50
rutine	-	**3.21**	3.26	3.98	-	-	3.55	3.88	7.13
kaempferol	**3.56**	-	3.64	4.87	-	-	3.94	-	7.52
isoquercitrin	-	-	**3.54**	4.35	3.59	-	4.57	4 .50	7.31
myricetin	3.56	3.48	**3.11**	4.26	3.47	-	4.58	-	7.50
hyperine	-	-	**3.62**	4.52	3.71	-	3.94	4.49	7.40
quercitrin	-	-	**3.50**	4.34	3.56	-	4.57	4.57	7.50
astragaline	-	-	**3.70**	4.34	-	-	4.57	4.30	7.39
isorhamnetin	**3.57**	-	3.64	5.36	-	-	4.58	-	7.38
morin	**3.57**	-	3.74	4.30	-	4.57	4.58	-	7.54
galangin	**3.62**	-	-	4.27	-	-	4.57	-	7.77
quercetin 3,4'-diglucoside	-	-	-	4.38	**3.83**	-	4.00	4.39	7.84
quercetin 4'-glucoside	**3.62**	-	-	4.86	3.81	-	3.95	4.32	7.42
guajavarin	-	-	**3.44**	4.18	3.47	-	4.58	4.50	7.65
reynoutrin	-	-	**3.42**	4.15	3.39	-	4.65	4.38	7.67

Table 3.6: Bond dissociation enthalpies and ionization potentials in vacuum for 15 flavonols. The empty boxes are for the inexistent radicals.

	PDE (eV)							
	rad 3	rad 3'	rad 4'	rad 5	rad 5'	rad 6'	rad 7	sacc
quercetin	9.73	9.54	**9.45**	10.42	-	-	10.11	-
rutine	-	**9.74**	9.80	10.51	-	-	10.08	10.42
kaempferol	**9.71**	-	9.78	11.02	-	-	10.08	-
isoquercitrin	-	-	**9.90**	10.70	9.95	-	10.93	10.86
myricetin	9.72	9.64	**9.28**	10.42	9.64	-	10.74	-
hyperine	-	-	**9.89**	10.80	9.98	-	10.21	10.76
quercitrin	-	-	**9.67**	10.50	9.72	-	10.73	10.73
astragaline	-	-	**9.98**	10.62	-	-	10.85	10.58
isorhamnetin	**9.86**	-	9.92	11.65	-	-	10.87	-
morin	**9.70**	-	9.87	10.42	-	10.70	10.71	-
galangin	**9.52**	-	-	10.17	-	-	10.48	-
quercetin 3,4'-diglucoside	-	-	-	10.22	**9.66**	-	9.83	10.22
quercetin 4'-glucoside	**9.87**	-	-	11.11	10.06	-	10.20	10.52
guajavarin	-	-	**9.46**	11.04	9.49	-	10.59	10.52
reynoutrin	-	-	**9.42**	10.83	9.39	-	10.64	10.38

Table 3.7: Proton dissociation enthalpies in vacuum for 15 flavonols. The empty boxes are for inexistent radicals.

	PA (eV)							
	anion 3	anion 3'	anion 4'	anion 5	anion 5'	anion 6'	anion 7	anion sacc
quercetin	15.06	14.70	**14.41**	15.26	-	-	14.68	-
rutine	-	14.75	14.97	*xxx*	-	-	14.58	15.64
kaempferol	15.03	-	14.69	15.22	-	-	**14.62**	-
isoquercitrin	-	-	**14.67**	15.77	15.27	-	15.09	15.84
myricetin	15.00	14.78	**14.32**	15.25	14.94	-	14.68	-
hyperine	-	-	14.90	15.80	**14.85**	-	15.13	15.80
quercitrin	-	-	14.66	15.32	*xxx*	-	15.00	15.62
astragaline	-	-	**14.72**	15.72	-	-	15.05	15.79
isorhamnetin	15.11	-	14.95	15.26	-	-	**14.66**	-
morin	14.98	-	14.71	15.08	-	14.91	**14.49**	-
galangin	14.94	-	-	15.14	-	-	**14.56**	-
quercetin 3,4'-diglucoside	-	-	-	10.22	**9.66**	-	9.83	10.22
quercetin 4'-glucoside	15.23	-	-	15.48	15.01	-	**14.90**	15.57
guajavarin	-	-	**14.61**	15.38	14.86	-	14.98	15.8
reynoutrin	-	-	**14.84**	15.93	14.97	-	15.07	15.73

Table 3.8: Proton affinities in vacuum for 15 flavonols. The empty boxes are for inexistent radicals.

| | ETE (eV) | | | | | | | |
	anion 3	anion 3'	anion 4'	anion 5	anion 5'	anion 6'	anion 7	anion sacc
quercetin	**2.21**	2.38	2.57	2.70	-	-	2.96	-
rutine	-	2.15	2.00	*xxx*	-	-	2.66	1.94
kaempferol	**2.23**	-	2.65	3.35	-	-	3.01	-
isoquercitrin	-	-	2.56	2.28	**2.02**	-	3.18	2.37
myricetin	2.26	2.40	2.50	2.70	**2.23**	-	3.60	-
hyperine	-	-	2.42	2.42	2.56	-	2.51	**2.39**
quercitrin	-	-	2.54	2.72	*xxx*	-	3.26	2.64
astragaline	-	-	2.68	2.32	-	-	3.22	**2.21**
isorhamnetin	**2.16**	-	2.39	3.80	-	-	3.62	-
morin	**2.30**	-	2.73	2.92	-	3.36	3.79	-
galangin	**2.38**	-	-	2.82	-	-	3.72	-
quercetin 3,4'-diglucoside	-	-	-	**2.23**	2.72	-	2.44	**2.23**
quercetin 4'-glucoside	**2.09**	-	-	3.08	2.50	-	2.75	2.45
guajavarin	-	-	2.53	2.61	**2.30**	-	3.29	2.34
reynoutrin	-	-	2.28	2.49	**2.21**	-	3.28	2.35

Table 3.9: Electron transfer enthalpies in vacuum for 15 flavonols. The empty boxes are for inexistent radicals.
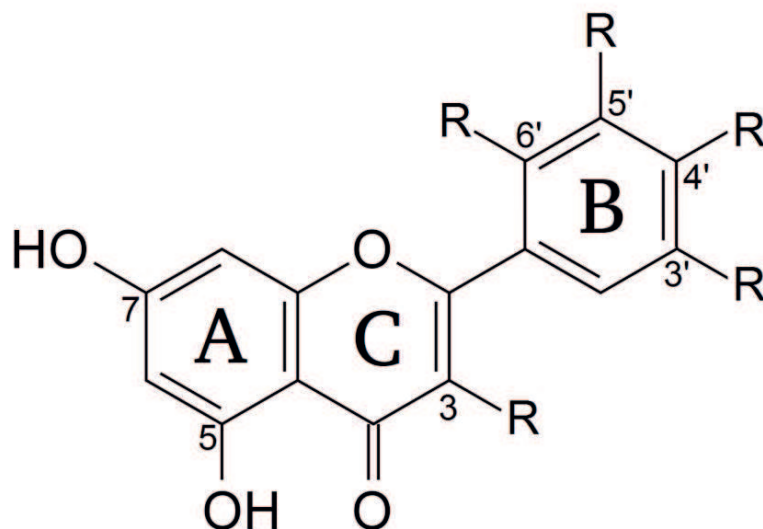
Figure 3.9: Generic sketch and atom labeling for flavonols.

conformation plays an important role on the radical stability too, reducing product energy, [82] as we can see comparing BDE of quercetin with its derivates. Isoquercitrin, hyperine, quercitrin, guajavarin, reynoutrin, 4'-glucoside-quercetin and 3,4'-diglucoside-quercetin are all derivates of quercetin and they show higher BDE respect to the simplest quercetin (ΔBDE=+0.14/+0.45). The same trend is evident by kaempferol and its derivates, such as astragaline: the presence of glucoside on position 3 prevents the realization of a planar conformation after the H$^+$ extraction (Fig.3.13), unlike kaempferol (Fig,3.14); the result is a worser delocalization of the electron on the molecule and an increment of astragaline BDE by 0.14 eV.

PAs and ETEs show different reaction sites than before, the different reaction mechanism and the character of electrophilicity (or acidity) of hydroxyl groups playing the main role.

Single-point energy calculations are carried out to take into account the effect of a solvent; as we expected, the energies, the favored reaction sites and the ranking drastically change. BDEs and IPs in water are reported in Table 3.10, PDEs, PAs and ETEs in water are reported respectively in Table 3.11, 3.12 and 3.13.

As for the global picture emerging from the energies in water, the main
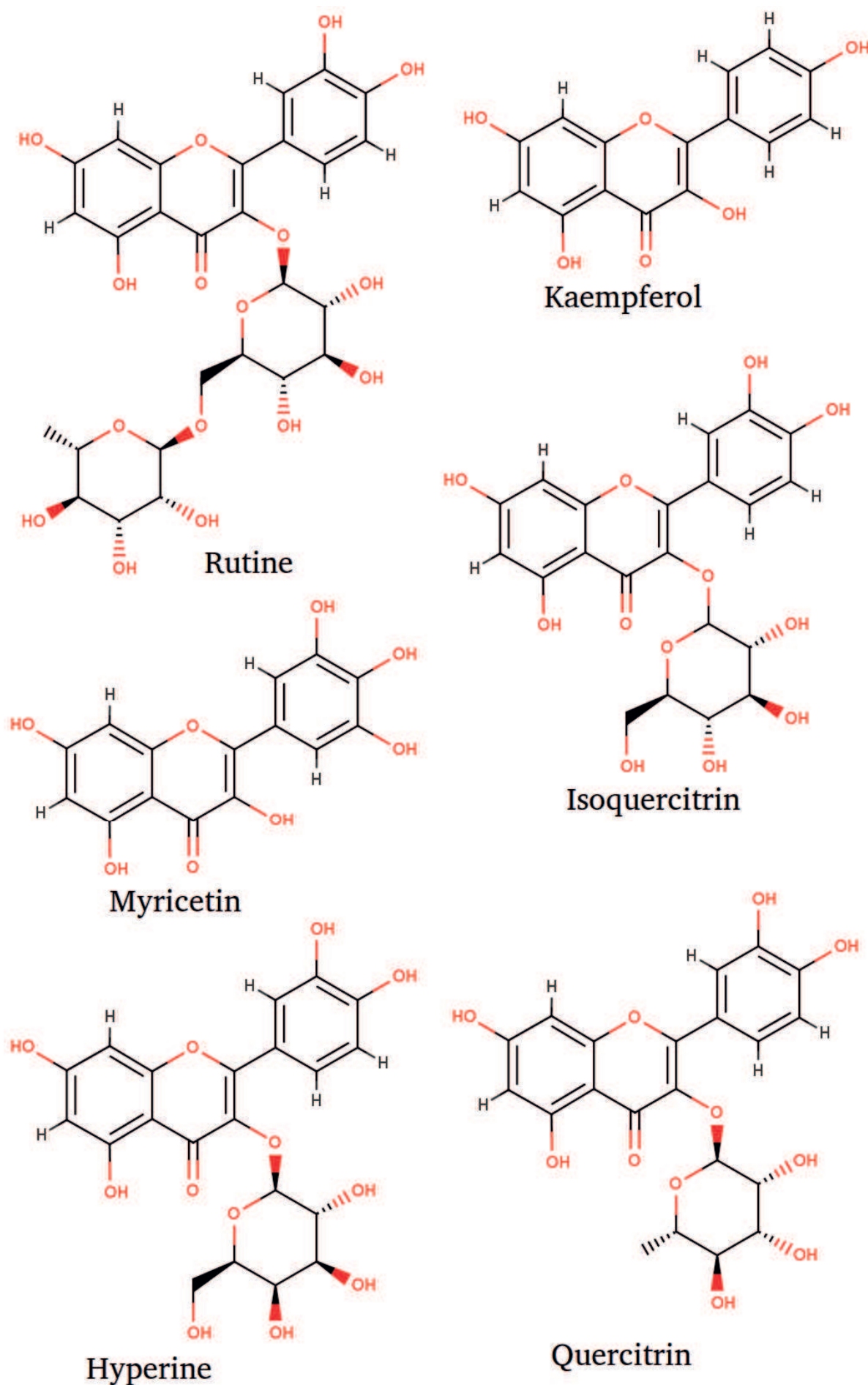
Figure 3.10: Structures of studied flavonols.
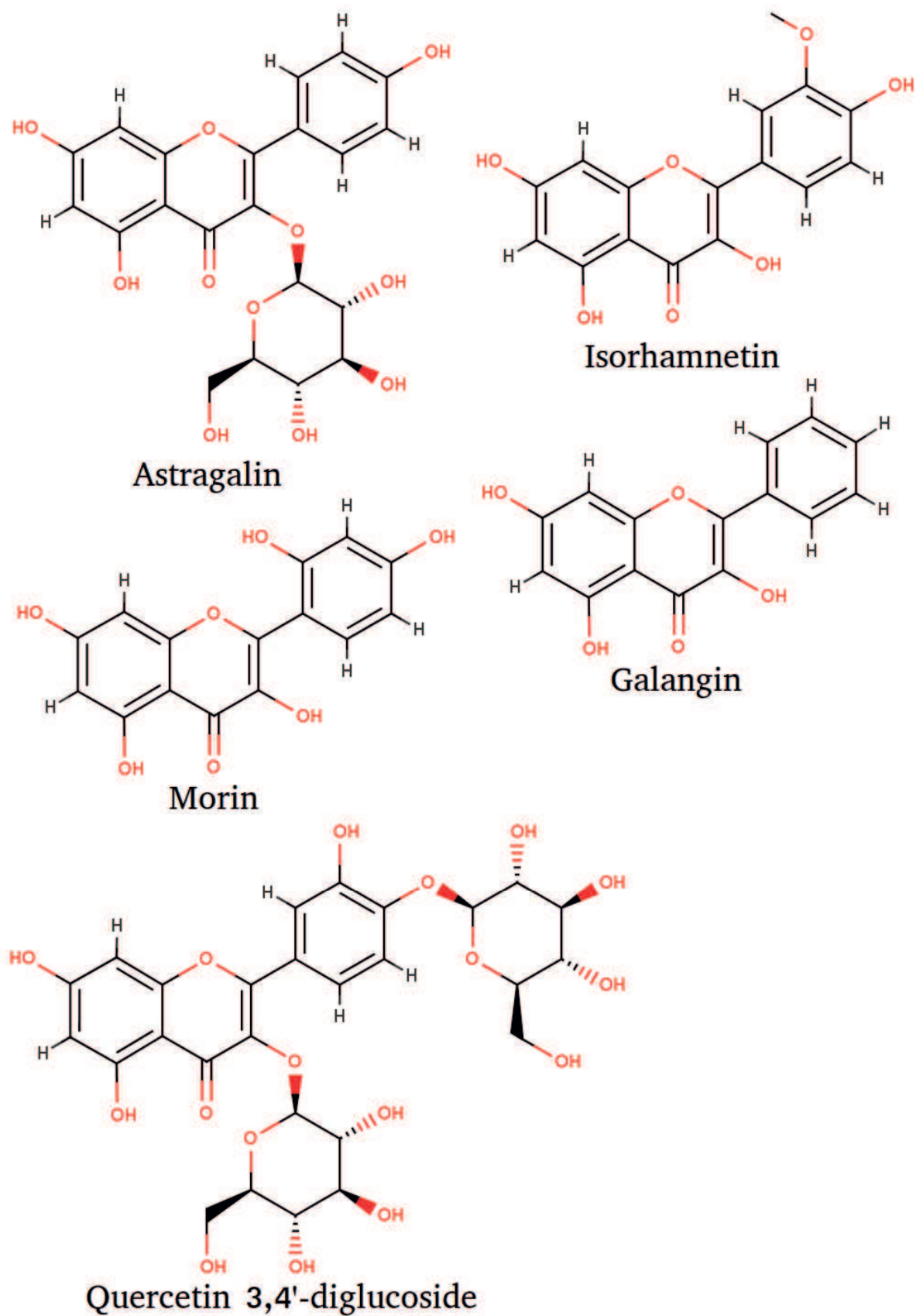
Figure 3.11: Structures of studied flavonols.
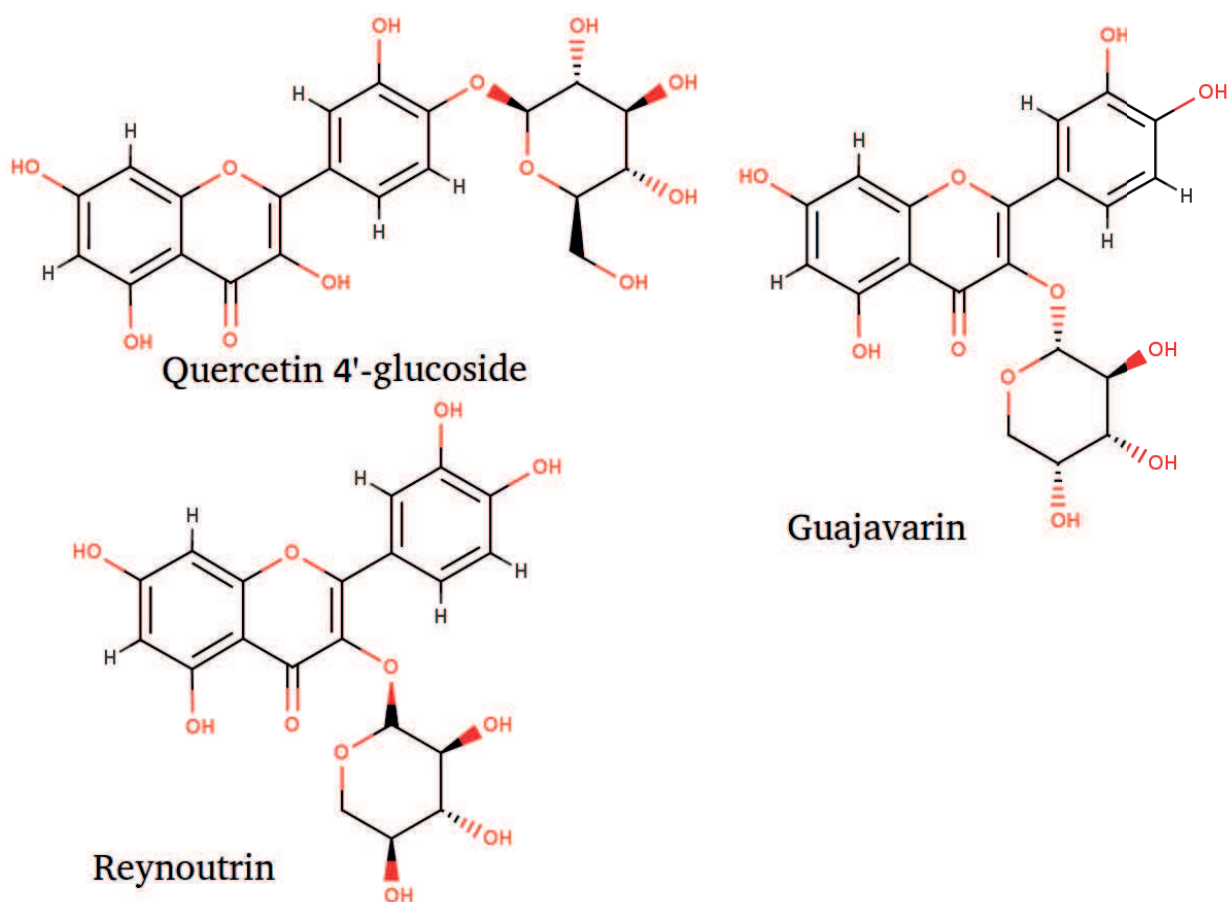
Figure 3.12: Structures of studied flavonols.
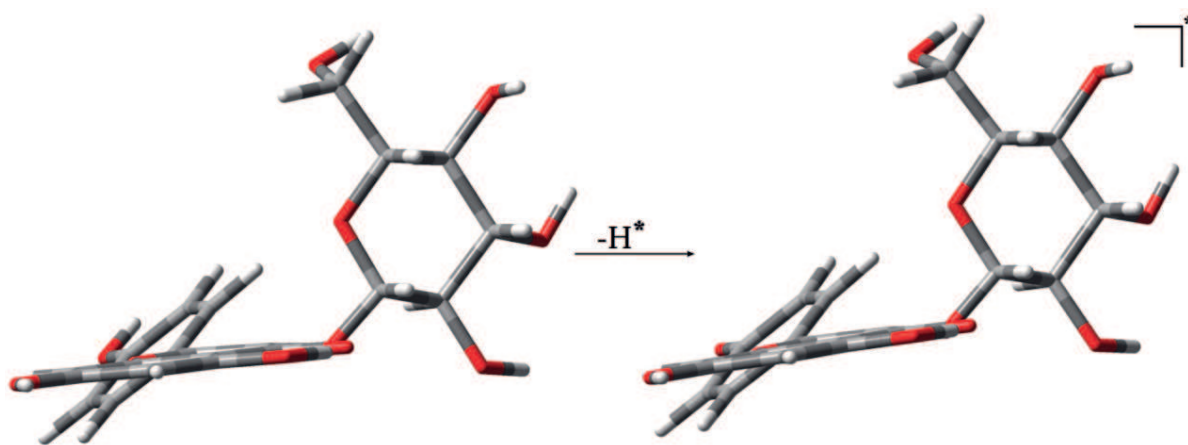
Figure 3.13: Geometries of astragalin during the extraction of H^+ of 4' hydroxyl.

	BDE (eV)								IP (eV)
	rad 3	rad 3'	rad 4'	rad 5	rad 5'	rad 6'	rad 7	sacc	
quercetin	3.42	3.43	**3.34**	4.03			3.91		6.00
rutine		**3.38**	**3.38**	3.90			3.74	4.20	6.10
kaempferol	**3.40**		3.61	4.80			3.90		5.99
isoquercitrin			**3.56**	4.12	3.66		4.67	4.58	6.16
myricetin	3.42	3.58	**3.16**	4.03	3.49		4.67		5.99
hyperine			**3.59**	4.25	3.69		3.95	4.57	6.29
quercitrin		*xxx*	**3.47**	4.11	6.51		4.66	4.52	6.22
astragaline			**3.70**	4.12			4.66	4.43	6.20
isorhamnetin	**3.41**		3.49	5.28			4.67		5.93
morin	**3.43**		3.70	4.06		4.62	4.67		6.00
galangin	**3.47**			4.03			4.66		6.20
quercetin 3,4'-diglucoside				4.19	**3.66**		3.99	4.44	6.61
quercetin 4'-glucoside	**3.47**			4.80	3.66		3.99	4.44	6.61
guajavarin			**3.42**	4.07	3.45		4.66	4.45	6.26
reynoutrin			3.46	4.13	**3.45**		4.71	4.45	6.30

Table 3.10: Bond dissociation enthalpies and ionization potentials in water for 15 flavonols. The empty boxes are for the inexistent radicals.

	rad 3	rad 3'	rad 4'	rad 5	rad 5'	rad 6'	rad 7	sacc
			PDE (eV)					
quercetin	0.67	0.68	**0.59**	1.28			1.16	
rutine		0.52	**0.52**	.05			0.88	1.35
kaempferol	**0.66**		0.87	2.06			1.16	
isoquercitrin			**0.65**	1.21	0.75		1.76	1.67
myricetin	0.68	0.74	**0.42**	1.28	0.75		1.76	1.67
hyperine			**0.55**	1.21	0.65		0.91	1.53
quercitrin			**0.50**	1.14	0.54		1.69	1.54
astragaline			**0.75**	1.17			1.71	1.48
isorhamnetin	**0.73**		0.82	2.60			1.99	
morin	**0.68**		0.94	1.30		1.87	1.92	
galangin	**0.52**			1.08			1.71	
quercetin 3,4'-diglucoside				0.83	**0.30**		0.63	1.09
quercetin 4'-glucoside	**0.63**			1.95	0.81		1.08	1.58
guajavarin			**0.42**	1.36	0.45		1.66	1.44
reynoutrin			**0.41**	1.11	0.40		1.66	1.40

Table 3.11: Proton dissociation enthalpies in water for 15 flavonols. The empty boxes are for the inexistent radicals.

	anion 3	anion 3'	anion 4'	anion 5	PA (eV) anion 5'	anion 6'	anion 7	anion sacc
quercetin	2.18	2.03	**1.92**	2.29			1.97	
rutine		1.89	1.95	*xxx*			**1.75**	2.54
kaempferol	2.18		2.11	2.29			**1.97**	
isoquercitrin			**1.90**	2.39	2.27		1.99	2.87
myricetin	2.15	2.04	**1.80**	2.28	2.10		1.97	
hyperine			2.19	2.42	2.12	& **2.02**	2.81	
quercitrin			**1.86**	2.27	2.31		2.04	2.67
astragaline			**1.92**	2.43			2.01	2.70
isorhamnetin	2.19		2.13	2.25		2.18	**1.93**	
morin	2.19		2.13	2.25		2.18	**1.93**	
galangin	2.13			2.26			**1.95**	
quercetin 3,4'-diglucoside				2.41	**1.98**		2.02	2.68
quercetin 4'-glucoside	2.15			2.28	2.25		**1.97**	2.63
guajavarin			**1.89**	2.40	2.01		2.02	2.76
reynoutrin			**1.96**	2.50	2.08		2.01	2.75

Table 3.12: Proton affinities in water for 15 flavonols. The empty boxes are for the inexistent radicals.

	anion 3	anion 3'	anion 4'	anion 5	ETE (eV) anion 5'	anion 6'	anion 7	anion sacc
quercetin	**3.40**	3.55	3.58	3.90			4.10	
rutine		3.65	**3.59**	*xxx*			4.15	3.82
kaempferol	**3.39**		3.66	4.68			4.10	
isoquercitrin			3.82	3.89	**3.55**		4.84	3.87
myricetin	**3.43**	3.60	3.52	3.91	3.55		4.86	
hyperine			**3.56**	3.99	3.73		4.09	3.92
quercitrin			3.78	4.01	**3.36**		4.79	4.01
astragaline			3.95	3.85			4.86	
isorhamnetin	**3.38**		3.47	5.15			4.86	
morin	**3.40**		3.73	3.97	3.97		4.60	4.90
galangin	**3.50**		3.93		4.60	4.90		
quercetin 3,4'-diglucoside				3.94	**3.84**		4.13	3.93
quercetin 4'-glucoside	**3.49**			4.68	3.57	4.13	3.96	
guajavarin			3.69	3.96	**3.60**		4.80	3.85
reynoutrin			3.66	3.89	**3.53**		4.86	3.86

Table 3.13: Electron transfer enthalpies in water for 15 flavonols. The empty boxes are for the inexistent radicals.
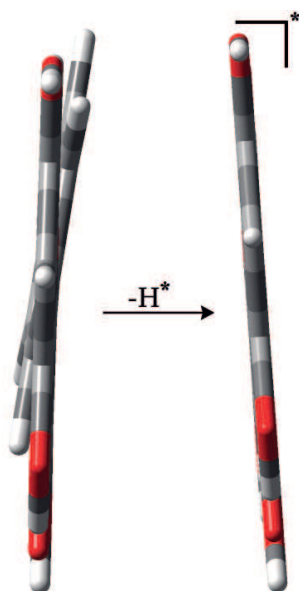
Figure 3.14: Geometries of kaempferol during the extraction of H^+ of 4' hydroxyl.

changes are in the decrease of IPs, PDEs and PAs values while BDEs and ETEs result slightly higher than in vacuum. The overview on energies computed in water evidences the falls of proton affinities and the electron transfer enthalpies, both related to the SPLET mechanism, suggesting that such mechanism can be the principal reactive path of antioxidants in solvent, according to other literature evidences. [90, 135–137]

The final aim of the study is to find out a single energy that can theoretically predict the activity of a new antioxidant respect to well known molecules avoiding the experimental measurements. To achieve the goal, the ORAC-FL values come from literature are directly compared to theoretical results (Table 3.14).

At first sight, there are few incongruity among experimental data: for example the opposite ranking of quercetin and rutine between the papers of Wolfe *et al.* [138] and Ou *et al.* [141] that could be originated from the little differences into procedure for the ORAC experimental measurement (for example, different mixing time during the preparation measurement or different reference fluorescent molecule). Moreover, Ho *et al.* [140] and Biloa Messi *et al.* [142] report the activity values in a logarithmic scale without any reference compounds mentioned. As first step, the comparison between the theoretical energies and all experimental ORAC-FL values from papers, where ORAC is expressed as function of fluores-

	Wolfe et al. [138]	Arung et al. [139]	Ho et al. [140][a]	Ou et al. [141]	Xue et al. [126]	Biloa Messi et al. [142][a]
quercetin	8.04±2.37	7.64±0.27	5.78±0.02	7.28±0.22	9.51±0.43	1.66±0.07
rutine	13.7±1.7	8.17±0.41		6.01±0.25		
kaempferol	7.19±1.29		5.84±0.05		7.87±0.72	
isoquercitrin		8.65±0.36				
myricetin	4.55±0.5		5.61±0.06			
hyperine		9.34±0.24				
quercitrin			5.47±0.05	6.47±0.29		
astragaline						2.96±0.27
isorhamnetin					8.07±0.13	
morin	6.12±1.95		5.68±0.06			
galangin	2.63±1.31					
quercetin 3,4'- -diglucoside		4.32±0.25				
quercetin 4'- -glucoside		4.82±0.67				
guajavarin			5.55±0.05			
reynoutrin			5.37±0.06			

Table 3.14: ORAC-FL in μmol TE/μmol of antioxidants with experimental error. [a] The values are in pEC50 (log EC50) without any reference compounds mentioned.
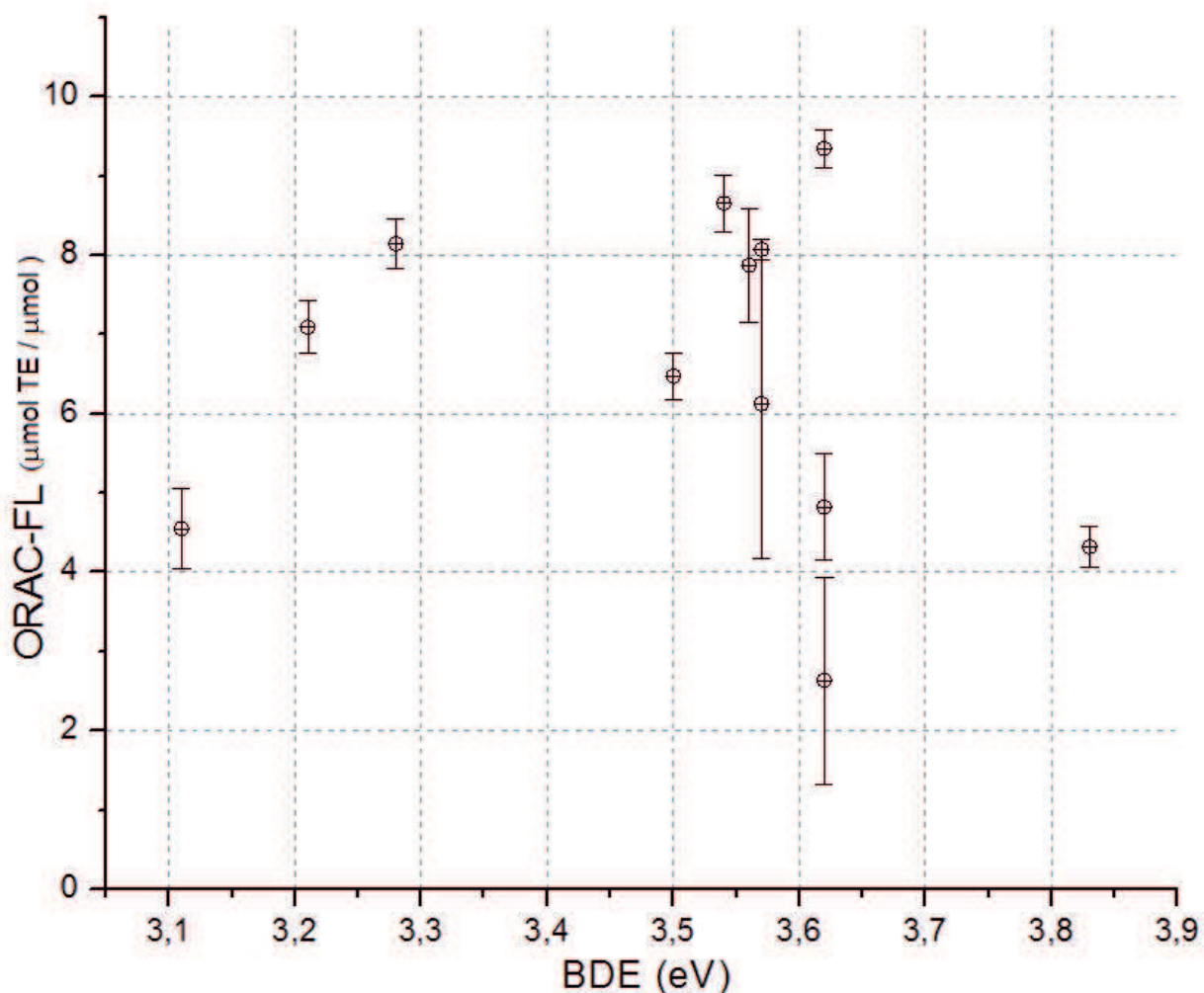
Figure 3.15: ORAC-FL values from literature (Table 3.14) vs BDEs in vacuum.

cein, is made. In Figure 3.15 ORAC-FLs are reported versus BDEs, in Figure 3.16 instead are reported versus IPs, all in vacuum: from both pictures we deduce that a comparison between all experimental data it is of little usefulness, due to the way measurements are carried out.

Trying to achieve the goal of the study, the data contained in each experimental paper were correlated singularly with with BDEs, IPs, PDEs, PAs and ETEs, both in vacuum and in water. Among all the possible combinations, the only experimental data that show correlation with our theoretical energies are the ORAC-FL from Wolfe *et al.*. [138]: for instance, we found correlation with the ionization potentials (IPs) in vacuum (Fig.3.17), the linear fit giving a good R^2 (0.88); however the IPs of quercetin and myricetin are very close, so it is impossible to distinguish which is the most reactive starting only from these the-
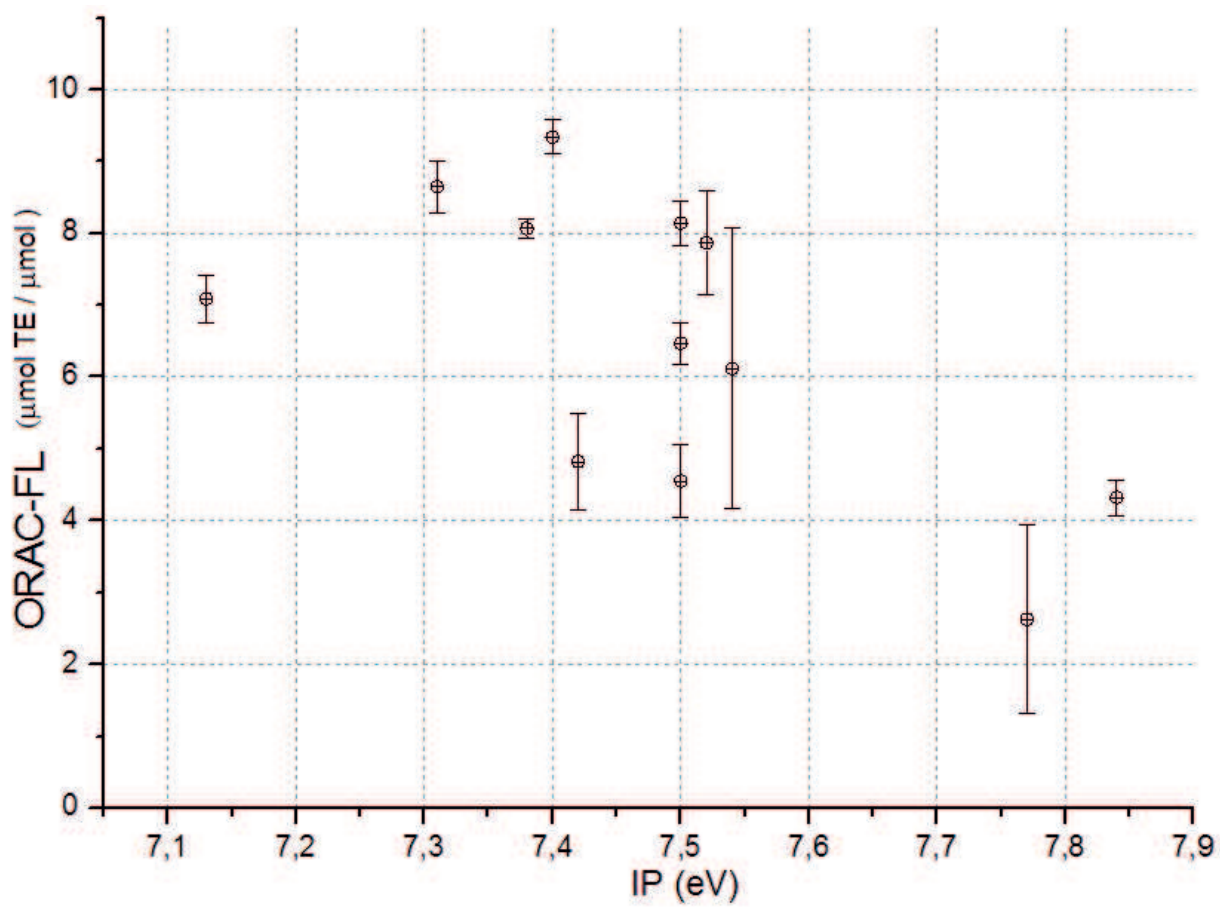
Figure 3.16: ORAC-FL values from (Table 3.14) vs IPs in vacuum.
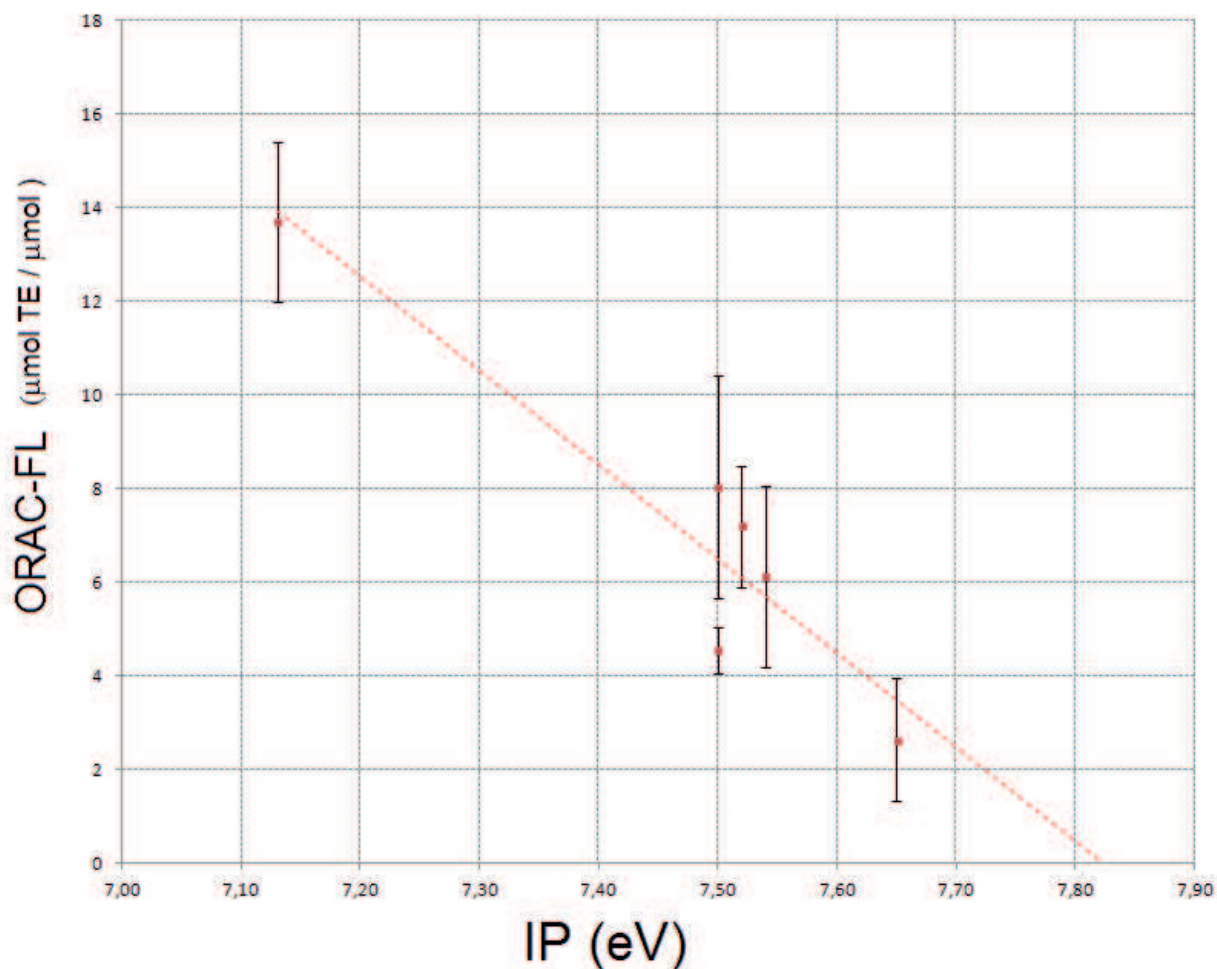
Figure 3.17: ORAC-FL from Wolfe with experimental errors versus IPs in vacuum. Red dashed line = fitted line.

oretical data. Instead, the correlation with electron transfer enthalpies (ETEs) in vacuum improves the situation (Fig.3.18); here the correlation is much better, the R^2 being 0.93 and all the data showing couples well separated. Correlation analyses produce bad results unless an antioxidant value is neglected: the ETEs in water (Fig.3.19) shows correlation only if rutine data is left out, giving a R^2 of 0.79. Anyway, quercetin's and morin's ETE are the same making indistinguishable the two antioxidant activity.

From this analysis we can deduce that the best correlations between experimental and theoretical data are obtained with the ionization potentials and the electron transfer enthalpies calculated in vacuum; looking for a correlation with an energetic parameter computed into a solvent, only a weak correlation with ETE is found. This results allow us to say that the main mechanism for the radi-
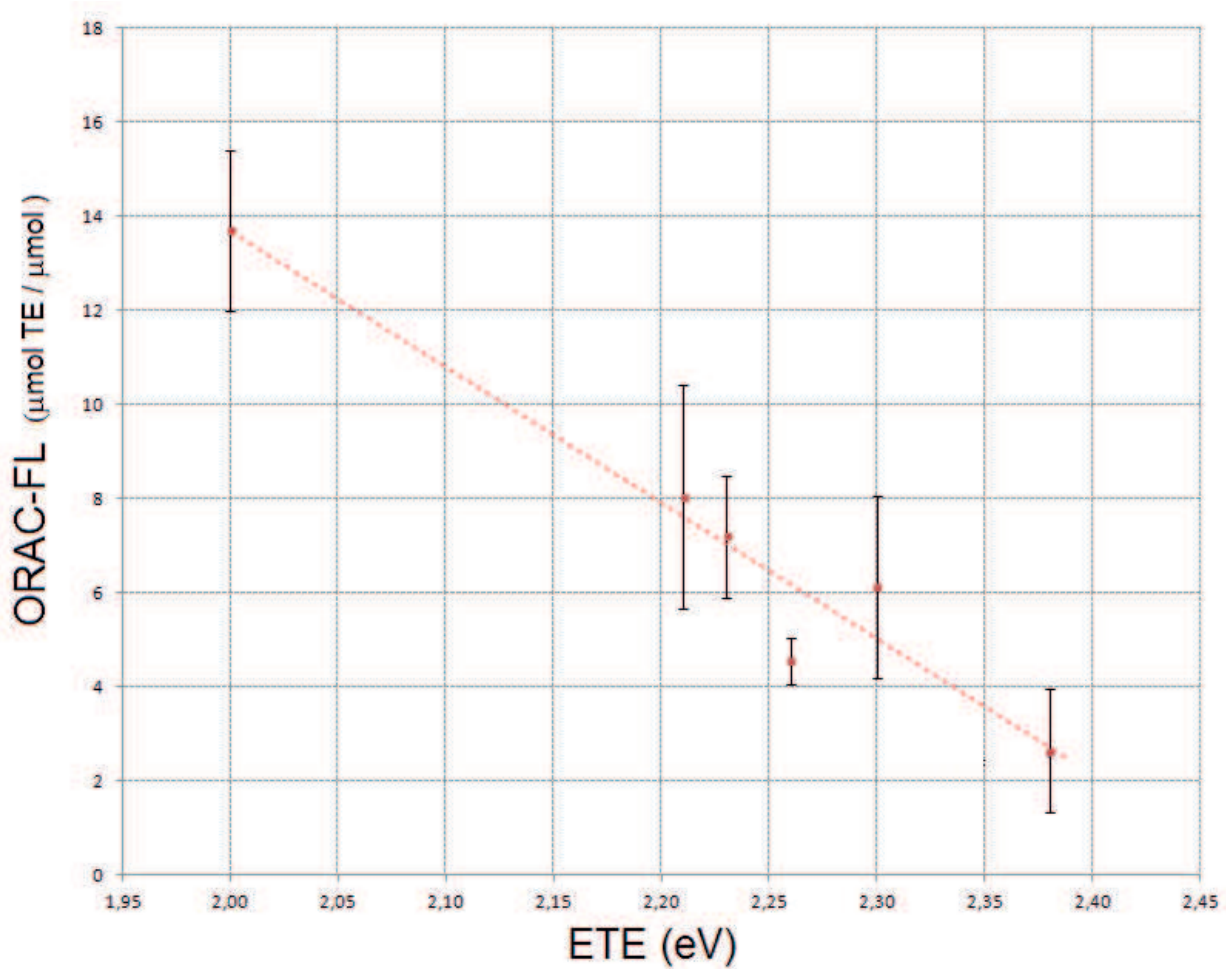
Figure 3.18: ORAC-FL from Wolfe with experimental errors versus ETEs in vacuum. Red dashed line = fitted line.
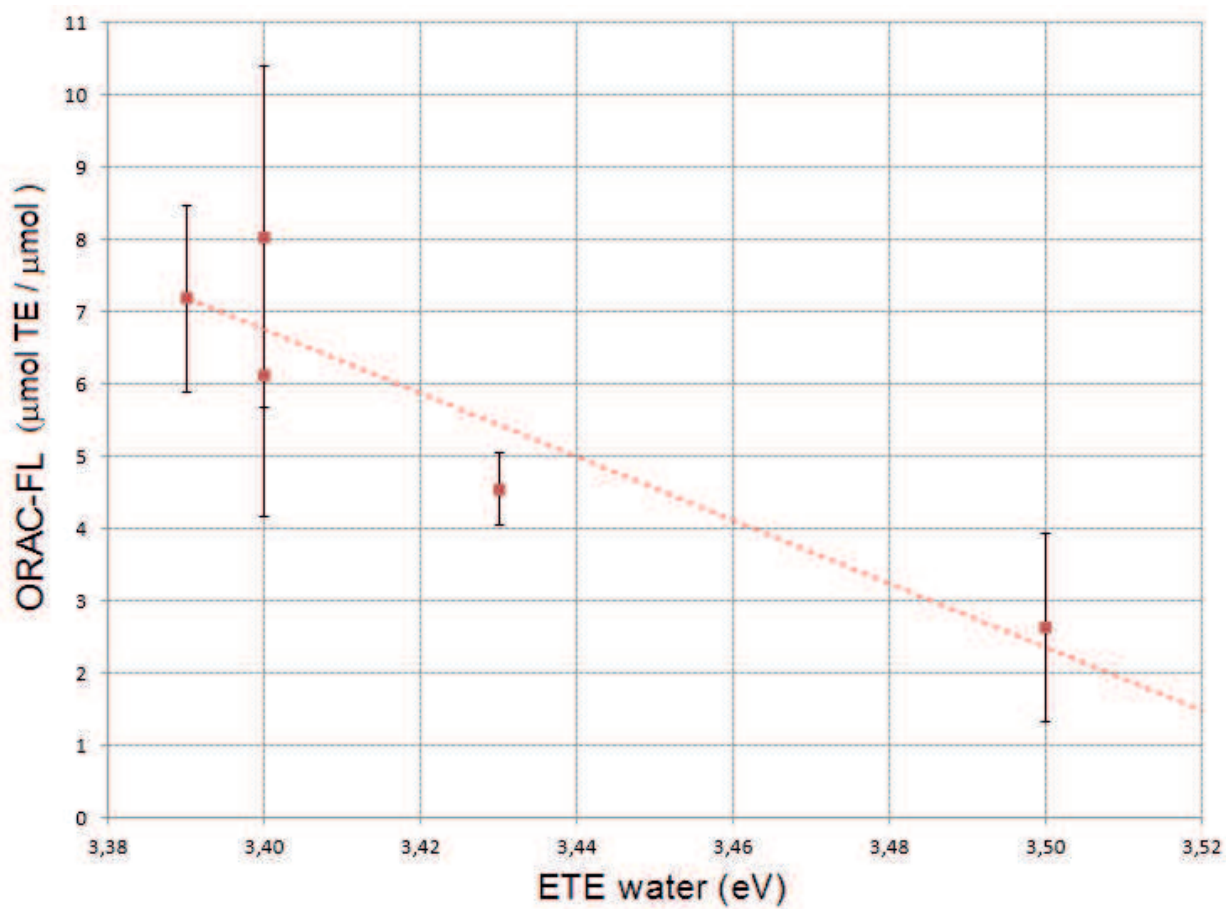
Figure 3.19: ORAC-FL from Wolfe with experimental errors versus ETEs in water. Red dashed line = fitted line.

cal scavenging reaction of flavonols could be SET-PT (linked to IPs) and SPLET (linked to ETEs).

3.5   Conclusions

Two prototype molecules, namely quercetin and edaravone, have been considered in order to test the performances of 21 exchange-correlation functionals in evaluating their anti-oxidant activity. This latter is related to two reactions mechanisms, hydrogen atom transfer and single electron transfer followed by proton transfer, whose thermodynamic is described by three parameters, bond dissociation enthalpy (BDE), ionization potential (IP) and proton dissociation enthalpy (PDE). The selected functionals are among the most commonly used belonging to three different classes of hybrids models, namely Global, Range Separated and Double Hybrids.

The obtained results show that the choice of exchange-correlation functional does not affect the stability order of the involved radicals. A coherent picture on the action mechanism thus appears for both quercetin and edaravone. Nevertheless, single properties, as BDEs and PDEs, are computed with different errors. A comparison with accurate reference values obtained at CBS-Q3 level, indicate that LC-ωPBE, M05-2X and M06-2X functionals are those giving the lowest errors. These methods are therefore suggested for an accurate, and fast, evaluation of energetic parameters related to anti-oxidant activity. Other computational parameters, such as basis set, have a minor role on both the global and relative trends.

Subsequently, 15 flavonols have been computationally studied in order to investigate if a single parameter may be used for the prediction of antioxidant activity. Three reaction mechanisms are taken into account, each of which is defined by a thermodynamic parameter: hydrogen atom transfer is linked to bond dissociation enthalpy (BDE), single electron transfer followed by proton transfer is linked to ionization potential (IP) and proton dissociation enthalpy (PDE), sequential proton loss electron transfer is linked to proton affinity (PA) and elec-

tron transfer enthalpy (ETE). All the theoretical parameters are computed by DFT methods in vacuum and in solvent in order to represent the possible sites of action for antioxidants. Among all thermodynamic parameters, BDE proves to be useful for the interpretation of the structural features of an antioxidant. Comparing theoretical enthalpies with experimental data sets, ETE is the only parameter that gives a reasonable correlation with experimental data; this allows us to suggest that sequential proton loss electron transfer could be the principal reaction pathway for flavonols during their radical scavenger activity and suggest that a theoretical evaluation of electron transfer enthalpies can be the right way for the prediction of antioxidant activity.

Chapter 4

Interpretation of Cu-catalyzed Alkoxyhalogenations of Ureas and Carbamates

4.1 Introduction

One among the most powerful methods for synthesis of biologically important heterocycles from simple unsaturated precursors is transition metal-catalyzed intramolecular cyclization. [143] Copper catalysts are very attractive because of their low cost, their tolerance toward many reactive functional groups and the common reaction conditions. In this field, the synergistic computational-experimental approach could be a way to clarify the synthetic strategies. In these respect, DFT contributed widely in previous literature to elucidate details of different copper-catalyzed reactions, such as alkynyl nitrile synthesis from simple alkynes, [144] azide cycloadditions, [145–147] retro-aldol reactions, [100] coupling reactions [148–151] and different kind of C-N/C-O/C-C bond formations. [152–156]

Another useful copper-catalyzed reaction is the alkoxyhalogenation of alkynyl ureas demonstrated by Gazzola et $al.$, [157] where simple $CuCl_2$ salt acts as catalyst during the production of nitrogenate heterocycles. In this situation, the 5-exo-O species is formed with good yield instead of the N-alkylated counterpart. Thus, to explain the experimental results and highlight the key step of reaction, we propose a DFT study regarding one of the experimentally used ureas,

N'-methyl-N-phenyl-N'-propargylurea. The analysis of tautomeric and monomer-dimer equilibria, complexes population and the relative energetics of intermediates and transition states thus performed an effect that allowed to propose a reasonable reaction mechanism. Subsequently, applying the same mechanistic approach to the $CuCl_2$ catalyzed cyclization of carbamates, we attempted to predict the selectivity of such reaction.

4.2 Computational Details

All calculations were carried out with the Gaussian 09 package. [50] Conformation analysis and geometry optimizations were carried out using the B3LYP functional. [51] A polarized/augmented double zeta basis set (6-31+G(d,p) for light atoms and the LANL2DZ basis set augmented with the diffuse function from the aug-cc-pVDZ set for th copper atom) was used in all the calculations of monomer pathways; effective core potentials (LANL) were also used for copper to reduce computational costs. The calculations involving dimers were carried out using the 6-31+g(d,p) basis set for all the atoms. The optimized structures were confirmed as true minima by vibrational analysis at the same level of theory. Solvent effects were evaluated using the PCM [55] model and acetonitrile solvent was selected in order to mimic the experimental conditions. MP2 [7, 158–162] and ROMP2 [158, 163, 164] single point energies were subsequently obtained for a few carbamates employing the B3LYP geometries.

4.3 Results and Discussion

The theoretical study has origin from the work of Broggini *et al.* focused on the reaction of alkynyl ureas; [157] the scheme and the conditions of the reaction involving the selected urea is reported in Figure 4.1. Unpublished results of carbamate are showed in Figure 4.2.

4.3.1 Urea Reaction Mechanism

To begin our study, an in depth analysis of solution equilibria in the reactive environment was made investigating how reagent conformational isomers can interact with $CuCl_2$. As it is known, dissolved urea derivates are involved in tautomeric
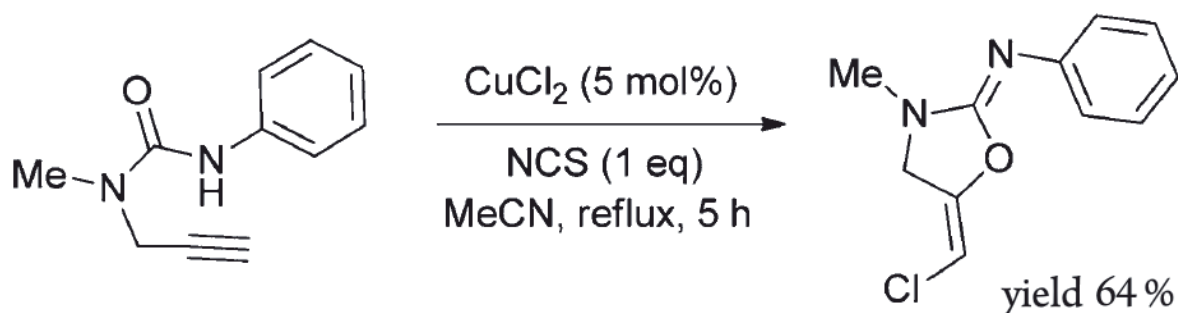
Figure 4.1: Reaction scheme of Cu(II)-catalyzed alkoxychlorination of an alkynyl urea.
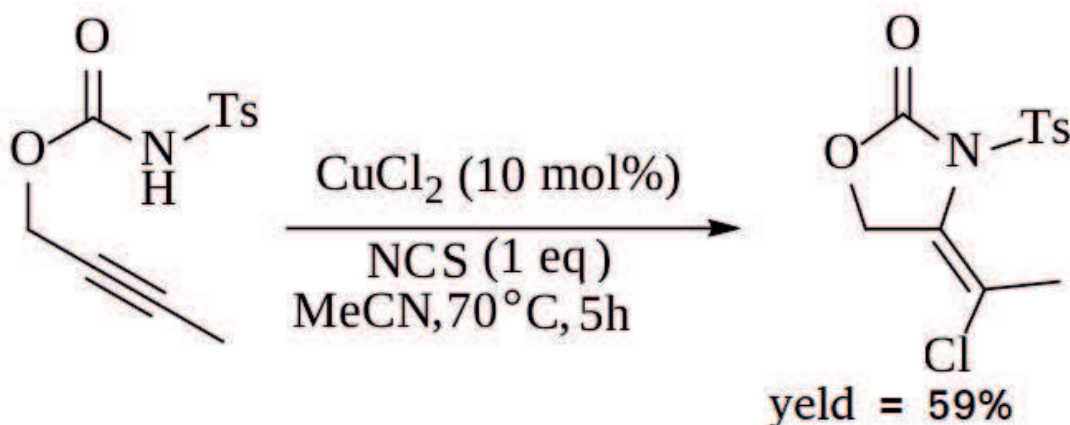
Figure 4.2: Reaction scheme of Cu(II)-catalyzed alkoxychlorination of an alkynyl carbamate.

equilibria between the iminic and the ketonic forms; [165] in presence of a co-ordinating salt, such as $CuCl_2$, the isomers relative energetics can be modified by the electrostatical interaction between the latter and the carbonyl oxygen, iminic nitrogen, potentially biasing the reaction pathway to follow alternative routes. Thus may happen also if the the C-C triple bonds coordinates to $CuCl_2$ (Fig.4.3). [166]
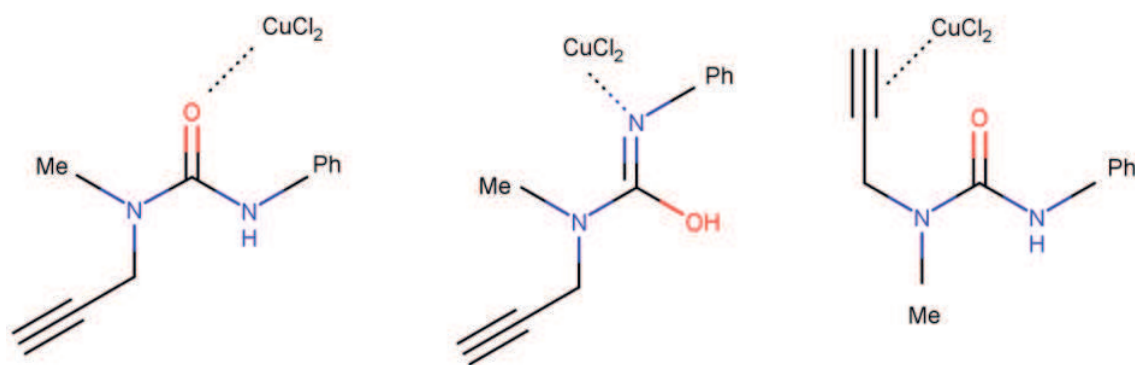
Figure 4.3: Urea tautomers with $CuCl_2$.
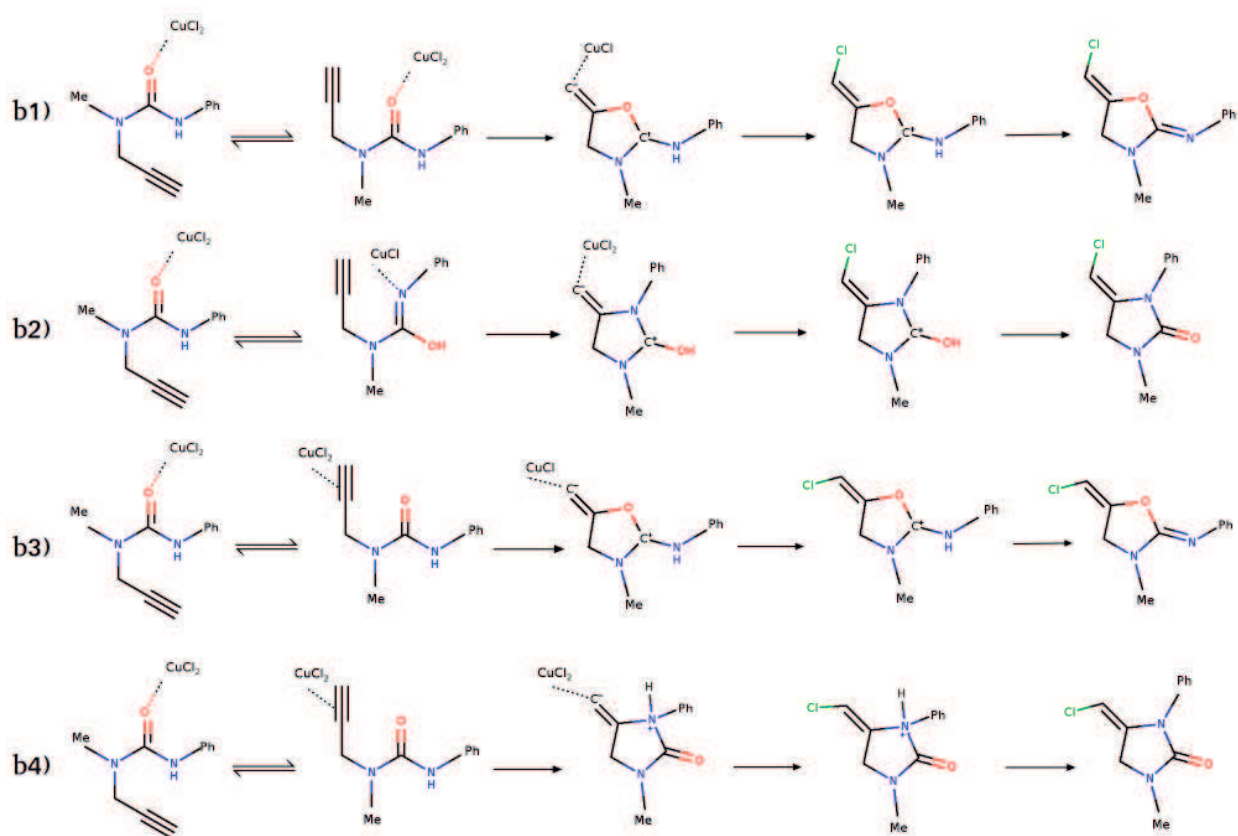
Figure 4.4: Four reaction schemes for alkoxyhalogenation of urea. From top to bottom: **b1**, **b2**, **b3**, **b4**.

Among all the possibilities, the coordination of $CuCl_2$ to the carbonyl oxygen gives the more stable species, followed by the species with copper coordinated to the iminic nitrogen of the other tautomer (ΔG=9.67 kcal/mol); lying even higher in energy there is the iminic tautomers with $CuCl_2$ on the C-C triple bond (ΔG=20.01 kcal/mol). Noteworthy, all those starting complexes could, in principle, be able to undergo ring-closing reaction thanks to the fundamental role of the catalyst, acting as electron withdrawing group. As common zero, the most stable conformer (Cu coordinated to C=O) is chosen in order to have comparable energies for all reaction pathways.

Starting from the three species in Figure 4.3 we investigated pathways potentially coherent with the experimental product (Fig.4.4); As the first step can involve either oxygen or nitrogen atoms, leading to different product, the reaction selectivity strongly depends on the relative energetic of the rate-determining steps.

In order of appearance, the path involves:

- *an intramolecular cyclization*: following the induction of a population of **min1** species from the lowest energy CuCl$_2$ coordinated species, the initial reactive event is the cyclization, during which the carbonyl oxygen approaches the C-C triple bond to create five member cycle *via* **TS1**. The formation of the new C-O bond leads to the localization of a negative charge on the terminal sp2 propargyl carbon, which is stabilized by CuCl$_2$ coordination, and a positive charge on the tertiary carbon of the cycle (**int1**). The latter is, however, stabilized *via* donation of its lone pair by nitrogens;

- *a chlorination step*: after the cyclization, (**int1**), N-chloride-succinimide transfer a Cl atom (formally chloride cation) to the Cu-bearing Carbon. Importantly, chlorination retains the C-C double bond configuration with the CuCl$_2$ moving away from the intermediate and approaching one of succinimide oxygens (**TS2**). Thanks to the latter displacement, CuCl$_2$ became again available to coordinate to the reactants. As a result intermediate 2 is obtained, which differs from the final product due to for the presence of an excess proton;

- *a deprotonation step*: the neutrality of the product is reached *via* the deprotonation of the aminic Nitrogen by any species that can act as bases (we chose here the succinimidyl anion) in the reaction environment.

We do not focus on the transition state of deprotonation because the energies are much lower than previous steps and the barriers will not be kinetically relevant for the reaction.

In Figure 4.5, the four lowest reaction paths are showed, the corresponding energies being reported in Table 4.1. The pathways show two principal features, a preequilibrium due to the cyclization and the rate-determining step nature of the chlorination. As example, the structure of two transition states, one of cyclization and one of chlorination, are shown in Figure 4.6. Focusing on the energetic of alcoholic tautomer **b2** (blue line in Fig.4.5), the activation energy of chlorination (**TS2**) is the lowest but its rate determining step is the cyclization (**TS1**) while for the other pathways the chlorination is the principal barrier (**TS2**).
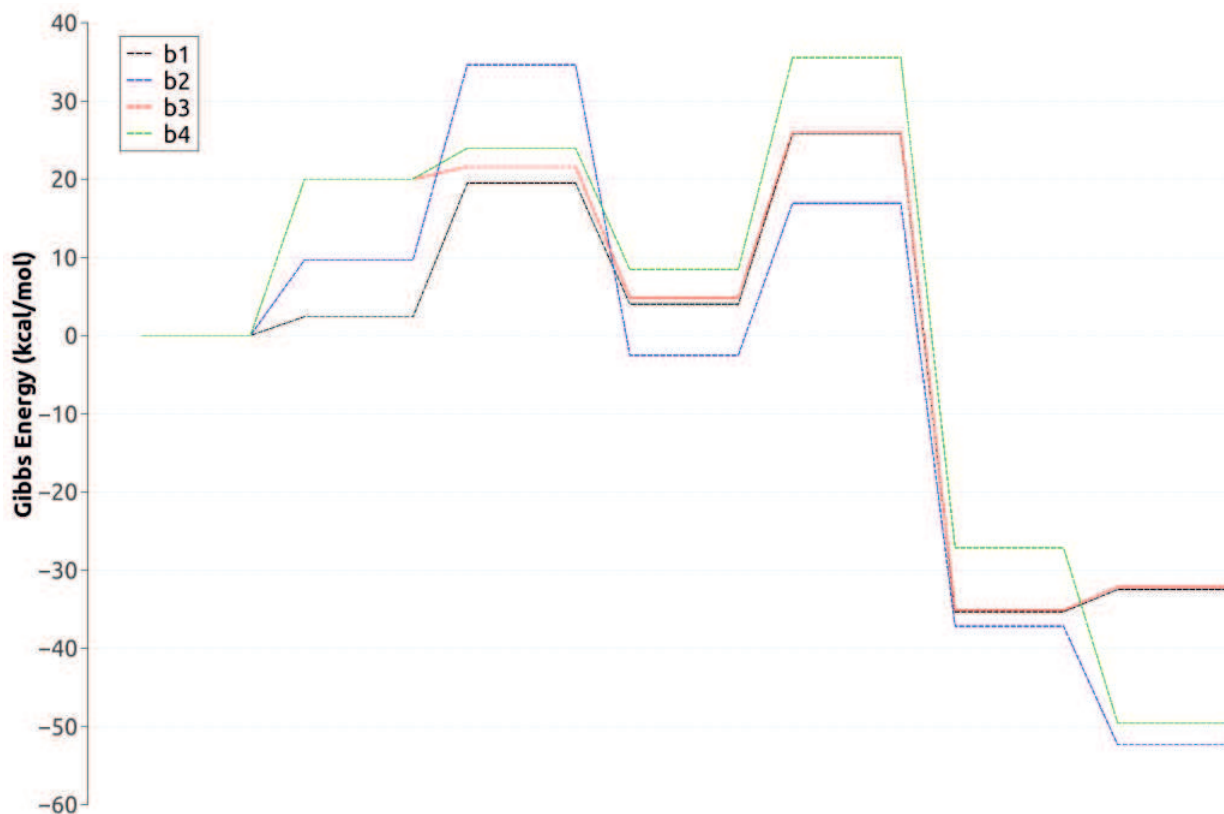
Figure 4.5: Gibbs' energy profiles for four urea alkoxyhalogenation pathways.

	Start	min1	TS1	int1	TS2	int2	Product
b1	0.00	2.41	19.47	3.99	25.82	-35.35	-32.48
b2	0.00	9.67	34.59	-2.52	16.91	-37.17	-52.36
b3	0.00	20.01	21.58	4.85	26.00	-35.15	-32.13
b4	0.00	20.01	23.95	8.41	34.03	-27.14	-49.58

Table 4.1: Complete energetics (in kcal/mol) of urea.

Comparing the energetic profiles we expect that the product will come from the cyclization of the aminic tautomer (corresponding to the black line and red line in Fig.4.5). The difference between the two reaction pathways is the final configuration of C=C double bond: X-ray data show us that the product has the E conformations while from the theoretical calculation comes out that both E and Z are possible.

The disagreement on steroselectivity between theoretical predictions and experimental products for the ureas may origin from a misconception related to the initial reacting state. Indeed, the nature of ureas could foster other kind of equi-
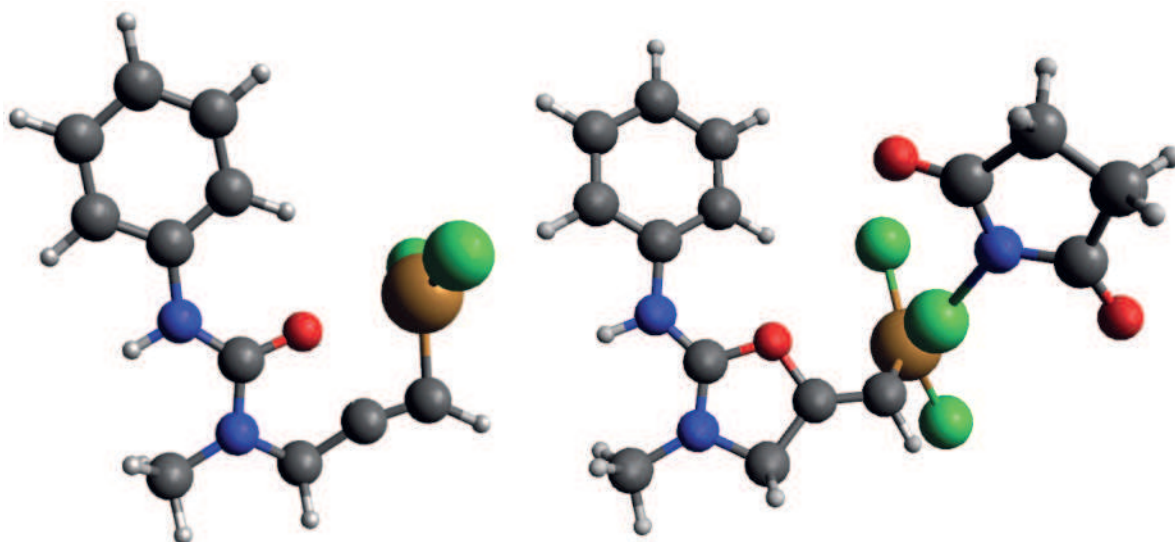
Figure 4.6: Optimized geometries of transition states detected in **b1** paths: on the left, TS of intramolecular cyclization, on the right, TS of chlorination by N-chlorine-succinimide.

libria in addition to the tautomeric one. For instance, the presence of iminic and hydroxyl groups may allow an attractive interaction between two monomers and the formation of a stable dimer. In fact, stable dimers of ureas were optimized *via* DFT: the two monomers interact *via* two hydrogen bond reaching a stable minimum, having a close-planar structure (Fig.4.7a). In thus context, also $CuCl_2$ may not be a passive player, as it can coordinate the dimers *via* electrostatic interaction. Even in thus case, two coordination sites are still available, namely the C-C triple bond and the heteroatoms. As to the latter case, the approach of $CuCl_2$ to the dimer's heteroatoms presents no barriers and leads to a $CuCl_2$ coordinated over the H-bonded groups in the dimer, and to a decrease in system energy of 10 kcal/mol ca. (Fig.4.7b). Albeit the new species is a stable minimum, it can easily lowers its energy even more by crossing the very low barrier (0.5 kcal/mol ca.); that leads to a symmetrically coordinated Cu. Importantly, the new geometry has an additional energetic gain (ΔG = -17 kcal/mol) and involve the copper cation in a new way (Fig.4.7c).

Noteworthy, the salt breaks the hydrogen bonds positioning itself between the two monomers: in this way, the copper atom can interact with two heteroatom while chlorides can interact with aminic hydrogen. The final energetic gain is around 28 kcal/mol respect to the dimer without the coordinated Copper salt, *de facto* suggesting that the new species may act as a kinetic trap for the reaction.

Figure 4.7: Optimized geometries of urea's dimers.

If so, one can expect that the salts coordination on two monomers (as in Figure 4.7) affects the electron donating effect of the heteroatom and reduces the capability to accept other electron density of Copper cation since it interacts with two heteroatoms. Such participation makes the heteroatom less electrophile reducing the ability to catalyze the intramolecular attack.

The formation of the dimers can justify the deactivation of the first two pathway in Fig.4.5 (**b1** and **b2**) leading to the product with final Z configuration of C=C double bond. In this way, the black pathway **b1** in Figure 4.5 is hindered in favor of the red one **b3**, that carry out the product with oxygenate heterocycle and the C=C double bond in the E configuration. The detailed path with schemes of geometries for each minimum and transition states is reported in Figure 4.8, the final proposed reaction mechanism is then shown in Figure 4.9.

4.3.2   Carbamate Mechanism Prediction

Motivated by the previous results, we applied the same approach to the reaction of carbamates with the $CuCl_2$ catalyst. In particular we discuss reactions involving, N-phenyl- and N-tosyl- carbamates. Importantly, carbamates present structural similarities with ureas, so one may expect that they would manifest a similar reactivity. For instance, one can expect that they establish tautomeric equilibria in solution and that $CuCl_2$ can be coordinated to different groups (Fig.4.10). Thus, we set to investigate a mechanism that is identical to the one for ureas (cyclization, chlorination and deprotonation, see Fig.4.11), with analogous theoretical tools.

The simplest of the two studied species has the phenyl group substituent on
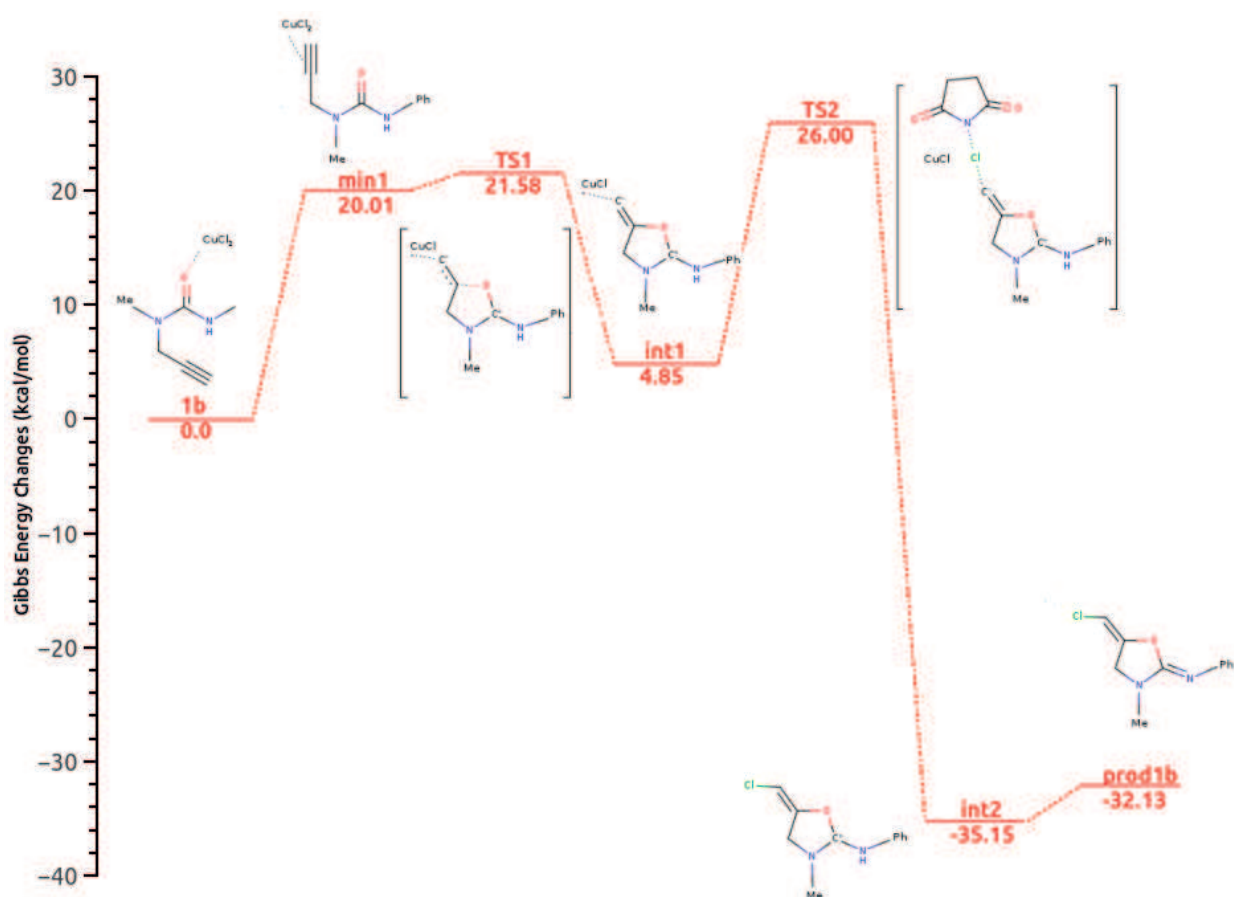
Figure 4.8: Gibbs' energy profile and structures calculated for the favorable pathway of the ureas alkoxyhalogenation (**b4**) in acetonitrile.
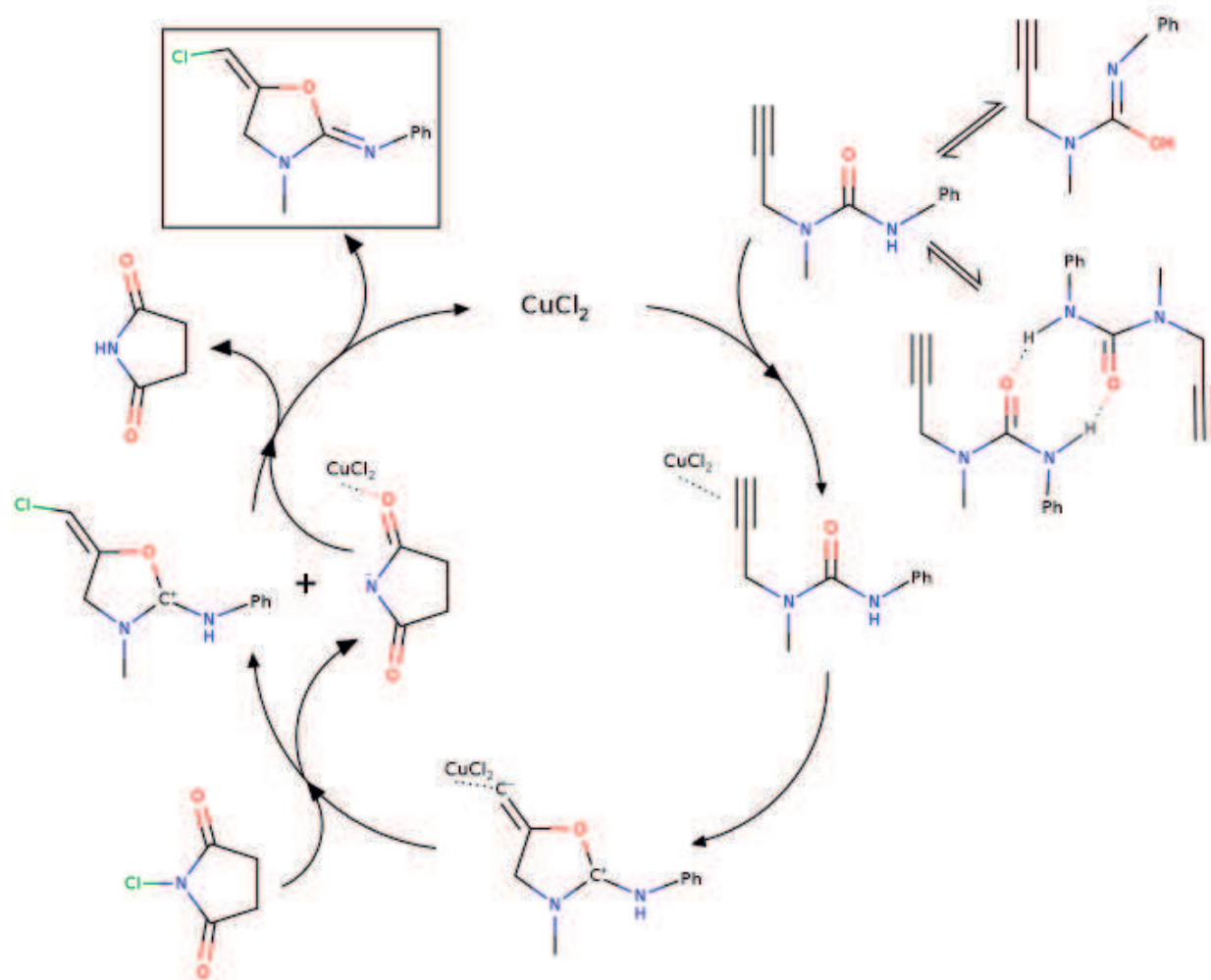
Figure 4.9: Reaction proposed mechanism catalyzed by CuCl₂.
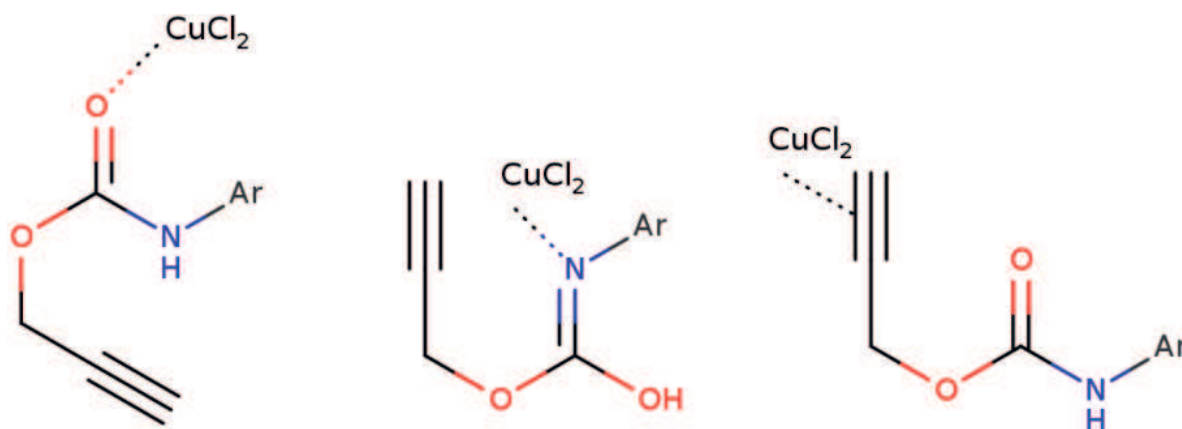
Figure 4.10: Carbamate tautomers with $CuCl_2$.

	Start	min1	TS1	int1	TS2	int2	Product
a1	0.00	2.19	20.44	9.43	35.14	-26.25	-30.68
a2	0.00	12.37	36.63	5.24	28.86	-7.49	-52.52
a3	0.00	14.26	19.34	10.67	36.10	-25.86	-30.23
a4	0.00	14.26	29.30	19.08	47.64	-15.96	-53.89

Table 4.2: Complete energetics (in kcal/mol) of carbamate.

the Nitrogen. From the energy profiles reported in Table 4.2 and related to the schemes in Figure 4.11, it is evident the competition between the activation energy of the cyclization (**TS1**) for the alcoholic tautomer **a2** and the energetic barriers of chlorination (**TS2**) of the other reagents. Thanks to the transition state theory, we can compare the rate-determining steps of different routes, the energies suggest that there is a strong kinetic competition between nitrogenated heterocycle product **a2** (blue line in Fig.4.12) and oxygenated heterocycle product **a1** and **a3** (black and red lines in Fig.4.12), due to the closeness of the barriers.

Our results correlates well with experiments, the reaction producing a complex mixture of products of difficult characterization. Experiments also show that using a tosyl instead of phenyl as aromatic group, the synthesis leads to a single product, with the heterocycle closed on the nitrogen and the C=C double bond with the E configuration. Thus we carried out also for this reactant, the DFT calculation: complete energetic being reported in Table 4.3, and schematically represented in Fig.4.11. Note that the experimental product is the one emerging from **ats4** paths in Figure 4.13.
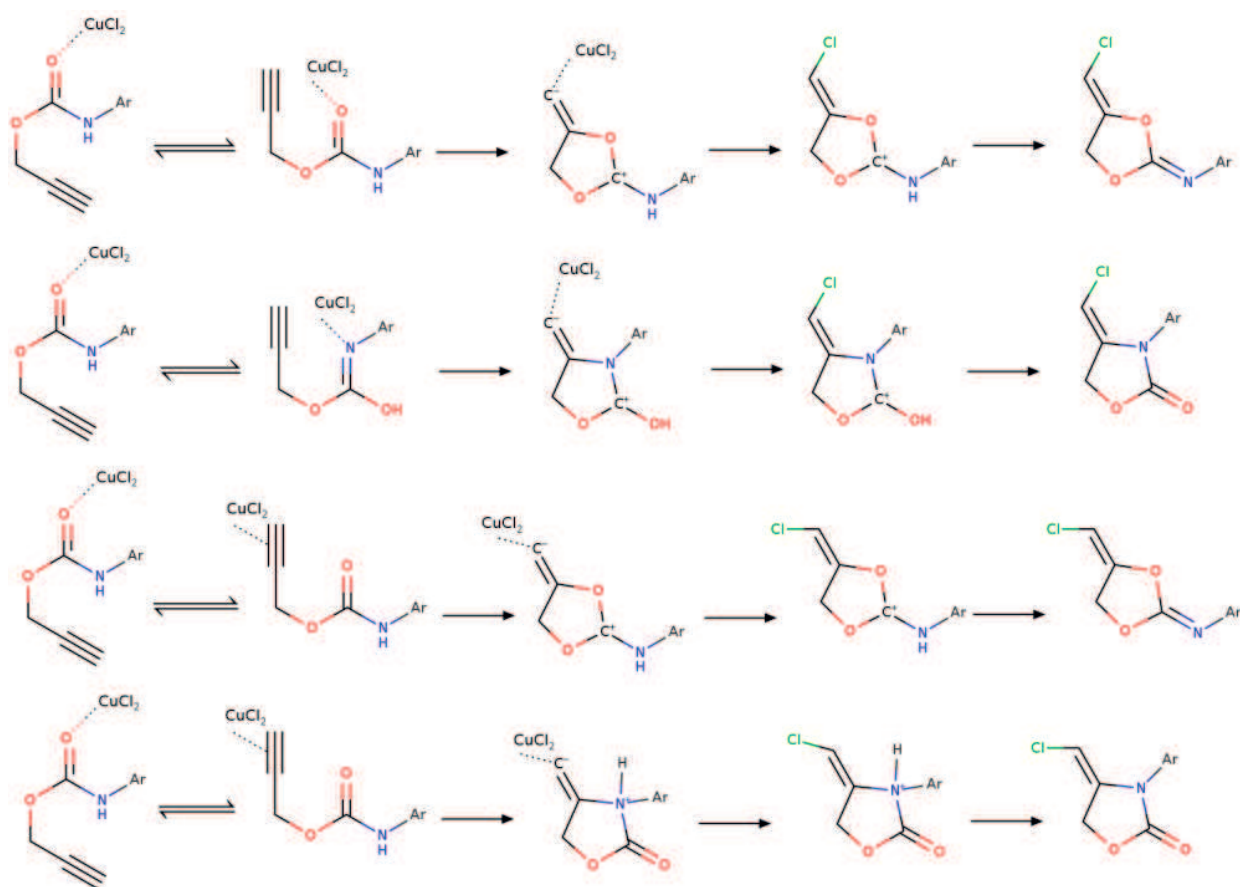
Figure 4.11: Four reaction schemes for alkoxyhalogenation of carbamate. From top to bottom: **a1**, **a2**, **a3**, **a4** with Ar=Ph; **ats1**, **ats2**, **ats3**, **ats4** with Ar=Tos.
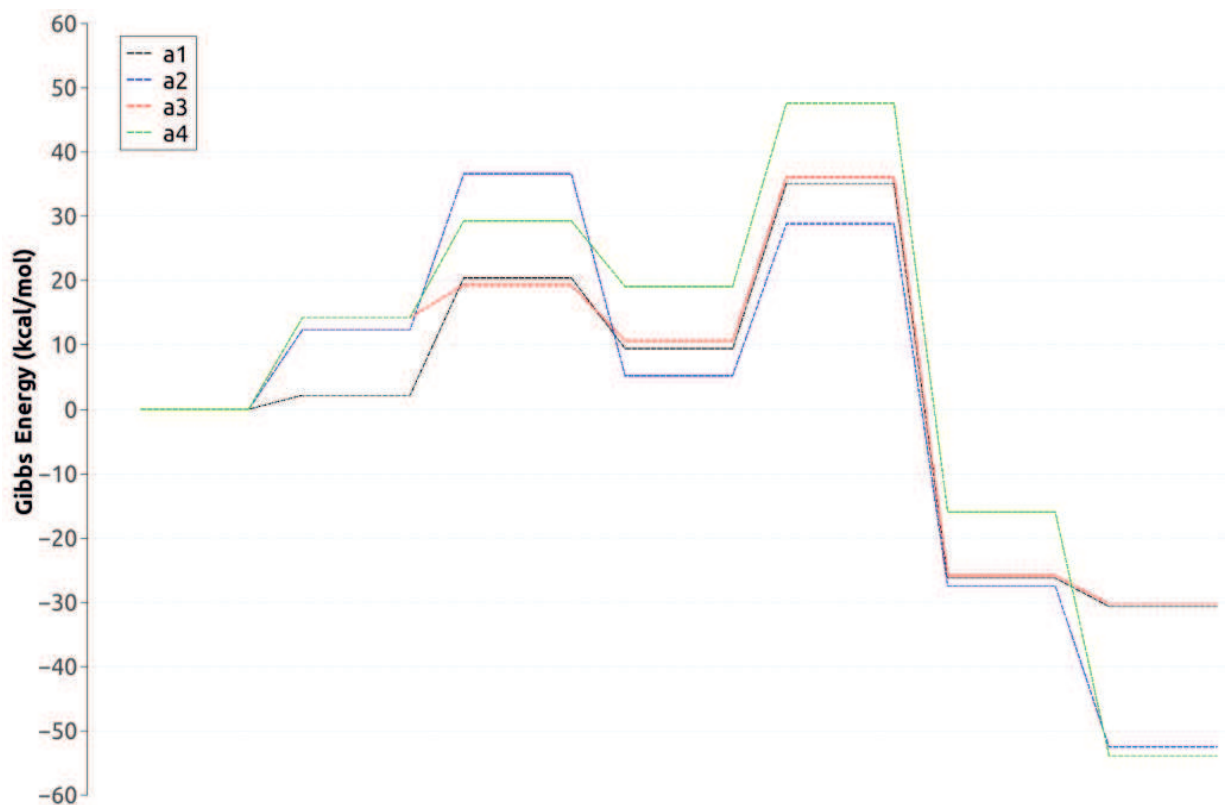
Figure 4.12: Gibbs' energy changes of four phenyl carbamate alkoxyhalogenation pathways.
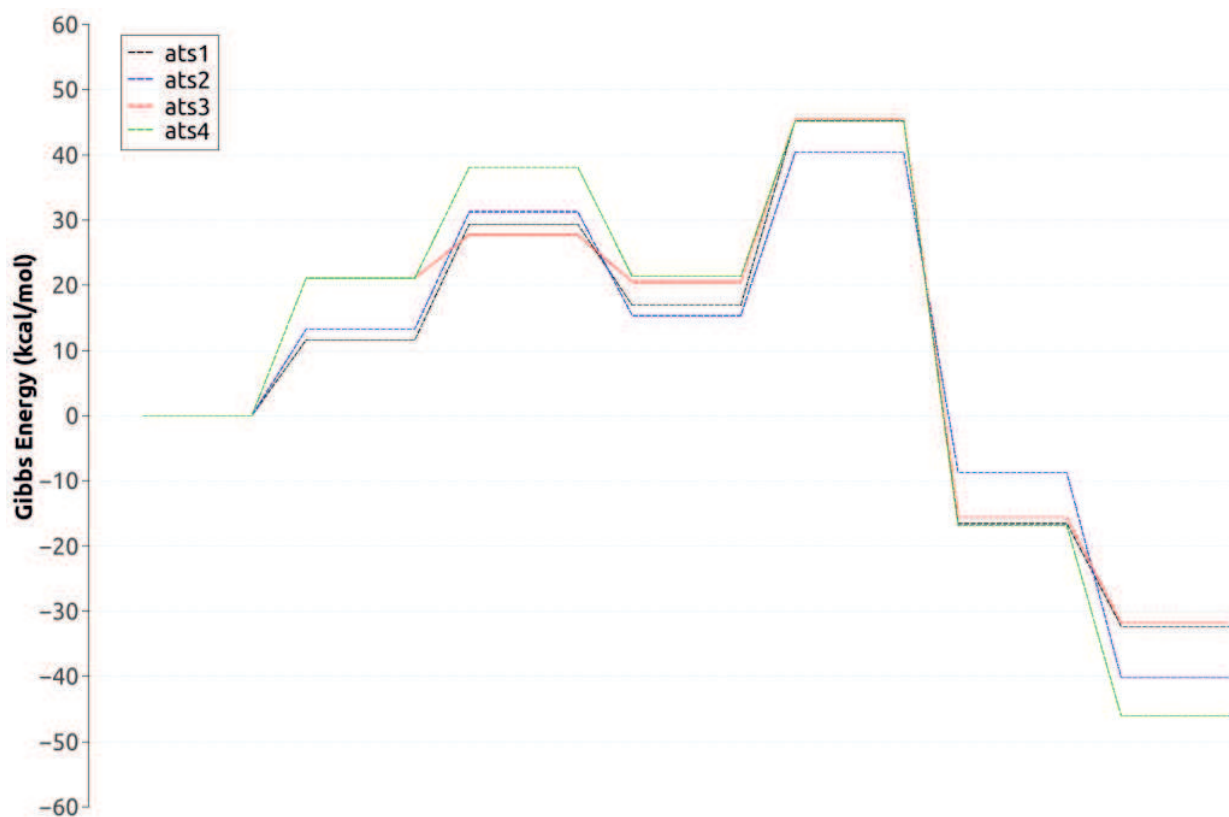
Figure 4.13: Gibbs' energy changes of four tosyl carbamate alkoxyhalogenation pathways.

	Start	min1	TS1	int1	TS2	int2	Product
ats1	0.00	11.63	29.36	16.94	45.35	-16.53	-32.32
ats2	0.00	13.28	31.27	15.35	40.38	-8.77	-40.18
ats3	0.00	21.10	27.72	20.53	45.40	-15.62	-31.78
ats4	0.00	21.10	38.10	21.37	45.16	-16.84	-46.07

Table 4.3: Complete energetics (in kcal/mol) of tosyl-carbamate.
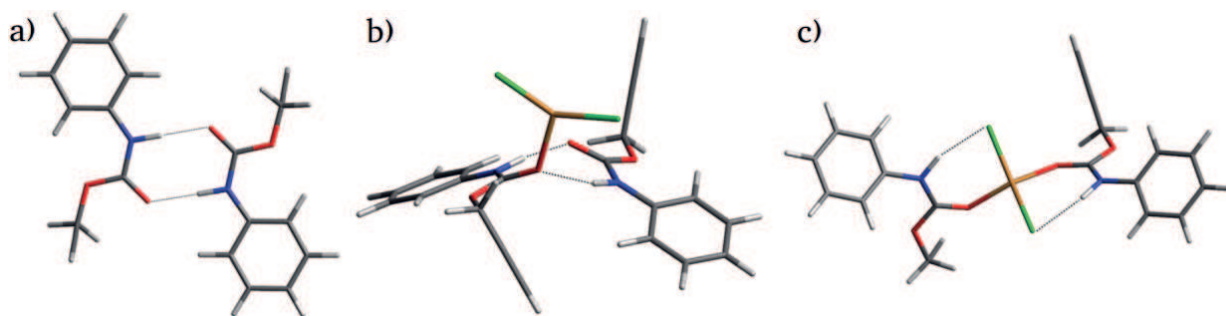
Figure 4.14: Optimized geometries of carbamate's dimers.

As for the theoretical results, we being noting that the tosyl markedly modifies the relative energy paths seen for the phenyl case. In particular we highlight an increase in the relative energies in the second half of the scheme, i.e. involving **int1** and **TS2** (chlorination). Differently from the phenyl carbamate, the rate determining step for all the pathways is the chlorination (**TS2**) simplifying the comparison.

Applying the same hypothesis of ureas, stable dimers of carbamates were optimized *via* DFT: the two monomers interact in the same way that ureas *via* two hydrogen bond, having a close-planar structure (Fig.4.14a).

Again, Copper coordinates the dimer on C-C triple bond or the heteroatoms. As to the case of ureas, the approach of $CuCl_2$ to the dimer's heteroatoms presents no barriers and leads to a $CuCl_2$ coordinated over the H-bonded groups in the dimer, and to a decrease in system energy of 5 kcal/mol ca. (Fig.4.14b). The new species can easily lowers its energy even more by crossing the very low barrier (0.5 kcal/mol ca.); that leads to a new geometry having an additional energetic gain of 11 kcal/mol (Fig.4.14c).

The salt positions itself between the two monomers: in this way, the copper atom can interact with two heteroatom while chlorides can interact with aminic hydrogen. The final energetic gain respect the dimer without the salt is around 17 kcal/mol, such possibility suggests the presence of a kinetic trap due to the new dimeric species. I.e. the Copper is coordinated with two heteroatoms receiving electron density by two species instead of one, thus reduce the catalytic feature being the Copper less electrophile and limiting deactivating the intramolecular

attack. Having said this, the first two pathway in Figure 4.13 for tosyl carbamate (**ats1** and **ats2**), that give the product with final Z configuration of C-C double bond, are hindered. So, the available pathways remain the red **ats3** and the green **ats4** (Fig.4.13) and these carry out the product whit oxygen and nitrogen heterocycle respectively and the correct configuration of double bond. Indeed, only the carbamate with nitrogen into the cycle is experimentally obtained.

Looking for a possible flaw into the theoretical approach, we notice an unique peculiarity of **ats4** path for tosyl-carbamate: after the ring closure, the intermediate 1 has charged quaternary nitrogen atom that is both involved in the cycle and bonded to the sulfur in the tosyl group. The same bonding pattern is concerned into transition state 2 (chlorination TS) and intermediate 2. Surprisingly, the N-S bond distances, from DFT optimized geometry, are 2.238Å in the **int1**, 2.514Å in the **TS2** and 2.339Å in the **int2**, versus bond distance in the starting material, 1.708Å, and bond distance of the product of **ats4**, 1.753Å. The N-S elongation bond on tetravalent Nitrogen induces remarkable changes on the whole carbamate structure: the $-SO_2-$ group loses the quasi-tetrahedrical geometry going toward a quasi-planar geometry, similarly to the nitrogen of the cycle. In the attempt to clarify if such bond length is due to methodological short comings, we increased the basis set up to 6-31+g(df,p) for all atoms, hoping to improve the description of Sulfur. Avoiding to use ECP and with the larger basis set reduces the distances at 2.177Å for the **int1** and 2.482Å for **TS2**. The difference between $\Delta G^{\ddagger}$ of **ats4** chlorination and $\Delta G^{\ddagger}$ of **ats3** chlorination also changes, going from -0.24 kcal/mol to +3.38 kcal/mol, suggesting **ats3** to be more likely despite leaning the two paths as competitive. As different approach, we choose single point energies computed with Møller-Plesset perturbation theory (MP2), the chlorination barriers are lowered of 1.5 kcal/mol c.a. but the $\Delta\Delta G^{\ddagger}$ remain almost the same (3.97 kcal/mol). As a final attempt, single point energy calculations with restricted open-shell Møller-Plesset theory were computed: unfortunately, the energies remain the same as the MP2 methods with a $\Delta\Delta G^{\ddagger}$ of 5.5 kcal/mol c.a..

In conclusion, despite the increase of the method, we are not able to discern between the two possible pathways of carbamates. Such gap could be filled

by further studies regarding, for example, a different methodological approach, enhancing the calculation *via* geometry optimizations with MP2 methods.

4.4 Conclusion

In this work we described the alkoxyhalogenation mechanism of alkynyl ureas catalyzed by Copper (II) salt *via* DFT method. Starting from experimental product, we proposed a mechanism consisting of an intramolecular cyclization step, a chlorination step by NCS and a proton extraction. Taking into account the tautomeric equilibrium and the $CuCl_2$ coordination, we studied four possible reaction pathways that lead to different products, differing for an Oxygen or a Nitrogen into the ring and for the E/Z configuration of C=C double bond. Energy paths suggested the E selectivity of the C=C configuration; moreover, the hypothesis about the assembling of stable dimers between ureas and $CuCl_2$ allowed us to indicate the 5-exo-O species as the expected product, consistently with experimental product. Successively, we attempt to apply the same mechanism to the Cu-catalyzed alkoxyhalogenation of two different carbamates. In this case, albeit the method was stressed, DFT calculations partially rationalize the experimental product, especially for the tosyl-N-carbamate, for which the method is not able to discriminate between two possible species. This suggest that the next step could be the improvement of the method in order to prove the truthfulness of the mechanism for carbamates.

Chapter 5

Prediction of Copolymer Composition

5.1 Introduction

One among the great challenges in polymer science is the deep understanding of the links between the catalyst features and its catalytic behavior toward monomers. Obviously, such goal has a great industrial and scientific interest for the design of copolymerization catalysts. In this respect, although the topic has been studied for more than fifty years, the certainties about the polymerization process by homogeneous catalyst are a few, for example the fundamental role of steric hindrance of catalyst is widely accepted. Conversely, a lot of features still remain somewhat unclear, among all the importance of the counterion, of the chain-control given by the ultimate or penultimate monomer and the competition between two different coordination sites. [167] Technological and scientific progress has allowed to produce huge number of different polymers, from homopolymers to copolymers, from alternating to block to gradient polymers, from linear to branched, from elastomer to thermosetting to thermoplastic, all of these made with widely different monomers. Among the most produced polymers in the world, there are the polyolefin elastomers; they have a block structure, are based on ethene and propene and, are important players in the field of synthetic rubbers because of the similarity with natural rubber. [168] In an ethene/propene elastomer, the way ethene and propene distribute themselves along the macromolecular chain and the nature of propene placement are the molecular features that control bulk properties and, in turn, the elastic behavior (Fig.5.1). [169]
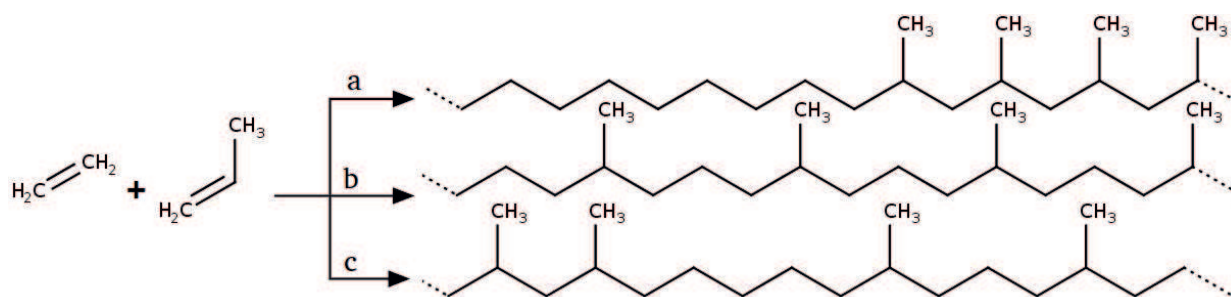
Figure 5.1: Copolymerization between ethene and propene to obtain: a) block copolymer, b) alternate copolymer, c) random copolymer.

In recent years, a class of single-site homogeneous catalyst has been developed reaching high stereoselectivity, high activity and a narrow molecular weight distribution of the produced polymer. [170–174]

Besides homogeneous catalysts, simpler catalytic systems are employed during the syntheses of other kind of copolymers, such as tailored functionalized copolymers. Ionic, radical, metathesis reactions are among the most used to obtain engineered materials with specific architectures, compositions and functionalities that are attractive for a variety of applications in the fields of biotechnology and nanotechnology. As an example, we recall here the acid-base properties of copolymers made by protonable monomers, which can act as polyelectrolytes, and depend on the monomers' distribution along the chains. [175] In turn, changes in polyelectrolytic behavior can affect interesting features, such as the antimicrobial activity. Despite the significant advances, however, a fine control over the distribution of the monomers along the copolymer chain still remains a challenge.

Turning to more fundamental aspect in the field of polymers, we recall that the fundamental thrust behind the theoretical study of copolymerizations comes from the in depth understanding of critical features that directly influence the reaction behavior during a copolymerization. As for this, the most appropriately starting point is the presentation of the kinetic descriptions that can be applied to the copolymerization mechanism and its historical application to several different copolymerization systems.

A suitable approach for the study of the copolymerizations' kinetic is the kinetic Monte Carlo method of the stochastic processes. In wider terms, a stochastic

process describes a system that statistically evolve during time. [176, 177] As an example, we could employ a system that can move between states from time n to time $n + 1$. Every available state i of the system has a probability P_i, so that the $P_i^{(n)}$ is the probability to find the system into state i at time n. Thanks to that, we define a probability distribution on the state space of the system.

To describe the system evolution from a state i at time n to a state j at time $n + 1$, we define a *transition* with the probability

$$P(X_{n+1} = j | X_n = i) \tag{5.1}$$

Transitions like the previous one, where P depends only on the current state, are defined as *Markovian*. If the probability P for the transition $i \to j$ is independent of n, we can define a time-homogeneous probability p_{ij} as

$$p_{ij} = P(X = j | Xn = 1)_{n=1} \tag{5.2}$$

the probabilities for each jump from i representing a probability distribution, which must satisfy the properties

$$p_{ij} \geq 0 \quad \text{and} \quad \sum_j p_{ij} = 1, \ i = 1, 2, \dots \tag{5.3}$$

As usual we can gather all probabilities into a single matrix, called *transition matrix*

$$T = \begin{bmatrix} p_{11} & p_{21} & \cdots \\ p_{12} & p_{22} & \cdots \\ \vdots & \vdots & \ddots \end{bmatrix} \tag{5.4}$$

Every elements p_{ij} of matrix 5.4 has to be positive and the sum of elements of every column is equal to one; given these, it is frequently called *stochastic matrix*. When the stochastic matrix is known, we can define an initial state of system and calculate the evolution of the probability distribution by matrix multiplication; however it is also possible to sample the probabilities and assign a new state to the system with an iterative approach: the system that evolves in that way is defined as a *Markovian chain*. [178, 179]

From the chemical point of view, the Monte Carlo simulation of Markov processes allows to describe quite different process, such as vapor condensation, [180] adsorption-desorption equilibria, [181] epitaxial growth, [182] diffusion effects; [183] the evolution of a chemical system where reactants are involved can be also simulated (for a complete theoretical dissertation, read [184–186]).

The key to apply these method lyes in the definition of probabilities p_{ij}; when reactants are present, a way to connect p_{ij} to a chemical process can exploit transition state theory (TST). [11–13] Assuming we know all the possible reactive pathways, we can compute the rate constant for each pathway as

$$k_{ij} = A \cdot e^{\frac{-\Delta G_{ij}^{\ddagger}}{RT}} \tag{5.5}$$

where k_{ij} is the rate constant from state i to state j, A is the pre-exponential factor, R is the universal gas constant, T is the temperature and $\Delta G_{ij}^{\ddagger}$ is the Gibbs' activation energy needed to jump from state i to state j. Employing high-quality TST rates into a stochastic model, the kinetic Monte Carlo is able to describe carefully the real dynamics on the potential energy surface, turning into an alternative to molecular dynamics. [187]

The link between constants k_{ij} and the probability p_{ij} can be built exploiting Equation 5.3. To define such probabilities, one can normalize the rates of reactions R_{ij} as follow:

$$p_{ij} = \frac{R_{ij}}{\sum_j R_{ij}} \tag{5.6}$$

where R_{ij} is the transition rates from the state i to j; each rate can be calculate as the product of molar concentrations of reactant and the rate constant k_{ij}, which can be simply derived as $k_{ij} = A \cdot e^{\frac{-\Delta G_{ij}^{\ddagger}}{RT}}$. Substituting the rates into Equation 5.6, the pre-exponential factor A will be simplified from the fraction.

The first approach employed for the description of copolymer compositions relied on the assumption that the chemical reactivity of propagating chain (which

may be a free radical, carbocation, or carbanion) in a copolymerization is dependent only on the identity of the monomer unit at the growing end and independent of the chain composition preceding the last monomer unit (this is referred to as the *first-order Markov* or *terminal model* of copolymerization). [169] Starting from the previous axiom, during a copolymerization of two monomers, M_1 and M_2, four propagation reactions are possible: each monomer can add either to a propagating chain ending in M_1 or one ending in M_2

$$M_1^* + M_1 \xrightarrow{k_{11}} M_1^* \tag{5.7}$$

$$M_1^* + M_2 \xrightarrow{k_{12}} M_2^* \tag{5.8}$$

$$M_2^* + M_1 \xrightarrow{k_{21}} M_1^* \tag{5.9}$$

$$M_2^* + M_2 \xrightarrow{k_{22}} M_2^* \tag{5.10}$$
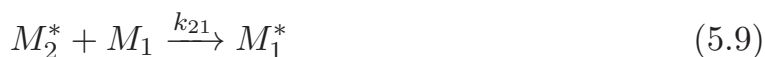
where k_{ij} are the rate constant for a propagating chain ending in M_i reacting with monomer M_j. If we assumed that all propagation reactions are irreversible, we could write the rates of disappearance of the two monomers (which are synonymous with their rates of enchainment), as

$$-\frac{\mathrm{d}[M_1]}{dt} = k_{11}[M_1^*][M_1] + k_{21}[M_2^*][M_1] \tag{5.11}$$

$$-\frac{\mathrm{d}[M_2]}{dt} = k_{12}[M_1^*][M_2] + k_{22}[M_2^*][M_2] \tag{5.12}$$

Dividing Equation 5.11 by Equation 5.12 yields the ratio of the rates at which the two monomers enter the copolymer as

$$\frac{\mathrm{d}[M_1]}{\mathrm{d}[M_2]} = \frac{k_{11}[M_1^*][M_1] + k_{21}[M_2^*][M_1]}{k_{12}[M_1^*][M_2] + k_{22}[M_2^*][M_2]} \tag{5.13}$$

To proceed further, the steady-state concentration may be assumed for M_1^* and M_2 separately: for these, to remain constant, thanks to their reactive nature the rates of reaction 5.8 and 5.9 have to be equal

$$k_{21}[M_2^*][M_1] = k_{12}[M_1^*][M_2] \tag{5.14}$$

Combining equation 5.14 with equation 5.13 one finally obtains

$$\frac{d[M_1]}{d[M_2]} = \frac{[M_1](r_1[M_1] + [M_2])}{[M_2]([M_1] + r_2[M_2])} \tag{5.15}$$

where the parameters r_1 and r_2 are called *reactivity ratio* and are defined by

$$r_1 = \frac{k_{11}}{k_{12}} \qquad\qquad r_2 = \frac{k_{22}}{k_{21}} \tag{5.16}$$

The Equation 5.15 is known as the *copolymerization equation* or the *copolymer composition equation*. Indicating with f_1 and f_2 the mole fractions of monomers M_1 and M_2 in the feed and F_1 and F_2 the mole fractions of M_1 and M_2 in the copolymer, the copolymerization equation (Eq.5.15) can be expressed in these quantities as

$$f_1 = 1 - f_2 = \frac{[M_1]}{[M_1] + [M_2]} \tag{5.17}$$

and

$$F_1 = 1 - F_2 = \frac{d[M_1]}{d[M_1] + d[M_2]} \tag{5.18}$$

Combining Equations 5.17 and 5.18 with 5.16 yields

$$F_1 = \frac{r_1 f_1^2 + f_1 f_2}{r_1 f_1^2 + 2 f_1 f_2 + r_2 f_2^2} \tag{5.19}$$

A parallel approach can be followed without the steady-state assumption, involving a statistical approach: the probability p_{11} of forming $M_1 M_1$ dyad in a copolymer chain is given by the ratio between the rate for M_1^* reacting with M_1 and the sum of the rates for M_1^* reacting with M_1 and M_2, that is

$$p_{11} = \frac{R_{11}}{R_{11} + R_{12}} \tag{5.20}$$

where R_{11} and R_{12} are the rates of reactions 5.7 and 5.8; substitution of the two expression for R into the 5.20 yields

$$p_{11} = \frac{r_1}{r_1 + ([M_2]/[M_1])} \tag{5.21}$$

Similarly, the transition probabilities for forming the other dyads follow the form of Equation 5.21. Of course, the sum of probabilities of addition to M_1^* and

M_2^* are each, separately, equal to 1 ($p_{11} + p_{12} = 1$ and $p_{21} + p_{22} = 1$).

The same reactivity ratios were introduced by Hayashi for an heterogeneous Ziegler-Natta catalytic systems; using a two-site first-order Markovian model, he fitted the experimental triad distribution and he obtained r_1 and r_2 from the probability parameters *via*

$$r_1 = \frac{P_{11}}{P_{12} \cdot q} \qquad\qquad r_2 = \frac{P_{22} \cdot q}{P_{21}} \qquad\qquad (5.22)$$

were q is equal to $[M_1]/[M_2]$. Likewise, a statistical approach based on a pure Markovian copolymerization model was introduce for a single center catalyst, [188] defining, again, the Markovian probabilities P_{ij} as

$$p_{12} = \frac{1}{1 + r_1 \cdot f} \qquad\qquad p_{21} = \frac{f}{f + r_2} \qquad\qquad (5.23)$$

The two reactivity ratios, specifically their product, are still used as a characterizing parameter for the copolymer microstructures: if $r_1 r_2 > 1$ the copolymer has block nature, if $r_1 r_2 = 1$ the copolymer is random while if $r_1 r_2 < 1$ one has an alternate copolymer. The common routine procedure for the estimation of reactivity ratios consists in the fitting of mathematical models (the most diffuse Mayo-Lewis, [189] Fineman-Ross [190] and Kelen-Tudos [191]) to experimental data. An alternative is represented by diad, triad, pentad or heptad fitting, as described by Galimberti. [192]

Until now, the equation refers to the instantaneous copolymer composition, that is the composition of the copolymer formed from a particular feed composition at very low conversion (say less than 5%) such that the composition of the comonomer feed is relatively unchanged from its initial value. In order to determine the instantaneous copolymer composition as a function of conversion for any given comonomer feed, one must resort to an integrated form of the copolymerization equation. A useful method for analyzing copolymer composition as a function of conversion was developed by Skeist: [193] consider a system with initially M total moles of monomers and a formed copolymer rich in monomer M_1, when dM moles of monomers have been copolymerized, the polymer will contain

$F_1 dM$ moles of monomer 1 and the feed $(M - dM)(f_1 - df_1)$ moles of monomer 1. For the mass balance, the moles of M_1 copolymerized must be equal to the difference in the moles of M_1 in the feed before and after reaction

$$MF_1 - (M - dM)(f_1 - df_1) = F_1 dM \tag{5.24}$$

It's possible to rearrange and convert to the integral form the Equation 5.24

$$\int_{M_0}^{M} \frac{dM}{M} = \int_{(f_1)_0}^{f_1} \frac{df_1}{(F_1 - f_1)} \tag{5.25}$$

A useful integrated closed form of equation 5.25 can be

$$1 - \frac{M}{M_0} = 1 - \left[\frac{f_1}{(f_1)_0}\right]^{\frac{r_2}{(1-r_2)}} \left[\frac{f_2}{(f_2)_0}\right]^{\frac{r_1}{(1-r_1)}} \left[\frac{(f_1)_0 - \frac{(1-r_2)}{(2-r_2-r_1)}}{f_1 - \frac{(1-r_2)}{(2-r_2-r_1)}}\right]^{\frac{(1-r_1 r_2)}{(1-r_1)(1-r_2)}} \tag{5.26}$$

which relates the conversion degree to changes in the comonomer feed composition; the zero subscripts indicate initial quantities.

With the needed kinetic tools being clarified, the following sections describe the theoretical investigation of, first, an example of a simple copolymerization reaction (an atomic-transfer radical-polymerization, ATRP). Subsequently, a more intricate copolymerization system is described, namely a homogeneous catalyzed copolymerization.

5.2 Functionalized Monomers ATRP

Tailored polymers with controlled physical and chemical properties are attractive for a variety of applications in the fields of biotechnology and nanotechnology, so that the demand in macromolecular synthesis precision in order to obtain macromolecules with specific architecture, composition and functionality is continuously increasing. [194–196]

The copolymerization processes, hence implying the simultaneous polymerization of different monomers, are the most used to obtain engineered materials

through polymerization techniques such as ionic, radical, metathesis reaction. However, despite the significant advances in the field of polymer synthesis, a fine control over all aspects characterizing the monomers along the copolymer chain, which provides a handle to impose specific physical properties to the final material, still remains somewhat a challenge. To stress the importance of the latter issue in biomedical related applications, we recall how both macroscopic (e.g. amount of hydrophobic pendants [197]) and subtler (for instance, stereo-regularity [198]) features strongly affected the conformation of polymers in solution and consequently the transport and protection of drugs that need to reach an intracellular target.

Another quantitative demonstration of how varying the chain composition impacts on physico-chemical properties of copolymers, whose backbone was designed to have specific biological properties at the nanoscale level, can be extracted from the recently synthesized linear and branched three-component copolymers [175,199] with a combined "block(b)-random(ran)" structure such as A-b-(B-ran-C)$_n$ (A = monomethossi polyethylene glycol; B = methylmethacrylate; C = alkyl aminoethyl methacrylate, AAEMA; n = 1, 2, or 4) obtained via a classic ATRP process using a catalyst based on Cu/bipyridine. For these, small variations in chemical composition were found to be fundamental in defining a few important physical properties (e.g. the amount of surface charge) impacting on their biological behavior, e.g. their antimicrobial activity.

Notably, it was found that the amount of AAEMA in plaques formed by the above reported copolymers influenced the capability of forming charged strong hydrogen bonds (c–H–bonds) between protonated and un-protonated amino pedantgroup, a strategic goal if one wishes to surpass the threshold of surface charge density needed to make plaques active against bacteria exploiting only water protonation. [200,201] As c–H–bond interactions are possible only between AAEMAs pedant groups that are first or second neighbors due to geometrical constraints, the plaque surface charge may be connected also to the distribution of comonomers along the chains. The latter observation, again, highlights the important role played by the chain microstructure in defining materials properties.

The latter issue may be of particular relevance for shorter mPEG-b-(MMA-ran-DMAEMA) chains, which were found to form polymersomes. [202–206] With these studied as drug delivery systems in solution due to their polyelectrolytic behavior, it was indeed found that the amount of DMAEMA in the copolymer back-bone controlled the extent of polymersomer swelling induced by a decrease in pH. [207, 208] A the swelling is expected to start from the aggregate external interphase, any inhomogeneity in the DMAEMA distribution may change the pH at which the swelling begins or the extent of its penetration in the double layer; in turn, these characteristics may impact on the selection of specific applications or the mass of drug released. They can also impact on the stability of the swollen aggregates, limiting the amount of polyelectrolytes dispersed in the human body. Thus, controlling comonomers distributions may, again, be key to tailor properties.

With a direct relevance to controlling copolymer microstructure, we recall that living anionic polymerization and controlled radical polymerization (CRP) techniques allowed the preparation of unprecedented microstructures such as multi-block copolymers or gradient copolymers. [209–212] In this case, attempts to produce tailor-made microstructures rely on the controlled sequential addition of comonomers during the copolymerization process or on the choice of comonomers with very different reactivity ratios, r_1 and r_2. Indeed, the latter scenario may even produce a copolymer with properties similar to the ones of a homopolymer at the beginning of the chain, which gradually includes more and more of the least reactive monomer.

Previous literature on MMA/DMAEMA copolymers (*vide infra* [213–216]) led to believe that $r_{MMA} \simeq r_{DMAEMA} \sim 1$. This idea was also supported by the similar electronic structure of the reactive functional groups and suggested that copolymers should be expected to present a random comonomer distribution. Surprisingly, instead, a strong preferential inclusion of DMAEMA with respect to MMA in the growing chain was found in the earlier experiments carried out by the group of Izzo at Salerno, so that we were forced to employ high MMA/DMAEMA feed ratio to obtain a copolymer composition appropriate for the intended applications. A second important consequence of the difference in

reactivity between MMA and DMAEMA is, of course, that the microstructure is likely to substantially deviate from the one of a random copolymer, so that the most rapidly polymerized monomer may form homo–sequences of some length. Given the possible formation of c–H–bonds between neighboring pendants along the chain, it would therefore be of interest to understand the dependence of the probability of finding a chosen monomer at a specific position along the chain, which correlates directly with its reaction probability (or rate) at a specific time during the polymerization, and the experimental conditions. Approaching this task from the experimental point of view is, however, made complicate by the inability of NMR to discriminate between different triads.

In order to reach a deeper understanding of the chemical behavior in ATR copolymerization (ATRcoP) of MMA and DMAEMA in order to produce materials with better tailored features, we re–evaluate the reactivity ratios (r_{MMA} and r_{DMAEMA}) of the two monomers with ATRP data obtained at different feed compositions. Apart from quantifying the relative monomer reactivity, these ratios allowed to stochastically simulate the copolymerization reactions within the framework of the "terminal model", [169] thus providing a complete representation of the chain micro–structural details "in lieu" of the lacking NMR data. In the attempt of understanding the origin of the difference in behavior between the copolymerizations discussed in the literature and our results, we also employed DFT electronic structures calculations to estimate reaction rates and the possible formation of dimers between monomers and a growing radical chain. In the latter respect, we notice, however, that the chemical nature of the monomers does not suggests the presence of chemically specific interactions, so that only weak intermolecular forces should be expected to play a role, if any.

5.2.1   Modelling Approach and Electronic Structure Calculations

The kinetic constants needed to define the reactivity ratios can, in principle, be obtained via electronic structure modelling assuming the validity of Transition State Theory [217] (TST) in its harmonic oscillator approximation (HTST). [218] For convenience, we adopt the Eyring's style-approach, [13] which requires estimating TS Gibbs' energy barriers, $\Delta G^{\ddagger}$. The latter are commonly computed as

difference between G's for the TS and asymptotic (i.e. at infinite distance) reactants. As for the latter, we modelled the terminal radical of the growing chains adding a methyl radical to MMA or DMAEMA so to generate a tertiary radical, which would then be made to react with both monomeric species. Notice that the tertiary radical is expected to be more stable than the alternative secondary counterparts, and hence more rapidly formed during chain propagation. With respect to this choice, we also mention that one could avoid study the very first chain propagation act, namely the reaction between the initiator and a monomer, within the framework of the *terminal model*. This possibility derives from the fact that only the very last enchained monomer has an impact on the chain propagation, *de facto* forcing the whole process to "loose memory" of such first act.

In our case, energies and frequencies needed for estimating kinetics constants were obtained employing DFT at the B3LYP/6-31++g(d,p) level of theory; [51] we also tested a few cases employing the B3LYP/6-311++G (2d,2p)//-B3LYP/6-31++g(d,p) level and found good agreement between $\Delta G^{\ddagger}$ values at the two levels. As polymerization experiments were carried out in solution, one may also wish to introduce solvent effects via self-consistent reaction field-type approaches [219]; these, however, are usually only able to adequately describe solvation effects due to polarization and charge displacements. Despite our monomers being polar, the impact of solvation on those interaction modalities in our case is unlikely to be more than weak, as the employed solvent is toluene ($\epsilon_r = 2.38$); it was thus decided to neglect the use of continuous model solvents. In literature there already are evidences supporting this idea in a work were cationic metallocenic complexes catalyzed olefin polymerization [167, 220], and preliminary calculations on a few cases indicated this to be correct also for radical polymerizations in absence of chemically specific interactions such as normal or charged hydrogen bonds [175, 199, 221, 222].

What may instead be more problematic in using continuous solvent models in the task we set to accomplish, it is their limited ability in correctly estimating the change in system entropy upon formation of the TS's from dissociated reactants. Such issue descends from the fact that reaction field models are not able to correctly describe the molecularity of the true solvent, which has to be

displaced from the first solvation shell of each species for the reactive collision to take place. This necessity usually requires some reversible work to be carried out, whose numerical value is determined by excluded volume, intermolecular attraction, thermal excitations and entropic effects (is the system more disordered when two monomers are associated due to the increase in entropy of the solvent or when are unassociated?). With the last effect being potentially dependent on the solvent and solutes (e.g. the association of hydrocarbons in water increases the system entropy, as does the endothermic dissolution of ionic salts), it seems to us that it may be preferable to avoid the usage of implicit solvent models, accepting the fact that computed $\Delta G^{\ddagger}$ shall always be affected by some form of systematic error, at least, in the estimation of $\Delta S^{\ddagger}$. This notwithstanding, we haste to notice that modelling copolymerization kinetics requires only ratios between kinetic constants (the r_{MMA} and r_{DMAEMA} previously discussed), so that one may reasonably hope to stumble upon some form of error cancellation when similar monomers are involved; we thus decided to avoid using model solvents altogether in our investigation.

When working with polar monomers as in our case, it is also important to remember that there may be some form of preferential monomer partitioning between the bulk solution and the growing radicalic end of the polymeric chain. This effect, a well known form of which goes under the name of "bootstrap" effect (BSE) [223], is in principle capable to induce local enrichment of one of the comonomers compared to its nominal composition and thus to increase its reaction rate. Such an effect is usually modelled defining *partition coefficients* [224]

$$K_{MMA} = \frac{[MMA]_M}{[MMA]_b} \frac{[DMAEMA]_b}{[DMAEMA]_M} \tag{5.27}$$

and

$$K_{DMAEMA} = \frac{[MMA]_D}{[MMA]_b} \frac{[DMAEMA]_b}{[DMAEMA]_D} \tag{5.28}$$

so that $K_{MMA}\frac{[MMA]_b}{[DMAEMA]_b}$ and $K_{DMAEMA}\frac{[MMA]_b}{[DMAEMA]_b}$ give the effective concentration ratios between MMA and DMAEMA in the vicinity of, respectively, the terminal MMA or DMAEMA radicals. In the previous formulae, $[MMA]_b$ represents the instantaneous nominal concentration of MMA in the bulk, so that

$q_b = \frac{[MMA]_b}{[DMAEMA]_b}$ is the instantaneous nominal monomer feed; also, $[MMA]_M$ and $[DMAEMA]_M$ are the concentrations of MMA and DMAEMA close to the terminal MMA radical of the chain. Notice that, with the assumption of preferential partitioning, all the details (the monomer reactivity ratios) of the propagation mechanism could, again, be considered as solvent-independent. [225]

Taking into account the microphase difference compositions within the framework of the bootstrap model, the usually determined reactivity ratios must be considered apparent reactivity ratios

$$r^s_{MMA} = r_{MMA} \cdot K_{MMA} \quad \text{and} \quad r^s_{DMAEMA} = r_{DMAEMA}/K_{DMAEMA} \quad (5.29)$$

where r_i (i=MMA,DMAEMA) are the true reactivity ratios and K_i are the coefficients defined above. The probabilities in the case of a radical copolymerization with BSE can be written in a way similar to Eq. 5.23

$$p_{MMA,DMAEMA} = (1 + r_{MMA} \cdot K_{MMA} \cdot q_b)^{-1} \quad (5.30)$$

and

$$p_{DMAEMA,MMA} = (1 + \frac{r_{DMAEMA}}{K_{DMAEMA} \cdot q_b})^{-1} \quad (5.31)$$

In principle, the K's could be computed via equilibrium Monte Carlo (MC) or Molecular Dynamics (MD) simulations employing explicit solvent models and appropriately tuned force fields. With the assumption that only a single monomer molecule at the time can preferentially "sit" close to the radical center due to the difference in partitioning, the local relative concentration of MMA and DMAEMA at the chain end is, in fact, governed by the formation and break-up of dimers with the latter, for instance as in the following equilibria

$$[\text{MMA}; \text{CH}_3-\text{MMA}\cdot]_{dim} + \text{DMAEMA} + \Delta G^o_{dim}(\text{MMA}, \text{MMA}) \rightleftharpoons \quad (5.32)$$

$$\text{MMA} + \text{DMAEMA} + \text{CH}_3-\text{MMA} \cdot$$

$$\rightleftharpoons [\text{DMAEMA}; \text{CH}_3-\text{MMA}\cdot]_{dim} + \text{MMA} + \Delta G^o_{dim}(\text{MMA}, \text{DMAEMA})$$
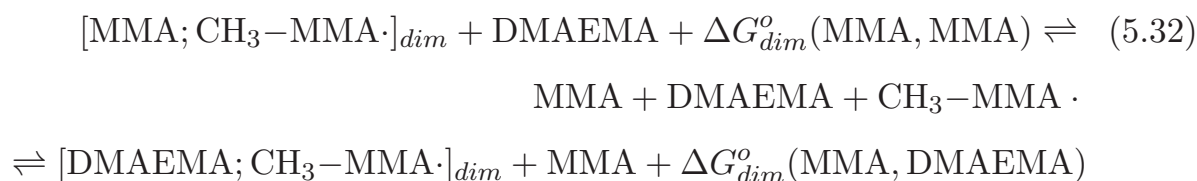
Here, $[X; Y\cdot]_{dim}$ is the dimer between monomer X and the radical-bearing last monomer of the chain, $Y\cdot$, and $\Delta G^o_{dim}(Y\cdot, X)$ is the change in Gibbs' energy

associated with the formation of the latter dimer. From Equation 5.32, it emerges that the change in Gibbs' energy the system has to sustain upon substituting with MMA the DMAEMA monomer in a dimer with the MMA radical amounts to

$$\Delta\Delta G^o_{dim}(MMA) = \Delta G^o_{dim}(MMA, MMA) - \Delta G^o_{dim}(MMA, DMAEMA)$$
(5.33)

the latter two quantities are the one that can be estimated via MC or MD.

As computing $\Delta G^o_{dim}(Y\cdot, X)$ is likely to require long and computationally expensive simulations involving extensive sampling of many conformational isomers for the dimer and its isolated composing fragments in a viscous environment, we shall make the attempt of modelling monomer partition substituting it with the standard Gibbs' energy change upon formation of a van der Waals dimer between the terminal Y· radical and the monomer X. Assuming for the moment that only a handful of isomers (or even a single one, how fairly often happens) for each of the involved species may be needed to appropriately describe their equilibrium statistical mechanics, the "harmonic superposition approximation" (HSA) [226] may be exploited to estimate the Gibbs' energy for model chain radicals, monomers and their dimers. Thus, instead of computing each $\Delta G^o_{dim}(MMA, X)$ via MC or MD to estimate $\Delta\Delta G^o_{dim}(MMA)$, one may simply optimize structural isomers with, e.g., the DFT approach discussed above, select the minima with the lowest Gibbs' energy G and that, hopefully, are well separated by the remaining isomers, estimate the G for such a subset of species via HSA, and, eventually, $\Delta G^o_{dim}(MMA, X)$ or $\Delta\Delta G^o_{dim}(MMA)$. Notice that, in doing so, one exploits once again the possibility of error cancellation, as the contribution to the change in entropy related to the loss of translational and rotational freedom upon dimerization is largely canceled out while computing $\Delta\Delta G^o_{dim}$. Similarly, one would hope that the differences between the solvent-accessible surface of, e.g., MMA/MMA and MMA/DMAEMA dimers may be largely neglected, so that change in solvent entropy and enthalpy largely cancel. Obviously, such an approach has already been used (e.g. see Refs. [227–233]) and shown to perform adequately even for carboxylic acid oligomers [231].

To conclude our methodological discussion, it is perhaps worth pointing out

that even in absence of solute-solute interactions relatively stronger than solute-solvent ones, as between acid molecules in weakly polar solvents [227,228,231,233], the proposed approach could still be applied if our radical-monomer dimers in solution maintained, at least, the nature of local free energy minima. In that case, HSA should still be valid, as we would expect a Gibbs' energy barrier along the intrinsic dissociation coordinate due to the necessity for the solvent to reorganize as a consequence of the change in the distance between monomers and radicals. To substantiate this idea, we begin mentioning that even pure toluene shows a local maximum (roughly 0.4 kcal/mol above the leftmost minimum) in the potential of mean force (minimum in the pair distribution function) along the distance between the center of mass of two molecules [234–237]. A similar, albeit more marked, feature is also seen in asphaltenes solutions in toluene [238, 239], with dissociation barriers varying in the range 2.6–12 kJ/mol [238–240]. More importantly for our interests, polar (PEG-or vinyl alcohol–like) side branches of star-like polymers also show marked aggregation effects in toluene [241], thus substantiating the claim that dimers of polar species would represent true minima over the Gibbs' energy surface of the monomers-growing chains solution.

5.2.2   Kinetic Monte Carlo Simulations and Code

As mentioned previously, we consider important to study chain growth by directly simulating subsequent monomer additions exploiting the intrinsic stochastic nature of the "ultimate model" kinetic scheme via kMC, assuming that depolymerization cannot take place. Apart from average properties that may be obtained also with analytical methods, doing so would allow us to obtain all the relevant distributions and correlation functions that may help in better understanding how the copolymer properties depends on the length of the short chains that we synthesised. For instance, the position dependence of composition and the probability of finding a DMAEMA-DMAEMA diad along the chain may be quite useful. To this end, the kinetic Monte Carlo code receives as input the $\Delta G^{\ddagger}$ of the four possible propagation steps between MMA and DMAEMA (or experimental reactivity ratios), two partition coefficients, the initial MMA/DMAEMA feed ratio, the number of chains we wish to generate, the system temperature and the total (i.e. with respect to the total amount of monomers) percent conversion.

After the calculation of reactivity ratios employing $\Delta G^{\ddagger}$ and TST, the core of simulation is articulated in few basic steps:

1. calculation of probabilities p_{12} and p_{21} (see Eq. 5.30 and 5.31) with a feed modified by subtracting the amount of each monomer already reacted;

2. determining the new adding monomer basing on the nature (MMA or DMAEMA) of the radical–bearing chain by comparing an uniformly distributed random number with either p_{12} or p_{21} (respectively);

3. increase chain length by saving the new monomer in an array, recomputing feed composition and increasing counters to estimate diads, triads and n-monomer distributions;

4. calculate total conversion M/M_0; if the instantaneous conversion is lower than the maximal conversion allowed, go back to step 1 and continue the copolymerization.

This set of pseudo-instructions generates a single chain; it is nested inside another cycle that produce the desired number of chains. Exploiting the ensemble of chains thus generated, we compute the relative MMA/DMAEMA polymer composition, the triad distributions and the related standard deviations.

5.2.3   Experimental Copolymerization Analysis

For the sake of linearity of presentation, we begin discussing the analysis of the experimental copolymerization results from which our theoretical study started. The schemes of reaction and the structure of the monomers and the copolymers are reported in Figure 5.2).

As for the literature, we found that random DMAEMA/MMA copolymers have been synthesized using different approaches such as Reversible Addition-Fragmentation Chain Transfer (RAFT), Radical Polymerization in presence of AIBN as initiator, or Atom Transfer Radical Polymerization (ATRP) using palladium acetylide as catalytic species. Interestingly, the reactivity ratios obtained showed an almost similar relative reactivity of the two monomers or, in few cases,
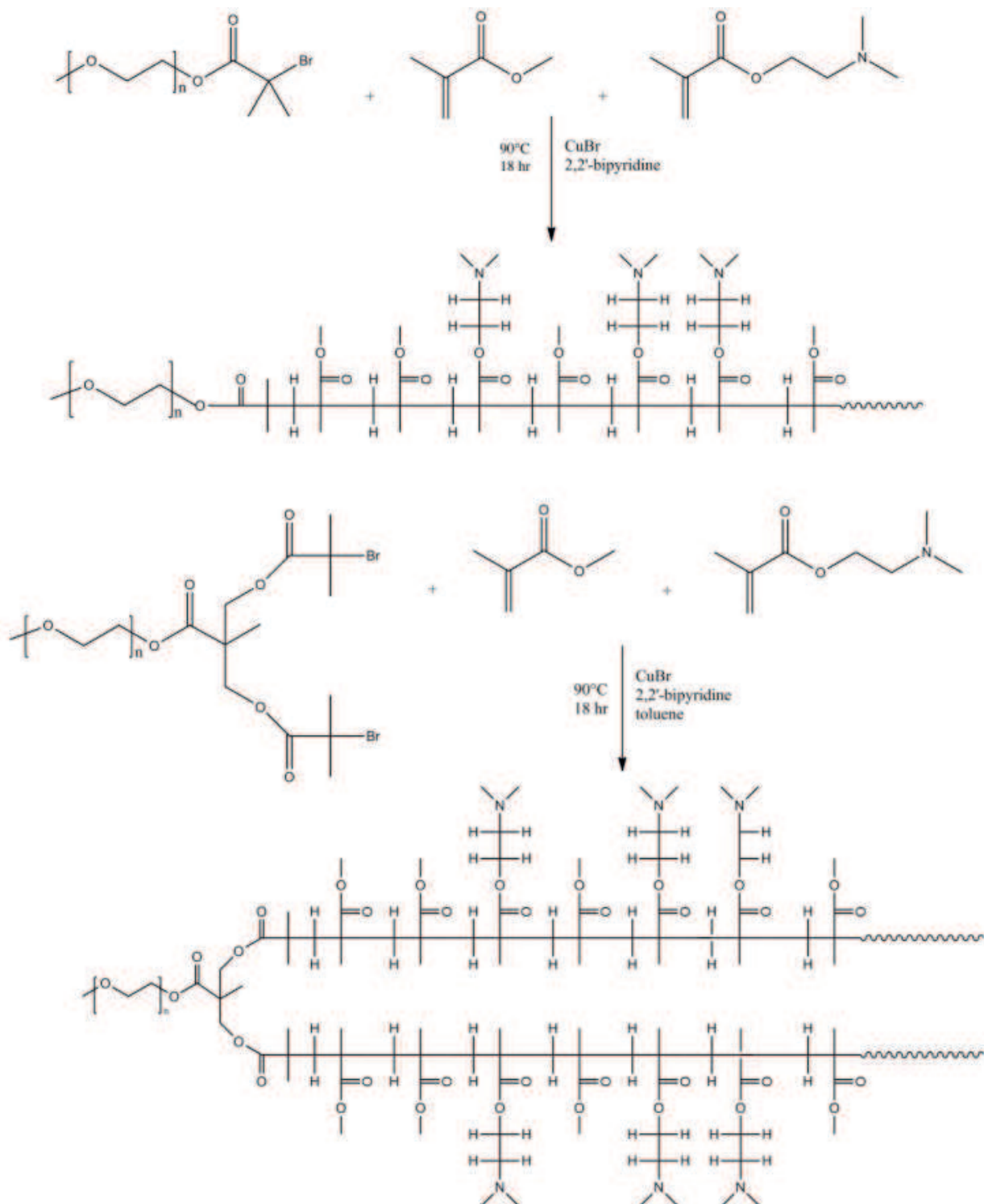
Figure 5.2: Chemical schemes for the synthesis of mPEG-*b*-(PMMA-*ran*-PDMAEMA) linear (top) and mPEG-*b*-(PMMA-*ran*-PDMAEMA)$_2$ (bottom) via ATRP.

Polym. method	Solvent	r_{MMA}	r_{DMAEMA}	Method
Radical copol. [215]	bulk	0.71	1.25	Kelen-Tudos
Radical copol. [216]	CHCl$_3$	1.13	1.07	Kelen-Tudos
RAFT [214]	DMF	0.925	0.854	Kelen-Tudos
RAFT [213]	ethanol	0.9	0.8	
ATRP[a]	toluene	0.36($\pm$10%)	2.76($\pm$15%)	Eq.5.26
ATRP[a]	toluene	0.48($\pm$8%)	1.60($\pm$26%)	Eq.5.19

Table 5.1: Reactivity ratios for radical and CRP polymerizations of MMA and DMAEMA. Also indicated, there are the solvent and numerical approach to estimate the r's. [a]Results obtained from our work.

a slightly higher reactivity of DMAEMA with respect to MMA despite the different experimental conditions (see Table 5.1). In principle, this similarity can be taken to indicate the fundamentally common radical nature of all processes, which was clearly supported for ATRP by the analysis of kinetic isotope effects via experimental and theoretical means. [242] The copolymers obtained were generally considered random copolymers in terms of the statistical distribution of the comonomers along the backbone.

To generate the copolymer from which the r's have been extracted, block-random microstructure for mPEG-b-(MMA-ran-DMAEMA) copolymers were synthesized via a classical ATRP of MMA and DMAEMA in toluene using an mPEG-based macroinitiator and CuBr/bpy as catalyst. Three different structures were obtained, a linear one and two branched architectures (mPEG-(MMA-DMAEMA)$_n$; n =1, 2, 4) using different feed compositions. Considering the relative reactivity ratios reported in the literature and since our intent was to obtain amphiphilic copolymers consisting of a MMA-based hydrophobic block having sporadic amino pedant groups into the back-bone, feed ratios q =[MMA]/[DMAEMA] were initially kept only slightly higher than 1, as reported in Table 5.2.

Surprisingly, ^{13}C-NMR characterization showed a greater tendency for DMAEMA to insert into the backbone with respect to MMA, independently of the copolymer structures. This result is clearly at variance with respect to what published before (see Table 5.1), even when an ATRP approach similar to the one discussed in this work was used, and we feel it is worth of further study. To this end, we attempted to extract experimental reactivity ratios from the data

Polymer	structure	q	$F_{\mathrm{MMA}}/F_{\mathrm{DMAEMA}}$	Conversion	$\mathrm{M}_n/10^3$	$\mathrm{M}_w/\mathrm{M}_n$
1 (M10)	mPEG–b–(PMMAx–ran–DMAEMAy)	7.9	4.2	0.53	38	1.4
2 (D4)	mPEG–b–(PMMAx–ran–DMAEMAy)	3.8	2.0	0.50	70	1.3
3 (M21)	mPEG–b–(PMMAx–ran–DMAEMAy)	3.1	1.4	0.44	48	1.3
4 (M11)	mPEG–b–(PMMAx–ran–DMAEMAy)	2.3	1.2	0.54	76	1.5
5 (D5)	mPEG–b–(PMMAx–ran–DMAEMAy)$_2$	17	11	0.66	61	1.5
6 (D6)	mPEG–b–(PMMAx–ran–DMAEMAy)$_2$	7.7	3.6	0.45	58	1.5
7 (D9)	mPEG–b–(PMMAx–ran–DMAEMAy)$_2$	3.1	1.7	0.54	62	1.4
8 (D10)	mPEG–b–(PMMAx–ran–DMAEMAy)$_2$	2.6	1.2	0.47	87	1.6
9 (D12)	mPEG–b–(PMMAx–ran–DMAEMAy)$_4$	7.7	3.8	0.49	75	1.5
10 (D13)	mPEG–b–(PMMAx–ran–DMAEMAy)$_4$	5.3	3.1	0.58	80	1.5
11 (D11)	mPEG–b–(PMMAx–ran–DMAEMAy)$_4$	3.8	2.2	0.56	90	1.5
12 (D14)	mPEG–b–(PMMAx–ran–DMAEMAy)$_4$	3.1	1.7	0.56	93	1.6

Table 5.2: Collection of experimental data from the group of Izzo.

shown in Table 5.2, and we did so by optimizing the parameters $r_1 = r_{MMA}$ and $r_2 = r_{DMAEMA}$ in Equations 5.19 and 5.26 in order to fit the behavior of the latter to the results. Worth a notice, it is the fact that the monomer conversion does not play any role when using Equation 5.19 to model the results, as the latter implies a constant value for the feed composition q; this assumption, however, does not represent accurately the experimental situations, as the DMAEMA monomer is present in smaller amount and should be consumed more rapidly than MMA.

The least square fitting of the parameters in both analytical forms was carried out employing the nonlinear least-squares (NLLS) Marquardt-Levenberg algorithm [243, 244] implemented in Gnuplot, [245] obtaining $r^s_{MMA} = 0.36$ ($\pm 10\%$) and $r^s_{DMAEMA} = 2.76$ ($\pm 15\%$) when using Equation 5.26, or $r^s_{MMA} = 0.483$ ($\pm 8\%$) and $r^s_{DMAEMA} = 1.60$ ($\pm 26\%$) when employing Equation 5.19.

The variance of the residuals for the two cases was, respectively, 0.0038 and 0.0474, which indicates the markedly better performance of the model that takes into account the change in feed composition as expected basing on the experimental conditions. Moreover, the absolute r values obtained employing both models suggest the preferred insertion of DMAEMA whatever the ultimate unit is. In turn, this behavior should be expected to generate a DMAEMA-rich blocky structure at the beginning of the copolymerization (i.e. close to the linking group with mPEG), that turn to a MMA-rich blocky one ofter a sufficiently high conversion of the most reactive monomer. *In absentia* of a NMR characterization of the chain triads, this aspect of the copolymerization would be discussed in Section 5.2.4 (*vide infra*) relying on kMC simulations exploiting the reactivity ratios just obtained.

As a last observation to conclude this analysis, we recall that, within the assumption of constant feed composition (or, at least, short polymerization time), Equation 5.19 provides indication on how the copolymer composition (i.e. F_{MMA}/F_{DMAEMA}) varies with f_{MMA}/f_{DMAEMA}. From this, one can derive that $F_{MMA}/F_{DMAEMA} < f_{MMA}/f_{DMAEMA}$ whenever $q > (1 - r^s_{DMAEMA})/(1 - r^s_{MMA})$; as both experiments and theoretical results indicate that $r^s_{DMAEMA} > r^s_{MMA}$, the latter condition is always fulfilled during our copolymerization at least
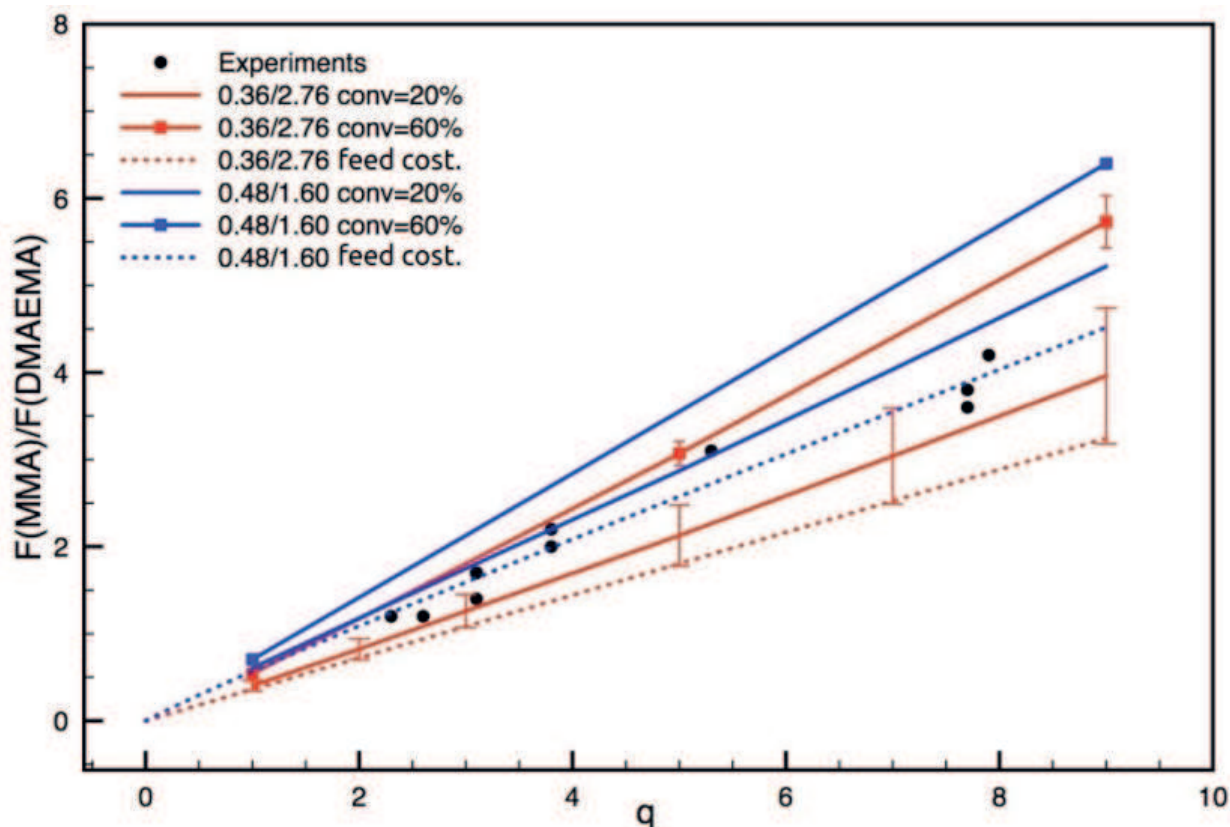
Figure 5.3: F_{MMA}/F_{DMAEMA} versus feed composition q obtained experimentally, via Equation 5.19 (dashed lines), or by means of kMC simulations with theoretical and experimentally obtained r^s. The vertical error bars represent the standard deviation of the sampled copolymer composition values at each q value generated employing the reactivity ratios obtained via Equation 5.26.

because $q_0 > 1$. This is clearly apparent from the plots of Equation 5.19 versus q_0 in Figure 5.3.

5.2.4   Results from kMC Simulations

Before discussing the kMC results obtained simulating copolymerizations with the three sets of reactive ratios discussed in the previous two Sections, it is worth recalling that chain propagation was interrupted after a chosen reaction time elapsed. As a consequence, monomer conversion varies from case to case, depending on the relative amount of the two monomers and their relative reaction rates, and spans the range 20–60%. To facilitate comparison between experiments and theoretical data, we therefore opted to stop simulations at a conversion that matches the just mentioned interval extrema, thus generating composition "bands" that should contains all the synthesised species.

Apart from representing Equation 5.19 with the three sets of r^s together with experimental polymer compositions, Figure 5.3 also shows copolymer relative composition (F_{MMA}/F_{DMAEMA}) versus initial feed composition ($q = f_{MMA}/f_{DMAEMA}$) as obtained from the kMC simulations. At a first glance, it immediately emerges that simulations employing the reactivity ratios obtained via Equation 5.26 provide upper and lower bounds to the experimental results, thus substantiating the usage of such relationship for the description of our copolymerizations. It is also apparent that the experimental data can be appropriately fit via Equation 5.19 (dashed blue line); however, the agreement worsen substantially when the variation in q value is properly taken in consideration, all simulations predicting higher values for F_{MMA}/F_{DMAEMA} than obtained from Equation 5.19 and the deviation increasing upon increasing the monomer conversion. Obviously, this descends from the preferential consumption of DMAEMA as the most reactive of the two monomers, and the consequent increase in q while the reaction takes place. It is also apparent that the behavior of F_{MMA}/F_{DMAEMA} versus q obtained via kMC at a chosen monomer conversion is substantially linear for $q > 1$ (i.e. the conditions in which the copolymerization took place). As for the latter, the slope of the straight line is clearly a function of the conversion degree, increasing toward a unit value upon increasing the conversion. Again, this effect is related to the initially faster consumption of DMAEMA.

Given the somewhat limited copolymer lengths, one would expect for the F_{MMA}/F_{DMAEMA} values to be distributed over a fractionally relevant range of compositions; to investigate such aspect, we also computed the standard deviation of the copolymer composition, which is shown in Figure 5.3 as error bars for the kMC results carried out using the r^s obtained via Equation 5.26. At first glance, it clearly appears that the distribution of composition values can be fairly wide (e.g up to 30–35% of the average value), decreasing markedly upon increasing the monomer conversion. Interestingly, the amplitude of the composition fluctuation shown by the kMC data seems of the same magnitude of the one shown by the experiment results, thus justifying the slight erratic behavior of the latter. In fact, we empirically found that all experimental results fall into the composition band defined by the fluctuation amplitudes obtained simulating with kMC copolymerization with $r^s_{MMA} = 0.36(\pm 10\%)$, $r^s_{DMAEMA} = 2.76(\pm 15\%)$ and

a conversion of 40% (not shown in the Figure).

Having somewhat verified the capability of the kMC simulations to reproduce composition data when employing fitted experimental results, the attention may be directed toward understanding the impact on the microstructural details that the difference in monomer reactivity ratios may have. To this end, we begin discussing how the probability of enchaining a given monomer (e.g., MMA) in a specific position along the chain may depend on the latter as a consequence of the variation in q during the copolymerization. Thus, Figure 5.4 presents the average (over at least 10^6 generated chains) probability of finding a MMA monomer in the n–th position along the chain at total monomer conversion of 60% and as a function of the feed ratio q. Only data obtained with $r^s_{MMA} = 0.36(\pm 10\%)$, $r^s_{DMAEMA} = 2.76(\pm 15\%)$ are show for sake of clarity. Results for lower conversions can be deduced from what shown in Figure 5.4 by, simply, selecting the chain length (i.e. the maximum value for n).

As expected, the probability of finding MMA along the chain increases along the chain, an effect, again, due to the decrease in DMAEMA content due to its relatively faster consumption. The relative change in MMA probability between the first and last enchained monomer goes from 20 to 80 % upon reducing q, a finding partially due to the longer chain obtained at low q values. Notice that the latter effect is not an artefact of our simulation approach, as also the experimental results indicate that, normalized to equal conversion, also the molar mass of the copolymers increases upon decreasing the feed composition (see Table 5.2). *De facto*, our choice to keep as constant the number of initial MMA monomers in the simulations and to vary DMAEMA monomers in accord with the chosen initial q closely follows the experimental approach (see Section 5.2.3). Thus, it seems correct to consider the copolymers discussed in Section 5.2.3 as proper members of the family of gradient copolymers. In this respect, one should also hasten to notice that the local properties (e.g. the behavior as weak polyelectrolyte) of the synthesised chains ought to depend on the position along the chain due to the composition change (for instance, see Reference [246], where the behavior of the lower critical aggregation temperature was discussed).
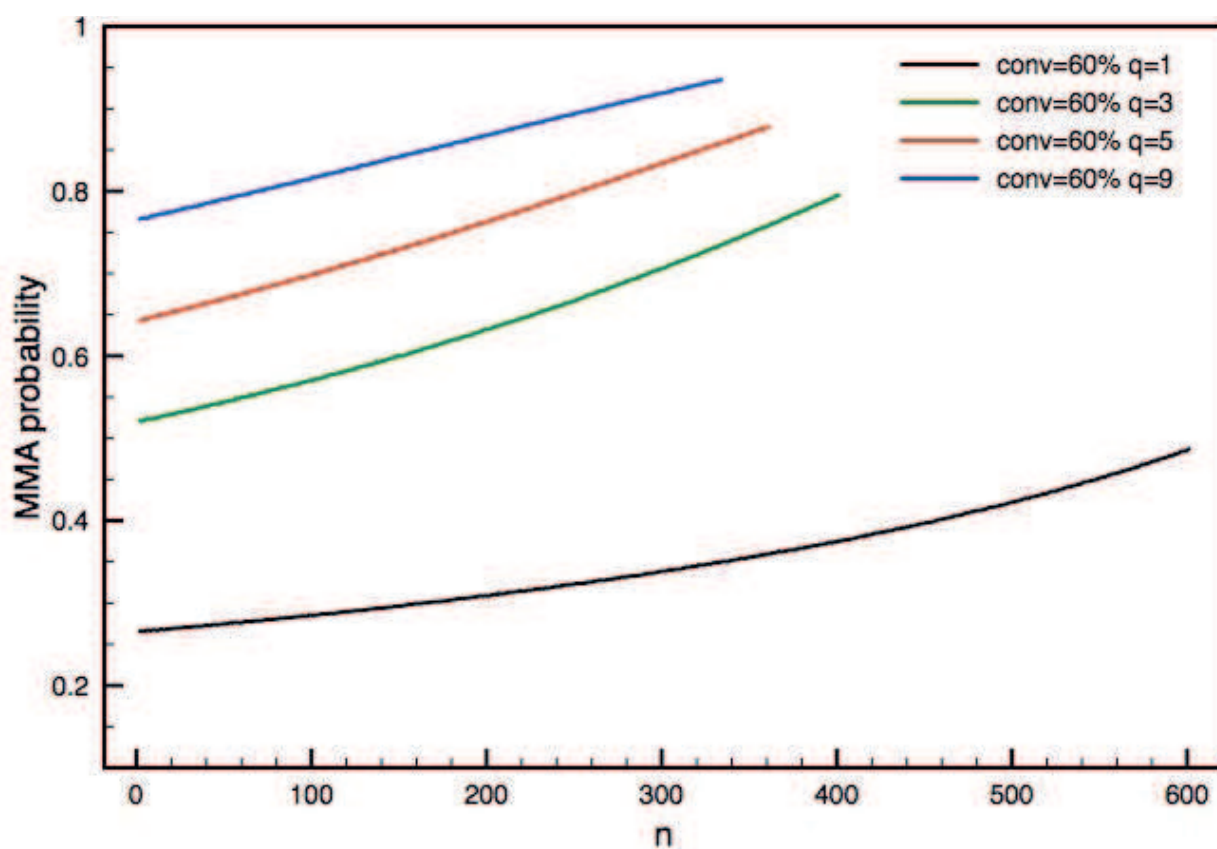
Figure 5.4: Probability of finding a MMA monomer enchained in position n along the chain versus feed composition q, obtained using $r^s_{MMA} = 0.36$ ($\pm 10\%$), $r^s_{DMAEMA} = 2.76$ ($\pm 15\%$) and a 60% monomer conversion.

Of a more direct relevance for drug delivery applications [207, 208] and the
theoretical foundations of the polymer design and of the analysis of the release ki-
netics [221, 222], we notice that the data shown in Figure 5.4 suggest the presence
of a higher DMAEMA concentration compared to the average composition in the
copolymer at the beginning of the chain. As in the polymeric structures discussed
in References [207, 208] the first monomer in the copolymer is directly connected
to a hydrophilic PEG branch, the DMAEMA-rich part of the copolymer is ex-
pected to sit close to the water–organic interphases of the vesicles obtained from
those species. We thus expect a higher density of ionizable sites (hence, a higher
surface charge) on the vesicle external interphase compared to what predictable
assuming an uniform composition along the chains. Similarly, the lower probabil-
ity of finding DMAEMA at the chain ends, which should be preferentially located
inside the vesicle double layer, should limit the penetration depth of protons in-
side the double layer, thus leading to a lower local concentration of pH-induced
charge. This, in turn, may be expected to reduce locally the double layer swelling,
impacting on the amount of channels percolating toward the surface and, thus, on
the release of active cargos loaded inside the double layer itself. Notice, however,
that having a lower density of ionizable hydrophilic sites (hence, an higher con-
centration of hydrophobic monomers) inside the vesicle double layer, as indicated
by our simulations, may positively impact on the overall structural robustness of
the aggregate themselves, the Gibbs' energy of the system likely of being at its
minimum when the hydrophobic chain ends remain clustered together.

Additional insights on the micro-structure of the MMA-DMAEMA copoly-
mers, which may have a substantial relevance for the drug delivery applications
just discussed and for the fine-tuning of their antimicrobial properties, emerge
noticing that a local decrease in probability of finding the ionizable monomer
along a chain, *de facto*, lowers the probability of finding two such monomers suf-
ficiently close to form a charged hydrogen bond interaction. [201, 247] To show
that this is just the case, we have collected the probability of forming any of
the possible triads as a function of the position of the first monomer in each
triad. Notice that we opted to investigate triads instead of the simpler diads as
the inherent flexibility of the ionizable pendants geometrically allows the forma-
tion of charged hydrogen bonds also between next neighbors, a situation present
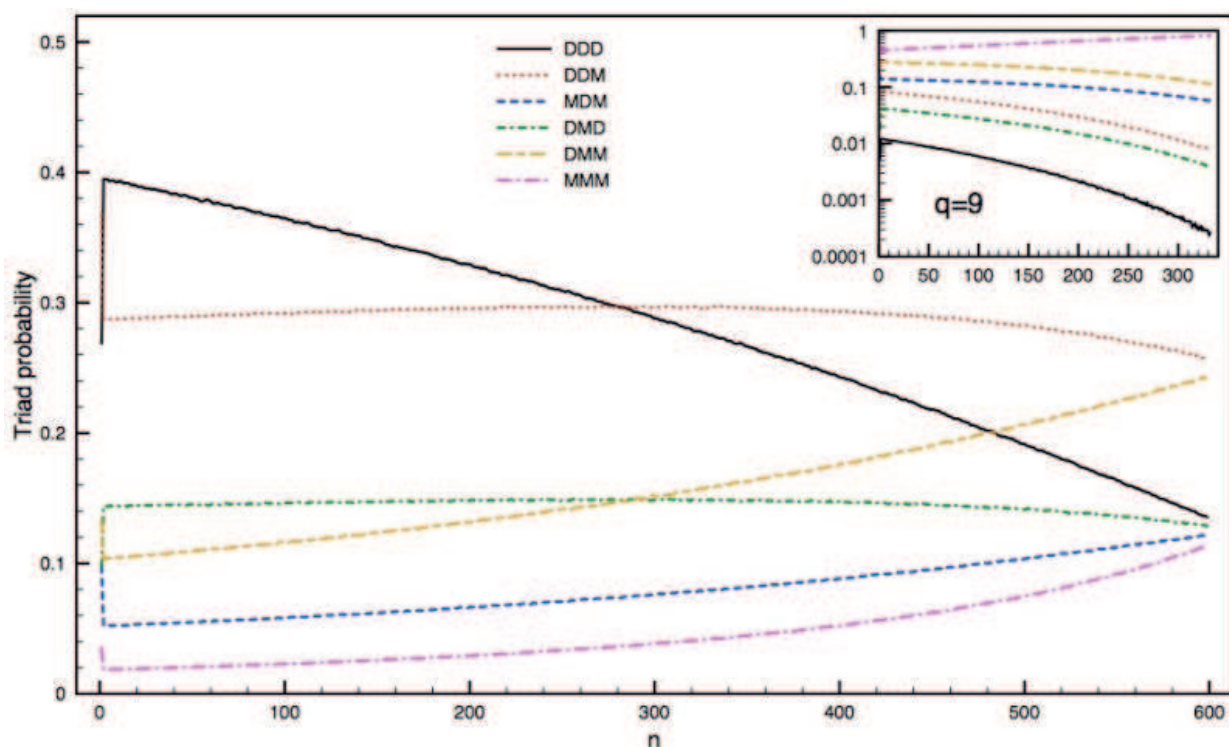
Figure 5.5: Probability of a specific triad with its first monomer sitting at position n along the chain when $q = 1$ and 9 (in the inset). D indicates DMAEMA, while M indicates MMA; the probabilities of DDM and MDD, as well as of MMD and DMM, are subsumed to preserve symmetry. Simulations were conducted with $r^s_{MMA} = 0.36(\pm 10\%)$, $r^s_{DMAEMA} = 2.76(\pm 15\%)$ and 60% monomer conversion.

in the case of DMD. The data for two cases ($q = 1$ and 9) simulated with $r^s_{DMAEMA} = 2.76(\pm 15\%)$ and a 60% monomer conversion are show in Figure 5.5. We have chosen these two specific cases to exemplify extremal behaviors that can be found during a copolymerization with a substantially different reactivity of the co-monomers.

From the data shown for the $q = 1$ case, it emerges that DMAEMA-richest triad DDD monotonically decreases along the chain due to the progressive consumption of this monomer while the polymerization progresses. Indeed, the decrease in DDD is quite marked, its probability dropping by roughly 50% while moving away from beginning of the chain. Notice, instead, that the other two DMAEMA-rich triads (DDM and DMD) do not follow a monotonic behavior, and are found to slightly increase at the beginning of the polymerization (by 3-4% maximum), and only subsequently to decrease due to the consumption of DMAEMA. Overall, the probability of finding two DMAEMA monomers at least as next neighbors drops from roughly 0.82 to 0.52 upon going toward the

chain end, a probability that nevertheless remains quite high and suggest the likelihood of charged hydrogen bonds formation. Obviously, one also notice the increase of MMA-rich triads (MMM, DMM, and MDM) parallel to the decrease in DMAEMA-rich triads. Perhaps also worth a mention, it is the very low probability of finding the MMM triad at the beginning of the chain, which suggests that only a very limited hydrophobic character should be displayed by the first part of the chain.

Turning to the $q = 9$ case, we notice the substantial decrease in DMEAMA-rich triads, whose overall probability is only 0.14 at the beginning of the chain and rapidly drops to 0.01 upon going toward the chain terminus. Clearly, this finding correlates well with the substantial reduction of DMAEMA in the feed. Apart from the faster decrease just discussed, the $q = 9$ case differs from the $q = 1$ one also due to the fact that only the MMM triad is seen increasing while the reaction progresses, DMM and MDM both decreasing due to the decreasing DMAEMA content in the feed. Importantly, the difference in behavior between the $q = 1$ and 9 cases is not an artefact of our simulation approach but an effect of the non–linear relationship between the instantaneous probability of inserting, e. g., a MDM triad and the feed composition, as discussed at length in Reference [169].

5.2.5   Rationalization of the Experimental Results

Having explored the impact on the microstructural details of the mPEG-*b*-(MMA-*ran*-DMAEMA)$_n$ copolymers deriving by the difference in reactivity ratios and by the choice of q_0, in this Section we present the results of our attempt of investigating the origin of the difference in r's found experimentally. For the sake of conciseness, we limit our discussion on the copolymerization energy profiles to the minimum amount of information needed to appreciate the conclusions.

Figure 5.6 shows the lowest Gibbs' energy conformers optimized for the monomers and radicals involved in the copolymerization. Figure 5.7 shows, instead, the stationary geometry of the lowest Gibbs' energy TS's involved in the four propagation reactions generating the copolymer; the energy barriers reported in the figure are computed with the asymptotic reactants as zero of the scale. Of
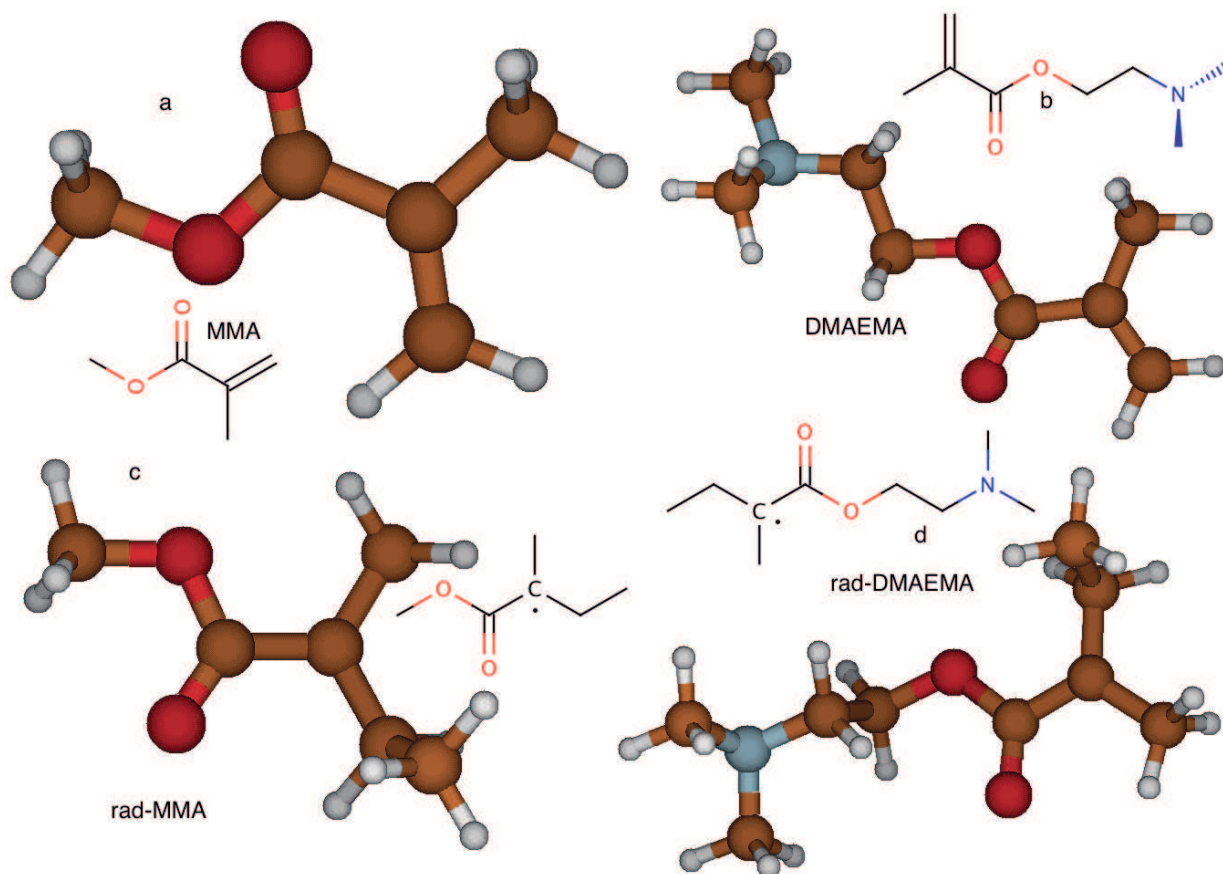
Figure 5.6: Lowest Gibbs' energy minima for a) MMA, b) DMAEMA, c) CH_3–MMA· radical, and d) CH_3–DMAEMA radical. For the sake of clarity, CH_3-MMA· and CH_3–DMAEMA· are labeled in the Figure as, respectively, rad-MMA and rad-DMAEMA.

direct relevance for our purpose, we notice that all computed barriers appear of very similar height.

Assuming that only the most stable reactant and TS species are relevant for the propagation reactions, one can easily compute the two reactive ratios necessary to quantitatively describe the copolymerization as described in Section 5.2.1, and these are shown also in Figure 5.7. As we obtain $r_{MMA}^{DFT} = 1.040$ and $r_{DMAEMA}^{DFT} = 0.767$, one should obtain a copolymer more rich in MMA than in DMAEMA compared to the composition of the feed (i.e. $F_{MMA}/F_{DMAEMA} > f_{MMA}/f_{DMAEMA}$), which is clearly at variance with what shown in Table 5.2. Instead, these results agree qualitatively with the reactivity listed in Refs. [213,214, 216], where $r_{MMA} > r_{DMAEMA}$ are found even though only by limited amounts.

To proceed further with the approach introduced in Section 5.2.1, the low-
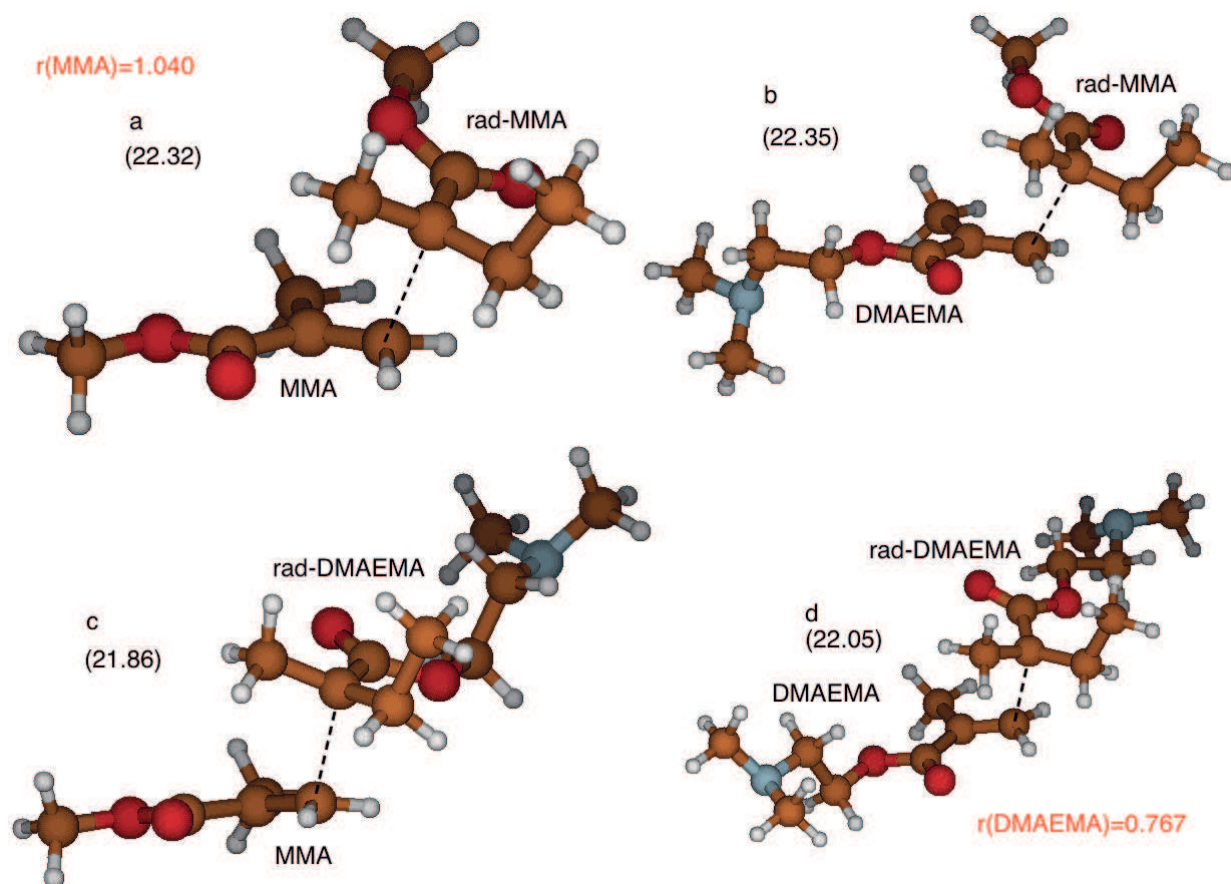
Figure 5.7: Lowest Gibbs' energy TS's for the reaction between a) CH_3–MMA·/MMA, b) CH_3-MMA·/DMAEMA, c) CH_3-DMAEMA·/MMA radical, and d) CH_3-DMAEMA·/DMAEMA radical. Also shown, there are the barrier heights from the asymptotic reactants (in black between brackets) and the corresponding reactivity ratio (in red). For the sake of clarity, CH_3-MMA· and CH_3-DMAEMA· are labeled in the Figure as, respectively, rad-MMA and rad-DMAEMA.
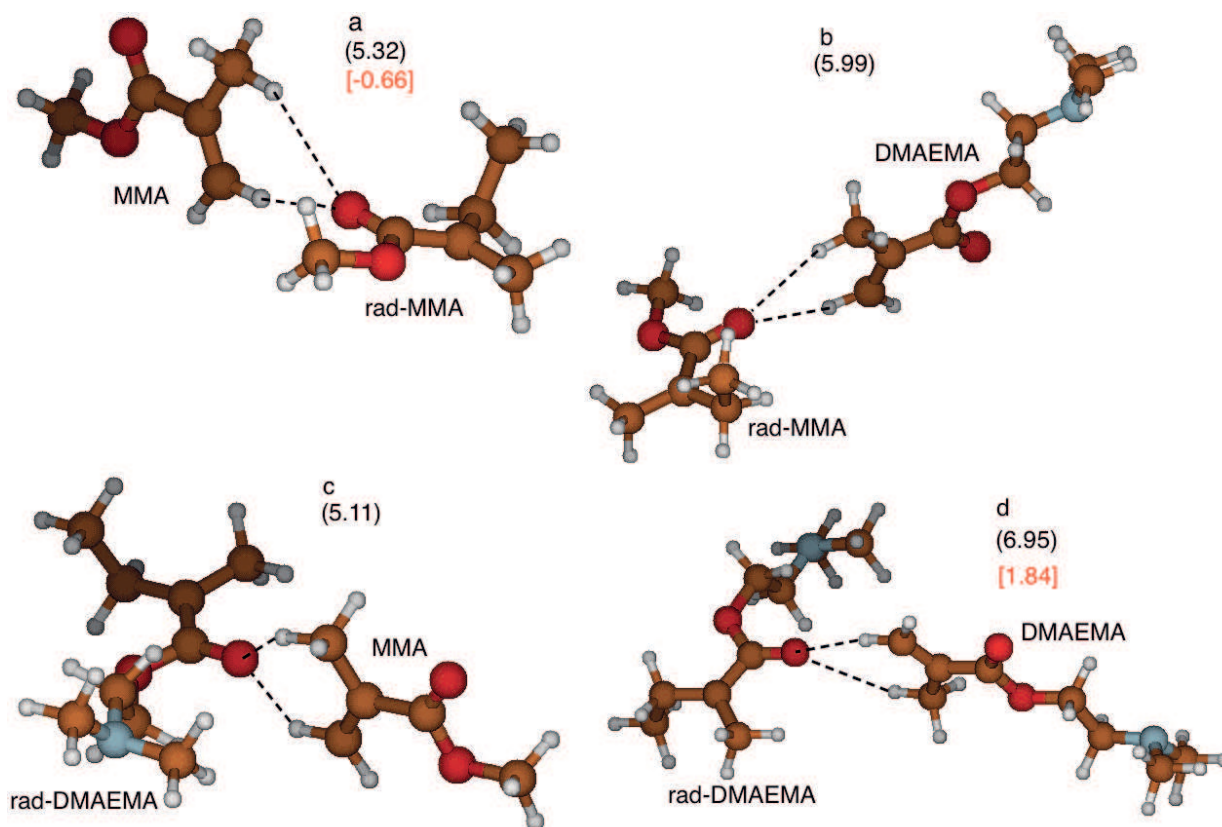
Figure 5.8: Lowest Gibbs' energy dimer for the reaction between a) CH$_3$-MMA·/MMA, b) CH$_3$-MMA·/DMAEMA, c) CH$_3$-DMAEMA ·/MMA, and d) CH$_3$-DMAEMA·/DMAEMA. Dimerization Gibbs' energies (kcal/mol), ΔG^o_{dim}, from the asymptotic reactants are shown (in black) between brackets; $\Delta \Delta G^o_{dim}$ computed assuming CH$_3$-MMA·/MMA and CH$_3$-DMAEMA·/DMAEMA as final state are shown (in red) between square brackets. For the sake of clarity, CH$_3$-MMA· and CH$_3$–DMAEMA· are labeled in the Figure as, respectively, rad-MMA and rad-DMAEMA.

est Gibbs' energy structure for all possible radical-monomer dimers are shown in Figure 5.8. This also presents values for the ΔG^o_{dim}, and $\Delta \Delta G^o_{dim}$ needed to compute the monomer partition coefficients and estimated as indicated in Equation 5.33 from the lowest energy conformers of monomers and radicals.

All $\Delta \Delta G^o_{dim}$ are positive, and from these one obtains $K_{MMA} = 2.51$ and $K_{DMAEMA} = 0.08$; these suggest that MMA preferentially partition closer to both radicals and thus the involved radical–monomer interactions do not provide a rationalization for the experimental results in Section 5.2.3.

With the results on $\Delta \Delta G^o_{dim}$ suggesting a behavior opposite to what experimentally found in terms of reactivity ratios, one may invoke the possibility that DMAEMA interacts with the CuBr/bpy complex needed to activate the

alkyl-halogen bond during the polymerization to justify $r_{MMA} < r_{DMAEMA}$; the net effect of such interaction could be the preferential partitioning of DMAEMA closer to a just formed radical disregarding its nature compared to MMA. That this could be the case, up to the point of modifying the coordination environment of Cu(I), has been shown by Haddleton *et al.* [248] by directly treating the catalyst N-propyl 2-pyridylmethanimine/copper(I) with DMAEMA in an NMR tube. A less direct, even though still compelling, evidence is also provided by the requirement of using tri- or tetra-dentate amino ligands in the ATRP synthesis of polyDMAEMA to avoid the displacement of the ligand on the copper complex. [249] If this was the case, one would *de facto* have the transport of DMAEMA close to a forming radical by the very catalyst that helps in generating the latter.

^{1}H-NMR experiments on various mixtures of the CuBr, bpy and DMAEMA species were carried out to experimentally test the possible coordination of DMAEMA to Cu(I). The results for two complementary regions of the proton chemical shifts are shown in Figure 5.9; from these, one can easily notice the change in proton chemical shifts of bpy due to the interaction with, first, CuBr, and successively DMAEMA. Similar shifts are also apparent for the hydrogen atoms on the sp^2 carbon of DMAEMA, thus suggesting that the complexation is indeed possible.

To quantitatively gauge the stability of the complex between DMAEMA and the catalyst used in this work, we optimized the CuBr/bpy and CuBr/bpy/-DMAEMA complexes to compute the relative energetics. In Figure 5.10, we show the geometry of the two stationary points together with the change in enthalpy and Gibbs' energy upon coordination; as it can be seen, the former complex has a triangular disposition of the coordinated atoms around Cu(I), while the additional coordination of DMAEMA distorts the geometry into a pyramid with a triangular base. As expected, the computed value of the coordination enthalpy ($\Delta H^o = -6.9$ kcal/mol) suggest the formation of the complex, the ΔG^o value instead suffering for the inappropriate entropy reduction previously discussed.

Also interesting, there are the results on the CuBr$_2$/bpy/DMAEMA complex,
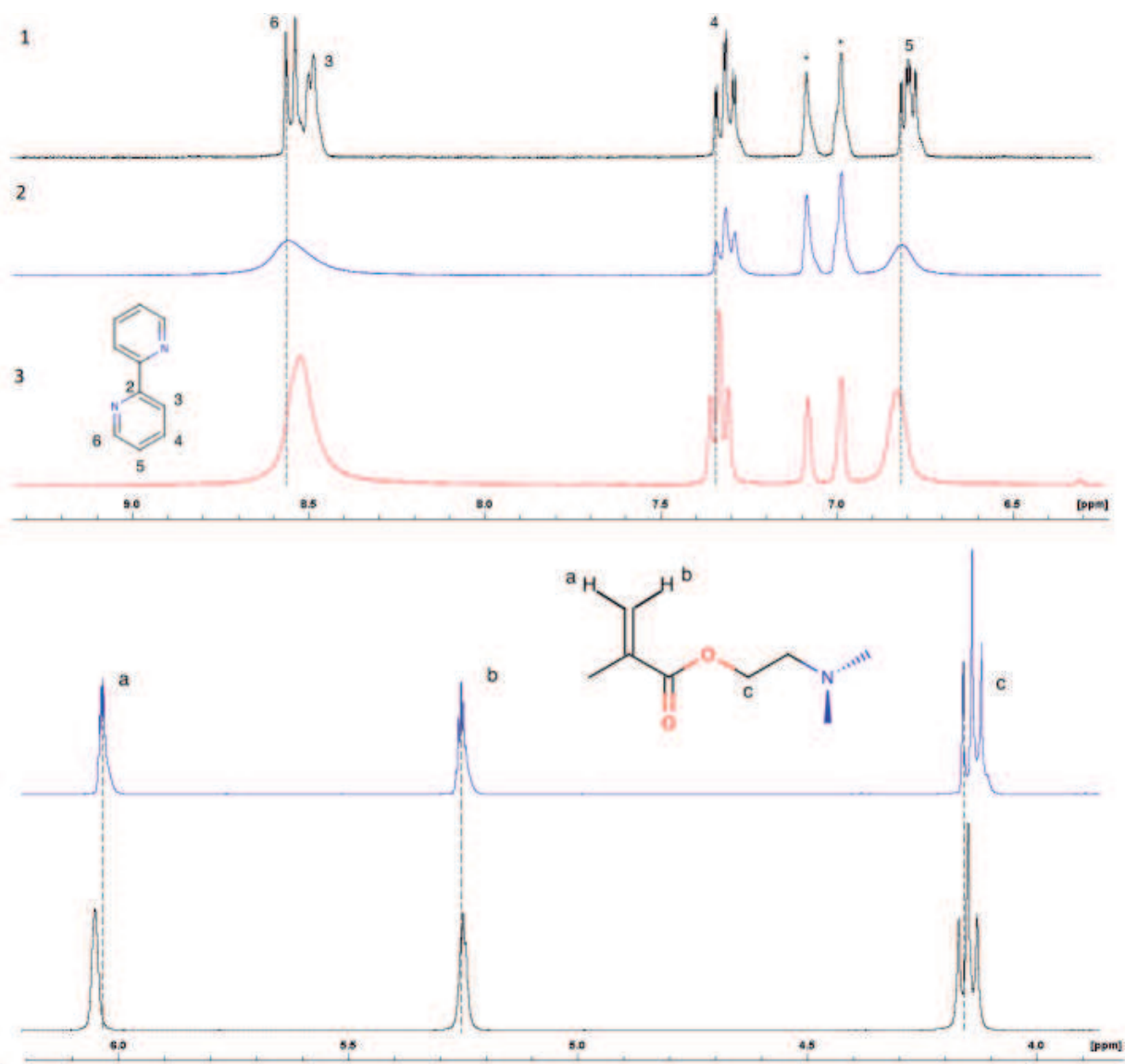
Figure 5.9: Top panel: ^{1}H-NMR in toluene at 90 °C of bpy (1), CuBr/bpy 1:2 (2), and CuBr/bpy/DMAEMA 1:2:10 (3). ∗ = toluene. Bottom panel: ^{1}H–NMR in toluene at 90 °C of DMAEMA (top) and CuBr/bpy/DMAEMA 1:2:10 (bottom).
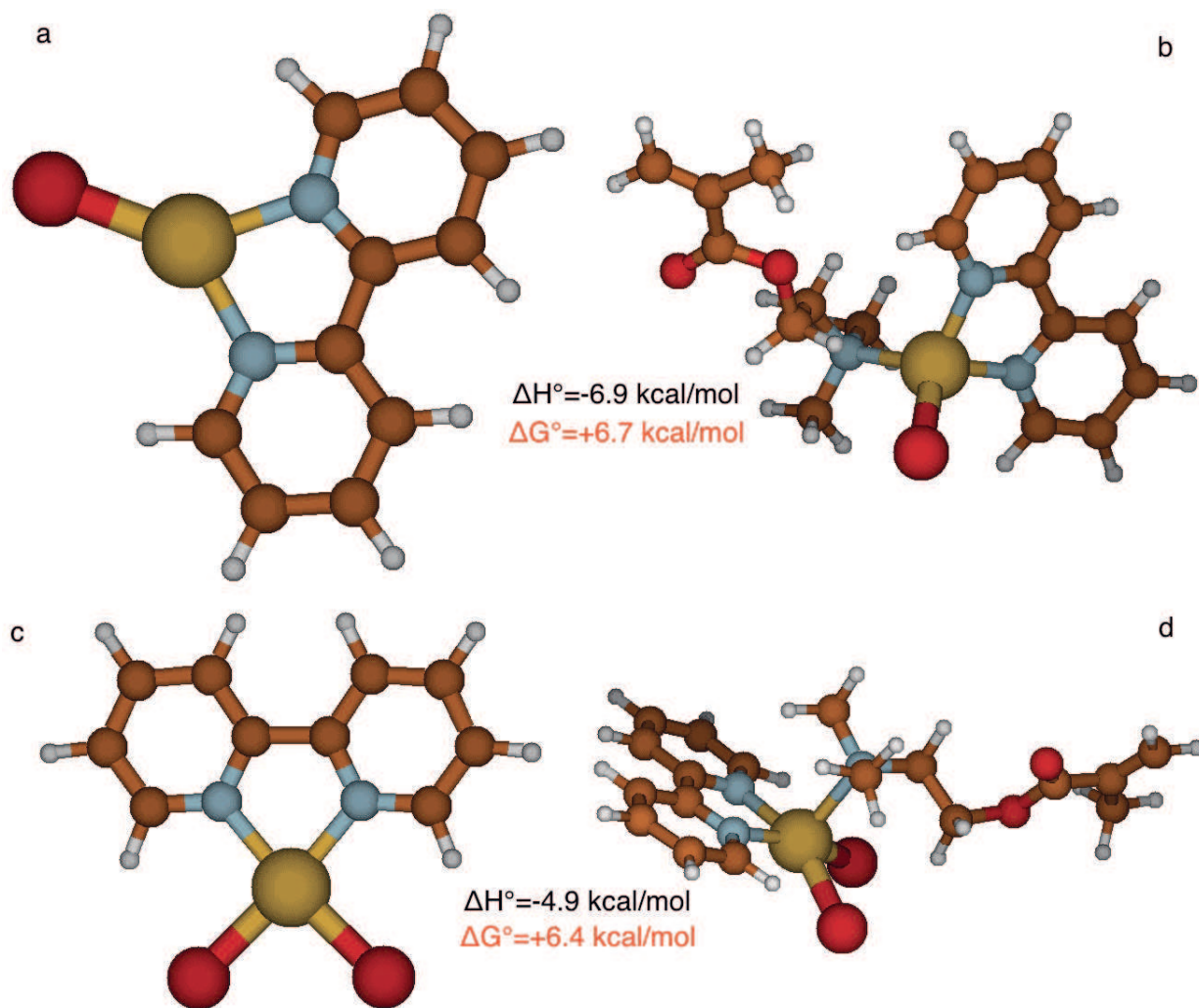
Figure 5.10:   Minimum energy geometry of a) CuBr/bpy, b) CuBr/bpy/DMAEMA, c) CuBr$_2$/bpy, d) CuBr$_2$/bpy/DMAEMA, and standard enthalpy (black) and Gibbs' energy (red) changes occurring upon ligation of DMAEMA to the copper complexes.

that may be formed upon extraction of the Br atoms from the dormant species. For this, we obtained a pyramidal minimum energy geometry with DMAEMA located at its vertex as fifth more weakly bound ligand, the two bromine atoms and bpy nitrogens nearly conserving the planar disposition (N-Br-N-Br dihedral angle $\simeq 175°$) of $CuBr_2$/bpy. Upon formation from DMAEMA and $CuBr_2$/bpy, also this species produces a negative enthalpy change, which suggests its likely presence in solution. The formed complex is however more labile than CuBr/bpy/DMAEMA, which is expected to favour the detachment of the copper complex from DMAEMA following the eventual addition to the growing chain.

As a last observation to conclude this theoretical analysis, we notice that the formation of a complex between DMAEMA and the copper(I) catalyst may also help to rationalize the reduction of $\frac{F_{MMA}}{F_{DMAEMA}}$ and yield upon going from toluene to the polar solvents acetonitrile and DMF. These are expected to make less negative the ΔH^o associated to the ligation decreasing more the reactant enthalpy and Gibbs' energy, which ought to reduce the equilibrium constant and hence the concentration of the complex.

5.2.6 General Discussion and Conclusions

Exploiting experimental results on the copolymerization of MMA and DMAEMA via ATRP in toluene, in this work we have provided evidences that unexpectedly marked reactivity effects can be induced even in absence of strong intermolecular forces such as hydrogen bonds [250–252] and between copolymerization methods that are usually considered to provide similar results. Such conclusion emerges by comparing the mentioned results with both literature and ATRP data (the latter, again, by ourselves) obtained in different reaction environments (bulk, DMF, chloroform, acetonitrile and dioxane). The large difference in the reactivity ratios ($r^s_{MMA} = 0.36$, $r^s_{DMAEMA} = 2.76$) extracted from our numerical analysis on the "feed versus polymer composition" data in toluene suggests that the copolymers obtained in the indicated conditions present gradient-like compositions, the initial part of the chains being always more rich in the ionizable monomer. In this respect, one should hasten to notice that the local properties (*e.g.* the behavior as weak polyelectrolyte) of the synthesised chains ought to depend on the position

along the chain due to the composition change (for instance, see Reference [246], where the behavior of the lower critical aggregation temperature was discussed). Besides, r^s_{MMA} extracted from our analysis represent the lowest value found in the literature [248, 253–255] in an ATRP copolymerization with functional monomers such as DMAEMA, PEGMA, HEMA or furfuryl methacrylate, a finding that we suggest to be due to the preferential coordination of the DMAEMA monomer to the copper catalyst.

Microstructural details related to the reactivity ratios have been investigated via kMC simulations closely mimicking the synthetic conditions. These indicated the presence of a higher DMAEMA concentration at the chain beginning (see Figure 5.4) compared to the average copolymer composition, a finding that has a direct relevance to both the theoretical foundations of the polymers designed for the discussed drug delivery applications [207, 208] and the analysis of the release kinetics from vesicles [221, 222]. Wishing to obtain copolymers of more uniform composition along a chain, a possible approach emerges from the modelling results in Section 5.2.5, which suggest a difference between MMA and DMAEMA partition coefficients due to the complexation of the latter. Thus, one may favour (disfavour) even more the partition of MMA (DMAEMA) from the bulk to the regions surrounding the growing polymer by appropriately choosing the reaction solvent, which impacts on the stability of the complex between DMAEMA and CuBr.

In conclusion, we consider worth mentioning a few possible lines of investigation emerging from the current work. For instance, we notice that from the experimental standpoint it would be interesting to investigate the impact of Cu(I) ligands on the DMAEMA reactivity ratios, which may allow fine tuning of the local relative amount of each monomer along the chain. Concerning possible theoretical work, an avenue of exploration may be represented by exploiting atomistic level simulations to investigate the eventuality of MMA and DMAEMA monomers partition close to a growing chain in the presence of explicit solvent molecules and coordinating catalysts.

5.3   Homogeneous Copolymerizations

Despite the fact that the kinetic description used for MMA/DMAEMA copolymers is theoretically built on a radical mechanism, it is very often employed for homogeneous systems as well. Even if the used probabilities are generic, in the latter situations it is not very clear if the obtained reactivity ratios (Eq.5.22, or the probabilities of Eq.5.23) are linked to the ratios of Equation 5.16 and whether or not way the kinetic assumptions are still valid. With respect to radical copolymerizations, the homogeneous catalyzed reactions could have a more complicated mechanism involving, for example, coordination preequilibria. A most correct label, from our point of view, could be the definition of reactivity ratios by observed kinetic constants k^{obs}

$$r_1 = \frac{k_{11}^{obs}}{k_{12}^{obs}} \qquad\qquad r_2 = \frac{k_{22}^{obs}}{k_{21}^{obs}} \qquad\qquad (5.34)$$

where k_{ij}^{obs} is a global constant obtained by the combination of several kinetic step, experimentally undetectable. Hoping to avoid any reliance on specific mechanism, an useful theoretical approach could start from the definition of a propagation probabilities matrix and the fitting of triads. [256, 257] Another way, when experimental kinetic constants are available, is the definition of the kinetic model, the computation of the transition matrix (*via* experimental kinetic constant) and the computation of the sequences percentages. [258] Indeed, the reaction mechanism of homogeneous catalyzed copolymerizations is often not clear or, at least, rarely studied. In depth, the first theoretical work aiming to clarify eventual equilibria between homogeneous catalysts, co-catalyst (methylaluminoxane) and monomers was generated by Zurek and Ziegler, in which, by DFT approach, they underlined the possible presence of stable coordination intermediates and more than one paths for the olefin interaction with metallic cation of catalyst. [259] An experimental characterization of energy profile was also carried out by Dahlmann *et al.*, [260] the kinetic analysis showing an addition/dissociation preequilibrium step preceding the rate-determining insertion *via* low temperature ^{1}H-NMR.

Summarizing, many catalyst features can take part in describing the catalytic behavior: the role of counter ion, the chain-control given by the ultimate
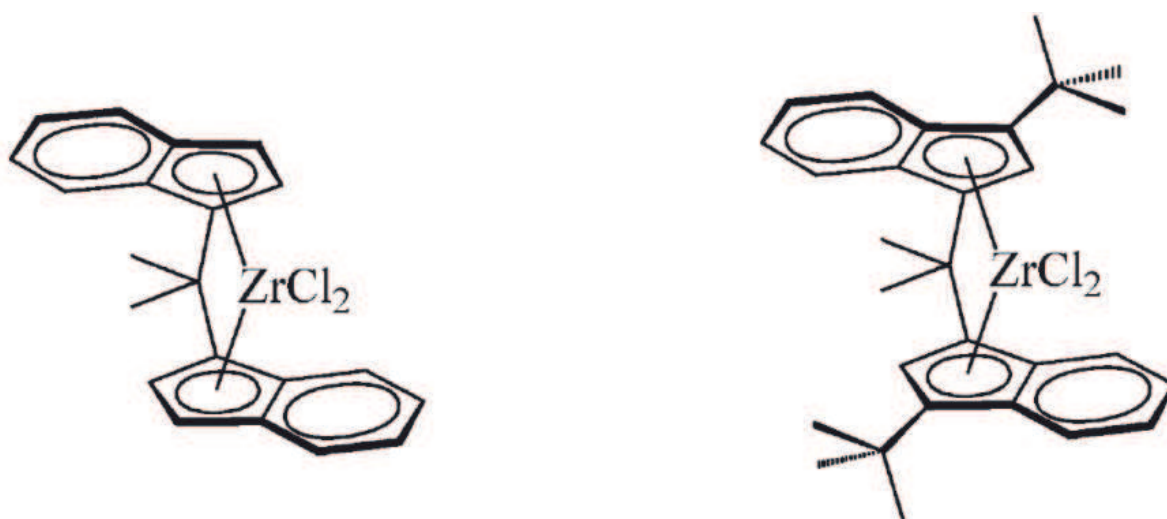
Figure 5.11: Structure of rac$-$Me$_2$C$-$Ind$_2$ZrCl$_2$ (left) and rac-Me$_2$C-(3- ^{t}Bu-Ind)$_2$ ZrCl$_2$ (right).

or penultimate monomer, the competition between different coordination sites and so on. [167]The in depth understanding of the relative importance of those effect on the blocky" nature of copolymer represent the aim of this study, in order to provide useful information to chemists during the design of new catalysts. In this regard, we propose a theoretical study of the elementary steps involved in the copolymerization of ethene and propene by two C$_2$-symmetric metallocene catalysts, rac$-$Me$_2$C$-$Ind$_2$ZrCl$_2$ and rac$-$Me$_2$C$-$(3$-^t$Bu$-$Ind)$_2$ZrCl$_2$. [261] While a DFT analysis of the reaction pathway would provide us the total energetic of insertion, a kinetic Monte Carlo model would be used to stochastically simulates the kinetic of copolymerization in order to shed some light on the relative importance of different catalyst features. The summary of the experimental procedures and results are reported in Table 5.3. [261]

5.3.1   Computational Details

Gas-phase electronic structure calculations were carried out using the Gaussian09 software, [50] employing BP86 density functional theory (DFT) with the local exchange-correlation potential by Vosko *et al.* [53] augmented in a self-consistent manner with Becke's exchange-gradient correction [262] and Perdew's correlation-gradient correction. [263] The basis set employed was LANL2DZ [264] with associate effective core potentials for second and third-row atoms and SVP [265] for

	Zr (μmol)	ethene/propene feed ratio		yield (g)	activity (g_{pol}/g_{Zr})	$E_{copolym}$ (mol%)	monomer conv. (%)	isoindex (%)	regioirr. (%)
		gas phase (mol/mol)	liquid phase (mol/mol)						
	1.7	5.58	1.33	0.7	4400	80.3	2.5	n.d.	n.d.
	1.7	2.59	0.61	0.04	250	65.4	<1	75.9	n.d.
rac-Me$_2$C-Ind$_2$-	3.5	1.29	0.30	1.9	6050	50.0	6.2	77.5	n.d.
-ZrCl$_2$	3.5	1.18	0.28	1.5	4650	50.9	4.8	71.0	n.d.
	3.5	0.55	0.13	2.3	7350	30.2	6.7	76.5	1.33
	1.2	2.28	0.54	0.9	8700	89.5	3.4	n.d.	n.d.
rac-Me$_2$C-3-	1.5	1.16	0.27	1.9	13900	71.8	6.7	100	n.d.
-(^{t}Bu-Ind)ZrCl$_2$	1.5	0.29	0.069	2.0	14650	37.0	6.3	100	none

Table 5.3: Ethene/Propene copolymerization with racemic metallocenes and MAO as catalytic system. Polymerization conditions: = 100 mL, Al/Zr = 1000 (mol/mol), T = 323 K, total pressure = 1.1 atm, flow rate of mixture = 1.5 L/min, time = 15 min (N.d = not detected).

the first-row atoms. On the basis of the low value of the dielectric constant for the solvent (toluene, ϵ=2.38) commonly employed during polymerization, gas-phase calculations were deemed to be appropriate, as we would not expect a large separation between ions during the coordination and enchainment processes. [167] The optimized structures were confirmed as true minima and true transition states by vibrational analysis at the same level of theory.

Chain growth was simulated *via* kMC code, treating the copolymerization as a stochastic process and assuming that the insertion step was irreversible. The feed composition is constant during the simulations in order to reproduce the experimental conditions (total conversion of $\sim$5%). Two version of the code were created, the first one simulating reactive scheme of the ultimate model, the second one the penultimate model (the complete code are reported respectively into Appendix B and Appendix C). The core of simulation is built on the following scheme:

1. determines the new reacting monomer basing of the solution feed composition;

2. reads the nature of ultimate (or ultimate plus penultimate) monomer(s) in the polymeril and calculates the probabilities p_{ij} (see eq. 5.5) from the $\Delta G^{\ddagger}$ given in input;

3. compares an uniformly distributed random number with the transition probabilities;

4. determine the new state of the system, by means of the transition probabilities, and evolve the system in the new state;

5. if the final state is the insertion state, storage the new monomer in an array and go back to point 1 and continue until a threshold number of monomer are inserted.; if the final state is the dissociated one, go back to point 1.

At the end of the copolymerization simulation, the ethene/propene ratio presented in into the chain and the triad distributions are computed. A stability analysis of these quantities was carried out providing an average percentage error on triad distributions of 2%.
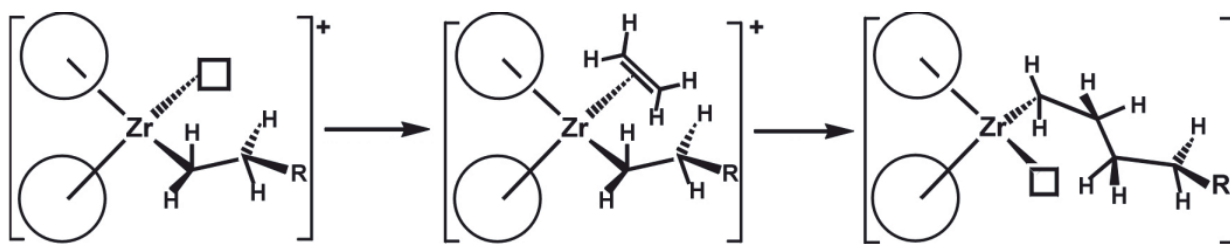
Figure 5.12: Schematic representation of the insertion step according to the Cossee mechanism.

5.3.2 Density Functional Theory Investigation

The DFT model can be built by the catalyst, the olefin and the polymeril, the latter one represented by four carbon atom (two monomers) when studying the ultimate effect, while further extended to six carbon atom (three monomers) if the penultimate effect is evaluated. Notice that the extension to a third monomer of the chain comes from the necessity to fix the position of the methyl group on the propene when it is located at the penultimate position in a growing chain.

The first step of the process that leads to olefin insertion one could image is the coordination of the olefin to a catalyst. In the case of the simplest imaginable polymerization model, a coordination site on metal cation will be free following an insertion and and a new olefin may approach the catalyst without experiencing hindrance along the way. This model was first proposed by Cossee and it is still employed as reference mechanism; a generic scheme is reported in Figure 5.12.

The empty coordinating site creating after the insertion (Fig.5.12), in the future discussion, will be called *far*, because of the distance between the olefin and the Zr-C bond that will be cleaved during the insertion (an example is shown in Figure 5.13.

The complex is characterized by a β-agostic interaction of H50 with Zr (Zr-H50 = 2.283Å) while the olefin distance (C55) from Zr is 2.798 Å. In order to have the *far* coordination, the olefin has to move from solution to the proximity of complex across an apparently free path; the process has been simulated computing a scan during which the distance Zr1-C55 has been reduced from 8.0 Å to the distance observed into minima. Coordination pathways are reported in Figure 5.14: the results actually suggest that the olefin's coordination process in
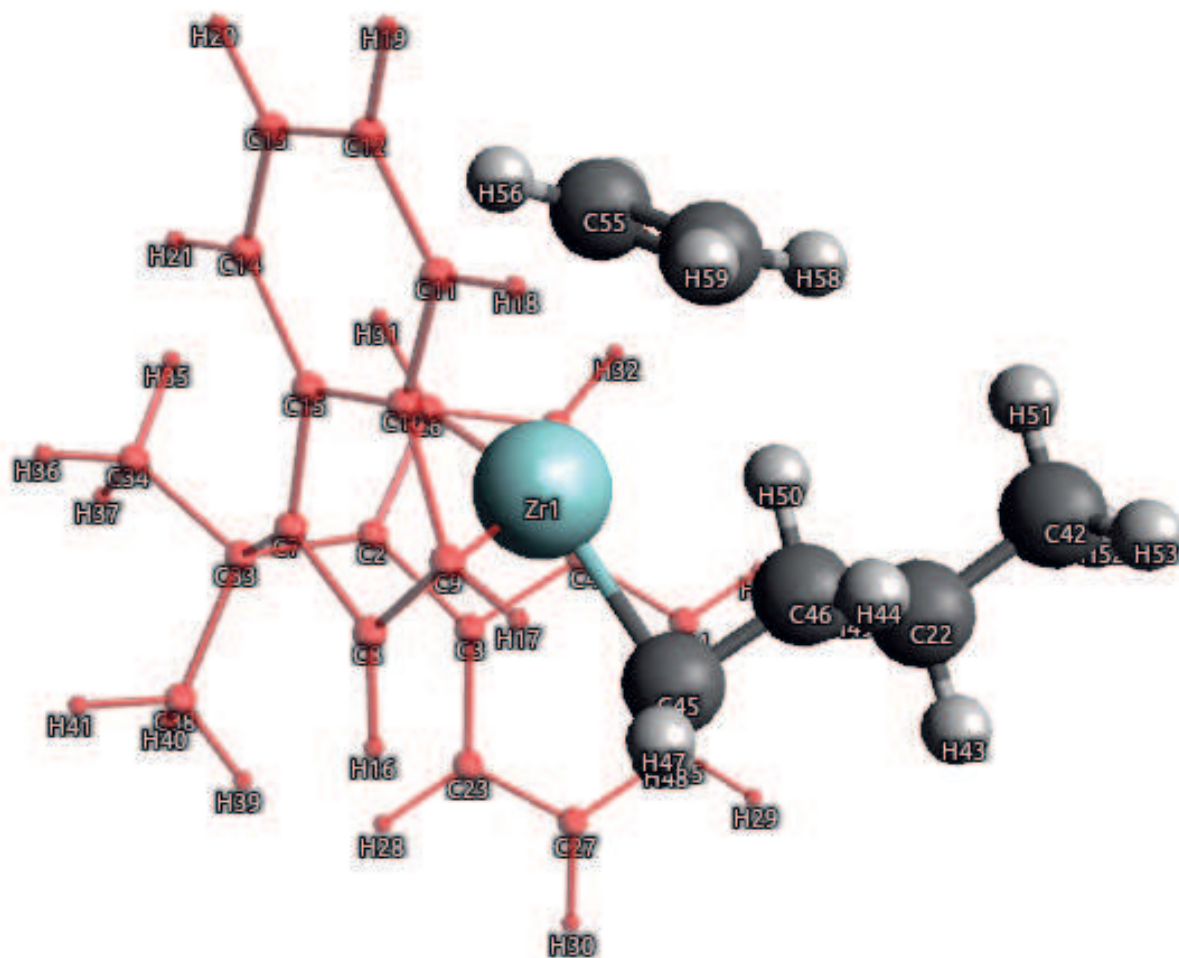
Figure 5.13: Schematic structure with symbols and atom numbers of a studied model; the red moiety is the ligant $Me_2C\text{-}Ind_2$.
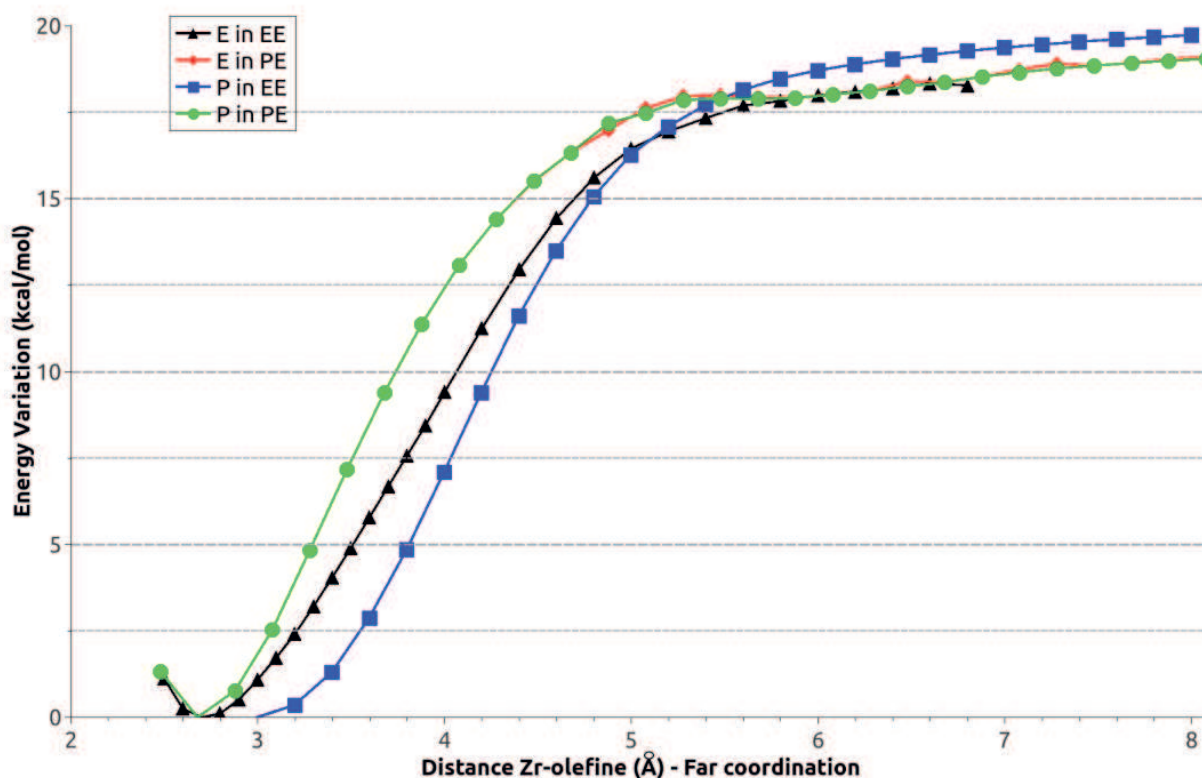
Figure 5.14: Scan energies for olefin's *far* coordination on Zr with two possible growing chains on rac-Me$_2$C-Ind$_2$ZrCl$_2$ catalyst.

far is barrierless and lead to an energetic gain of 20 kcal/mol; in a few cases it is possible to notice a little energetic drop around 6Å but it is connected to the freedom that the olefin had to reorient close to the indenyles just because being the scan only a distance restriction. When the olefin is closest to the indenyl, the system betrays the presence of the catalyst's ligand by rising the energy. No indication of the presence of a real van der Waals minimum emerges, moreover repeating the scan in the opposite directions provides the same energetic profiles.

After the olefin reaches the *far* coordination, the system can be led to evolve toward a geometry where the C45-C46 bond is closer to the olefin and leaving the β-agostic interaction to reach a more stretched configuration by changing the dihedral angle Zr-C45-C46-C22. The final minimum (Fig.5.15) has a quasi-α-agostic interaction involving H48 and shows geometry that is arranged in favor of the insertion. The new minimum is not the only one we obtained *via* DFT, in fact the system crosses more than one barrier passing other local minima, as reported in Figure 5.16.
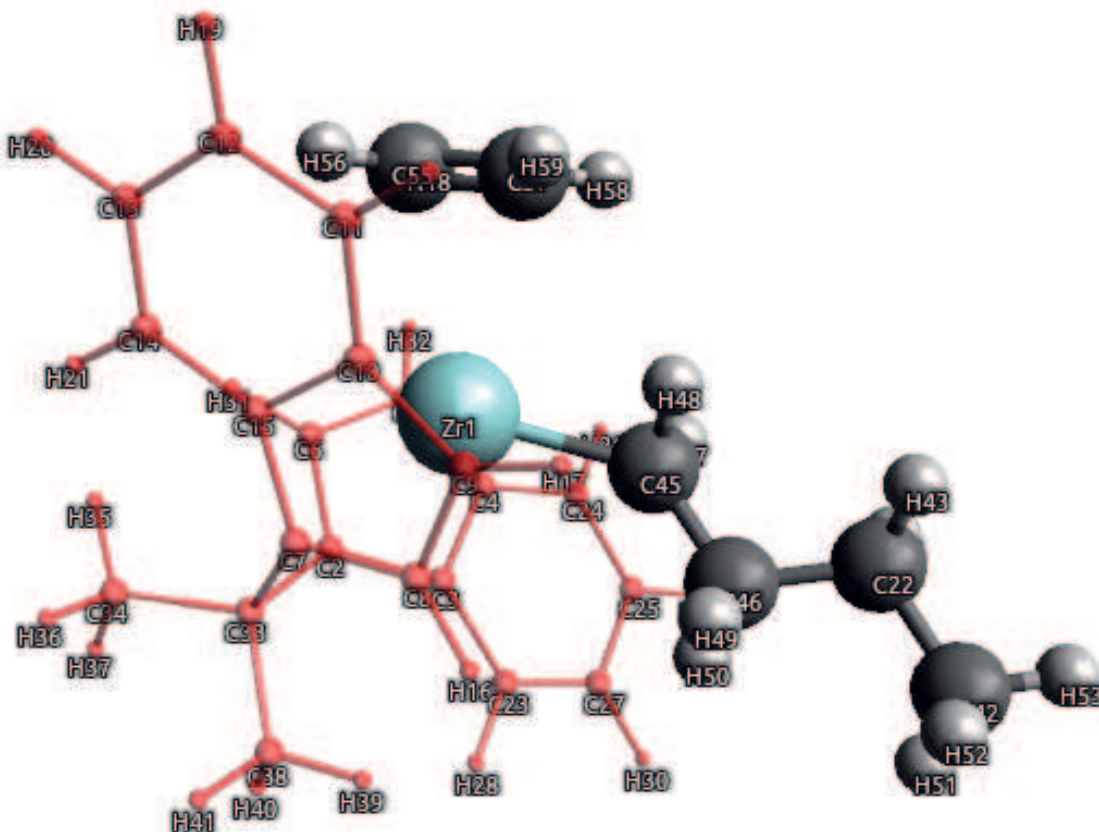
Figure 5.15: Schematic structure with symbols and atom numbers of "stretched" minimum; the red moiety is the ligant $Me_2C\text{-}Ind_2$.

The geometry shown in Figure 5.17 represent a good starting point for the insertion, as demonstrated by the last profile obtained by scanning the Zr-C45-C46 bending, which leads to the insertion's transition state. The scan forces the chain to decrease the angle and to restore a β-agostic interaction between H50 and Zirconium after a local maximum; finally the olefin is able to insert into Zr-C45 bond increasing the number of monomers into the chain (Fig.5.18).

Indications about coordination alternative to the one leading into the *far* coordination paths are proposed in literature: [167, 259] these suggested us that in the case of a C2 symmetric catalyst at least one more site should be found, here called *close* site. Again, the label *close* derives from the geometry that the olefin reaches after the coordination; the olefin double bond is really close to the Zr-C45 bond, suggesting that an easier insertion reaction profile could be found
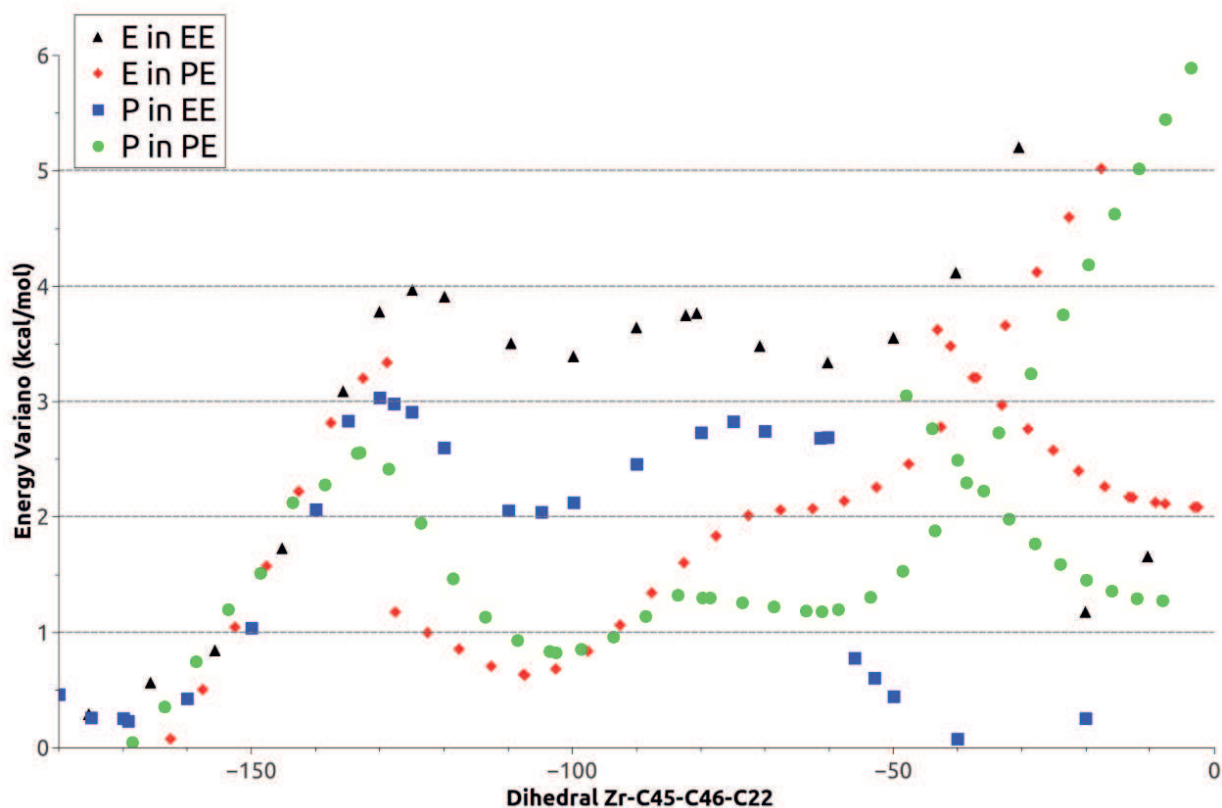
Figure 5.16: Scan energies of Zr-C45-C46-C22 dihedral torsion for four olefin/chain combinations on rac-Me$_2$C-Ind$_2$ZrCl$_2$ catalyst.

with respect to the *far* site. Again, the coordination process was investigated by reducing the olefin-catalyst distance with a scan (energetic profiles are reported in Fig.5.19). A first clear difference with the *far* coordination is the presence of a barrier that the olefin has to surmount to reach the coordinating minimum. The barrier is due to the steric hindrance of chain: the olefin need to force the chain to slide in order to find space for the coordination on the metal cation. The second difference is the presence of a local minimum around 6 Å most pronounced than in the *far* geometry. The coordinated complex has the geometry reported in Figure 5.17; it is also seen that the close configuration allows the chain to conserve a β-agostic interaction *via* H50.

After the coordination, the bending of the angle Zr-C45-C46 leads easily to the transition state for the insertion, so the total profile is much simpler than before, with only two transition states, one for the coordination and one for the insertion.

As mentioned, all local minima and transition states were characterized *via*
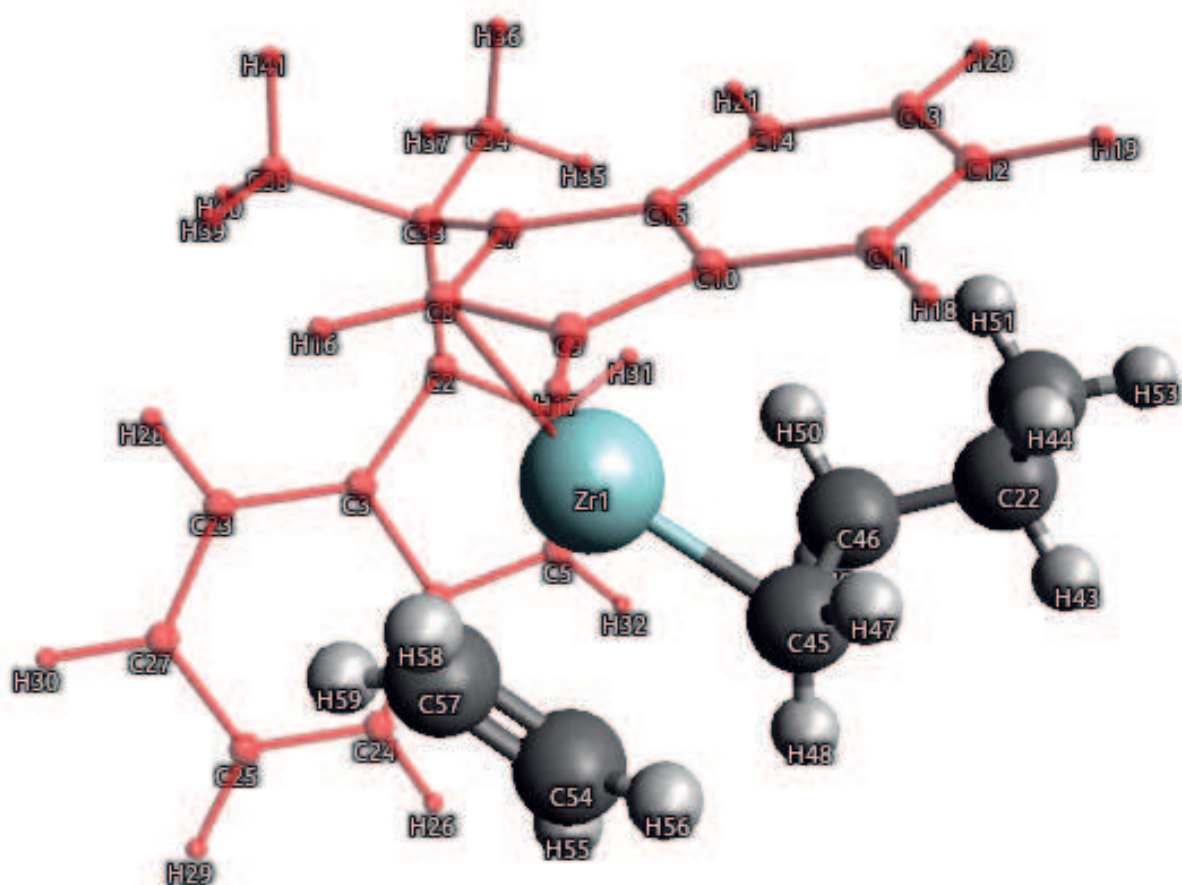
Figure 5.17: Schematic structure with symbols and atom numbers of *close* coordinated olefin; the red moiety is the ligand Me_2C-Ind_2.
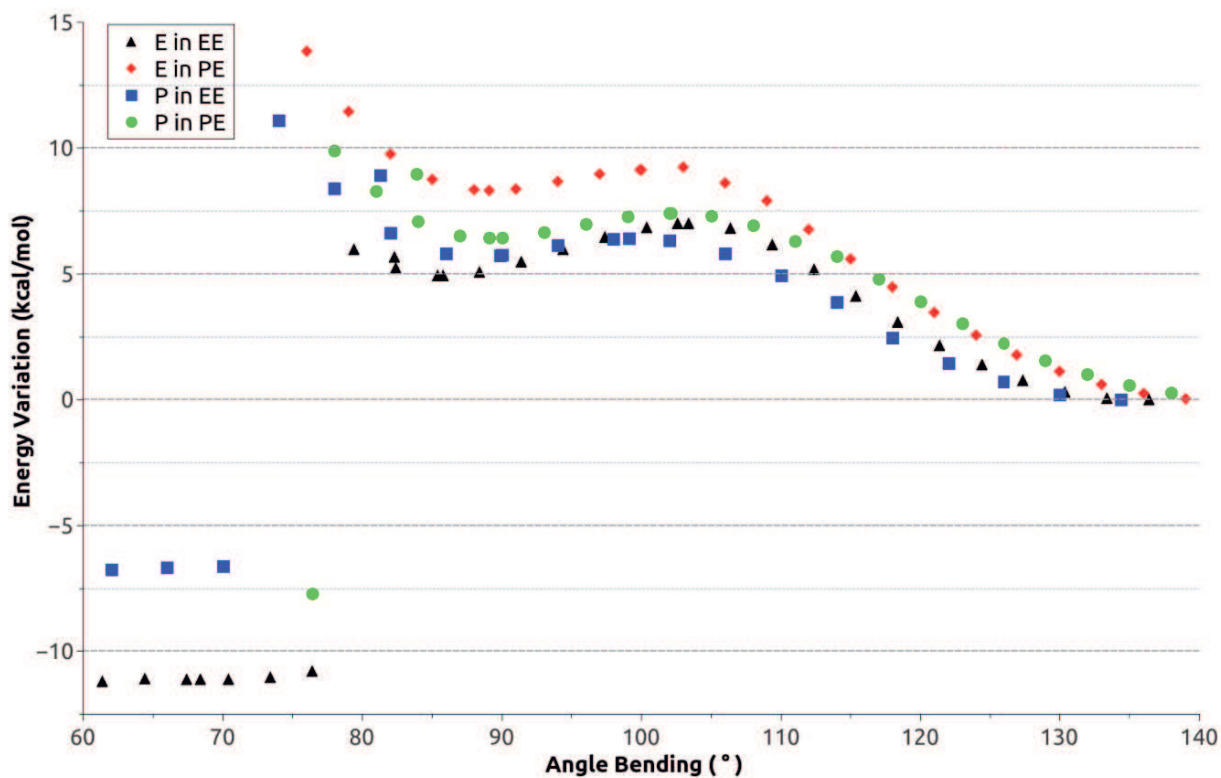
Figure 5.18: Scan energies of Zr-C45-C46 bending for four olefin/chain combinations on rac-Me_2C-Ind_2ZrCl_2 catalyst.
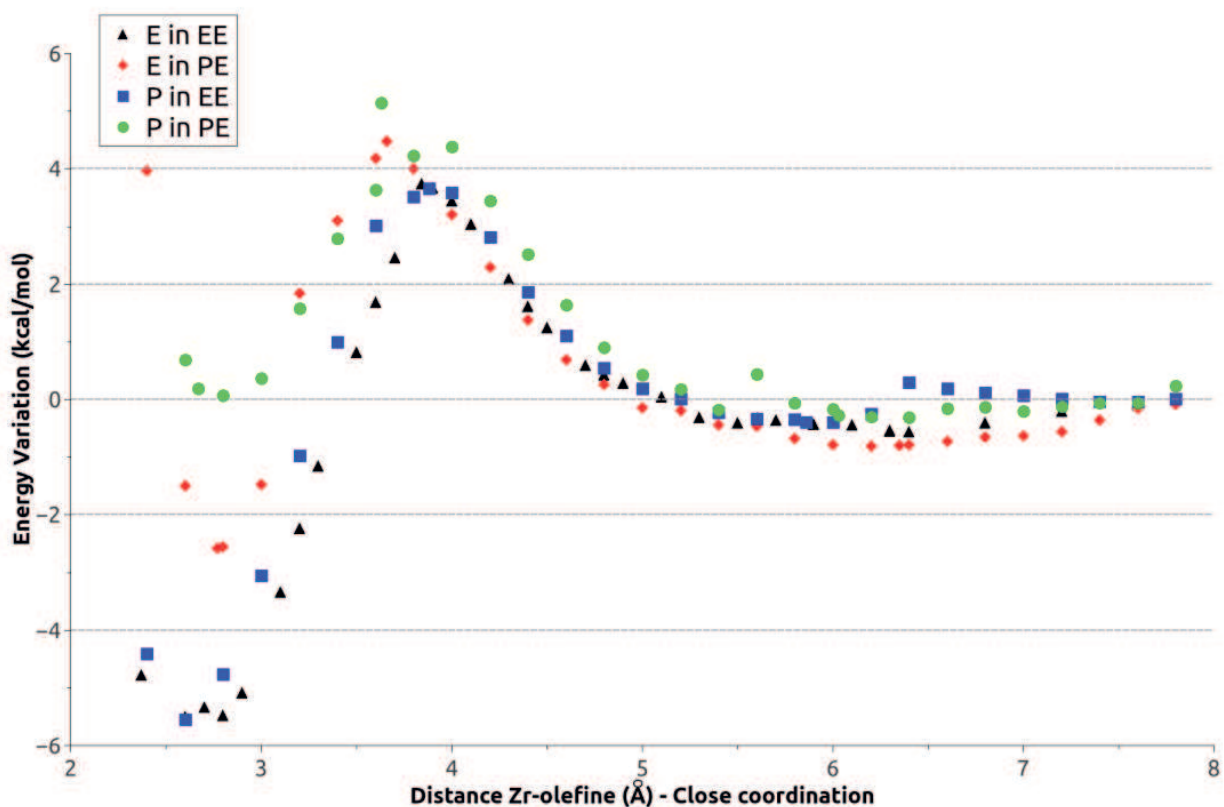
Figure 5.19: Scan energies for olefin's *close* coordination on Zr with two possible growing chains on rac-Me_2C-Ind_2ZrCl_2 catalyst.

vibrational analysis, this allows us to generate Gibbs' energetic pathways for all possible combinations of olefin/ultimate monomer/penultimate monomer, as reported in Table 5.4 for the *far* pathways and in Table 5.5 for the *close* pathways. As zero, the van der Waals minimum at ∼6Å is chosen for each combination.

The global picture that emerges from DFT investigation is quite complicate and makes difficult any straightforward rationalization of which are the most important aspect that influence the copolymer blockyness. An interesting characteristic emerging from DFT results is the lack of a coordination barrier in the *far* profiles that, at first, could be suggest that the only active paths is the *far* ones, turning the *close* coordination into an inactive path; a more careful analysis suggest, instead, that the two coordinating paths are in kinetic competition because the $\Delta G^{\ddagger}$ of *far*-insertion, *close*-coordination and *close*-insertion are comparable.

In view of the complicate reaction profiles extracted *via* DFT we are left, at the moment, with the impression that DFT alone would never be able to definitively suggest a specific reaction mechanism, especially due to the many computing processes that can take place. All this reveal the inability to discern the relative effect of several system features over the copolymer blockyness. To average over the latter, we thus wish to exploit kMC simulations relying on our DFT data; this would transfer the kinetic equations into a stochastic process, akin to a Markov chain. To make this possible, a transition matrix has to be defined, a task that would be optimally based on the kinetic constants. This choice, however, requires reconsidering the issues related to the *far* coordination process: with the two sites in direct competition entrance only on the *far* site will be the coordinated one without an energetic barrier. Considering the molecular level of the coordination process, one could conceive that an energetic barrier had to be present, even if the solvent has a low dielectric constant; in fact, the coordinating olefin must displace the solvent molecules screening the catalyst coordinating site. A rate constant for such process could be estimated assuming a poorly diffusive behavior, so that, as first approximation, could be taken from the *Solc-Stockmayer theory*: [266–268]

	Dihedral Scan					Angle Bending				
	min1	TS1	min2	TS2	min2	min3	TS3	min4	TSins	min5
E in EE	-3.45	-0.60	-1.14	-0.06	-1.11	-4.10	3.64	2.70	5.63	-11.97
E in PE	-3.17	-0.39	-3.24			-2.59	8.20	7.35	7.66	-9.63
E in EP	-4.19	-1.06	-1.93	-0.43	-0.87	-4.54	3.31	1.98	4.41	-12.45
E in PP	-3.56	-1.22	-3.98			-3.33	7.53	5.93	7.79	-9.71
P in EE	-4.23	-1.57	-3.69	-1.84	-2.90	-5.43	2.54	2.17	7.13	-9.57
P in PE	-2.33	-1.06	-4.13	-2.94	-4.05	-3.70	5.56	4.63	10.21	-7.31
P in EP	-3.80	-3.48	-3.86	-2.60	-3.20	-6.25	1.81	1.03	6.09	-9.40
P in PP	-4.35	-3.49	-5.57	-3.49	-4.15	-4.22	5.20	4.64	8.87	-6.24

Table 5.4: ΔG in kcal/mol of all minima and transition states computed for *far* coordinated olefin to rac-Me$_2$C-Ind$_2$ZrCl$_2$ catalyst.

	Coordination		Insertion	
	TScoord	min6	TSins	min5
E in EE	8.54	2.70	5.63	-11.97
E in PE	10.11	5.62	7.66	-9.63
E in EP	7.57	1.98	4.41	-12.45
E in PP	10.78	6.02	7.79	-9.71
P in EE	6.61	2.17	7.13	-8.03
P in PE	7.46	6.42	10.21	-7.32
P in EP	6.66	1.03	6.09	-9.40
P in PP	9.26	7.77	8.87	-6.24

Table 5.5: ΔG in kcal/mol of all minima and transition states computed for *close* coordinated olefin to rac-Me$_2$C-Ind$_2$ZrCl$_2$ catalyst.

$$k_{DC} = \frac{4\pi D R^2 k(1 - cos\theta_0)}{2D + kR(1 - cos\theta_0)} \tag{5.35}$$

where k_{DC} is the diffusion kinetic constant, D is the diffusion constant (as sum of translational diffusion constants for two reacting particles), R is the radius of the largest particle, θ_0 is an angular coordinate giving the amplitude of the active cone on the largest and k is a measure of the extent of diffusion control. When k$\rightarrow \infty$ (completely diffusion-controlled limit) the kinetic constant turn into a simpler form

$$k_{DC} = 4\pi D R \tag{5.36}$$

An estimate of the diffusion constant D for the complex and the olefin can be made *via* the *Stokes-Einstein-Sutherland equation* [268]

$$D = \frac{k_B T}{6\pi\eta r} \tag{5.37}$$

where k$_B$ is the Boltzmann constant, T is the temperature, η is the dynamic viscosity and r is the radius of a diffusing particle. With the tabulated dynamic viscosity of toluene, assuming approximating radii for ethene, propene and the catalyst from DFT optimized geometries ,it is possible to calculate the diffusion constant for the process of ethene and propene coordination to catalytic complex. Converting them into reactive constants, and subsequently in energy barriers, the two estimated values are: $\Delta G^{\ddagger}_{coord}$(ethene) = 4.26 kcal/mol and

$\Delta G^{\ddagger}_{coord}$(propene) = 4.45 kcal/mol. Notice that the energies depend only from the olefin because the external portion of the growing chain is treated as non-active respect to the rest of the molecule.

Turning to the second catalyst (rac-Me$_2$C-(3-^{t}Bu-Ind)$_2$ZrCl$_2$), we exploited the same approach as before: investigation of the coordination process *via* a relaxed scan along the olefin-Zr distance, of the changes induced by rotating along the Zr-C45-C46-C22 dihedral and over the bending angle Zr-C45-C46. The results obtained are similar to the one from the catalyst without the *t*-Bu groups, with the same features displayed by the *far/close* paths, local minima and TSs. As an example, the dihedral scan is reported in Figure 5.20. All local minima and transition states were characterized *via* vibrational analysis and the whole energetic pathways for all possible combinations of olefin/ultimate monomer/penultimate being reported in Table 5.6 for the *far* pathway and in Table 5.7 for the *close* pathway. The energy zeros chosen for each combination are the van der Waals minimum at ∼6Å. First indications from simulated model suggested that only a few steady states are needed for the Monte Carlo model; consequently, the extension on penultimate monomer concerned only few minima and transition states.

As for rac−Me$_2$C−Ind$_2$ZrCl$_2$, the relaxed scans for the *far*-coordination on rac−Me$_2$C−(3− ^{t}Bu−Ind)$_2$ZrCl$_2$ were barrierless, leading to the necessity of an effect which gives rise to a *far*-coordination barrier. Again, the diffusive barriers are calculated as described before (eq.5.36 and eq.5.37) and give $\Delta G^{\ddagger}_{coord}$(ethene) = 3.63 kcal/mol and $\Delta G^{\ddagger}_{coord}$(propene) = 3.97 kcal/mol.

During the copolymerization however, the catalyst and the monomers are not the only species in solution and we thus feel compelled to include in our model the counter ion (CI). The nature of the counter ions in the polymerizations can change the catalyst performance, then different kind of species were proposed in literature, among all one o the most diffuse is the methylaluminoxane (MAO). After the activation step, during which the CI sequester one of the methyl from the catalyst, the counter ion is usually assumed to stay in the proximity of a catalyst acting as an electrostatic counterpart without influencing the reactivity. In solution, the MAO has a no-well defined structure and it is made difficult a
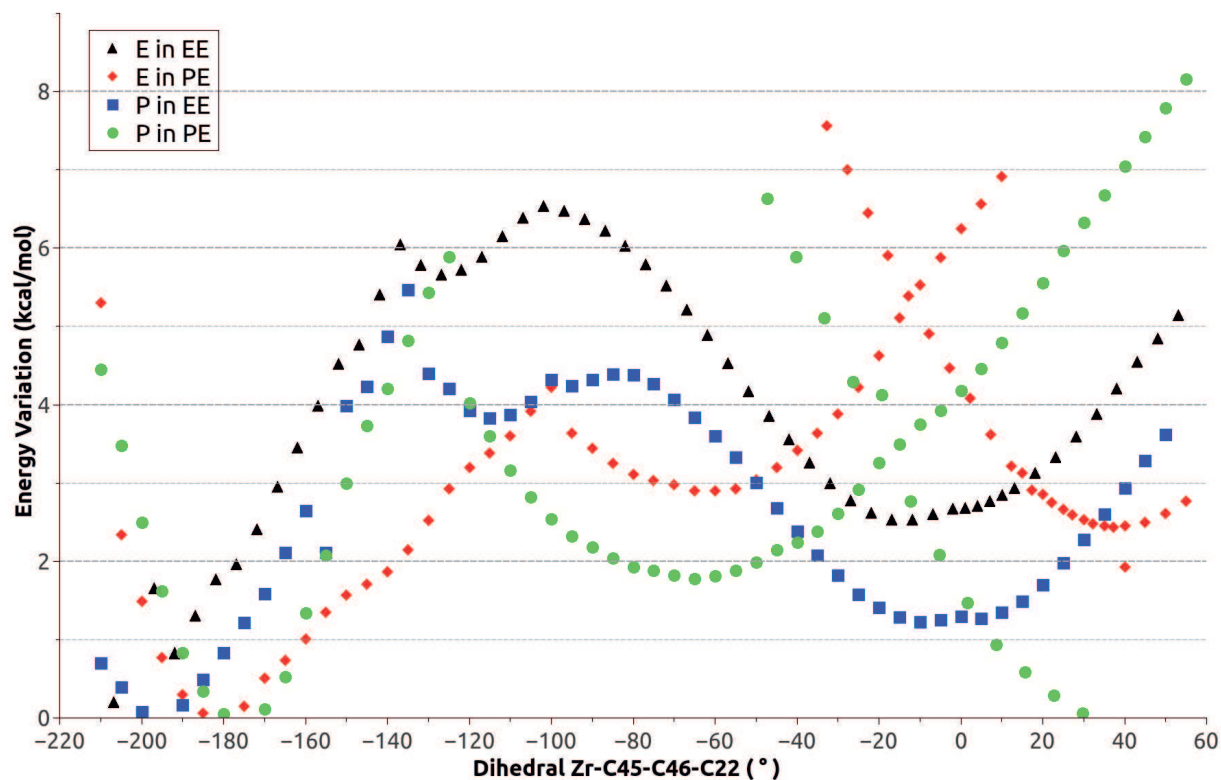
Figure 5.20: Scan energies of Zr-C45-C46-C22 dihedral torsion for four olefin/chain combinations on rac-Me$_2$C-(3-^{t}Bu-Ind)$_2$ ZrCl$_2$ catalyst.

	Dihedral Scan					Angle Bending			
	min1	TS1	min2	TS2	min3	TS3	min4	TSins	min5
E in EE	1.03	7.48	4.42	5.20	0.97	9.21	8.53	9.13	-11.25
E in PE	2.25	5.45	4.50	9.58	3.64	13.67	11.41	15.70	/
E in EP	2.16	/	/	/	/	/	/	10.73	/
E in PP	-1.25	/	/	/	/	/	/	/	/
P in EE	2.16	4.83	5.35	6.12	1.90	10.50	9.98	14.89	-6.12
P in PE	0.62	5.26	1.45	4.08	0.59	11.28	10.06	19.46	-7.57
P in EP	-0.19	/	/	/	/	/	/	13.72	/
P in PP	1.13	/	/	/	/	/	/	11.81	/

Table 5.6: ΔG in kcal/mol of all minima and transition states computed for *far* coordinated olefin to rac-Me$_2$C-(3-^{t}Bu-Ind)$_2$ZrCl$_2$ catalyst.

	Coordination		Insertion	
	TScoord	min6	TSins	min5
E in EE	13.83	8.50	9.13	-11.27
E in PE	20.59	14.00	15.70	/
E in EP	14.91	9.15	10.73	/
E in PP	21.00	11.04	/	/
P in EE	15.29	9.99	14.89	-6.12
P in PE	18.54	10.08	19.46	-7.57
P in EP	12.78	8.94	13.72	/
P in PP	20.24	10.95	11.81	/

Table 5.7: ΔG in kcal/mol of all minima and transition states computed for *close* coordinated olefin to rac-Me$_2$C-(3-^{t}Bu-Ind)$_2$ZrCl$_2$ catalyst.

DFT study; luckily, only the portion that directly interact with the metal seems to influence the energy of couple CI-catalyst, and that makes possible to generalize energetic features of a kind of counter ion to a more large class. [259] In our specific case, for sake of simplicity, we chose the tris(pentafluorophenyl)borane (B(C$_5$F$_5$)$_3$) that seems to be slightly less coordinating than MAO. [172, 269–271]

The anion MeB(C$_5$F$_5$)$_3^-$, resulting from the activation of catalyst, is a weak counter ion that stabilize the negative charge by means of the inductive effect of Fluorines. In order to find how the CI interact with the catalyst, we performed DFT investigation in absence of the olefin on the catalyst. The first obtained geometry is shown in Figure 5.21. The structure is similar to those of the initiation step, being an energetic gain of 46 kcal/mol. An other geometry for the catalyst-CI complex was found making a relaxed optimization of the system containing the catalyst and the counter ion in the proximity of the Me$_2$CInd$_2$. Surprisingly, the system evolves itself reaching the coordination *via* a Fluorine of the CI instead of the methyl (Fig.5.22); this new geometry has an energetic gain of 41 kcal/mol (only 5 kcal/mol higher than the previous case).

This new feature is interesting because it shows how the counter ion can interact with the catalyst after the olefin insertion, potentially becoming a hurdle for the next coordinating monomer; thus allow us to suppose that the CI can affect the *far*-coordination giving rise to an energy barrier. First scans following a coordination IRC scans were made in order to evaluate the impact of the CI presence,
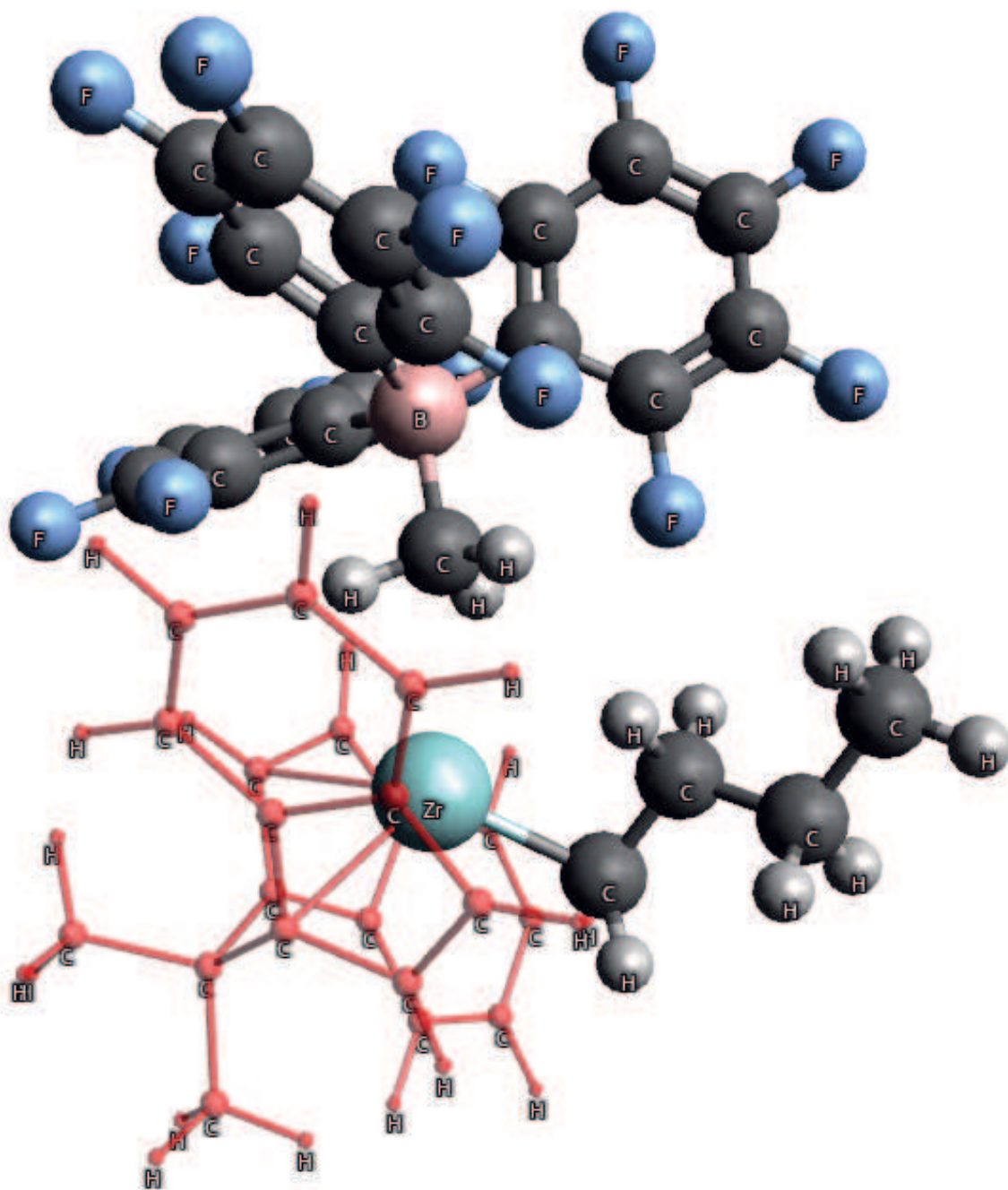
Figure 5.21: Schematic structure with symbols and of MeB(C$_5$F$_5$)$_3^-$ coordinated *via* methyl; the red moiety is the ligand Me$_2$C-Ind$_2$.
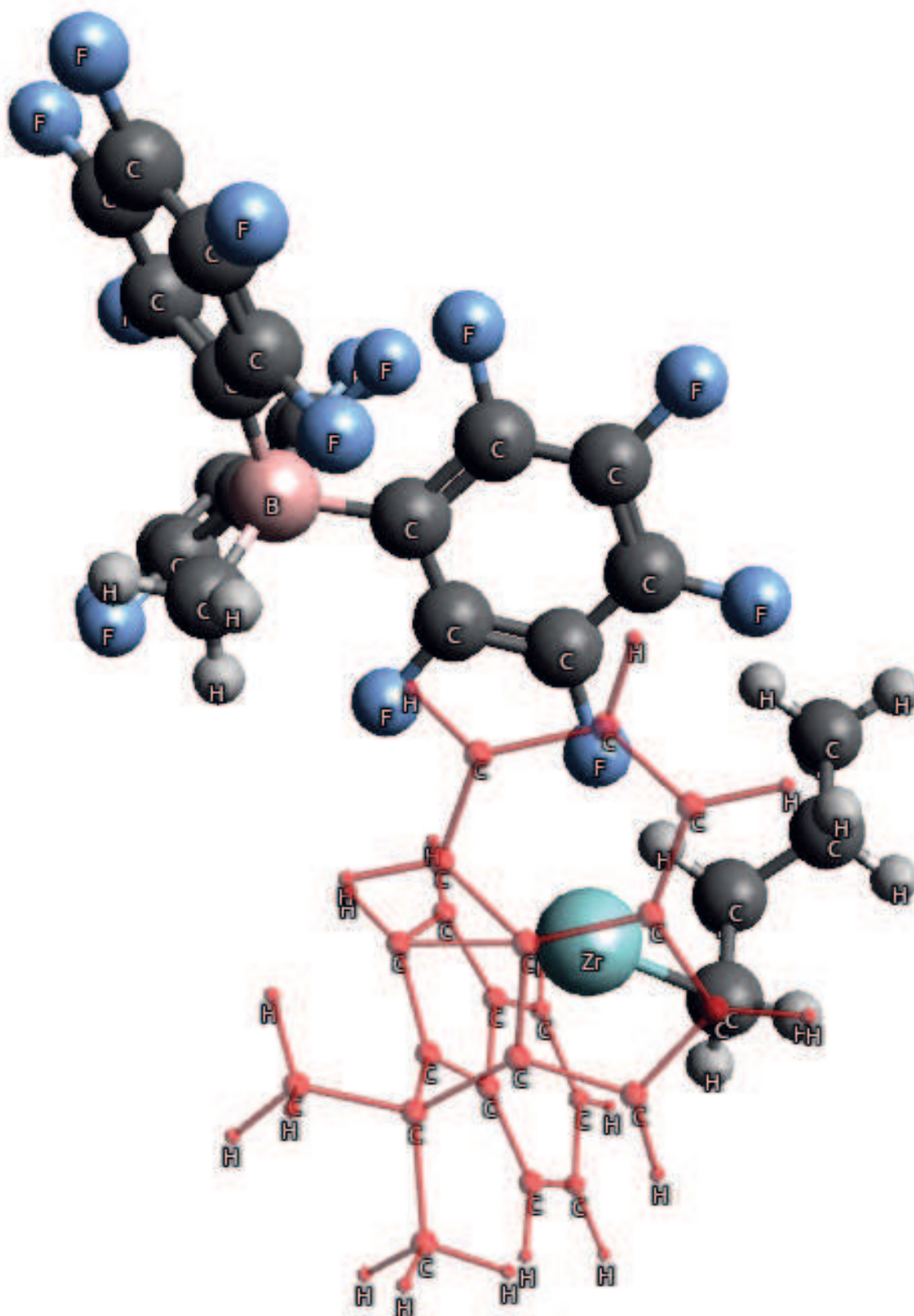
Figure 5.22: Schematic structure with symbols and of $MeB(C_5F_5)_3^-$ coordinated *via* fluorine; the red moiety is the ligant $Me_2C\text{-}Ind_2$.
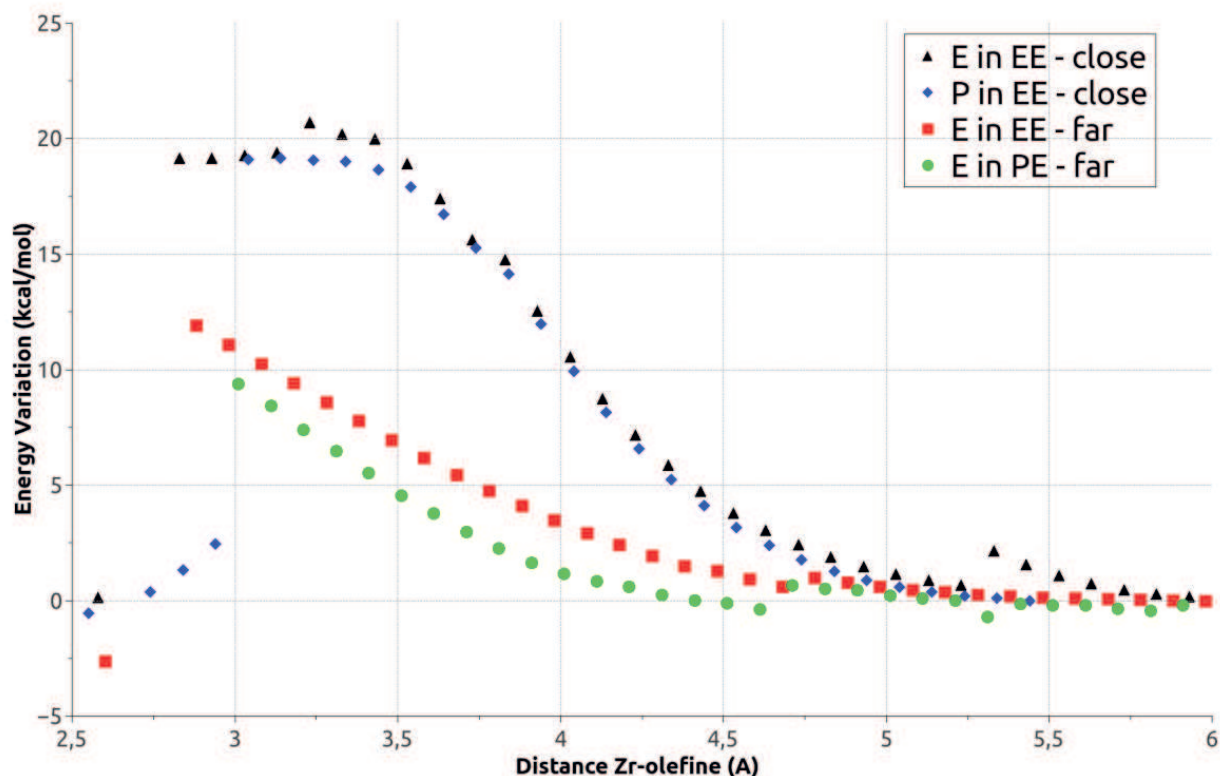
Figure 5.23: Scan energies for olefin's coordination on the complex rac-Me$_2$C-Ind$_2$ZrCl$_2$ / MeB(C$_5$F$_5$)$_3^-$ coordinated *via* fluorine.

showing the barriers also for the *far* paths (Fig.5.23). The complexity of the system, however, complicates the characterization of the transition states because of a mixing between the olefin-Zr distance and the CI-catalyst distance; despite this, this finding could provides an alternative source for the *far*-coordination barrier, differing from the diffusion process. In first approximation, we took energy values by a comparable system previously studied, [167] being 10.6 kcal/mol for the $\Delta G^\ddagger$ for the coordination and 6.8 kcal/mol for the $\Delta G^\ddagger$ of retrodissociation.

The principal aim of this study is to reveal the most important aspect that influence the blockyness of the copolymers; the amount of results from DFT calculations however make difficult any rationalization about which feature control the resulting microstructure between the CI effect, the two coordinative paths and the ultimate/penultimate model. Since DFT seemes to be not enough, we propose a kinetic Monte Carlo approach, employing DFT energies, as a suitable method for the achievement of our goal. The flexibility of Monte Carlo allows us to built several models including each effect and to evaluate the relative effect on

the final copolymer microstructure.

5.3.3 kinetic Monte Carlo Model

The kinetic Monte Carlo can simulate the state-to-state dynamics of the simulations when high-quality transition state theory rates are available. [187] The fundamental key is the definition of transition matrices for each mechanism, to do that few approximation are made:

1. chosen an olefin as monomer, only three states are available for the system, the separated state (the zero energy for all the combinations) corresponding to the retrodissociated state, the coordinated state and the inserted state (the final one);

2. the other characterized steady states are born of internal displacements and they do not represent kinetically relevant processes (**TS1**, **min2**, **TS2**, **min2**, **TS3**, **min4** in Table 5.4 and 5.6);

3. the *far*-coordinating barrier can be produced by either diffusion effect or counter ion presence;

4. the E/P coordination probabilities depend only from the molar fraction of monomers into solution;

5. the inserted state is irreversible, so the polymeril cannot undergo an elimination reaction, as for example β-elimination, or chain-transfer;

6. the state changes are independent form the previous ones; in other words, the process behaves like a *Markov chain*.

The reduction in state number leads to a simplification of the reaction pathways; Figure 5.24 reports a generic profile and the labels assigned to the states. The state with **1** tag represents the zero of the paths and it is the same for the *far* and the *close* paths. After the first barrier, the systems reach the coordinated states, which is labeled **2** for the *close* site and **4** for the *far* site. The second barrier is related to the insertion TS and leads to the states with the inserted monomers, labeled **3** and **5**, respectively, for the evolution from the *close* and *far* coordinated states. The states **3** and **5** are irreversible, as said in assumption 5,
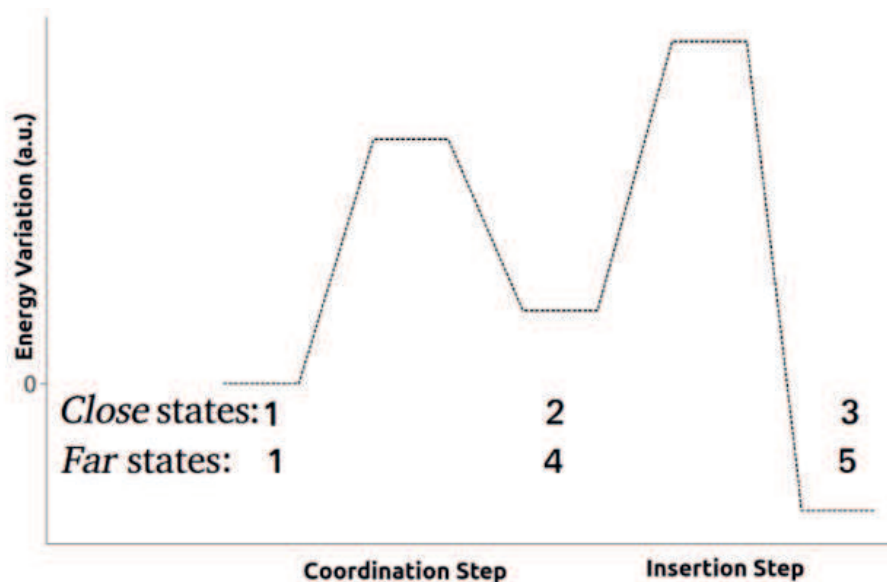
Figure 5.24: Schematic reaction pathways with labels for *close* and *far* paths.

so the probabilities $p_{3,2}$ and $p_{5,4}$ are equal to zero. Once defined the states, a transition matrix can be built for each combination of olefin-ultimate monomer, in order to simulate the ultimate effect, and olefin-ultimate-penultimate monomer, in order to simulate the penultimate effect. The matrix organization is reported as generic example in the Equation 5.38, where $p_{i,j}$ is the probability of the system to evolve from the state i to the state j.

$$E/P \ in \ (E/P)(E/P) = \begin{bmatrix} 0 & p_{1,2} & 0 & p_{1,4} & 0 \\ p_{2,1} & 0 & p_{2,3} & 0 & 0 \\ 0 & 0 & 0 & 0 & 0 \\ p_{1,4} & 0 & 0 & 0 & p_{4,5} \\ 0 & 0 & 0 & 0 & 0 \end{bmatrix} \qquad (5.38)$$

The simulation of the ultimate effect employs in input four different matrices, descending from monomer ethene/propene reacting with a catalyst bearing a chain composed of an ethene/propene as ultimate monomer and a fixed ethene as penultimate; the relative code is reported in Appendix B. The simulation of the penultimate effect employs in input eight different matrices, the doubling deriving from the presence of two different penultimate monomers; the relative code is reported in Appendix C. The probabilities depends, of course, on the

catalyst, moreover, the terms $p_{1,4}$ and $p_{4,1}$ change if the model include the diffusion effect or the counter ion on the coordination barriers. As output from the simulations, one obtains the triad distributions plus the polymer composition; to validate or approach, theoretical results are plotted with the distributions came from a random copolymerization and the experimental data from Ref. [261]. The interest about the copolymer's blockyness make useful the representation of the homotriads (EEE and PPP) versus the chain composition.

5.3.4 rac-Me$_2$C-Ind$_2$ZrCl$_2$ Catalyst

To begin our discussion on the simulation results, we report first data on the catalyst rac-Me$_2$C-Ind$_2$ZrCl$_2$ assuming a diffusive kinetic control on the *far*-coordination. The most interesting triad distributions for a potentially "blocky" polymer are reported in Figure 5.25 and 5.26, while the relation between ethene/-propene ratio in the solution feed and in the chain is reported in Figure 5.27. Experimental copolymerizations produce random copolymers that show homotriad distributions close to an uncontrolled copolymerization for every E/P ratio value. Diffusive control on *close* coordination seems to carries out good results for both ultimate and penultimate models: in EEE distribution (Fig.5.26) the models give really close results, the difference is more clear in the PPP distribution (Fig.5.25) with the ultimate model that better reproduces the experimental data; unlike the triads, in the E/P ratio in chain vs. E/P in feed (Fig.5.27) the penultimate model is closer than the ultimate model to the experimentally measured data.

A numerical way to compare the simulation results with experimental data is the statistical approach for the evaluation of reactivity ratios r_1 and r_2 (see Eq.5.16 and Eq.5.22) *via* the method proposed by Galimberti *et al.*, its complete mathematical presentation having been explained in the Ref. [192]). Briefly, the statistic procedure consists of:

1. evaluates of two transition probabilities $P_{E,P}$ and $P_{P,E}$, analogously to Equation 5.22, using two initial values for r_1 and r_2;

2. calculates of triads distributions as non-linear expression of the two probabilities;
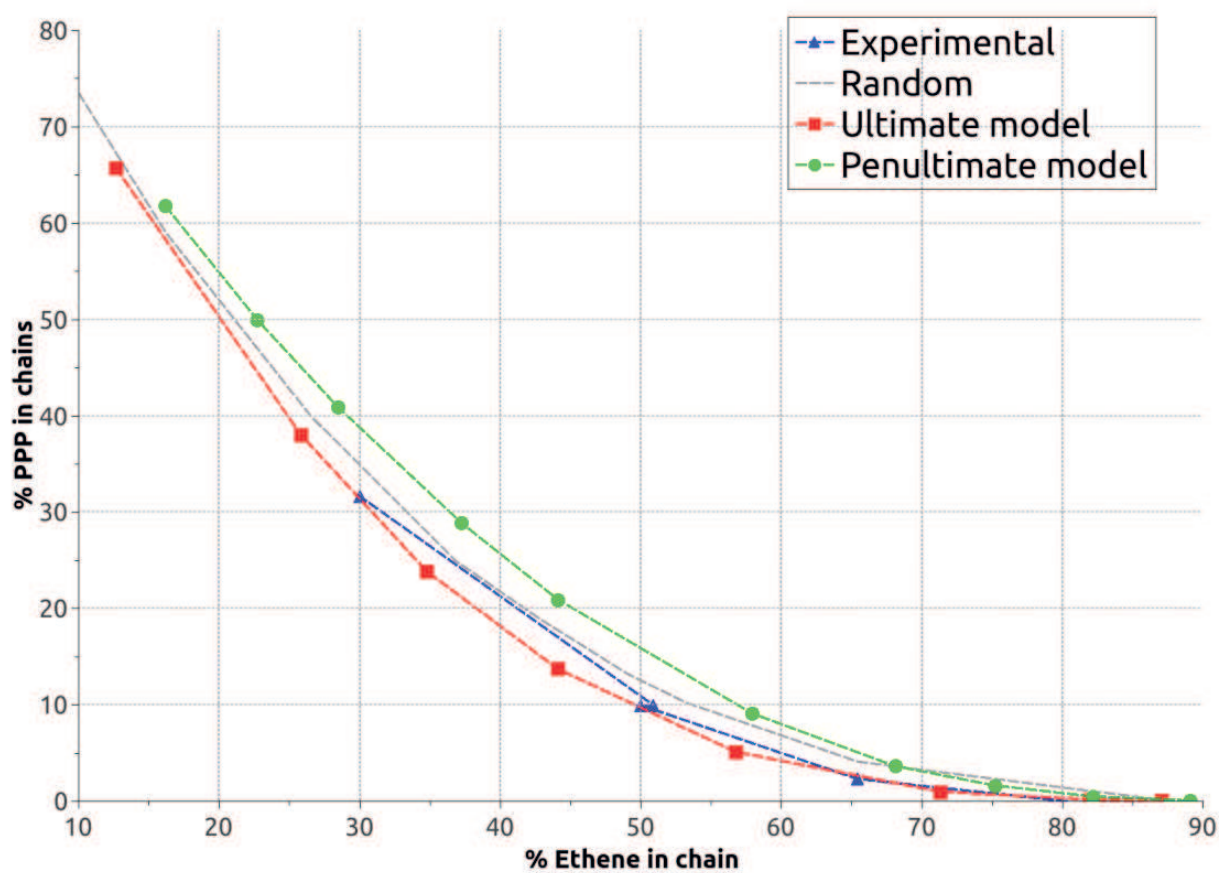
Figure 5.25: % PPP in the chains versus the % E/P in the chains for the system with Me$_2$C-Ind$_2$ZrCl$_2$ and diffusion control on the *far*-coordination.

Figure 5.26: % EEE in the chains versus the % E/P in the chains for the system with Me_2C-Ind_2ZrCl_2 and diffusion control on the *far*-coordination.
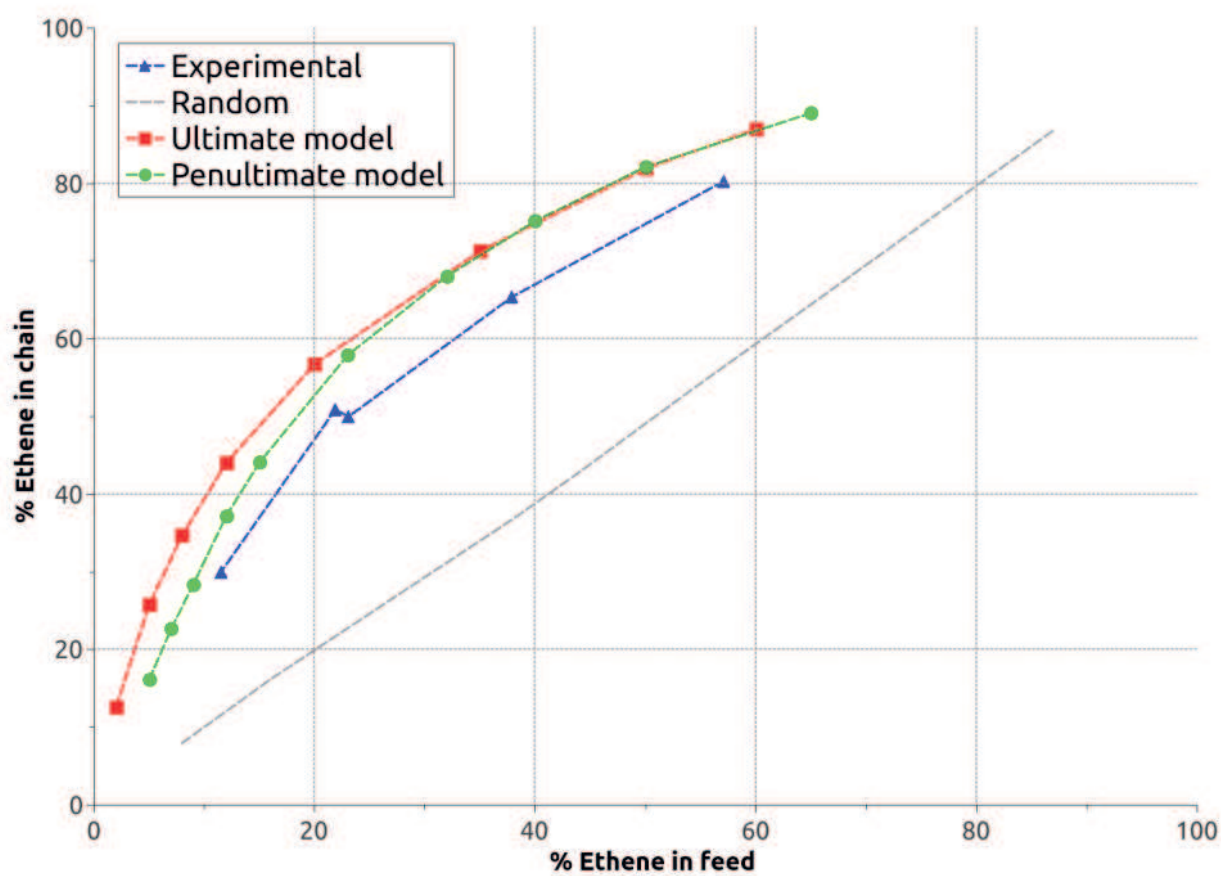
Figure 5.27: % E/P in the chains versus the % E/P in the feed for the system with Me$_2$C-Ind$_2$ZrCl$_2$ and diffusion control on the *far*-coordination.

	r_1	r_2	$r_1 r_2$
ultimate model	4.04	0.13	0.54
penultimate model	4.78	0.35	1.69
experimental data	2.30 ± 0.19	0.21 ± 0.02	0.48 ± 0.09

Table 5.8: Reactivity ratios for the catalyst $Me_2CInd_2ZrCl_2$ with *far*-diffusion control.

3. sums the squares of the deviations between experimental and calculated triads' distributions for each copolymer sample, subsequently sums all the errors into an unique value over all copolymer samples;

4. minimizes the sum of total square deviations changing the values of r_1 and r_2.

The approach suggested (and used in the reference papers) by Galimberti leads to obtain the reactivity ratios starting from the six triad distributions obtained *via* ^{1}H-NMR spectra and the copolymer composition; the number of the degrees of freedom is 28, thus maybe makes too much adaptable the model but it represents a way to carry out a numerical value describing the copolymers. So we decide to analyze our simulated results each graphically and numerically.

Compared to the reactivity ratios derived from experimental data, the two models suggest higher ratios than the experimental ones, especially for the r_1 (the parameter indicating how much the chain ending with an ethene prefers to react with an other ethene). We suspect the incongruence to derive from the overestimation of the E/P ratio in the chain. Apart from this, the ultimate model produces a more similar $r_1 r_2$ to the experiments so it seems to be the one that better describe the reality. The complete set of calculated ratios are reported in Table 5.8.

While the results in Figure 5.25, 5.26 and 5.27 were obtained assuming the absence of CI effects, the model could be more physically based assuming the presence of a *far*-coordinating barrier due to the counter ion itself. [167] The simulation of the ultimate and penultimate models were performed as before, the homotriad distributions PPP (Fig.5.28), EEE (Fig.5.29) and the E/P ratio in the chains vs. feed composition (Fig.5.30) being showed. We begin noting that the
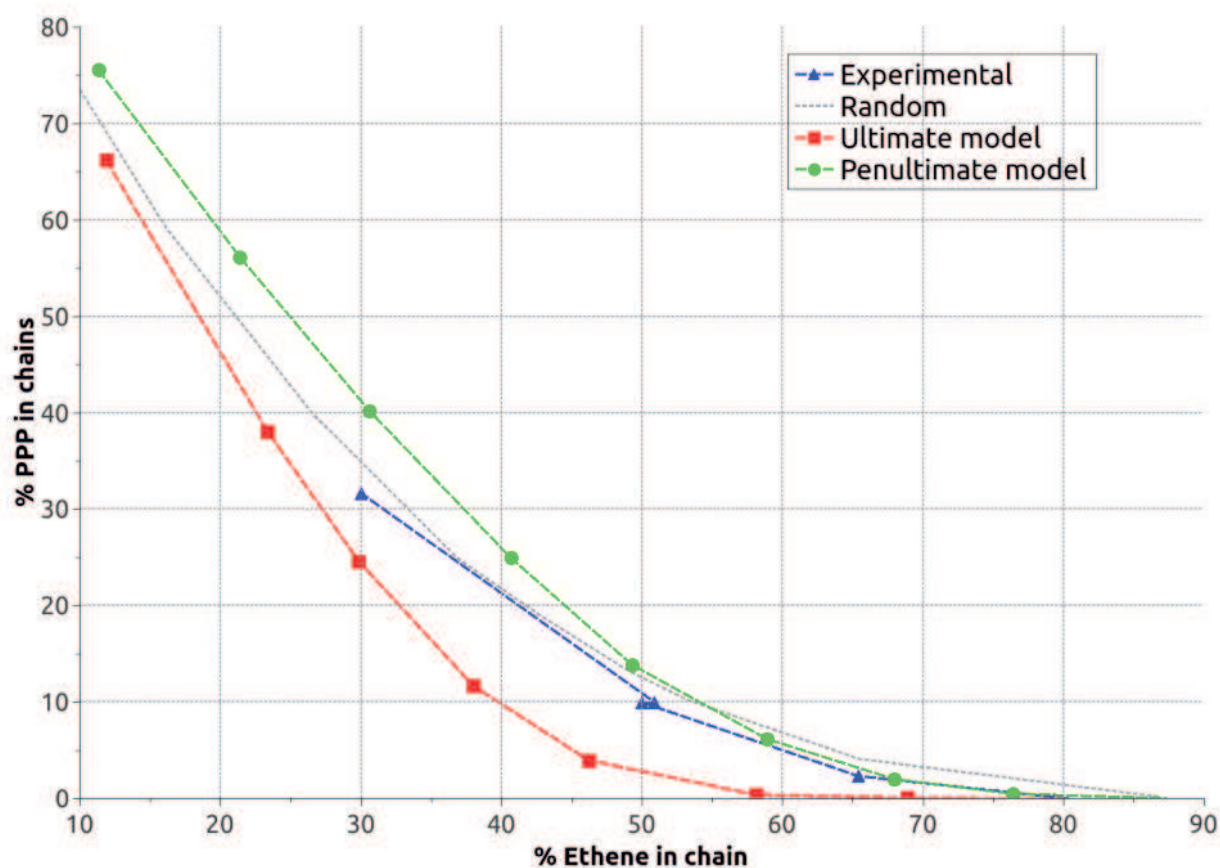
Figure 5.28: % PPP in the chains versus the % E/P in the chains for the system with Me$_2$C-Ind$_2$ZrCl$_2$ and CI effect on the *far*-coordination.

inclusion of the counter ion effect induces a substantial differentiation between the models. In particular, the ultimate model looses the agreement with the experimental data for all triad distributions and the composition dependence of chains while the penultimate model produces very good results. The agreement looks excellent for the EEE distributions and the E/P ratios vs. ethene in the feed, while the model is somewhat less accurate on the PPP triad for an ethene molar fraction lower than 0.5.

Once again, simulated data were statistically analyzed in order to extract r_1 and r_2 values as mentioned before, the results being reported in Table 5.9. From the quantitative point of view, the penultimate model with the counter ion effect on *far*-coordination is the one agreeing best with the experimental reactivity ratios. Such result spurs several remarks: the penultimate monomer on the growing chain seems to have an important effect on the chain's microstructure, influencing directly the preference toward monomers. Moreover, the presence of counter ion

Figure 5.29: % EEE in the chains versus the % E/P in the chains for the system with Me_2C-Ind_2ZrCl_2 and CI effect on the *far*-coordination.

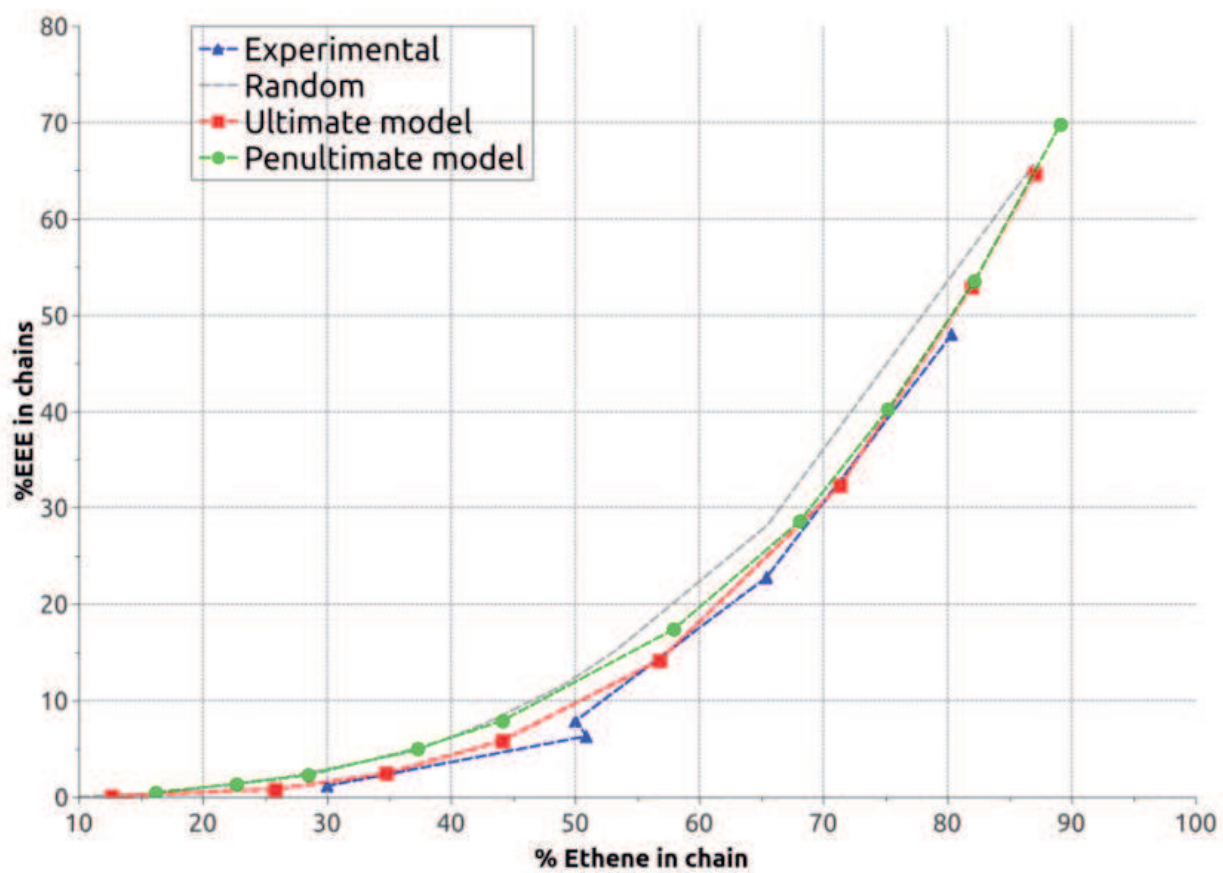Figure 5.30: % E/P in the chains versus the % E/P in the feed for the system with Me$_2$C-Ind$_2$ZrCl$_2$ and CI effect on the *far*-coordination.

	r_1	r_2	$r_1 r_2$
ultimate model	3.11	0.02	0.06
penultimate model	2.56	0.28	0.73
experimental data	2.30 ± 0.19	0.21 ± 0.02	0.48 ± 0.09

Table 5.9: Reactivity ratios for the catalyst $Me_2C\text{-}Ind_2ZrCl_2$ with *far*-counterion hindrance.

seems to be important for a good success of the simulations. This evidences underline the importance of the counter ion during the process of copolymerization.

5.3.5   rac-Me_2C-(3-^{t}Bu-Ind)$_2$ZrCl$_2$ Catalyst

In simulating the $Me_2C-(3-{}^tBu-Ind)_2ZrCl_2$ catalyst, we aimed at evaluating the effect of steric hindrance due to the *t*-Bu groups on the indenyles. Again, two possible *far*-coordination barriers' origin were simulated, due to the diffusion control or to the counter ion presence. Applying the *Stokes-Einstein-Sutherland equation* [268] and the *Solc-Stockmayer theory* [266–268], barriers of 3.85 kcal/-mol for ethene and 3.97 kcal/mol for propene were calculated, the counter ion presence is assumed to induce the same barrier than before (10.6 kcal/mol). We focus on the latter case as the usage of diffusion barriers in the models led the to insertion only of the ethene, providing homopolymers; propene insertion being observed only if its molar fraction is more than 0.99.

With the latter comment in mind, it accounts that the counter ion presence affects the model in a significant way, leading the simulation toward interesting results: with experimental data revealing a blocky nature of the resulting copolymers, the simulations seems to reproduce the experimental indications fairly well. In fact, comparing the homotriads EEE and PPP highlights similar results for the simulated and experimental triad distributions (Fig.5.31 for PPP triads and Fig.5.32 for EEE triads). The EEE distribution is a bit overestimated while the agreement for PPP triads is better. The quality of results decreases when the chain compositions are compared: as it possible to see in Figure 5.33, the model overestimates the preference toward ethene with respect to the experimentally detected chain composition; consequently, reactivity ratios' estimation will be
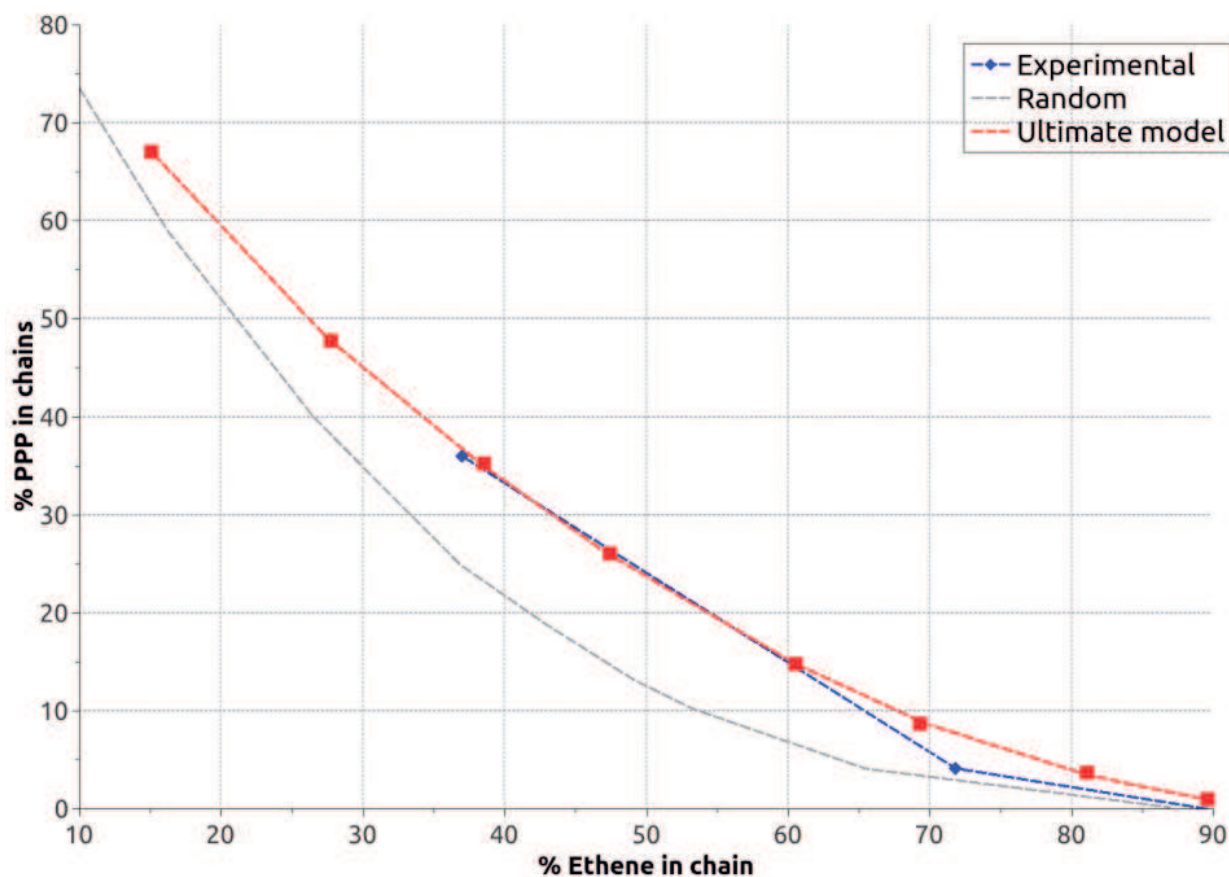
Figure 5.31: % PPP in the chains versus the % E/P in the chains for the system with Me_2C-$(3\text{-}{}^tBu\text{-}Ind)_2ZrCl_2$ and the CI effect on the *far*-coordination.

deeply affected from this discrepancy.

The $Me_2C-(3-{}^tBu-Ind)_2ZrCl_2$ catalyst is simulated only *via* ultimate model because of the penultimate model does not have complete DFT energetic picture. The following step will be the conclusion of DFT barriers' calculations and then the penultimate model simulations.

Despite the partial results, we can suggest a few conclusions: the influence of the counter ion in this case seems to be more important than the other catalyst, *de facto*, the simulation of the process with diffusion control on *far*-coordination not providing any copolymer chains. Instead, the simulations including the effect of the counter ion on the coordination barrier provide good results, especially for the E/P microstructure composition; unfortunately, the incongruity between simulated and experimental data about the composition of chains and solution feed is clear, i.e. the model tends to insert more ethene than experimentally
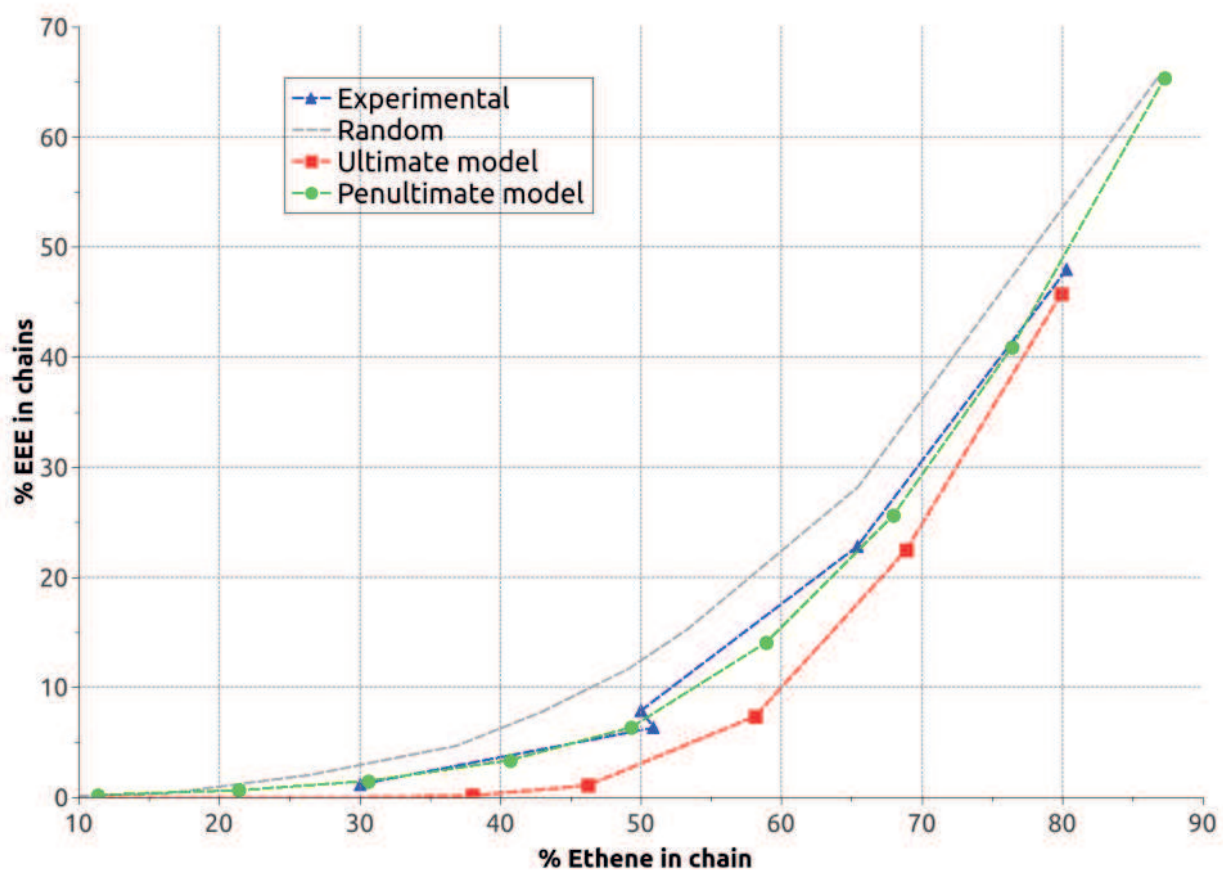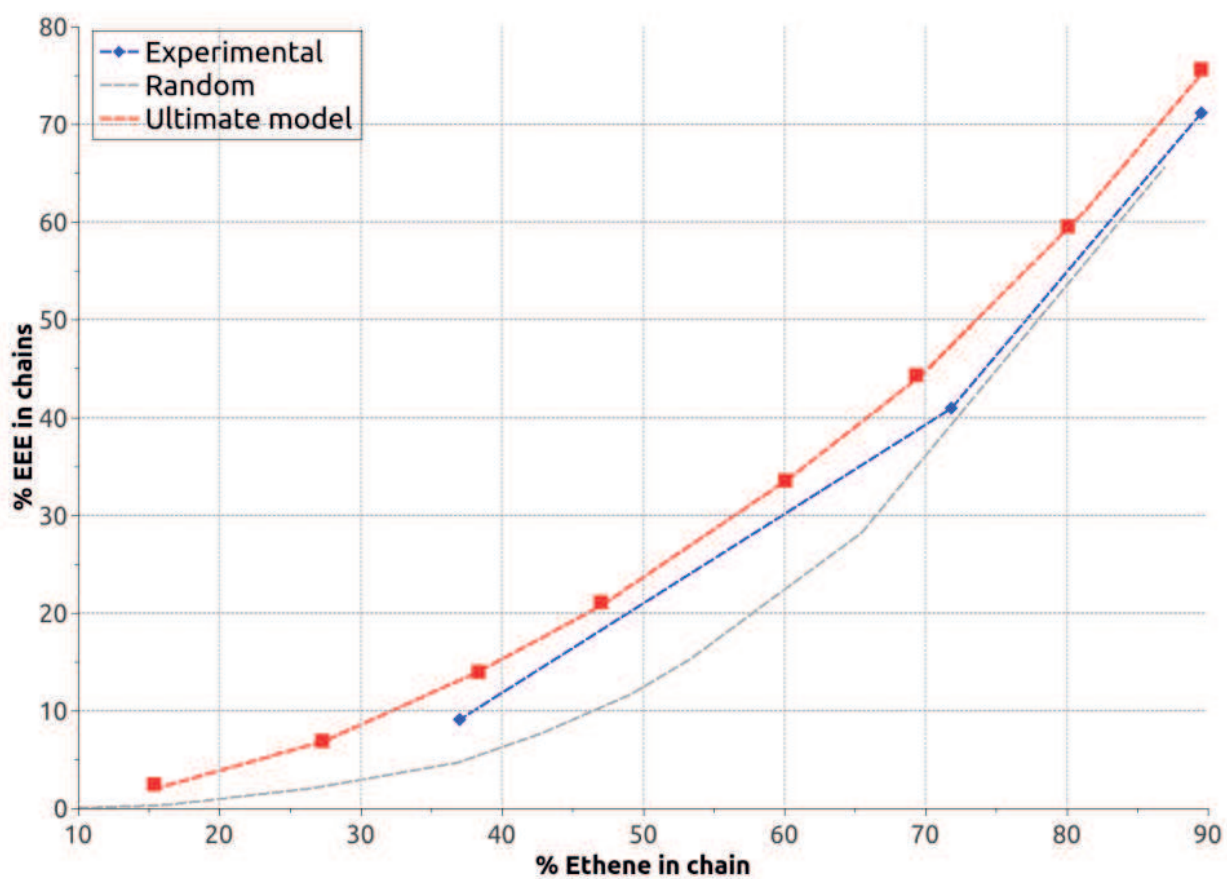
Figure 5.32: % EEE in the chains versus the % E/P in the chains for the system with Me$_2$C-(3-^{t}Bu-Ind)$_2$ZrCl$_2$ and the CI effect on the *far*-coordination.
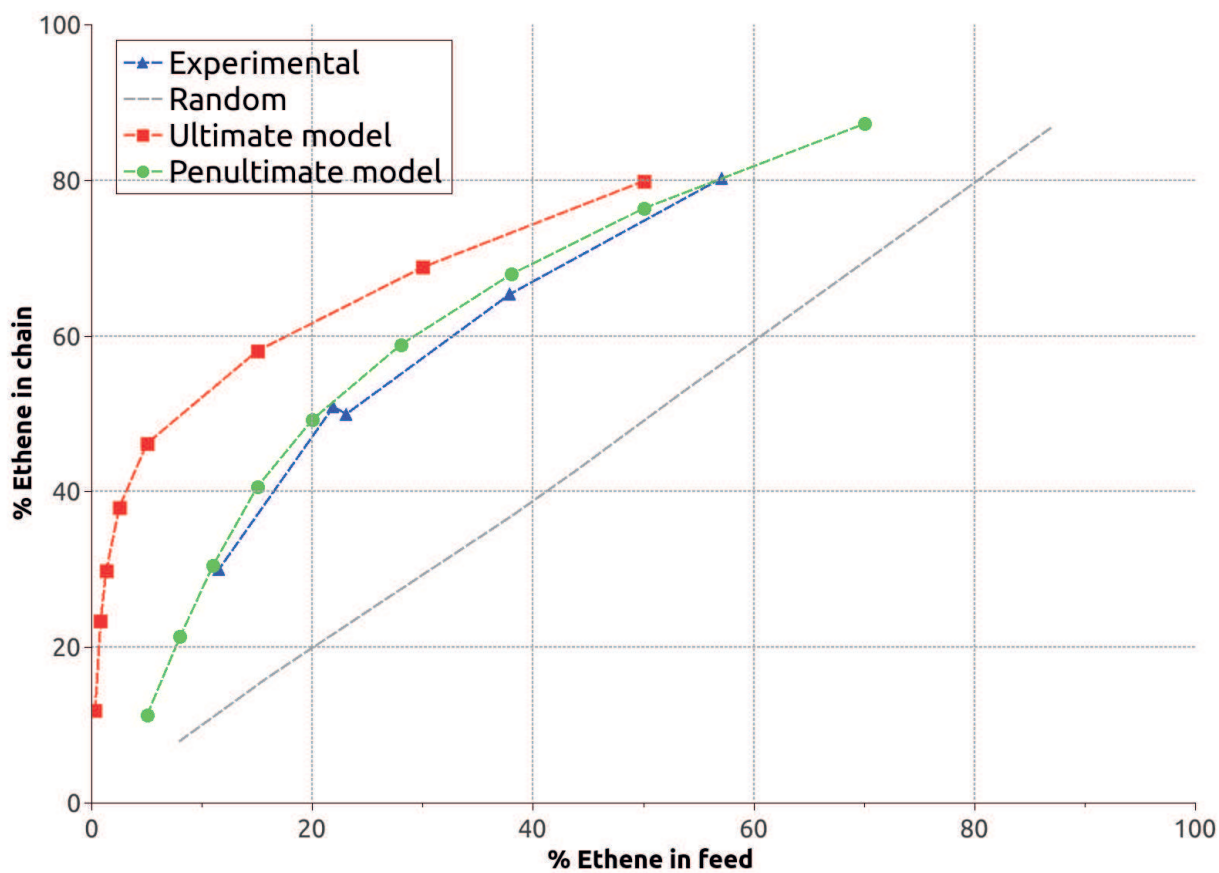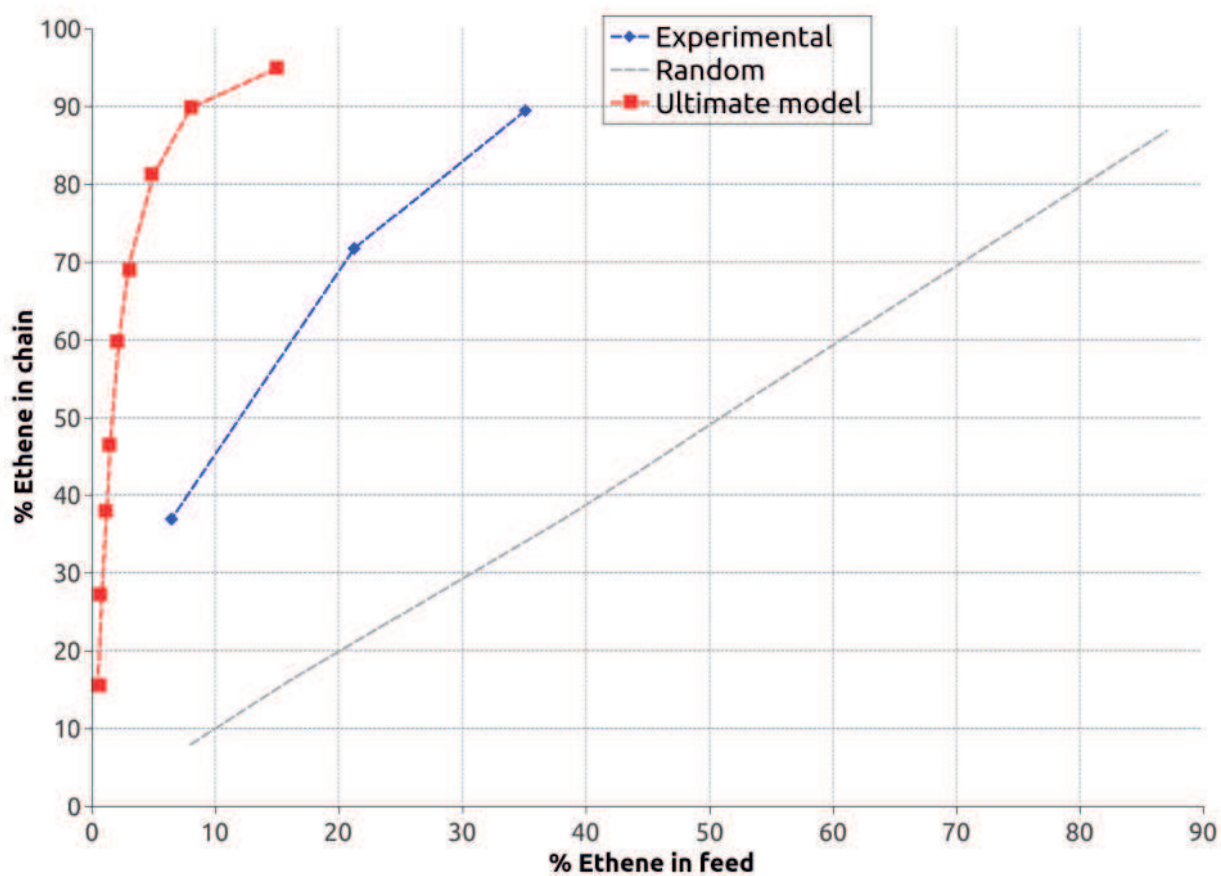
Figure 5.33: % E/P in the chains versus the % E/P in the feed for the system with Me$_2$C-(3-^{t}Bu-Ind)$_2$ZrCl$_2$ and the CI effect on the *far*-coordination.

reactions. Such disagreement leads to a wrong calculation of the reactivity ratios, as in their calculations we have to take into account the E/P chain's composition too. This notwithstanding, the first results appear promising because they were obtained with an approximated input data set, having two approximated insertion barriers and a qualitative estimation of the coordination barriers.

5.4 Conclusions

In this work, we employed a synergistic kMC-DFT approach to elucidate the importance of several effect that influence the copolymerization process, with the aim to find a way for the prediction of copolymer's micrustructure. First, we studied the atomic-transfer radical-polymerization of MMA and DMAEMA: by means of DFT calculation, we carried out the minima and the transition states involved in the reaction of propagation and their related energy barriers; then, such barriers were employed into a kinetic Monte Carlo code, taking into account the partition effect in solution *via* the *bootstrap model* and the variation of the feed composition during the simulation. As result, simulating the copolymerization with several couple of reactivity ratios showed us which theoretical model had the best agreement with experimental fitted r and brought to light the existence of a partition effect. The reactivity ratios obtained *via* experimental data fitting were then used in order to carry out the copolymer microstructure and the relative triad's distributions along the chain: the latter simulations showed the gradient nature of the copolymer and carried out useful indication about the way how the triads' distribution change along the chain. The aforementioned method can help experimental chemists in the rationalization of the chemical behavior of MMA/DMAEMA materials, "in lieu" of the lacking NMR data.

The second studied system was homogeneous catalyze copolymerization of ethene and propene. We computed the electronic structures of two C2-symmetric catalysts complexes, considering all the possible combination between the monomers, the ultimate monomers and the penultimate monomers in the chain. A kMC code allowed us to simulate different kind of models evaluating the effect of several contribution on the final microstructure, such as the steric hindrance of the catalyst, the penultimate effect and the influence of the counter ion. Albeit the

models are not well characterized at all, first evidence suggest that the presence of the counter ion is mandatory for a good description of the copolymerization; moreover, when the catalyst has not bulky groups, the penultimate monomer on the chain seems to have an important rule, leading the selectivity toward the monomers on the right direction. These results open the way to a new theoretical protocol that could give useful informations about the microstructure of the copolymers, trying to achieve the goal of a method able to predict the product of a copolymerization.

Chapter 6

Conclusions

The thesis showed how *ab initio* and DFT quantum chemical methods can be useful toward the interpretation and the prediction of chemical properties and reactivities. Well know post-Hartree-Fock quantum chemical methods and stochastic simulation approaches are intermixed, the synergy between them providing all the tools needed to evaluate the impact and validity of reaction mechanisms, for instance helping to rationalize radical and homogeneously catalyzed copolymerizations. The potentially positive impact that theoretical chemistry can have in those contexts was exploited to put the basis of new theoretical protocols able to predict the chemical features, that is still an attractive goal in academic and industrial field.

The first study regarded an example of how theoretical chemistry can provide information otherwise not achievable from experimental measurement. Specifically, by means of *ab initio* perturbation theory, we studied novel anion receptors acting *via* hydrogen-bonding and halogen-bonding: UV-Vis and ^{1}H-NMR titration showed that Iodine on the target receptor enhance the anion binding tendencies and X-ray structures evidenced the formation of halogen-bonding. The geometries in solution computed *via* MP2, however, revealed few possible conformers of the proposed molecules: theoretical energies allowed the calculation of the ion pair dissociation energy (IPDE) as a way to evaluate the affinity between the molecules and an anion. IPDE values gave the same trend of experimental affinity constants, confirming the experimental constant affinities; moreover, computed chemical shifts of conformers helped the interpretation of ^{1}H-NMR

titrations, giving the right importance at the HB and XB conformers in solution.

The second topic was the prediction of the antioxidant activity through a theoretical approach, that led to the benchmark of DFT methods. The in depth study of two prototype molecules, edaravone and quercetin, carried out the bond dissociation enthalpy (BDE), the ionization potential (IP) and the proton dissociation enthalpy (PDE); the examination of the cumulative mean absolute error on the three parameters, compared to CBS-Q3 reference values, indicate the most suitable methods (LC-ωPDE, M05-2X and M06-2X). Once the method was defined, we studied 15 antioxidant belonging to the flavonols family, computating BDE, IP, PDE, proton affinity (PA) and electron transfer enthalpy (ETE) in vacuum and in water; these theoretical parameters were then correlated individually to several experimental data set. Among all attempts, the best correlation was found with ETE in vacuum (showing a R^2=0.93 on 6 data set), that allows us to suppose that ETE is the theoretical parameter determining for prediction of antioxidant activity.

After the analysis about the properties of a single molecule, DFT was employed to rationalize the products of a chemical reaction. In particular, we studied the alkoxyhalogenation of alkynyl ureas and carbamates catalyzed by $CuCl_2$, with the final aim of defining the reactive step that influence the selectivity. First, we proposed a mechanism coherent with experimental product, characterizing all the minima and the transition states *via* DFT vibrational analysis. Studying in depth the equilibria involved at the beginning of the reaction, we characterized the two tautomers and two coordination site of $CuCl_2$, the C-C triple bond and the heteroatom; moreover, we described the formation of dimers between two urea and the catalyst. Dimers' stabilization plus the comparison of the energy paths led to expect the production of the 5-exo-O product, in total accord with experiments. Successively, we attempt to apply the same mechanism on two carbamates, following the same approach than before. The results however rationalize only partially the experiments, in fact, for the phenyl-N-carbamate we observe a strong kinetic competition between two paths, at the same time the experiments carry out a mixture of products; instead, the reaction on tosyl-N-carbamate experimentally leads to a single product, while the theoretical investigation is not able to dis-

criminate between two different products.

In the last Chapter we aimed higher, trying to predict the copolymer features boosting the DFT method with stochastic simulations; the ability to predict the microstructure of a copolymer would be a great help during the design process and the set up of a catalyzed copolymerization. In this regards, we decided to study the copolymerization of methyl methacrylate (MMA) and 2-(dimethylamino)ethyl methacrylate (DMAEMA) obtained *via* atomic-transfer radical-polymerization (ATRP), since the macroscopic properties used in biological fields are strictly related to the microscopic structure. Here we proposed a synergistic DFT/kinetic Monte Carlo approach: by means of DFT, we computed the energies of monomers, dimers and transition states, thanks to which we calculated the reactivity ratios r_1 and r_2; employing the DFT data, we wrote a kMC code that, treating the copolymerization as a Markov chain, carried out the chains' microstructure, the distributions of monomers, diads and triads along the chains. The results give indication about the presence of a preferential partitioning of one of the two monomers close to each one of the two radicals, known as bootstrap effect. Moreover, the triad distributions along the chain reveal the gradient nature of the copolymer, suggesting different features of the chains at the proximity of the core of PEG and at the end, influencing directly the behavior of the materials in solution. Then, our attention moved on the homogeneous-catalyzed copolymerization. The aim of the investigation pointed the attention on the characterization of copolymerization mechanism and on the effect of penultimate monomers and the counter ion on the reactivity. The synergistic DFT-kMC approach was applied on the ethene/propene copolymerization catalyzed by two C2-symmetric catalyst, carrying out several interesting results; among all simulated systems, we reproduced the experimental data only taking into account specific features. In order to obtain results close to the experiments, the model has to include: the presence of two coordination sites, both giving active paths for the insertion, the coordination preequilibrium as well-defined step, the influence of the counter ion on the coordination barriers. These claim underline the importance of several aspect generally overlooked during the copolymerization; moreover, the ability to reproduce the experimental results can open the way to a theoretical model able to predict the product of a homogeneous catalyzed

copolymerization.

To conclude, the thesis explore several chemical field in which *ab initio*-DFT methods can result a powerful tool to integrate the experimental results regarding the molecular properties, to understand the reaction mechanism or even try to predict the result of a copolymerization. Further work must be done to complete the presented results, among which:

- statistically proving the DFT methods for the prediction of the antioxidant activity (Chapter 3), adding more couple of experimental/theoretical data;

- supplementary investigation about the Cu-catalyzed reaction (Chapter 4), such as the computation of different starting carbamates;

- increasing the complexity of the copolymerization models (Chapter 5), considering new preequilibria involving the ligands, the catalyst and the monomers in the ATRcoP; about the homogeneous copolymerizations, the investigation of transition states for the "penultimate effect" must be completed, in addition to a more detailed characterization of the counterion behavior.

Appendix A

kMC Radical-BSE Model Code

```fortran
program kMC ATRP
implicit none
real*8 DG(4),T,r,rnd,molarfracpoli,xA,pAA,pMA,
.conv,stopdo,pfeed,polyfeed(1000000),stddev,fA,fM,inifM,
.Ka,Km,jj,kk,ll,mm,aMMM(10),aMMA(10),aAMA(10),aMAM(10),
.aAAM(10),aAAA(10),dist(10000),tMMM,tMMA,tAMA,tMAM,tAAM,
.tAAA,tottri,nn,ss,intr,errstd,mtMMM,mtMMA,mtAMA,mtMAM,
.mtAAM,mtAAA,stdMMM,stdMMA,stdAMA,stdMAM,stdAAM,stdAAA,eMMM,
.eMMA,eAMA,eMAM,eAAM,eAAA
real*8 fcorr(10000,6)
integer i,j,k,nA,nM,iseed,p,chains,q,z,kmax
character*1 ult(100000)
logical lpolyA,lpolyM,MMM,MMA,AMM,AMA,MAM,MAA,AAM,AAA

write(*,*) 'Write MMA/x feed in solution'
read(*,*) xA
write(*,*) 'Write the final total convertion in percentage'
read(*,*) conv
write(*,*) 'Write the number of chain to simulate (max 1Mln)'
read(*,*) chains
write(*,*) 'Write the copolymerization temperature'
read(*,*) T

T = 363.15
chains = 1000000
intr = (chains+0.d0)/(10.d0)

read(*,*) Ka !effective r_MMA, i.e. multiplied by the parti-
             tion coefficient
write(*,*) 'effective r_MMA',Ka
read(*,*) Km !effective r_DxAEMA, i.e. multiplied by the
             partition coefficient
write(*,*) 'effective r_DMAEMA',Km
```

```fortran
      open(12,file='polyfeed.data',status='new',access='append')

      iseed=time()
      call setrnd(iseed)

      jj  = 0
      kk  = 0
      ll  = 0
      mm  = 0
      nn  = 0
      ss  = 0
      z   = 1
      kmax = 0

      do i=1,10000
        dist(i) = 0.d0
        do j=1,6
           fcorr(i,j) = 0.d0
        enddo
      enddo

      do p=1,chains

      nA = 0
      nM = 0
      fA = 500
      inifM = fA/xA
      inifM = int(inifM)
      fM = inifM
      stopdo=0.0

      r = rnd()
      if (r.lt.(fA/(fA+fM))) then
        ult(1) = 'A'
        dist(1) = 1.d0
      else
        ult(1) = 'M'
      endif

      k = 2

20    continue

      PAA = 1.d0 - 1.d0/(Ka*fA/fM+1.d0)
      PMA = 1.d0/(Km*fM/fA+1.d0)

      lpolyA = (ult(k-1).eq.'A')
      lpolyM = (ult(k-1).eq.'M')

      if (lpolyA) then
```

```
 r= rnd ()
  if (r.lt .PAA) then
    ult (k) = 'A'
    dist (k) = dist (k) + 1.0
   nA = nA + 1
   fA = fA − 1
  else
    ult (k) = 'M'
   nM = nM + 1
   fM = fM − 1
  endif
 else
  r= rnd ()
   if (r.lt .PMA) then
    ult (k) = 'A'
    dist (k) = dist (k) + 1.0
    nA = nA + 1
    fA = fA −1
   else
    ult (k) = 'M'
   nM = nM + 1
   fM = fM −1
  endif
 endif


 stopdo = ((nM+nA)/( inifM +500))*100

 if (k.ge.3) then
  MMM = ( ult (k).eq. 'M' ).AND.( ult (k−1).eq. 'M' ).AND.
.( ult (k−2).eq. 'M')
 MMA = ( ult (k).eq. 'M' ).AND.( ult (k−1).eq. 'M' ).AND.
.( ult (k−2).eq. 'A')
 AMM = ( ult (k).eq. 'A' ).AND.( ult (k−1).eq. 'M' ).AND.
.( ult (k−2).eq. 'M')
 AMA = ( ult (k).eq. 'A' ).AND.( ult (k−1).eq. 'M' ).AND.
.( ult (k−2).eq. 'A')
 MAM = ( ult (k).eq. 'M' ).AND.( ult (k−1).eq. 'A' ).AND.
.( ult (k−2).eq. 'M')
 MAA = ( ult (k).eq. 'M' ).AND.( ult (k−1).eq. 'A' ).AND.
.( ult (k−2).eq. 'A')
 AAM = ( ult (k).eq. 'A' ).AND.( ult (k−1).eq. 'A' ).AND.
.( ult (k−2).eq. 'M')
 AAA = ( ult (k).eq. 'A' ).AND.( ult (k−1).eq. 'A' ).AND.
.( ult (k−2).eq. 'A')

 if (MMM) then
    jj = jj + 1
    fcorr (k−2,1) = fcorr (k−2,1) + 1.d0
  else if ((MMA).or .(AMM)) then
```

```fortran
        kk = kk + 1
        fcorr(k-2,2) = fcorr(k-2,2) + 1.d0
      else if (AMA) then
        ll = ll + 1
        fcorr(k-2,3) = fcorr(k-2,3) + 1.d0
      else if (MAM) then
       mm = mm + 1
        fcorr(k-2,4) = fcorr(k-2,4) + 1.d0
      else if ((MAA).or.(AAM)) then
       nn = nn + 1
        fcorr(k-2,5) = fcorr(k-2,5) + 1.d0
      else if (AAA) then
        ss = ss + 1
        fcorr(k-2,6) = fcorr(k-2,6) + 1.d0
     endif
    endif


    k = k + 1

    if (stopdo.lt.conv) goto 20
    if (kmax.lt.k) kmax = k

    polyfeed(p) = (nA+0.d0)/(nM+0.d0)
    write(12,105) polyfeed(p)

    if (mod(p,(chains/10)).eq.0) then
     write(*,104) (int(p/(chains/100)))
    aMMM(z) = jj
    aMMA(z) = kk
    aAMA(z) = ll
    aMAM(z) = mm
    aAAM(z) = nn
    aAAA(z) = ss
    if (p.ne.chains) then
     jj = 0.0
     kk = 0.0
     ll = 0.0
     mm = 0.0
     nn = 0.0
     ss = 0.0
    endif
    z = z + 1
    endif
    enddo
    close(12)

    tMMM = 0.d0
    tMMM = SUM(aMMM(1:10))
    tMMA = 0.d0
    tMMA = SUM(aMMA(1:10))
```

```fortran
      tAMA = 0.d0
      tAMA = SUM(aAMA(1:10))
      tMAM = 0.d0
      tMAM = SUM(aMAM(1:10))
      tAAM = 0.d0
      tAAM = SUM(aAAM(1:10))
      tAAA = 0.d0
      tAAA = SUM(aAAA(1:10))

      open(15,file='distribuzione',status='unknown')
      do i=1,kmax
        dist(i) = (dist(i)/(chains+0.d0))
        write(15,107) dist(i)
      enddo
      close(15)

      mtMMM = tMMM/10
      stdMMM = SQRT(SUM((aMMM(1:10)-mtMMM)**2)/9)
      mtMMA = tMMA/10
      stdMMA = SQRT(SUM((aMMA(1:10)-mtMMA)**2)/9)
      mtAMA = tAMA/10
      stdAMA = SQRT(SUM((aAMA(1:10)-mtAMA)**2)/9)
      mtMAM = tMAM/10
      stdMAM = SQRT(SUM((aMAM(1:10)-mtMAM)**2)/9)
      mtAAM = tAAM/10
      stdAAM = SQRT(SUM((aAAM(1:10)-mtAAM)**2)/9)
      mtAAA = tAAA/10
      stdAAA = SQRT(SUM((aAAA(1:10)-mtAAA)**2)/9)

      tottri = tMMM+tMMA+tAMA+tMAM+tAAM+tAAA

      tMMM = tMMM/tottri
      eMMM = stdMMM/sqrt(10.d0)/tottri
      tMMA = tMMA/tottri
      eMMA = stdMMA/sqrt(10.d0)/tottri
      tAMA = tAMA/tottri
      eAMA = stdAMA/sqrt(10.d0)/tottri
      tMAM = tMAM/tottri
      eMAM = stdMAM/sqrt(10.d0)/tottri
      tAAM = tAAM/tottri
      eAAM = stdAAM/sqrt(10.d0)/tottri
      tAAA = tAAA/tottri
      eAAA = stdAAA/sqrt(10.d0)/tottri

      write(*,*) 'sterr:',eMMM,eMAM,eAAA

      open(16,file='fcorr.dat',status='unknown')
      open(17,file='fcorr_l.dat',status='unknown')
      write(16,*) '# 1=MMM 2=MMA 3=AMA 4=MAM 5=MAA 6=AAA'
      write(17,*) '# 1=MMM 2=MMA 3=AMA 4=MAM 5=MAA 6=AAA'
```

```fortran
      do  i=1,kmax-2
         do  j=1,6
            write(16,*) i,j,fcorr(i,j)/tottri
         enddo
         write(16,*)
         write(17,*) i,(fcorr(i,j)/chains,j=1,6)
      enddo
      close(16)
      close(17)

      pfeed = SUM(polyfeed(1:chains))/chains
      stddev = SQRT(SUM((polyfeed(1:chains)-pfeed)**2)/chains)
      errstd = stddev/(SQRT(chains-1.d0))
      molarfracpoli=(nA + 0.d0)/(nA + nM)
      open(8,file='chain.poly',status='unknown')
      write(8,102) T,xA,molarfracpoli
      write(8,101) (ult(k),k=1,kmax)
      close(8)

      write(*,103) pfeed,stddev,errstd
      write(*,108) tMMM,eMMM,tMMA,eMMA,tAMA,eAMA,tMAM,eMAM,tAAM,eAAM,
     .tAAA,eAAA

101   format(10000A1)
102   format('Temperatura ',F6.2,' x MMA in soluzione ',F5.3,' x
     .MMA in polimero = ',F8.4)
103   format('Feed A/M nel polimero =',F8.4,' standard dev =',F8.4,
     .' err std =',F8.4)
104   format('Avanzamento:',I3,'%')
105   format(F11.8)
107   format(F8.4)
108   format('MMM ',F7.5,'+-',F7.5,' MMA ',F7.5,'+-',F7.5,' AMA ',F7.5,
     .'+-',F7.5,' MAM ',F7.5,'+-',F7.5,' AAM ',F7.5,'+-',F7.5,
     .' AAA ',F7.5,'+-',F7.5)

      end




****************** Random number generator ********************

      double precision function rnd()
      common /mz/ is,js,ks,ns
      save /mz/
      mzran = is - ks
      if (mzran .lt. 0) then
       mzran = mzran +  2147483579
      endif
      is = js
      js = ks
      ks = mzran
```

```
      ns = 69069*ns + 1013904243
      mzran = mzran + ns
      rnd = 0.5d0 + mzran/2.d0**32
      return
      end
      block data
      common /mz/ is ,js ,ks ,ns
      save /mz/
      data is ,js ,ks ,ns/521288629,362436069,16163801,1131199299/
      end
* * *
      subroutine setrnd(iseed)
      common /mz/ is ,js ,ks ,ns
      save /mz/
      ns = 1 + IABS(iseed)
      return
      end
```

Appendix B

kMC Ultimate Model Code

```fortran
      program kMC ultimate E/P
      implicit none
      real*8 EE(7,7),EP(7,7),PE(7,7),PP(7,7),molarfrac,
     .T,r,rnd,molarfracpoli,m
      integer i,j,k,ne,np,iseed
      character*1 ult(100000),E,P
      logical insertion,false,true,lEE,lPP,lEP,lPE

      write(*,*) 'Insert the copolymerization temperature.
     . and the molar fraction in ethene of feed'
      read(*,*) T,molarfrac

********** matrix reading with activation energies ******

      open(7,file='kinetic_ultimate',status='old')
      do i=1,4
       read(7,*) (EE(i,j),j=1,5)
         do j=1,5
          EE(i,j)=exp(-(EE(i,j)*1000)/(1.987*T))
         enddo
      enddo
      do i=1,4
       read(7,*) (EP(i,j),j=1,5)
         do j=1,5
          EP(i,j)=exp(-(EP(i,j)*1000)/(1.987*T))
         enddo
      enddo
      do i=1,4
       read(7,*) (PE(i,j),j=1,5)
         do j=1,5
          PE(i,j)=exp(-(PE(i,j)*1000)/(1.987*T))
       enddo
      enddo
      do i=1,4
       read(7,*) (PP(i,j),j=1,5)
```

```fortran
        do j=1,5
          PP(i,j)=exp(-(PP(i,j)*1000)/(1.987*T))
        enddo
      enddo
      continue
      close(7)


****************** end matrix reading ********************
********* insertion sequence by penultimate effect **********

      open(11,file='chain_column',status='new',access='append')

      iseed=time()
      call setrnd(iseed)
      true=.TRUE.
      false=.FALSE.
      ult(1) = 'E'
      ne = 0
      np = 0

      do k=2,10000

40    m = rnd()

      lEE = (m.lt.molarfrac).and.(ult(k-1).eq.'E')
      lEP = (m.lt.molarfrac).and.(ult(k-1).eq.'P')
      lPE = (m.gt.molarfrac).and.(ult(k-1).eq.'E')
      lPP = (m.gt.molarfrac).and.(ult(k-1).eq.'P')

      if (lEE) then
        call statejump(EE,insertion)
        if (insertion.eqv.true) then
          ult(k) = 'E'
          ne = ne + 1
        endif
      else if (lEP) then
        call statejump(EP,insertion)
        if (insertion.eqv.true) then
          ult(k) = 'E'
          ne = ne + 1
        endif
      else if (lPE) then
        call statejump(PE,insertion)
        if (insertion.eqv.true) then
          ult(k) = 'P'
          np = np + 1
        endif
      else if (lPP) then
        call statejump(PP,insertion)
        if (insertion.eqv.true) then
```

```fortran
          ult(k) = 'P'
           np = np + 1
         endif
       endif
       if (insertion.eqv.false) goto 40

       write(11,*) ult(k)
       enddo

       close(11)

       molarfracpoli = (ne + 0.d0 )/(ne + np)
       open(8,file='chain.poly',status='new')
       write(8,102) T,molarfrac,molarfracpoli
       write(8,101) (ult(k),k=1,10000)

       close(8)
       write(*,*) molarfracpoli
101    format(10000A1)
102    format('Temperature ',F6.2,' x Ethene in feed ',F5.3,
      .' x Ethene in polymer = ',F8.4)

       end
```

`*************** Random number generator  ********************`

```fortran
       double precision function rnd()
       common /mz/ is,js,ks,ns
       save /mz/
       mzran = is - ks
       if (mzran .lt. 0) then
        mzran = mzran +  2147483579
       endif
       is = js
       js = ks
       ks = mzran
       ns = 69069*ns + 1013904243
       mzran = mzran + ns
       rnd = 0.5d0 + mzran/2.d0**32
       return
       end
       block data
       common /mz/ is,js,ks,ns
       save /mz/
       data is,js,ks,ns/521288629,362436069,16163801,1131199299/
       end
```
`* * *`
```fortran
       subroutine setrnd(iseed)
       common /mz/ is,js,ks,ns
       save /mz/
```

```fortran
      ns = 1 + IABS(iseed)
      return
      end
```

*********** State evolution probabilities calculation *************

```fortran
      subroutine statejump(MU, insertion)
      implicit none
      real*8 MU(7,7),r,rnd
      logical insertion

      r = rnd()
      if (r.lt.(MU(1,2)/(MU(1,2)+MU(1,4)))) then
       r = rnd()
       if (r.lt.(MU(2,1)/(MU(2,1)+MU(2,3)))) then
         insertion = .FALSE.
        elseif (r.gt.(MU(2,1)/(MU(2,1)+MU(2,3)))) then
         insertion = .TRUE.
       endif
      elseif (r.gt.(MU(1,2)/(MU(1,2)+MU(1,4)))) then
       r = rnd()
       if (r.lt.(MU(4,1)/(MU(4,1)+MU(4,5)))) then
         insertion= .FALSE.
        elseif (r.gt.(MU(4,1)/(MU(4,1)+MU(4,5)))) then
         insertion = .TRUE.
       endif
      endif

109   continue
      return
      end
```

Appendix C

kMC Penultimate Model Code

```fortran
      program kMC penultimate E/P
      implicit none
      real*8 EEEm(7,7),EPEm(7,7),PEEm(7,7),PPEm(7,7),EEPm(7,7),
     .EPPm(7,7),PEPm(7,7),PPPm(7,7),molarfrac,T,r,rnd,MU(7,7),
     .molarfracpoli
      integer i,j,k,ne,np,iseed
      character*1 ult(100000),E,P
      logical insertion,false,true,EEE,EPE,PEE,PPE,EEP,EPP,PEP,
     .PPP

      write(*,*) 'Insert the copolymerization temperature.
     . and the molar fraction in ethene of feed'
      read(*,*) T,molarfrac

********** matrix reading with activation energies ******

      open(7,file='kinetic_penultimate',status='old')
      do i=1,4
          read(7,*) (EEEm(i,j),j=1,5)
              do j=1,5
                  EEEm(i,j)=exp(-(EEEm(i,j)*1000)/(1.987*T))
              enddo
      enddo
      do i=1,4
          read(7,*) (EPEm(i,j),j=1,5)
              do j=1,5
                  EPEm(i,j)=exp(-(EPEm(i,j)*1000)/(1.987*T))
              enddo
      enddo
      do i=1,4
          read(7,*) (PEEm(i,j),j=1,5)
              do j=1,5
                  PEEm(i,j)=exp(-(PEEm(i,j)*1000)/(1.987*T))
              enddo
```

167

```fortran
        enddo
        do  i=1,4
            read (7,*)  (PPEm( i , j ) , j =1,5)
                do  j=1,5
                    PPEm( i , j)=exp(−(PPEm( i , j )∗1000)/(1.987∗T))
                enddo
        enddo
        do  i=1,4
            read (7,*)  (EEPm( i , j ) , j =1,5)
                do  j=1,5
                    EEPm( i , j)=exp(−(EEPm( i , j )∗1000)/(1.987∗T))
                enddo
        enddo
        do  i=1,4
            read (7,*)  (EPPm( i , j ) , j =1,5)
                do  j=1,5
                    EPPm( i , j)=exp(−(EPPm( i , j )∗1000)/(1.987∗T))
                enddo
        enddo
        do  i=1,4
            read (7,*)  (PEPm( i , j ) , j =1,5)
                do  j=1,5
                    PEPm( i , j)=exp(−(PEPm( i , j )∗1000)/(1.987∗T))
                enddo
        enddo
        do  i=1,4
            read (7,*)  (PPPm( i , j ) , j =1,5)
                do  j=1,5
                    PPPm( i , j)=exp(−(PPPm( i , j )∗1000)/(1.987∗T))
                enddo
        enddo

9       continue
        close (7)

******************** end matrix reading ********************
********* insertion sequence by penultimate effect **********

        open(11 , file='chain_column ' , status='new ' , access='append ')

        iseed=time ()
        call setrnd ( iseed )
        true=.TRUE.
        false =.FALSE.
        ne = 0
        np = 0
        ult (1) = 'E'
        ult (2) = 'E'

        do k=3,10000
```

```
40      r = rnd()

        EEE = (r.lt.molarfrac).and.(ult(k−1).eq.'E').and
        .(ult(k−2).eq.'E')
        EPE = (r.lt.molarfrac).and.(ult(k−1).eq.'P').and
        .(ult(k−2).eq.'E')
        PEE = (r.gt.molarfrac).and.(ult(k−1).eq.'E').and
        .(ult(k−2).eq.'E')
        PPE = (r.gt.molarfrac).and.(ult(k−1).eq.'P').and
        .(ult(k−2).eq.'E')
        EEP = (r.lt.molarfrac).and.(ult(k−1).eq.'E').and
        .(ult(k−2).eq.'P')
        EPP = (r.lt.molarfrac).and.(ult(k−1).eq.'P').and
        .(ult(k−2).eq.'P')
        PEP = (r.gt.molarfrac).and.(ult(k−1).eq.'E').and
        .(ult(k−2).eq.'P')
        PPP = (r.gt.molarfrac).and.(ult(k−1).eq.'P').and
        .(ult(k−2).eq.'P')

        if (EEE) then
         call statejump(EEEm, insertion)
          if (insertion.eqv.true) then
           ult(k) = 'E'
           ne = ne + 1
          endif
         else if (EPE) then
          call statejump(EPEm, insertion)
           if (insertion.eqv.true) then
            ult(k) = 'E'
            ne = ne + 1
           endif
         else if (PEE) then
          call statejump(PEEm, insertion)
           if (insertion.eqv.true) then
            ult(k) = 'P'
            np = np + 1
           endif
         else if (PPE) then
          call statejump(PPEm, insertion)
           if (insertion.eqv.true) then
            ult(k) = 'P'
            np = np + 1
           endif
         else if (EEP) then
          call statejump(EEPm, insertion)
           if (insertion.eqv.true) then
            ult(k) = 'E'
            ne = ne + 1
           endif
```

```fortran
       else if (EPP) then
        call statejump(EPPm,insertion)
         if (insertion.eqv.true) then
          ult(k) = 'E'
          ne = ne + 1
         endif
       else if (PEP) then
        call statejump(PEPm,insertion)
         if (insertion.eqv.true) then
          ult(k) = 'P'
          np = np + 1
         endif
       elseif (PPP) then
        call statejump(PPPm,insertion)
         if (insertion.eqv.true) then
          ult(k) = 'P'
          np = np + 1
         endif
      endif

      if (insertion.eqv.false) goto 40

      write(11,*) ult(k)
      enddo
      close(11)

      molarfracpoli = (ne + 0.d0 )/( ne + np)

      open(8,file='penultimate.poly',status='new')
      write(8,102) T,molarfrac,molarfracpoli

      write(8,101) (ult(k),k=1,10000)

      close(8)
      write(*,*) molarfracpoli
101   format(10000A1)
102   format('Temperature ',F6.2,' x Ethene in feed ',F8.3,
     .' x Ethene in polymer ',F8.4)

      end
```

```
************** Random number generator ********************
```

```fortran
      double precision function rnd()
      common /mz/ is,js,ks,ns
      save /mz/
      mzran = is - ks
      if (mzran.lt.0) then
        mzran = mzran + 2147483579
      endif
```

```
      is = js
      js = ks
      ks = mzran
      ns = 69069*ns + 1013904243
      mzran = mzran + ns
      rnd = 0.5d0 + mzran/2.d0**32
      return
      end


      block data
      common /mz/ is ,js ,ks ,ns
      save /mz/
      data is ,js ,ks ,ns/521288629,362436069,16163801,1131199299/
      end


      subroutine setrnd(iseed)
      common /mz/ is ,js ,ks ,ns
      save /mz/
      ns = 1 + IABS(iseed)
      return
      end
```

******** State evolution probabilities calculation **********

```
      subroutine statejump(MU, insertion)
      implicit none
      real*8 MU(7 ,7) ,r ,rnd
      logical insertion

      r = rnd()
      if (r.lt .(MU(1 ,2)/(MU(1 ,2)+MU(1 ,4)))) then
       r = rnd()
        if (r.lt .(MU(2 ,1)/(MU(2 ,1)+MU(2 ,3)))) then
          insertion = .FALSE.
         elseif (r.gt .(MU(2 ,1)/(MU(2 ,1)+MU(2 ,3)))) then
          insertion = .TRUE.
        endif
      elseif (r.gt .(MU(1 ,2)/(MU(1 ,2)+MU(1 ,4)))) then
104    r = rnd()
        if (r.lt .(MU(4 ,1)/(MU(4 ,1)+MU(4 ,5)))) then
          insertion= .FALSE.
         elseif (r.gt .(MU(4 ,1)/(MU(4 ,1)+MU(4 ,5)))) then
          insertion = .TRUE.
        endif
      endif


109    continue
      return
      end
```

Bibliography

[1] E. Schrödinger, *Physical Review* **1926**, 1049–1970. 1

[2] W. Pauli, *Zeitschrift fur Physik* **1925**, 765–783. 1

[3] P. A. M. Dirac, *Proceeding of the Royal Society of London A* **1926**, 661–677. 1

[4] W. K. Heisenberg, *Physical Review* **1926**, 411–426. 1

[5] J. C. Slater, *Physical Review* **1929**, 1293–1322. 1

[6] T. Tsuneda, *Density Functional Theory in Quantum Chemistry*, Springer Japan, **2014**. 2

[7] C. Møller, M. S. Plesset, *Physical Review* **1934**, *46*, 618–622. 2, 64

[8] T. Helgaker, P. Jorgensen, J. Olsen, *Molecular Electronic Structure Theory*, Wiley, **2000**. 2

[9] V. Amendola, G. Bergamaschi, M. Boiocchi, N. Fusco, M. V. La Rocca, L. Linati, E. Lo Presti, M. Mella, P. Metrangolo, A. Miljkovic, *RSC Advances* **2016**, *6*, 67540–67549. 2, 8

[10] M. V. La Rocca, M. Rutkowski, S. Ringeissen, J. Gomar, M.-C. Frantz, S. Ngom, C. Adamo, *Journal of Molecular Modeling* **2016**, *22*, 250. 4

[11] M. R. Marcelin in *Annales de Physique*, EDP Sciences, pp. 120–231. 5, 82

[12] E. Wigner, *Zeitschrift für Physikalische Chemie* **1932**, *19*, 203–216. 5, 82

[13] H. Eyring, *The Journal of Chemical Physics* **1935**, *3*, 107–115. 5, 82, 89

[14] M. Massimo, L. R. M. Vincenzo, M. Ylenia, I. Lorella, *Journal of Polymer Science Part A: Polymer Chemistry* **2018**, *56*, 1366–1382. 5

[15] N. Busschaert, C. Caltagirone, W. Van Rossom, P. Gale, *Chemical Reviews* **2015**, *115*, 8038–8155, cited By 225. 7

[16] P. Gale, C. Caltagirone, *Chemical Society Reviews* **2015**, *44*, 4212–4227, cited By 130. 7

[17] M. Giese, M. Albrecht, K. Rissanen, *Chemical Reviews* **2015**, *115*, 8867–8895, cited By 47. 7

[18] V. Blazek Bregovic, N. Basaric, K. Mlinaric-Majerski, *Coordination Chemistry Reviews* **2015**, *295*, 80–124, cited By 48. 7

[19] I. Saha, J. Lee, C.-H. Lee, *European Journal of Organic Chemistry* **2015**, *2015*, 3859–3885, cited By 21. 7

[20] R. Elmes, K. Jolliffe, *Chemical Communications* **2015**, *51*, 4951–4968, cited By 30. 7

[21] K.-C. Chang, S.-S. Sun, M. Odago, A. Lees, *Coordination Chemistry Reviews* **2015**, *284*, 111–123, cited By 40. 7

[22] E. Graf, J.-M. Lehn, *Journal of the American Chemical Society* **1976**, *98*, 6403–6405, cited By 202. 7

[23] J.-M. Lehn, *Accounts of Chemical Research* **1978**, *11*, 49–57, cited By 732. 7

[24] J. Sessler, P. Gale, W. Cho, *Anion Receptor Chemistry*, RSC Publishing, **2006**. 7

[25] K. Bowman-James, A. Bianchi, E. Garcia-España, *Anion Coordination Chemistry*, John Wiley & Sons, New York, **2011**. 7

[26] J. Cai, J. Sessler, *Chemical Society Reviews* **2014**, *43*, 6198–6213, cited By 82. 7

[27] P. Metrangolo, H. Neukirch, T. Pilati, G. Resnati, *Accounts of Chemical Research* **2005**, *38*, 386–395, cited By 1262. 8

[28] P. Metrangolo, F. Meyer, T. Pilati, G. Resnati, G. Terraneo, *Angewandte Chemie - International Edition* **2008**, *47*, 6114–6127, cited By 919. 8

[29] G. Cavallo, P. Metrangolo, T. Pilati, G. Resnati, M. Sansotera, G. Terraneo, *Chemical Society Reviews* **2010**, *39*, 3772–3783, cited By 282. 8

[30] G. Cavallo, P. Metrangolo, R. Milani, T. Pilati, A. Priimagi, G. Resnati, G. Terraneo, *Chemical Reviews* **2016**, *116*, 2478–2601, cited By 322. 8

[31] M. Langton, P. Beer, *Accounts of Chemical Research* **2014**, *47*, 1935–1949, cited By 89. 8

[32] M. Chudzinski, C. McClary, M. Taylor, *Journal of the American Chemical Society* **2011**, *133*, 10559–10567, cited By 199. 8

[33] S. Walter, F. Kniep, L. Rout, F. Schmidtchen, E. Herdtweck, S. Huber, *Journal of the American Chemical Society* **2012**, *134*, 8507–8512, cited By 72. 8

[34] A. Vargas Jentzsch, A. Hennig, J. Mareda, S. Matile, *Accounts of Chemical Research* **2013**, *46*, 2791–2800, cited By 106. 8

[35] B. Schulze, U. Schubert, *Chemical Society Reviews* **2014**, *43*, 2522–2571, cited By 236. 8

[36] R. Tepper, B. Schulze, M. Jäger, C. Friebe, D. Scharf, H. Görls, U. Schubert, *Journal of Organic Chemistry* **2015**, *80*, 3139–3150, cited By 35. 8

[37] S. Chakraborty, R. Dutta, P. Ghosh, *Chemical Communications* **2015**, *51*, 14793–14796, cited By 11. 8

[38] H. Takezawa, T. Murase, G. Resnati, P. Metrangolo, M. Fujita, *Angewandte Chemie - International Edition* **2015**, *54*, 8411–8414, cited By 18. 8

[39] G. Jeffrey, W. Saenger, *Hydrogen Bonding in Biological Structures* **1991**, cited By 3882. 8

[40] G. Cavallo, P. Metrangolo, T. Pilati, G. Resnati, G. Terraneo, *Crystal Growth and Design* **2014**, *14*, 2697–2702, cited By 26. 8

[41] G. Desiraju, P. Shing Ho, L. Kloo, A. Legon, R. Marquardt, P. Metrangolo, P. Politzer, G. Resnati, K. Rissanen, *Pure and Applied Chemistry* **2013**, *85*, 1711–1713, cited By 392. 8

[42] A. Karpfen, *Structure and Bonding* **2008**, *126*, 1–15, cited By 40. 8

[43] M. Fourmigué, *Current Opinion in Solid State and Materials Science* **2009**, *13*, 36–45, cited By 195. 8

[44] B. Nepal, S. Scheiner, *Journal of Physical Chemistry A* **2015**, *119*, 13064–13073, cited By 12. 8

[45] H. Wang, W. Wang, W. Jin, *Chemical Reviews* **2016**, *116*, 5072–5104, cited By 63. 8

[46] S. Cornes, C. Davies, D. Blyghton, M. Sambrook, P. Beer, *Organic and Biomolecular Chemistry* **2015**, *13*, 2582–2587, cited By 15. 8

[47] J. Mercurio, A. Caballero, J. Cookson, P. Beer, *RSC Advances* **2015**, *5*, 9298–9306, cited By 9. 8

[48] V. Amendola, G. Alberti, G. Bergamaschi, R. Biesuz, M. Boiocchi, S. Ferrito, F.-P. Schmidtchen, *European Journal of Inorganic Chemistry* **2012**, 3410–3417, cited By 15. 8

[49] R. Alberto, G. Bergamaschi, H. Braband, T. Fox, V. Amendola, *Angewandte Chemie - International Edition* **2012**, *51*, 9772–9776, cited By 26. 8

[50] M. J. Frisch, G. W. Trucks, H. B. Schlegel, G. E. Scuseria, M. A. Robb, J. R. Cheeseman, G. Scalmani, V. Barone, B. Mennucci, G. A. Petersson, H. Nakatsuji, M. Caricato, X. Li, H. P. Hratchian, A. F. Izmaylov, J. Bloino, G. Zheng, J. L. Sonnenberg, M. Hada, M. Ehara, K. Toyota, R. Fukuda, J. Hasegawa, M. Ishida, T. Nakajima, Y. Honda, O. Kitao, H. Nakai, T. Vreven, J. A. Montgomery, Jr., J. E. Peralta, F. Ogliaro, M. Bearpark, J. J. Heyd, E. Brothers, K. N. Kudin, V. N. Staroverov, R. Kobayashi, J. Normand, K. Raghavachari, A. Rendell, J. C. Burant, S. S. Iyengar, J. Tomasi, M. Cossi, N. Rega, J. M. Millam, M. Klene, J. E. Knox, J. B. Cross, V. Bakken, C. Adamo, J. Jaramillo, R. Gomperts, R. E. Stratmann, O. Yazyev, A. J. Austin, R. Cammi, C. Pomelli, J. W. Ochterski, R. L. Martin, K. Morokuma, V. G. Zakrzewski, G. A. Voth, P. Salvador, J. J. Dannenberg, S. Dapprich, A. D. Daniels, Farkas, J. B. Foresman, J. V. Ortiz, J. Cioslowski, D. J. Fox, *Gaussian 09 Revision B.01*, Gaussian Inc. Wallingford CT 2009. 9, 25, 64, 116

[51] A. D. Becke, *The Journal of Chemical Physics* **1993**, *98*, 5648–5652. 9, 23, 25, 26, 64, 90

[52] C. Lee, W. Yang, R. G. Parr, *Physical Review B* **1988**, *37*, 785. 9

[53] S. H. Vosko, L. Wilk, M. Nusair, *Canadian Journal of physics* **1980**, *58*, 1200–1211. 9, 116

[54] P. J. Stephens, F. J. Devlin, C. F. Chabalowski, M. J. Frisch, *The Journal of Physical Chemistry* **1994**, *98*, 11623–11627. 9, 26

[55] M. Cossi, N. Rega, G. Scalmani, V. Barone, *Journal of Computational Chemistry* **2003**, *24*, 669–681. 9, 26, 27, 64

[56] R. Ditchfield, *Molecular Physics* **1974**, *27*, 789–807, cited By 2973. 9

[57] K. Wolinski, J. Hinton, P. Pulay, *Journal of the American Chemical Society* **1990**, *112*, 8251–8260, cited By 4455. 9

[58] B. Hay, R. Custelcean, *Crystal Growth and Design* **2009**, *9*, 2539–2545, cited By 85. 11

[59] M. Cametti, K. Raatikainen, P. Metrangolo, T. Pilati, G. Terraneo, G. Resnati, *Organic and Biomolecular Chemistry* **2012**, *10*, 1329–1333, cited By 64. 11

[60] V. Amendola, M. Boiocchi, L. Fabbrizzi, A. Palchetti, *Chemistry - A European Journal* **2005**, *11*, 120–127, cited By 94. 12, 15, 17

[61] K. Wallace, W. Belcher, D. Turner, K. Syed, J. Steed, *Chem.-Eur. J.* **2005**, *11*, 5648–5660, cited By 1. 15

[62] V. Amendola, M. Boiocchi, L. Fabbrizzi, A. Palchetti, *Chemistry - A European Journal* **2005**, *11*, 5648–5660, cited By 103. 15, 17

[63] E. Niki, *Free Radical Research* **2000**, *33*, 693–704. 21

[64] M. E. Inal, G. Kanbak, E. Sunal, *Clinica Chimica Acta* **2001**, *305*, 75–80. 21

[65] M. C. Morris, D. A. Evans, J. L. Bienias, C. C. Tangney, D. A. Bennett, N. Aggarwal, R. S. Wilson, P. A. Scherr, *Journal of the American Medical Association* **2002**, *287*, 3230–3237. 21

[66] A. Capobianco, T. Caruso, M. Celentano, M. V. La Rocca, A. Peluso, *The Journal of Chemical Physics* **2013**, *139*, 145101. 21

[67] W. R. Markesbery, J. M. Carney, *Brain Pathology* **1999**, *9*, 133–146. 21

[68] A. Agarwal, S. Gupta, L. Sekhon, R. Shah, *Antioxidants & Redox Signaling* **2008**, *10*, 1375–1404. 21

[69] G. T. Wondrak, *Antioxidants & Redox Signaling* **2009**, *11*, 3013–3069. 21

[70] H. E. de Vries, M. Witte, D. Hondius, A. J. M. Rozemuller, B. Drukarch, J. Hoozemans, J. van Horssen, *Free Radical Biology and Medicine* **2008**, *45*, 1375–1383. 21

[71] M. S. Cooke, M. D. Evans, M. Dizdaroglu, J. Lunec, *The FASEB Journal* **2003**, *17*, 1195–1214. 21

[72] M. G. L. Hertog, E. J. M. Feskens, D. Kromhout, P. C. H. Hollman, M. B. Katan, *The Lancet* **1993**, *342*, 1007–1011. 21

[73] A. Trichopoulou, E. Vasilopoulou, *British Journal of Nutrition* **2000**, *84*, S205—-S209. 21

[74] P. Trouillas, P. Marsal, D. Siri, R. Lazzaroni, J.-L. Duroux, *Food Chemistry* **2006**, *97*, 679–688. 21, 24, 27, 33

[75] E. Cadenas, L. Packer, *Handbook of Antioxidants, 2002.* 21

[76] J. S. Wright, E. R. Johnson, G. a. DiLabio, *Journal of the American Chemical Society* **2001**, *123*, 1173–1183. 21

[77] L.-F. Wang, H.-Y. Zhang, *Bioorganic & Medicinal Chemistry Letters* **2003**, *13*, 3789–3792. 22, 23

[78] J. P. Cerón-Carrasco, H. M. Roy, J. Cerezo, D. Jacquemin, A. D. Laurent, *Chemical Physics Letters* **2014**, *599*, 73–79. 22, 23

[79] G. Mazzone, N. Malaj, N. Russo, M. Toscano, *Food Chemistry* **2013**, *141*, 2017–24. 23, 24, 41

[80] D. Kozlowski, P. Trouillas, C. Calliste, P. Marsal, R. Lazzaroni, J.-L. Duroux, *The Journal of Physical Chemistry A* **2007**, *111*, 1138–45. 23, 24, 26

[81] R. S. Borges, A. N. Queiroz, J. R. Silva, A. P. S. Mendes, A. M. Herculano, A. M. J. Chaves Neto, A. B. F. da Silva, *Structural Chemistry* **2012**, *24*, 349–355. 23, 27

[82] K. Sadasivam, R. Kumaresan, *Molecular Physics* **2011**, *109*, 839–852. 23, 46

[83] M. Leopoldini, N. Russo, M. Toscano, *Food Chemistry* **2011**, *125*, 288–306. 23, 24, 26, 27, 28, 41

[84] A. Bentes, R. Borges, W. Monteiro, L. De Macedo, C. Alves, *Molecules* **2011**, *16*, 1749–1760. 23

[85] G. Wang, Y. Xue, L. An, Y. Zheng, Y. Dou, L. Zhang, Y. Liu, *Food Chemistry* **2015**, *171*, 89–97. 23

[86] A. Pérez-González, A. M. Rebollar-Zepeda, J. R. León-carmona, A. Galano, D. D. Química, U. Autónoma, M.-i. S. Rafael, C. Vicentina, *Journal of Mexican Chemical Society* **2012**, *56*, 241–249. 23, 26

[87] A. Pérez-González, A. Galano, *The Journal of Physical Chemistry. B* **2011**, *115*, 1306–1314. 23, 24, 38

[88] A. Pérez-González, A. Galano, *International Journal of Quantum Chemistry* **2012**, *112*, 3441–3448. 23, 24, 38

[89] N. Nenadis, M. Z. Tsimidou, *Food Research International* **2012**, *48*, 538–543. 23, 24, 26

[90] E. Klein, V. Luke, *Journal of Physical Chemistry A* **2006**, 12312–12320. 23, 24, 26, 54

[91] E. Klein, V. Lukeš, M. Ilčin, *Chemical Physics* **2007**, *336*, 51–57. 23, 24

[92] I. Borges, J. A. Aquino, A. Ko, R. Nieman, W. L. Hase, L. X. Chen, H. Lischka, *Journal of the American Chemical Society* **2013**, 10–13. 23, 33

[93] M. Leopoldini, T. Marino, N. Russo, M. Toscano, *Theoretical Chemistry Accounts: Theory, Computation, and Modeling (Theoretica Chimica Acta)* **2004**, *111*, 210–216. 23, 27, 28

[94] A. Galano, M. F. Marquez, *Chemical Research in Toxicology* **2014**, *27*, 904–918. 23, 24

[95] A. Vega-Rodriguez, J. R. Alvarez-Idaboy, *Physical Chemistry Chemical Physics* **2009**, *11*, 7649–7658. 23

[96] B. Chan, L. Radom, *Theoretical Chemistry Accounts* **2011**, *130*, 251–260. 23

[97] Y. Zhao, D. G. Truhlar, *Accounts of Chemical Research* **2008**, *41*, 157–167. 23, 25, 26

[98] J. A. Montgomery Jr, M. J. Frisch, J. W. Ochterski, G. A. Petersson, *The Journal of Chemical Physics* **1999**, *110*, 2822–2827. 24, 27

[99] J. A. Montgomery Jr, M. J. Frisch, J. W. Ochterski, G. A. Petersson, *The Journal of Chemical Physics* **2000**, *112*, 6532–6542. 24, 27

[100] S. Zhang, Z.-Q. Deng, *Organic & Biomolecular Chemistry* **2016**, *4*, 1166–1169. 24, 63

[101] T. Watanabe, S. Yuki, M. Egawa, H. Nishi, *Journal of Pharmacology and Experimental Therapeutics* **1994**, *268*, 1597–1604. 24

[102] B. H. Havsteen, *Pharmacology & Therapeutics* **2002**, *96*, 67–202. 24

[103] S.-Y. Jung, H.-J. Kim, J.-Y. Lee, J.-S. Cho, Y.-S. Lee, C.-B. Jin, *Bulletin of the Korean Chemical Society* **2012**, *33*, 2443–2446. 24

[104] A. Amić, Z. Marković, J. M. D. Marković, V. Stepanić, B. Lučić, D. Amić, *Food Chemistry* **2014**, *152*, 578–585. 25

[105] P. J. Wilson, T. J. Bradley, D. J. Tozer, *The Journal of Chemical Physics* **2001**, *115*, 9233–9242. 25, 26

[106] C. Adamo, V. Barone, *Chemical Physics Letters* **1997**, *274*, 242–250. 25, 26

[107] A. D. Boese, J. M. L. Martin, *The Journal of Chemical Physics* **2004**, *121*, 3405–3416. 25, 26

[108] X. Xu, W. A. Goddard, *Proceedings of the National Academy of Sciences of the United States of America* **2004**, *101*, 2673–2677. 25, 26

[109] S. Grimme, *Journal of Computational Chemistry* **2006**, *27*, 1787–1799. 25, 26

[110] A. D. Becke, *The Journal of Chemical Physics* **1993**, *98*, 1372–1377. 25, 26

[111] C. Adamo, V. Barone, *The Journal of Chemical Physics* **1998**, *108*, 664–675. 25, 26

[112] B. J. Lynch, P. L. Fast, M. Harris, D. G. Truhlar, *The Journal of Physical Chemistry A* **2000**, *104*, 4811–4815. 25, 26

[113] C. Adamo, V. Barone, *The Journal of Chemical Physics* **1999**, *110*, 6158–6170. 25, 26

[114] M. Ernzerhof, G. E. Scuseria, *The Journal of Chemical Physics* **1999**, *110*, 5029–5036. 25, 26

[115] Y. Zhao, D. G. Truhlar, *The Journal of Physical Chemistry A* **2006**, *110*, 13126–13130. 25, 26

[116] Y. Zhao, N. E. Schultz, D. G. Truhlar, *Journal of Chemical Theory and Computation* **2006**, *2*, 364–382. 25, 26, 27

[117] T. Yanai, D. P. Tew, N. C. Handy, *Chemical Physics Letters* **2004**, *393*, 51–57. 25, 26

[118] H. Iikura, T. Tsuneda, T. Yanai, K. Hirao, *The Journal of Chemical Physics* **2001**, *115*, 3540–3544. 25, 26

[119] O. A. Vydrov, J. Heyd, A. V. Krukau, G. E. Scuseria, *The Journal of Chemical Physics* **2006**, *125*, 74106. 25, 26

[120] O. A. Vydrov, G. E. Scuseria, *The Journal of Chemical Physics* **2006**, *125*, 234109. 25, 26

[121] J.-D. Chai, M. Head-Gordon, *Physical Chemistry Chemical Physics* **2008**, *10*, 6615–6620. 25, 26

[122] J.-D. Chai, M. Head-Gordon, *The Journal of Chemical Physics* **2008**, *128*, 84106. 25, 26

[123] S. Grimme, *The Journal of Chemical Physics* **2006**, *124*, 34108. 25, 26

[124] V. Barone, C. Adamo, *Chemical Physics Letters* **1994**, *224*, 432–438. 26

[125] J. Rimarčík, V. Lukeš, E. Klein, M. Ilčin, *Journal of Molecular Structure: THEOCHEM* **2010**, *952*, 25–30. 26

[126] Y. Xue, L. Zhang, Y. Li, D. Yu, Y. Zheng, L. An, X. Gong, Y. Liu, *Journal of Physical Organic Chemistry* **2013**, *26*, 240–248. 27, 41, 55

[127] T. Vondrok, Z. Bastl, S. Bohm, *Journal of the Chemical Society, Perkin Transactions 2* **1988**, 641. 27

[128] N. Russo, M. Toscano, N. Uccella, *Journal of Agricultural and Food Chemistry* **2000**, *48*, 3232–3237. 28

[129] J. Tomasi, B. Mennucci, R. Cammi, *Chemical Reviews* **2005**, *105*, 2999–3094. 31

[130] C. Adamo, F. Lelj, *Chemical Physics Letters* **1994**, *223*, 54–60. 31

[131] I. Ciofini, H. Chermette, C. Adamo, *Chemical Physics Letters* **2003**, *380*, 12–20. 33

[132] G. F. Mangiatordi, E. Bremond, C. Adamo, *Journal of Chemical Theory and Computation* **2012**, *8*, 3082–3088. 36

[133] M. Savarese, É. Brémond, C. Adamo, *Theoretical Chemistry Accounts* **2016**, *135*, 99. 40

[134] L. Goerigk, *The Journal of Physical Chemistry Letters* **2015**, *6*, 3891–3896. 40

[135] K. Dropkova, J. Lengyel, E. Klein, A. Vaganek, J. Rimarc, *Computational and Theoretical Chemistry* **2014**, *1050*, 31–38. 54

[136] A. Benayahoum, H. Amira-Guebailia, O. Houache, *Computational and Theoretical Chemistry* **2014**, *1037*, 1–9. 54

[137] M. Najafi, K. H. Mood, M. Zahedi, E. Klein, *Computational and Theoretical Chemistry* **2011**, *969*, 1–12. 54

[138] K. L. Wolfe, R. H. Liu, *Journal of Agricultural and Food Chemistry* **2008**, *56*, 8404–8411. 54, 55, 56

[139] E. T. Arung, S. Furuta, H. Ishikawa, I. W. Kusuma, K. Shimizu, R. Kondo, *Food Chemistry* **2011**, *124*, 1024–1028. 55

[140] R. Ho, A. Violette, D. Cressend, P. Raharivelomanana, P.-A. Carrupt, K. Hostettmann, *Natural Product Research* **2012**, *26*, 274–277. 54, 55

[141] B. Ou, M. Hampsch-Woodill, R. L. Prior, *Journal of Agricultural and Food Chemistry* **2001**, *49*, 4619–4626. 54, 55

[142] B. Biloa Messi, R. Ho, A. Meli Lannang, D. Cressend, K. Perron, A. E. Nkengfack, P.-A. Carrupt, K. Hostettmann, M. Cuendet, *Pharmaceutical Biology* **2014**, *52*, 706–711. 54, 55

[143] M. Lautens, W. Klute, W. Tam, *Chemical Review* **1996**, *96*, 49–92. 63

[144] N. J. Xiaoqiang Huang, Zinyao Li, *Chemical Science* **2015**, *6*, 6355–6360. 63

[145] R. Berg, B. F. Straub, *Beilstein Journal of Organic Chemistry* **2013**, *9*, 2715–2750. 63

[146] C. Özen, N. Tüzün, *Journal of Molecular Graphics and Modelling* **2012**, *34*, 101–107. 63

[147] I. Kalvet, J. Tammiku-Taul, U. Mäeorg, K. Tämm, P. Burk, L. Sikk, *ChemCatChem* **2016**, *8*, 1804–1808. 63

[148] Q. Xiao, L. Ling, F. Ye, R. Tan, L. Tian, Y. Zhang, Y. Li, J. Wang, *Journal of Organic Chemistry* **2013**, *78*, 3879–3885. 63

[149] G. Y. Ruan, Y. Zhang, Z. H. Qi, D. X. Ai, W. Liu, Y. Wang, *Computational and Theoretical Chemistry* **2015**, *1054*, 16–21. 63

[150] L.-L. Zhang, S.-J. Li, L. Zhang, D.-C. Fang, *Organic & Biomolecular Chemistry* **2016**, *14*, 4426–4435. 63

[151] Y. Zhao, Y. Liu, S. Bi, Y. Liu, *Journal of Organometallic Chemistry* **2013**, *745-746*, 166–172. 63

[152] G. Lefevre, G. Franc, A. Tlili, C. Adamo, M. Taillefer, I. Ciofini, A. Jutand, *Organometallics* **2012**, *31*, 7694–7707. 63

[153] L. Belding, S. Chemler, T. Dudding, *The Journal of Organic Chemistry* **2013**, 10288–10297. 63

[154] I. Alonso, J. Esquivias, R. Gómez-Arrayás, J. C. Carretero, *Journal of Organic Chemistry* **2008**, *73*, 6401–6404. 63

[155] C. E. Kefalidis, A. A. Kanakis, J. K. Gallos, C. A. Tsipis, *Journal of Organometallic Chemistry* **2010**, *695*, 2030–2038. 63

[156] J. Jover, F. Maseras, *The Journal of Organic Chemistry* **2014**, *79*, 11981–11987. 63

[157] S. Gazzola, E. M. Beccalli, T. Borelli, C. Castellano, M. A. Chiacchio, D. Diamante, G. Broggini, *Journal of Organic Chemistry* **2015**, *80*, 7226–7234. 63, 64

[158] M. J. Frisch, M. Head-Gordon, J. A. Pople, *Chemical Physics Letters* **1990**, *166*, 275–280. 64

[159] M. J. Frisch, M. Head-Gordon, J. A. Pople, *Chemical Physics Letters* **1990**, *166*, 281–289. 64

[160] M. Head-Gordon, J. A. Pople, M. J. Frish, *Chemical Physics Letters* **1988**, *153*, 503–506. 64

[161] S. Saevo, J. Almlof, *Chemical Physics Letters* **1989**, *154*, 83–89. 64

[162] M. Head-Gordon, T. Head-Gordon, *Chemical Physics Letters* **1994**, *220*, 122–128. 64

[163] W. J. Lauderdale, J. F. Stanton, J. Gauss, J. D. Watts, R. J. Bartlett, *Chemical Physics Letters* **1991**, *187*, 21–28. 64

[164] W. J. Lauderdale, J. F. Stanton, J. Gauss, J. D. Watts, R. J. Bartlett, *The Journal of Chemical Physics* **1992**, *97*, 6606–6620. 64

[165] Y. Dang, X. Deng, J. Guo, C. Song, W. Hu, Z. X. Wang, *Journal of the American Chemical Society* **2016**, *138*, 2712–2723. 65

[166] Y. Li, Z. Lin, *Organometallics* **2015**, *34*, 3538–3545. 65

[167] L. Izzo, M. Mella, *Organometallics* **2013**, *32*, 3192–3202. 79, 90, 116, 118, 122, 134, 141

[168] G. Guerra, M. Galimberti, F. Piemontesi, O. de Ballesteros, *Journal of the American Chemical Society* **2002**, *124*, 1566–1567. 79

[169] G. Odian, *Principles of Copolymerization, 3rd ed.*, Wiley & Sons: New York, **1991**. 79, 83, 89, 106

[170] K. Angermund, G. Fink, V. R. Jensen, R. Kleinschmidt, *Chemical Reviews* **2000**, *100*, 1457–1470. 80

[171] G. W. Coates, *Chemical Reviews* **2000**, *100*, 1223–1252. 80

[172] E. Y.-X. Chen, T. J. Marks, *Chemical Reviews* **2000**, *100*, 1391–1434. 80, 131

[173] A. K. Rappe', W. M. Skiff, C. J. Casewit, *Chemical Reviews* **2000**, *100*, 1435–1456. 80

[174] G. W. Coates, *Journal of the Chemical Society, Dalton Transaction* **2002**, 467–475. 80

[175] G. Vigliotta, M. Mella, D. Rega, L. Izzo, *Biomacromolecules* **2012**, *13*, 833–841. 80, 87, 90

[176] N. T. J. Bailey, *The Elements of Stochastic Processes*, Wiley, New York, **1964**. 81

[177] J. L. Doob, *Stochastic Processes*, Wiley, New York, **1953**. 81

[178] R. Norris, *Markov Chains*, Cambridge University Press, UK, **1997**. 81

[179] W. Feller, *An Introduction to Probability Theory and its Applications, Vol. 1*, Wiley, New York, **1966**. 81

[180] D. T. Gillespie, *The Journal of Chemical Physics* **1981**, *74*, 661–678. 82

[181] K. A. Fichthorn, W. H. Weinberg, *The Journal of Chemical Physics* **1991**, *95*, 1090–1096. 82

[182] P. Kratzer, *arXiv: 0904.2556v1* **2009**. 82

[183] D. Bernstei, *Physical Review E - Statistical, Nonlinear, and Soft Matter Physics* **2005**, *71*, 1–13. 82

[184] K. Reuter, *Modeling and Simulation of Heterogeneous Catalytic Reactions* **2011**, 71–111. 82

[185] D. T. Gillespie, *Journal of Computational Physics* **1976**, *22*, 403–434. 82

[186] D. T. Gillespie, *The journal of Physical Chemistry* **1977**, *81*, 2340–2361. 82

[187] A. F. Voter, *Introduction to the Kinetic Monte Carlo Method*, Springer Netherlands, Dordrecht, **2007**. 82, 135

[188] G. Natta, G. Mazzanti, A. Valvassori, G. Sartori, D. Morero, *Chimica e Industria (Milan)* **1960**, *42*, 125. 85

[189] F. R. Mayo, F. M. Lewis, *Journal of the American Chemical Society* **1944**, *66*, 1594–1601. 85

[190] M. Fineman, S. D. Ross, *Journal of Polymer Science* **1950**, *5*, 259–262. 85

[191] T. Kelen, F. Tudos, *Journal of Macromolecular Science: Part A - Chemistry* **1975**, *9*, 1–27. 85

[192] M. Galimberti, F. Piemontesi, O. Fusco, I. Camurati, M. Destro, *Macromolecules* **1998**, *31*, 3409–3416. 85, 137

[193] I. Skeist, *Journal of American Chemical Society* **1946**. 85

[194] E.-R. Kenawy, S. D. Worley, R. Broughton, *Biomacromolecules* **2007**, *8*, 1359–1384. 86

[195] N. G. Hoogeveen, M. A. C. Stuart, G. J. Fleer, *Colloids and Surfaces A: Physicochemical and Engineering Aspects* **1996**, *117*, 77–88. 86

[196] S. Zhu, N. Yang, D. Zhang, *Materials Chemistry and Physics* **2009**, *113*, 784–789. 86

[197] M. Mella, L. Izzo, *Polymer* **2010**, *51*, 3582 – 3589. 87

[198] L. Izzo, P. C. Griffiths, R. Nilmini, S. M. King, K.-L. Wallom, E. L. Ferguson, R. Duncan, *International Journal of Pharmaceutics* **2011**, *408*, 213 – 222. 87

[199] S. Matrella, C. Vitiello, M. Mella, G. Vigliotta, L. Izzo, *Macromolecular Bioscience* **2015**, *15*, 927–940. 87, 90

[200] M. Meuwly, M. Karplus, *The Journal of Chemical Physics* **2002**, *116*, 2572–2585. 87

[201] A. Ponti, M. Mella, *The Journal of Physical Chemistry A* **2003**, *107*, 7589–7596. 87, 104

[202] V. Butun, S. P. Armes, N. C. Billingham, *Polymer* **2001**, *42*, 5993–6008. 88

[203] A. J. Limer, A. K. Rullay, V. S. Miguel, C. Peinado, S. Keely, E. Fitzpatrick, S. D. Carrington, D. Brayden, D. M. Haddleton, *Reactive and Functional Polymers* **2006**, *66*, 51–64. 88

[204] S. B. Lee, R. R. Koepsel, S. W. Morley, K. Matyjaszewski, Y. Sun, A. J. Russell, *Biomacromolecules* **2004**, *5*, 877–882. 88

[205] S. Lenoir, C. Pagnoulle, C. Detrembleur, M. Galleni, R. Jerome, *e-Polymers* **2005**. 88

[206] J. Huang, H. Murata, R. R. Koepsel, A. J. Russell, K. Matyjaszewski, *Biomacromolecules* **2007**, *8*, 1396–1399. 88

[207] S. Villani, R. Adami, E. Reverchon, A. M. Ferretti, A. Ponti, M. Lepretti, I. Caputo, L. Izzo, *Journal of Drug Targeting* **2017**, *25*, 899–909. 88, 104, 114

[208] M. C. Barrella, A. Di Capua, R. Adami, E. Reverchon, M. Mella, L. Izzo, *Supramolecular Chemistry* **2017**, *29*, 796–807. 88, 104, 114

[209] K. Matyjaszewski, *Progress in Polymer Science* **2005**, *30*, 858 – 875, Plenary Lectures. 88

[210] K. Matyjaszewski, M. J. Ziegler, S. V. Arehart, D. Greszta, T. Pakula, *Journal of Physical Organic Chemistry* **2000**, *13*, 775–786. 88

[211] C. J. Hawker, A. W. Bosman, E. Harth, *Chemical Reviews* **2001**, *101*, 3661–3688, PMID: 11740918. 88

[212] N. Hadjichristidis, H. Iatrou, M. Pitsikalis, J. Mays, *Progress in Polymer Science* **2006**, *31*, 1068 – 1132, 50 years of living polymerization. 88

[213] P. Cotanda, D. B. Wright, M. Tyler, R. K. O'Reilly, *Journal of Polymer Science Part A: Polymer Chemistry* **2013**, *51*, 3333–3338. 88, 97, 107

[214] S. G. Roy, K. Bauri, S. Pal, A. Goswami, G. Madras, P. De, *Polymer International* **2013**, *62*, 463–473. 88, 97, 107

[215] M. Camail, H. Essaoudi, A. Margaillan, J. Vernet, *European Polymer Journal* **1995**, *31*, 1119 – 1125. 88, 97

[216] X. Pang, H. SWun, Q. Shen, *Polymer* **2004**, *45*, 4029 – 4035. 88, 97, 107

[217] E. Wigner, *Transactions of the Faraday Society* **1938**, *34*. 89

[218] G. H. Vineyard, *Journal of Physics and Chemistry of Solids* **1957**, *3*, 121 – 127. 89

[219] R. E. Skyner, J. L. McDonagh, C. R. Groom, T. van Mourik, J. B. O. Mitchell, *Physical Chemistry and Chemical Physics* **2015**, *17*, 6174–6191. 90

[220] M. Mella, L. Izzo, C. Capacchione, *ACS Catal.* **2011**, *1*, 1460. 90

[221] M. Mella, L. Mollica, L. Izzo, *Journal of Polymer Physics: Part B* **2015**, *53*, 650. 90, 104, 114

[222] M. Mella, L. Izzo, *Journal of Polymer Physics: Part B* **2017**, *55*, 1088. 90, 104, 114

[223] H. J. Harwood, *Makromolekulare Chemie. Macromolecular Symposia* **1987**, *10-11*, 331– 354. 91

[224] B. Klumperman, K. F. O. Driseoll, *Polymer* **1993**, *34*, 1032–1037. 91

[225] L. K. Christov, G. S. Georgiev, *Macromolecular Theory and Simulations* **2000**, *9*, 715–724. 92

[226] D. J. Wales, *International Reviews in Physical Chemistry* **2006**, *25*, 237–282. 93

[227] J. Chocholoušová, J. Vacek, P. Hobza, *The Journal of Physical Chemistry A* **2003**, *107*, 3086–3092. 93, 94

[228] D. Di Tommaso, *CrystEngComm* **2013**, *15*, 6564–6577. 93, 94

[229] F. Ramondo, L. Bencivenni, R. Caminiti, A. Pieretti, L. Gontrani, *Physical Chemistry Chemical Physics* **2007**, *9*, 2206–2215. 93

[230] R. F. Ribeiro, A. V. Marenich, C. J. Cramer, D. G. Truhlar, *Physical Chemistry Chemical Physics* **2011**, *13*, 10908–10922. 93

[231] D. Di Tommaso, K. L. Watson, *The Journal of Physical Chemistry A* **2014**, *118*, 11098–11113. 93, 94

[232] H. Pašalić, A. J. A. Aquino, D. Tunega, G. Haberhauer, M. H. Gerzabek, H. C. Georg, T. F. Moraes, K. Coutinho, S. Canuto, H. Lischka, *Journal of Computational Chemistry* **2010**, *31*, 2046–2055. 93

[233] P. Friant-Michel, M. F. Ruiz-López, *ChemPhysChem* **2010**, *11*, 3499–3504. 93, 94

[234] M. Fioroni, D. Vogt, *The Journal of Physical Chemistry B* **2004**, *108*, 11774–11781. 94

[235] P. E. M. Lopes, G. Lamoureux, B. Roux, A. D. MacKerell, *The Journal of Physical Chemistry B* **2007**, *111*, 2873–2885. 94

[236] C. M. Baker, G. H. Grant, *Journal of Chemical Theory and Computation* **2007**, *3*, 530–548. 94

[237] C. Nieto-Draghi, P. Bonnaud, P. Ungerer, *The Journal of Physical Chemistry C* **2007**, *111*, 15686–15699. 94

[238] T. Kuznicki, J. H. Masliyah, S. Bhattacharjee, *Energy & Fuels* **2008**, *22*, 2379–2389. 94

[239] T. F. Headen, E. S. Boek, N. T. Skipper, *Energy & Fuels* **2009**, *23*, 1220–1229. 94

[240] M. Sedghi, L. Goual, W. Welch, J. Kubelka, *The Journal of Physical Chemistry B* **2013**, *117*, 5765–5776. 94

[241] A. Sharma, L. Liu, S. Parameswaran, S. M. Grayson, H. S. Ashbaugh, S. W. Rick, *The Journal of Physical Chemistry B* **2016**, *120*, 10603–10610. 94

[242] D. A. Singleton, D. T. Nowlan, N. Jahed, K. Matyjaszewski, *Macromolecules* **2003**, *36*, 8609–8616. 97

[243] K. Levenberg, *Quarterly of Applied Mathematics* **1944**, *2*, 164–168. 99

[244] D. W. Marquardt, *Journal of the Society for Industrial and Applied Mathematics* **1963**, *11*, 431–441. 99

[245] T. Williams, C. Kelley, many others, *Gnuplot 4.4: an interactive plotting program*, http://gnuplot.sourceforge.net/, **2010**. 99

[246] D. Fournier, R. Hoogenboom, H. M. L. Thijs, R. M. Paulus, U. S. Schubert, *Macromolecules* **2007**, *40*, 915–920. 102, 114

[247] M. Mella, A. Ponti, *ChemPhysChem* **2006**, 894. 104

[248] J. Lad, S. Harrisson, G. Mantovani, D. M. Haddleton, *Dalton Transactions* **2003**, 4175–4180. 110, 114

[249] V. Coessens, T. Pintauer, K. Matyjaszewski, *Progress in Polymer Science* **2001**, *26*, 337 – 377. 110

[250] G. Martinez, M. Sanchez-Chaves, E. Lopez Madruga, *Journal of Polymer Science Part A: Polymer Chemistry* **2002**, *40*, 2427–2434. 113

[251] C. Fernández-Monreal, G. Martínez, M. Sánchez-Chaves, E. López Madruga, *Journal of Polymer Science Part A: Polymer Chemistry* **2001**, *39*, 2043–2048. 113

[252] L. Martín-Gomis, R. Cuervo-Rodriguez, M. C. Fernández-Monreal, E. L. Madruga, M. Fernández-García, *Journal of Polymer Science Part A: Polymer Chemistry* **2003**, *41*, 2659–2666. 113

[253] A. A. Kavitha, N. K. Singha, *Macromolecular Chemistry and Physics* **2007**, *208*, 2569–2577. 114

[254] P. Maksym-Bębenek, T. Biela, D. Neugebauer, *Reactive and Functional Polymers* **2014**, *82*, 33 – 40. 114

[255] I. Ydens, P. Degée, D. M. Haddleton, P. Dubois, *European Polymer Journal* **2005**, *41*, 2255 – 2263. 114

[256] F. G. Karssenberg, V. B. F. Mathot, T. J. G. Zwartkruis, *Journal of Polymer Science Part B: Polymer Physics* **2006**, *44*, 722–737. 115

[257] F. G. Karssenberg, C. Piel, A. Hopf, V. B. F. Mathot, W. Kaminsky, *Journal of Polymer Science, Part B: Polymer Physics* **2006**, *44*, 747–755. 115

[258] G. Monaco, *Macromolecules* **2001**, *34*, 4406–4415. 115

[259] E. Zurek, T. Ziegler, *Progress in Polymer Science* **2004**, *29*, 107–148. 115, 122, 131

[260] M. Dahlmann, G. Erker, K. Bergander, *Journal of American Chemical Society* **2000**, *122*, 7986–7998. 115

[261] M. Galimberti, F. Piemontesi, N. Mascellani, I. Camurati, O. Fusco, M. Destro, *Macromolecules* **1999**, *32*, 7968–7976. 116, 137

[262] A. D. Becke, *Physical Review B* **1986**, *33*, 8822. 116

[263] J. P. Perdew, *Physical Review B* **1986**, *33*, 8822. 116

[264] P. J. Hay, W. R. Wadt, *The Journal of Chemical Physics* **1985**, *82*, 299–310. 116

[265] A. Schafer, C. Huber, R. Ahlrichs, *The Journal of Chemical Physics* **1994**, *100*, 5829–5835. 116

[266] K. Šolc, W. H. Stockmayer, *The Journal of Chemical Physics* **1971**, *54*, 2981–2988. 126, 145

[267] K. Šolc, W. H. Stockmayer, *International Journal of Chemical Kinetics* **1973**, *5*, 733–752. 126, 145

[268] D. Shoup, G. Lipari, A. Szabo, *Biophysical Journal* **1981**, *36*, 697–714. 126, 128, 145

[269] Y.-X. Chen, M. V. Metz, L. Li, C. L. Stern, T. J. Marks, *Journal of the American Chemical Society* **1998**, *120*, 6287–6305. 131

[270] X. Yang, C. L. Stern, T. J. Marks, *Organometallics* **1991**, *10*, 840–842. 131

[271] L. Jia, X. Yang, A. Ishihara, T. J. Marks, *Organometallics* **1995**, *14*, 3135–3137. 131